

**Examination of the Feasibility of Transferred Electron  
Devices For Optoelectronic Interaction :  
Theory and Experiment**

A Thesis submitted to the Faculty of Engineering  
of the University of Glasgow for the Degree of

**Doctor of Philosophy**

by

**Matthew Kilburn**

**October 1994**

ProQuest Number: 13815448

All rights reserved

INFORMATION TO ALL USERS

The quality of this reproduction is dependent upon the quality of the copy submitted.

In the unlikely event that the author did not send a complete manuscript and there are missing pages, these will be noted. Also, if material had to be removed, a note will indicate the deletion.



ProQuest 13815448

Published by ProQuest LLC (2018). Copyright of the Dissertation is held by the Author.

All rights reserved.

This work is protected against unauthorized copying under Title 17, United States Code  
Microform Edition © ProQuest LLC.

ProQuest LLC.  
789 East Eisenhower Parkway  
P.O. Box 1346  
Ann Arbor, MI 48106 – 1346

Thesis  
10082  
Copy 1



## **Acknowledgements**

Primary acknowledgements are given to G. Hopkins, for her invaluable assistance in the Dry-etching facility. Many thanks are given to the Head of Department, Prof. Peter Laybourn, and his administrative secretary, Mrs. Jessica Reid, for their support and assistance in the submission procedure.

Significant appreciation is expressed for the CASE sponsorship of the project work shown in this thesis, courtesy of Dr. N.G. Walker, Optical Subsystems Group, BT Laboratories, Martlesham Heath, Ipswich, Suffolk, IP5 7RE.

Many thanks to Miss Tara Brown for her warmth, understanding and support throughout my final year in Glasgow, and to her appreciation of my efforts at critical stages. It would not have been possible without her.

## **Proposed Publications**

Scripts are in the process of editing / modification for re-submission, at the time of binding of this thesis. The titles of these proposed papers include :-

[1] KILBURN, M., STANLEY, C. R. : "Cathode Boundary Determination Through Annealed Contact Metallisation - Injection-Limited TEDs", submitted February 1994 to IEEE Trans. Elec. Dev. Will be re-submitted to IEEE Trans. Microwave Theory and Techniques

[2] KILBURN, M. : "Derivation of a Theoretical Current-Voltage Function for Tapered and Non-Tapered Transferred Electron Devices", submitted March 1994 to Appl. Phys. Lett. Will be re-submitted to IEEE Trans. Microwave Theory and Techniques as either one or two separate papers.

# Contents

<u>Contents</u>	<u>Page Number</u>
<b>Acknowledgements</b>	<b>i</b>
<b>Proposed publications</b>	<b>i</b>
<b>Contents</b>	<b>ii</b>
<b>Summary</b>	<b>vi</b>
<b>Chapter 1 :- Introduction</b>	<b>1</b>
1.1 The Gallium Arsenide-Aluminium Gallium Arsenide Material System	1
1.2 Justification for Research	4
<b>Chapter 2 :- The Transferred Electron Effect</b>	<b>7</b>
2.1 The Intervalley Transfer Mechanism	7
2.2 The Development of Inhomogeneities - Linear Analysis	
2.2.1 Nucleation of Disturbances	9
2.3 Transit ("Gunn") mode	11
2.4 The Cathode Boundary conditions	12
2.4.1 Imperfect Cathode Boundary Conditions	13
<b>Chapter 3 :- Theory of Modulation in Transferred Electron Devices</b>	<b>17</b>
3.1 Franz-Keldysh Electroabsorption	17
3.2 Free carrier effects- Absorption and Index Depression	18
3.3 The Linear Electro-optic Effect	21
3.4 Estimation of Modulation depths	23
3.5 Conclusions	27
<b>Chapter 4 :- Device Design and Fabrication</b>	<b>28</b>
4.1 Design of Vertical Devices	28
4.1.1 Capacitance Considerations of Vertical devices	30
4.2 Design of Planar Devices	34

4.3 Comparison between Vertical and Planar Devices	35
4.4 Fabrication Process	36
4.4.1 Silicon Tetrachloride Dry-etching of GaAs / AlGaAs	36
4.4.2 Chamber Contamination	38
4.4.3 Reactive Ion etching	39
4.4.4 Photographic assessment of Etch quality - Quartz plate assisted etching	44
4.4.5 General aspects	45
4.5 Fabrication of Vertical Devices	46
4.6 Fabrication of Planar Devices	49
4.7 Rib Waveguide Modelling and Analysis	49
4.7.1 Calculation of the Base Refractive index	50
4.7.2 FWave III Output for Device designs	51
4.8 Conclusions	52
<b>Chapter 5 :- Theoretical Analysis of the Graded Area Element</b>	<b>54</b>
5.1 DC Current - voltage characteristic of a Graded Device	54
5.1.1 Determination of Electric field variation	55
5.2 The Spatial Variation of Electric Field	56
5.3 Functional relationship between decay-length and voltage	60
5.4 Functional dependence of Current with Voltage	62
5.5 Disturbance Saturation Function	66
5.6 Superposition of Intervalley Transfer upon the Theoretical Current -Voltage Function	68
5.7 Disturbance Growth in a Tapered (graded area) device	71
5.8 Fundamental voltage dependency of Transit distance (frequency)	74
5.9 Conclusions	77

<b>Chapter 6 :- Device Analysis and Experimentation</b>	<b>79</b>
6.1 D.C. Current-Voltage traces in Transferred Electron Devices	79
6.2 Practical DC Current-voltage Characteristics	81
6.3 Waveguide Distortion and Thermal Runaway	85
6.4 Comparison Between Theoretical Current-voltage Trace Functions and Real data - Curve fitting	87
6.4.1 Evaluation of the Electric Field Value at the Curve Maxima	87
6.4.2 Functional Dependency for $\eta_0$	93
6.4.3 Disturbance Discontinuity and Real Data	96
6.4.4 The Direct Influence of Annealing Time and Temperature upon the Curved-matched I- $\Phi$ Function	99
6.4.5 Comparison between Tapered and Non-tapered Devices	101
6.4.9 Comparison between Real Data and Predictive Formulae	101
6.5 Conjectured Mechanism For Annealing Dependence	102
6.6 Injected Cathode Current - the $\eta$ coefficients	106
6.7 Optical Experimentation	110
6.8 Simple Resonant Circuit	113
6.9 Conclusions	116
<b>Chapter 7 :- Thermal Feasibility of Vertical Devices</b>	<b>122</b>
7.1 Simple Thermal Resistance Calculations	122
7.2 Thermal Resistance of defined Structures	123
7.3 Thermal Calculations with Uniform Current Density	124
7.3.1 Numerical Calculations for Typical Devices	125
7.3.2 Temperature increase due to electrical biasing	127
7.4 Temperature Rise with Pulsed Operation	128
7.4.1 Evaluation of the Temperature at the Rib-Substrate Interface	129
7.4.2 Application of Laplace Transforms	130
7.5 Estimation of the Maximum Permissible Bias-pulse Width	133

7.6 Further Reappraisal of Vertical devices	135
7.7 Overall Conclusions	136
<b>Chapter 8 :- Conclusions</b>	<b>139</b>
<b>Bibliography and References</b>	<b>144</b>

## Summary

The engineering feasibility of Transferred Electron Devices (TEDs), configured as modulators, was explored. Vertical and planar implementations of the same device were pursued concurrently. An existing "side-wall bonding pad" vertical device was replaced by a revised structure, incorporating dual anode contacts and dielectric isolation. Natural self-resonant frequency inhibition with device capacitance was assessed for both of these vertical devices. The reappraisal was shown to provide benefits of reduced capacitance, reduced current capacity and greater symmetry of the electric field distribution in the active region.

Modelling of the optical confinement attributes of rib waveguides for device designs was performed using the FWAVE III and LWAVE application programs. Confinement afforded by the rib-substrate interface and 33 % AlGaAs layers, in vertical and planar devices respectively, was determined for multi-moded propagation. Efficiently confined propagation at infrared wavelengths was observed.

Theoretical predictions for modulation depths were calculated for rib waveguide devices. The modulation potential of mechanisms such as Pöckels effect, Franz-Keldysh electro-absorption and free carrier influences were analysed. These evaluations were made employing very idealised conditions, leading to consistent over-estimates of modulation indices. The requirements for deep modulation were identified in the context of the engineering designs of real devices.

The prospect for voltage-controlled frequency modulation in planar devices, required the development of analytical theory for tapered (graded area) devices. The functional variation of the pre-threshold electric field distribution was obtained. This permitted the derivation of a predictive current-voltage function for a general transferred electron device with defined semiconductor and physical parameters. The time constant governing growth / decay of nucleated disturbances in tapered devices was sought, verifying the possibility of transit mode operation. A fully calculable function, encapsulating the influences of inter-valley transfer and dipole formation, was developed and quoted.

Both vertical and planar devices were fabricated and assessed experimentally. The theoretical current voltage function was used as a fulcrum for the analysis of the influence of the cathode boundary conditions in planar devices. The behaviour of graded and non-graded elements was modified by varying the annealing conditions in a standard contact metal recipe. A mechanism was conjectured to explain these variations in the context of the Kroemer hypothesis. The resulting empirical functions were used

to assess the inhibition of injected electrons at the cathode. Endfire analysis was performed on waveguide devices, with electrical biasing applied in-situ.

In response to theoretical thermal modelling, in conjunction with practical observations of real devices, a circular mesa form of waveguide device was proposed and fabricated. Estimates of maximum permissible pulse width were made, assisted by Laplace transform analysis of a thermal - electrical analogue circuit. A simple formula for rib-substrate thermal resistance was derived for this analysis. Permissible pulse widths were demonstrated to be incompatible with the notion of a viable modulator operating near to CW.

# Chapter 1

## Introduction

### 1.1 The Gallium Arsenide - Aluminium gallium arsenide Material System

The merits of gallium arsenide (GaAs) as a material in the electronics industry are now well catalogued [1] [2] [3]. Its physical-crystalline and particle transport properties provide GaAs with an aptitude for particular applications. When compared with its major technological competitor, silicon (Si), GaAs is seen to produce faster transit-time devices [2] due to its superior low-field electron mobility (i.e.  $\mu_{\text{GaAs}} = 8500 \text{ cm}^2\text{V}^{-1}\text{s}^{-1}$  as compared to  $\mu_{\text{Si}} = 1300 \text{ cm}^2\text{V}^{-1}\text{s}^{-1}$ ).

However, the applicability of a material is determined by a combination of properties of the material. Silicon has advantages over GaAs in that it produces high-quality material interfaces with its natural oxide ( $\text{SiO}_2$ ), which is readily grown and acts as an adaptable isolation layer. These high quality interfaces are normally a consequence of the large, high lattice purity and low defect densities achievable with silicon substrates. Equivalent physical attributes were less routinely acquired in GaAs substrate technology until recently. Gallium arsenide devices have become increasingly economically viable and performance justified.

A further vital property of GaAs is its ability to participate in epitaxially-grown heterostructures [4], (ternary and quarternary) which leads to "band-gap" engineering. The semiconductor phenomena exhibited by hetero- and homojunction devices in GaAs has initiated research and development of devices using fast electron transport e.g. High Electron Mobility Transistors (HEMTs) [5], Heterojunction Bipolar Transistors (HBTs), and other forms of unique transistor devices. Recent experimental devices have operating speeds in excess of 40 GHz, and offer low-noise, longevity and reliable operation at these elevated frequencies. These device characteristics are a requirement for economic and commercial viability.

The most important feature of modern GaAs technology is the growth of a high-quality interface GaAs /  $\text{Al}_x\text{Ga}_{1-x}\text{As}$  heterojunction, upon which most semiconductor lasers in the modern age are based. The inclusion of these layers in series with GaAs induces an abrupt increase in the effective low-field bandgap (e.g. 1.425 eV in GaAs and 1.76 eV in  $\text{Al}_{0.3}\text{Ga}_{0.7}\text{As}$ ). The gallium atom could be substitutionally displaced by other atoms of valency III (e.g. In) to generate ternary

derivatives and provide a reduction in bandgap. The scope for bandgap engineering has been significantly widened by such innovations. It should be noted that until the first GaAs / AlGaAs junction in 1969 [6] [7], CW laser operation at temperatures approaching room temperature was not sustainable in exclusively direct bandgap materials. The heterojunction may be viewed as invaluable and influential in quantum physics and semiconductor technology. In addition to the heterostructures ability to modify electron transport, the refractive index dependence upon the effective band-gap [3] also leads to properties of optical confinement.

A majority of the research efforts in discrete electronics components has been directed towards semiconductor lasers, due to their importance as the radiation source for any optically-based network, Figure 1.1(a & b)

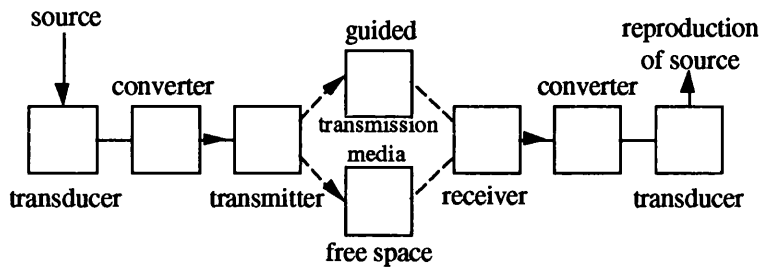


**Figure 1.1(a) :- general communication system**

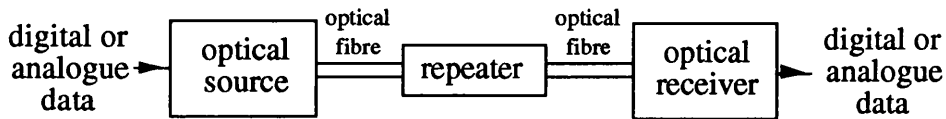


**Figure 1.1(b) :- Optical Network**

To capitalise upon improvements in quality and performance of such sources, other system components e.g. photodetectors / light transducers and control elements have had to be developed to a similar standard. These elements are assessed through signal / noise ratio and maximum bandwidth of operation. Significant advances in both of these parameters have been achieved in recent times.

Optical systems are fundamentally characterised by the application of optical radiation for the transmission of information, as opposed to electron transfer as in electrical signals. The advantages of OEICs {Optoelectronic Integrated Circuits} [8] are those afforded by optical fibres :- i.e. electromagnetic compatibility, compaction, enhanced signal / noise ratios, low losses etc.

Information content can be placed on a beam of radiation through the adjustment of its amplitude, wavelength or phase, with the general process being denoted as modulation. This can be achieved by exploiting the sensitivity of material parameters to electric / magnetic fields. Control of the

radiation beam parameters through the application of external logic signals (electrical / optical) becomes possible.

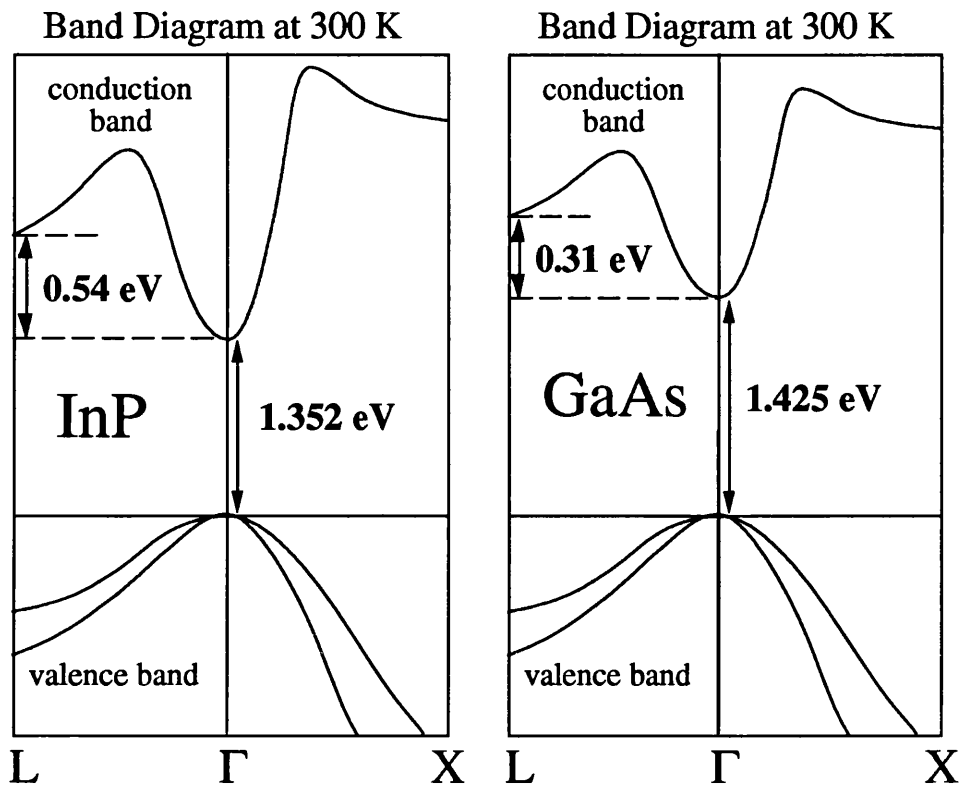


**Figure 1.2 :- Band structures of GaAs and InP**

To this effect, ferroelectric materials such as lithium niobate ( $\text{LiNbO}_3$ ) have been extensively used in novel interactive devices in the past decade [8]. They have a considerable advantage over their III-V equivalents, in that they possess much larger electro-optic coefficients. In essence, the maximum attainable perturbation of the optical characteristics in  $\text{LiNbO}_3$  is greater than that available in GaAs (e.g.  $r_{33} = 30.0 \times 10^{-12} \text{ mV}^{-1}$  in  $\text{LiNbO}_3$ , @ 633 nm, and  $r_{42} = 1.2 \times 10^{-12} \text{ mV}^{-1}$  in GaAs @ 900 nm). However, it is not possible to produce source, detector and control components on one substrate using lithium niobate - it is optically active and electrically passive. This is in contrast to GaAs, which has increasingly excelled as a multipurpose material for monolithic integration. Its popularity was based on a combination of appropriate physical, electrical and optical characteristics.

Monovalent semiconductor elements (silicon and germanium) differ from bi-valent III-V materials in the nature of electron transport. GaAs and InP possess complex band structures with higher and lower valleys in different crystallographic orientations (Figure 1.2). Secondary transport phenomena (e.g. Transferred Electron Effect) are possible in GaAs as result of an inter-valley mobility disparity. Silicon and germanium lattices provide isotropic electron transport environments. Internal

homogeneities are ordinarily difficult to nucleate and sustain at room-temperature in mono-valent element substrates. The transferred electron effect in GaAs / InP ultimately leads to regions of net negative differential mobility (NDM) and hence negative differential resistance (NDR). This can be harnessed to induce positive feedback and coherent oscillations in circuits, or as an isolated element.

In summary, the GaAs/AlGaAs system has proven its versatility in the electronics component industry [9], with its participation in MESFETs, optical transducers, LEDs, lasers [6] [7] and avalanche photodiodes. Monolithic integration will remain as a subject of research interest, with innovative fabrication techniques and device principles resulting from this work.

## 1.2 Justification for Research

### Moreland Structure

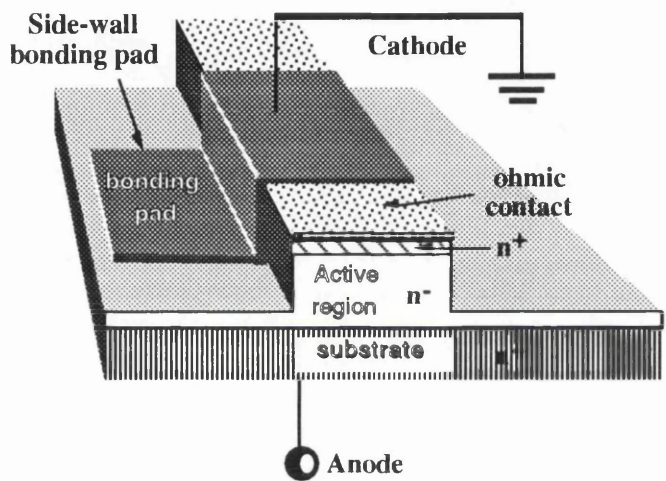


**Figure 1.3 :- The Moreland vertical device design**

The level of communication traffic and its relative information content has increased over the past two decades [9]. This has given impetus to the quest to discover new and improved methods of generating information carriers and the compression of its information. This information could be data, television, telephony or radar signals. The potential of optical wavelength radiation for the transmission of data has long been acknowledged, and efforts to exploit this potential has raised interest in the field of microwave devices [10].

In 1966, Cohen et al [11] claimed that incident optical radiation could be shown to be modulated by a passing "domain" in a 100 MHz transferred electron oscillator. Some years later (1975) Ohta et al [12] made similar claims and observations, and further attempted to quantify the exact components of the modulation. However, characteristic of both of these publications was the token

nature of the modulation depths claimed, and the time elapsed between them. For realisation and justification of a practically viable device, the modulation depths would need to be dramatically improved.

Work performed in the sixties concentrated on the analysis of the propagation of radiation in optical waveguides and the blossoming area of optical fibres [4], using techniques reserved for microwave waveguides. The papers of Cohen et al [11] and Ohta et al [12] were examples of attempts to produce microwave control circuitry for high-speed optical elements.

Similarly, Lau et al [13] [14] [15], in published work, and D. Moreland in a Ph.D thesis, {University of Glasgow, 1989}, reported observations of modulation by a domain type disturbance in an n-type GaAs diode at 24 GHz. Modulation depths in excess of 20 % in a device with an integrated rib-waveguide and surface Schottky bonding pad were cited. The vertical diode structure of Moreland is illustrated in Figure 1.3.

In view of this previous work, intended research included fabrication and testing of a Transferred Electron modulator in a rib-waveguide integrated form with an additional feature of an experimental Hot Electron Injector (HEI) [16] [17]. This HEI was a linearly-graded AlGaAs layer inserted between the real cathode and virtual cathode of the diode device. For planar geometry devices, the cathode contact had implications in addition to those of an "ohmic" contact.

In 1968, Kroemer [18] [19] [20] introduced the concept of the control characteristic to assess the injection environment for carriers at the cathode of Transferred Electron Devices [TEDs]. Kroemer demonstrated that the nature of the control characteristic, and its position relative to the current-density-field characteristic of the neutral interior crystal, could be used to explain many forms of anomalous behaviour in n-type GaAs samples. The appearance of oscillations at fields in excess of that predicted, non-oscillation and persistent stationary states and voltage-dependent oscillation frequencies at low efficiencies, were all common anomalies familiar to those experimentally active in the field of TEDs. Kroemer was able to reconcile these empirical observations with existing theory by examining the role of the region of perturbed crystal at the metal-semiconductor interface, i.e. the control region.

More recently, Bonilla and Higuera [21] [22] in 1992 examined in detail the behaviour of n-GaAs elements and the influence of the cathode boundary conditions through Non-Linear Dynamic systems [NLD] simulations. Their primary conclusions incorporated the following :- (1) lower

resistivity cathode contacts (injecting plane) lead to stationary states and / or monopoles while (2) higher resistivity contacts initiated dipole type disturbances. Fully-matured dipoles resulted with active regions of sufficient length. Some critical resistivity value was demonstrated to signify the transition between monopolar and bipolar space-charge waves, and hence lead to hybrid behaviour. In response to the potential for device-control, and the persistent low yields of TEDs in commercial production, the influence of the cathode metallisation was to be investigated such that natural yields could be improved.

Devices operating up to 50 GHz were proposed in the research schedule. This 50 GHz was inconsistent with the existence of "domains". As stated by previous groups [23] [24] [25], fully-matured domains were thought not to exist in GaAs devices above 10 GHz operation. The rate of disturbance maturation was shown to be material dependent. This had serious implications concerning the potential operation and prospects for measurable modulation in devices significantly above 10 GHz.

In view of previous research and its practical limitations, the schedule of research included :-

(A) Development of new forms of the device, incorporating an integrated waveguide. The nucleation of a self-organised spatio-temporal structure within the active region must not be disrupted by the inclusion of a waveguiding element.

For the device to be viable it must possess :-

- (i) The ability to support a fully-matured high-field electric disturbance, which is reliably nucleated ;
  - (ii) High optical confinement i.e. low-loss single-moded waveguiding ;
  - (iii) A stable natural (Transit mode) operating frequency which is pre-determinable at the design stage ;
- (B) Verification of the possibility of oscillation and modulation in any of the resultant devices ;
- (C) Theoretical developments required to analyse or propose new device profiles, and to assess the implications of the cathode boundary in the context of the Kroemer hypothesis.

Hence the research conducted was separated into two identifiable sections, namely (i) the pursuit of modulation in TEDs and (ii) the determination of the influence of the cathode boundary conditions through annealed contact metallisation.

# Chapter 2

## The Transferred Electron Effect

### 2.1 The Intervalley Transfer Mechanism

In 1961, Ridley and Watkins [26] first recognised the potential of GaAs, and other materials with similar conduction band structures, for the formation of dynamic negative differential resistance elements. They proposed a mechanism based on the coherent transfer of electrons between valleys in the conduction band of these materials. Hilsum [27], in 1962, made similar proposals independently of Ridley and Watkins, who were the proponents of self-organised spatio-temporal pattern formation in these elements.

It was not until two years after these hypotheses were presented that J.B. Gunn [28] [29] [30] (1963), while exploring the short high-power pulse response of n type gallium arsenide and indium phosphide samples, first observed coherent microwave output from n-GaAs. Through the application of a DC electric field in excess of an apparent threshold value (approximately  $3.2 \text{ kVcm}^{-1}$ ), to a randomly oriented specimen, current oscillations were observed. At the time of these experimental observations, Gunn was not aware of the mechanism of their origin. However, in 1964 [18] Herbert Kroemer offered a reconciliation of the hypotheses of Ridley & Watkins and Hilsum, and the experimentation of Gunn, to confirm that periodic high-field domains resulted from the transferred electron principle. This mechanism demonstrated how a fundamentally homogeneous background crystal could sustain a heterogeneous entity (domain). It was observed to nucleate at the cathode, grow and mature, stabilise, and propagate towards the anode, where it collapsed and was absorbed into the anode. This process was then repeated periodically, with the appearance and disappearance of the high-field entity accompanied by a decrease and increase of the device current respectively. The domain propagated at a standardised velocity of  $10^7 \text{ cm s}^{-1}$  in GaAs.

In addition to GaAs, other bi-valent compound semiconductors were seen to support the transferred electron effect. Indium phosphide (InP) (III-V), zinc selenide (ZnSe) (II-VI) and cadmium telluride (CdTe) (II-VI) have all been used to create oscillators, due to their appropriate band structures.

Evidence to support the inter-valley transfer hypothesis was provided by the pressure experiments of Hutson et al [31], and the solid solution ternary compound experiments of Allen et al [32]. They confirmed the validity of the transfer mechanism by analysing the dependency of the threshold field for the onset of oscillation. The effective intervalley energy separation,  $\Delta E$ , was modified by pressure and phosphorus fraction respectively.

Hutson et al [31] discovered that  $\Delta E$  had a sensitivity of the order of  $9.0 \times 10^{-3} \text{ eV/kbar}^{-1}$  with the application of hydrostatic pressure. The threshold field decreased with increasing pressure as the inter-valley separation between the central  $\Gamma$  - valley and the satellite L valley minima decreased. At 26 kbar no oscillations were observed in the sample. Allen et al achieved modifications of the valley separation, and hence the threshold field, by growing  $\text{GaAs}_x\text{P}_{1-x}$  samples with different  $x$  values (i.e. 1.0 - 0.52).  $\Delta E$  was observed to vary from 0.31 eV to zero.

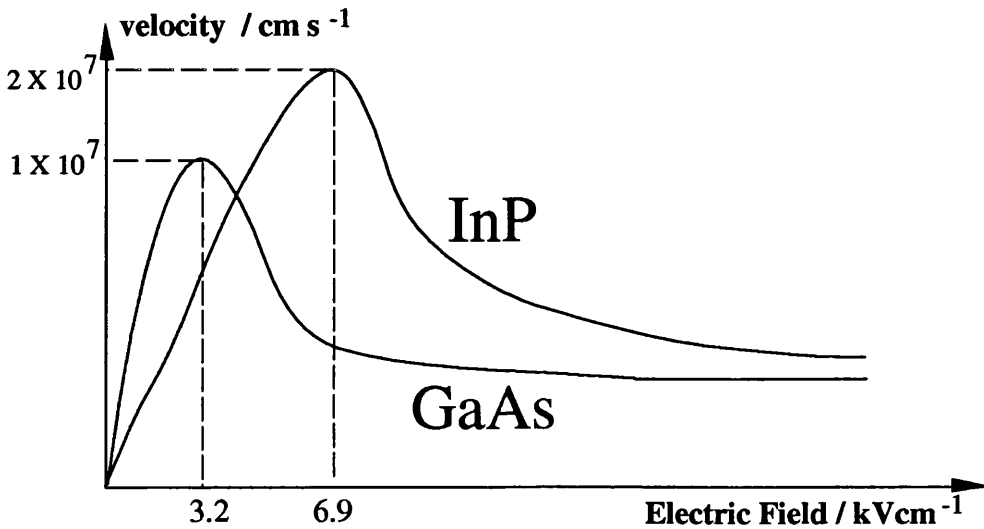


Figure 2.1 :- Velocity-field variations for InP and GaAs

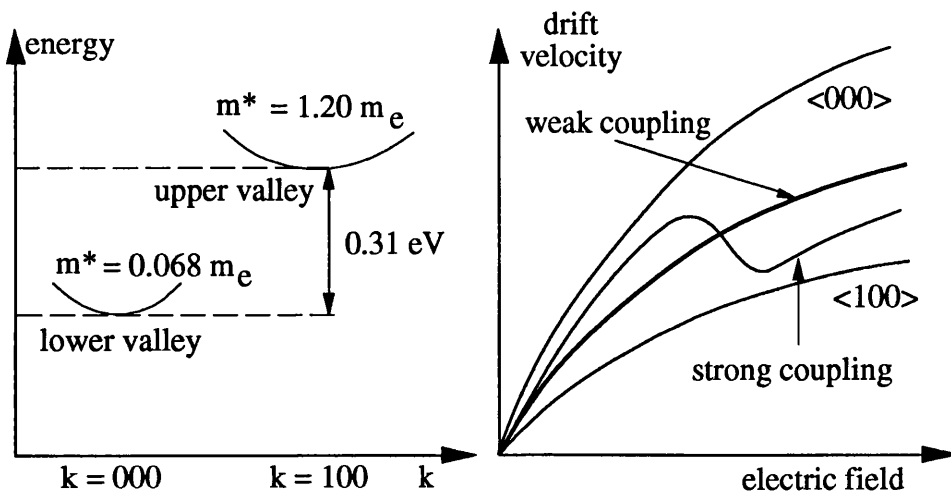
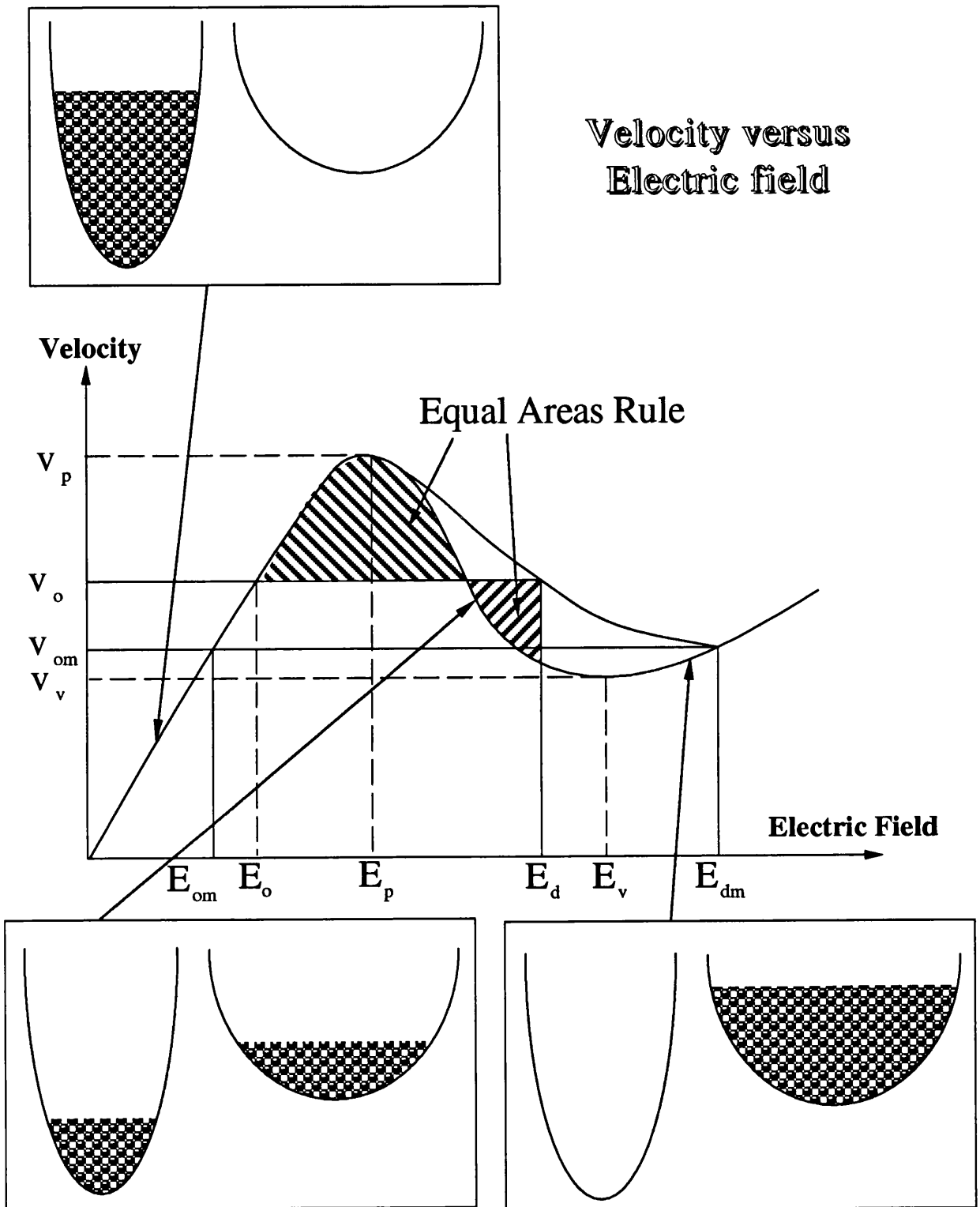


Figure 2.2 :- Simple schematic of intervalley transfer mechanism



**Figure 2.4**

# Disturbance Development

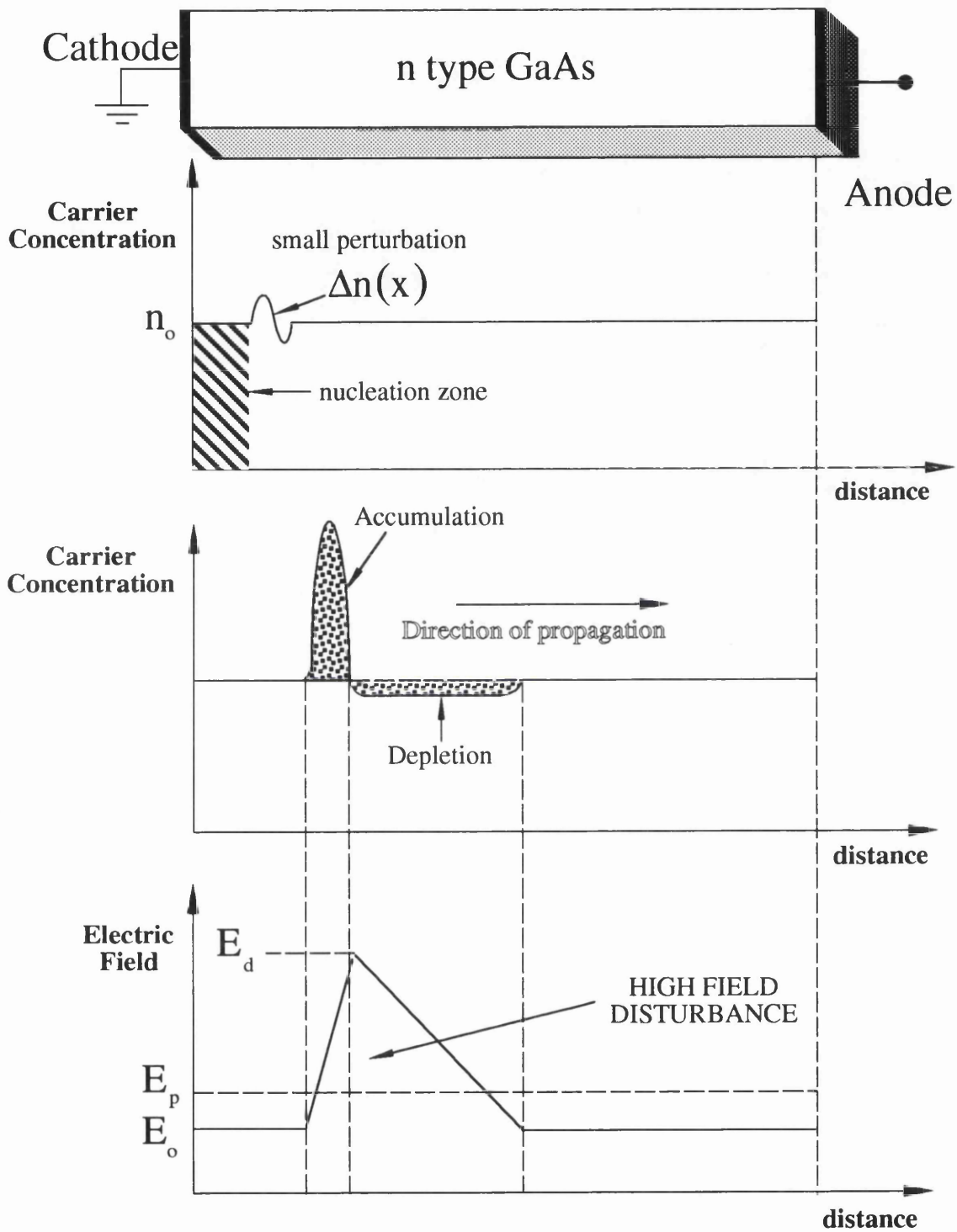


Figure 2.5

## **2.2 The Development of Inhomogeneities - Linear Analysis**

### **2.2.1 Nucleation of Disturbances**

Consider a sample of some semiconductor material in which the intervalley transfer mechanism previously described is in effect [33] [34] [35] [36] [37]. At low field values the element is essentially ohmic (or pseudo-ohmic). As the electric field is increased, the upper valleys begin to populate (Figure 2.4), and a region of net dynamic negative differential mobility emerges. At higher fields, virtually all of the carriers reside in the upper valleys, and the dynamic differential phenomena vanishes. Electrons continuously back-scatter to the lower valley, leading to a state of dynamic equilibrium. If the field is increased into the NDM range, the field could remain at this value indefinitely, if no perturbation was present. However, suppose that a notional spatial perturbation was introduced to the field distribution through noise or other transient processes. Carriers in this disturbed locality could then transfer to a higher valley if the field disturbance surpassed the necessary threshold value. At this spatial point, an exponentially growing disturbance is nucleated. As increasing numbers of carriers begin to transfer, the instantaneous reduction in velocity causes initial accumulation at the cathode side of the nucleation point, and depletion on the anode side. The charge density distribution in this locality causes an increase in the field, further promotion of electrons, and reinforces the status of the disturbance. Once nucleated [34] [38], this disturbance grows and propagates towards the anode at a saturated velocity. As the disturbance progresses spatially, its voltage content increases also, causing the electric field exterior to the disturbance to fall to accommodate the constant voltage stipulation. Where the disturbance matures, it may be termed a high-field domain in samples with propagation zones greater than 10  $\mu\text{m}$ . It is also possible to nucleate a low-field domain, by instantaneously jumping to a high field value, and gradually reducing it such that the region of dynamic negative differential mobility was approached from above the threshold. With voltages increased naturally from lower to higher values, high-field disturbances predominate.

Negative differential mobility (NDM) elements such as Transferred Electron Devices [39] [40] operate (1) by controlled large signal instabilities and (2) as negative conductance elements characterised by small signal instability. A perturbation at a displacement  $x_1$  will be communicated downstream from the cathode and contribute to the change in field at the point  $x_2$  ( $>x_1$ ). The field change at  $x_2$  hence receives two separate contributions ; a non-local contribution from  $x_1$  and a local contribution

from  $x_2$ . As a consequence, there is a transit time delay between the origin of a perturbation and its effect at different points along its trajectory. The time delay results from the finite velocities of carriers, and introduces a phase displacement between current and voltage through and across the device respectively. In certain ranges of frequencies there will be gain, and in others it provides loss.

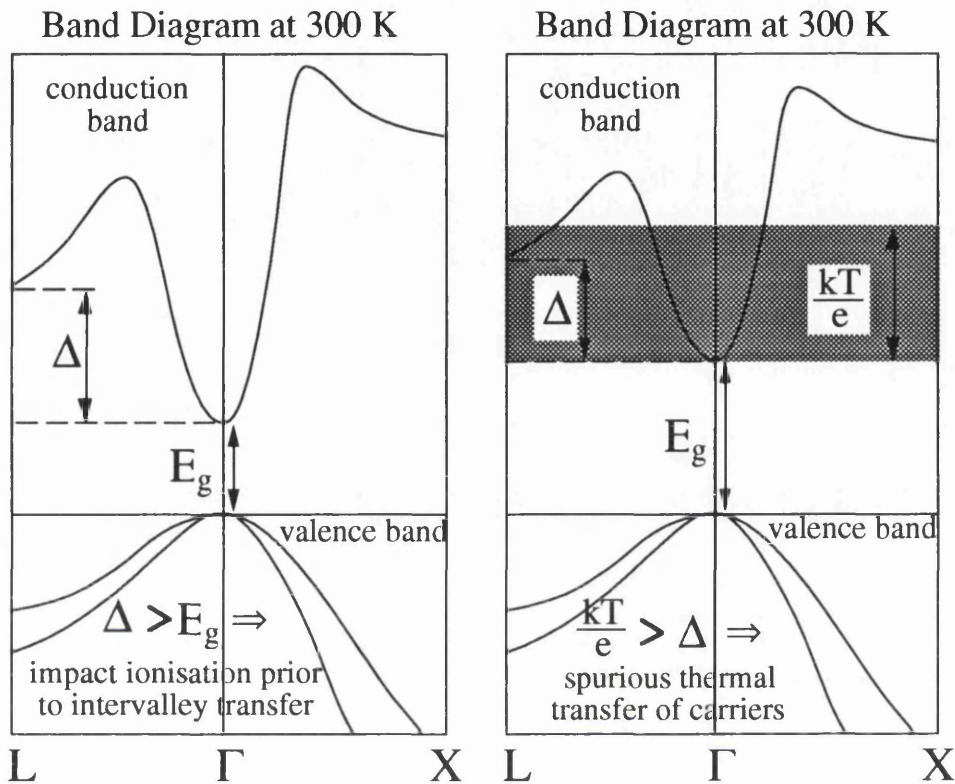


**Figure 2.3 :- Criteria for Transferred Electron Instabilities**

For a material to be capable of supporting a Transferred Electron Effect instability, then it must possess the following (Figure 2.3) :-

(a) The necessary electrical or semiconductor characteristics i.e. :-

- (i) the intervalley separation must be significantly greater than the thermal energy of the carriers residing in its lower valley. This is to retain exclusivity of the electric field dependency of the intervalley transfer process, i.e. no electrons should be spuriously transferred through thermal excitation alone ( $kT / e = 0.025$  eV). The upper valleys should not be significantly populated at low electric fields ;
- (ii) the fundamental band-gap of the material ( $E_g = 1.425$  eV for GaAs) should be significantly larger than the intervalley separation. If the energy separation,  $\Delta$ , of the first and second subsidiary minima approaches that of the material bandgap, the probability of coherent impact ionisation prior to intervalley transfer increases dramatically ;
- (iii) The material must have a non-

equivalent multi-valley conduction band (Figure 2.2), with a mobility disparity between the lower and upper valleys. The upper effective mass ( $m_2^* = 1.2 m_e$ ) must be greater than that in the lower valley ( $m_1^* = 0.068 m_e$ ), leading to a mobility disparity. Mobilities in the lower and upper valleys in GaAs are  $8500 \text{ cm}^2\text{V}^{-1}\text{s}^{-1}$  and  $200 \text{ cm}^2\text{V}^{-1}\text{s}^{-1}$  respectively.

(b) An oscillatory or resonant circuit / cavity in which it operates, or in a basic resistive circuit with no appended resonances.

(c) The necessary cathode and anode boundary conditions for charge injection and collection respectively within the device so-defined.

### **2.3 Transit ("Gunn") mode**

Transit mode is the most orthodox mode, and is achieved by simply applying a DC bias in excess of the threshold voltage value. A fully-matured dipole disturbance exists with this mode in samples of sufficient active region length [33] [34] [35] [36] [37]. The disturbance propagates from the virtual cathode to the virtual anode, and traverses the whole of the potential propagation zone. Since the biasing is DC, no circuit resonances are applicable and the environment is purely resistive. The disturbance when it arrives at the anode, initiates a current pulse and subsequent rearrangement of the internal field distribution. Transit mode operation leads to a non-tunable fixed fundamental frequency in uniform orthodox devices. For a disturbance propagation velocity of  $10^7 \text{ cm s}^{-1}$  in GaAs, then the fundamental frequency is approximated by :-

$$L_{\mu\text{m}} f_{\text{GHz}} \approx 100$$

The  $n_0L > 10^{12} \text{ cm}^{-2}$  (nL product) criteria must be met for all [33] of these modes to exist in the designed element. A dissimilarity may be drawn between constant voltage and constant current operation. At an arbitrary displacement,  $x$ , in the propagation zone, the electric field will be perturbed on two occasions in the constant voltage case; once when the disturbance is nucleated, and once when the dipole passes by the point  $x$  in the active region. In contrast, the field is only perturbed on one isolated occasion per time of flight in the constant current alternative, i.e when the disturbance passes through  $x$ .

This dissimilarity had implications for the aptitude of modes in coherent modulators. Modulation results from localised modification of the optical characteristics of the material. In the

constant current situation, only one modification of these optical characteristics occurs per disturbance transit, which is a desirable feature for a modulator. In addition, multiple disturbances may be supported in this device. This has proven difficult to harness due to the uncontrollable and unpredictable nucleation of spurious patterns in low quality crystals.

### 2.4 The Cathode Boundary conditions

The **Transferred Electron Oscillator (TEO)** supports coherent oscillations in only a basic dc environment. Unlike other devices (IMPATTs, BARITTs or RTDs), it has a **physical** manifestation of its oscillations, i.e. a propagating **domain**. A TEO exhibits four fundamental types of signal behaviour, occurring in discrete electric field ranges [39] [40] [41] [42] [43]. In order of increasing bias, they are {a} Unequivocal stability ; {b} Microwave amplification ; {c} **Large-signal** oscillations ; {d} Conventional Transit mode Gunn oscillations.

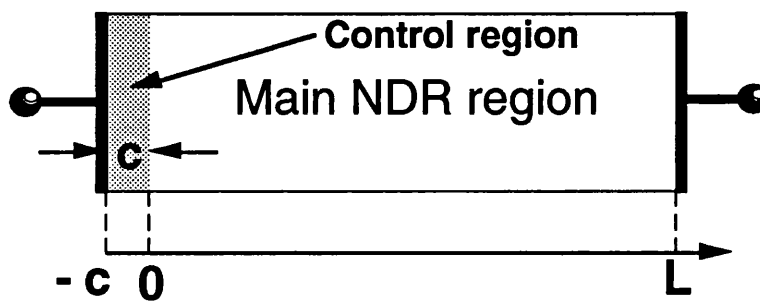


Figure 2.7 :- Control region and Main section principle

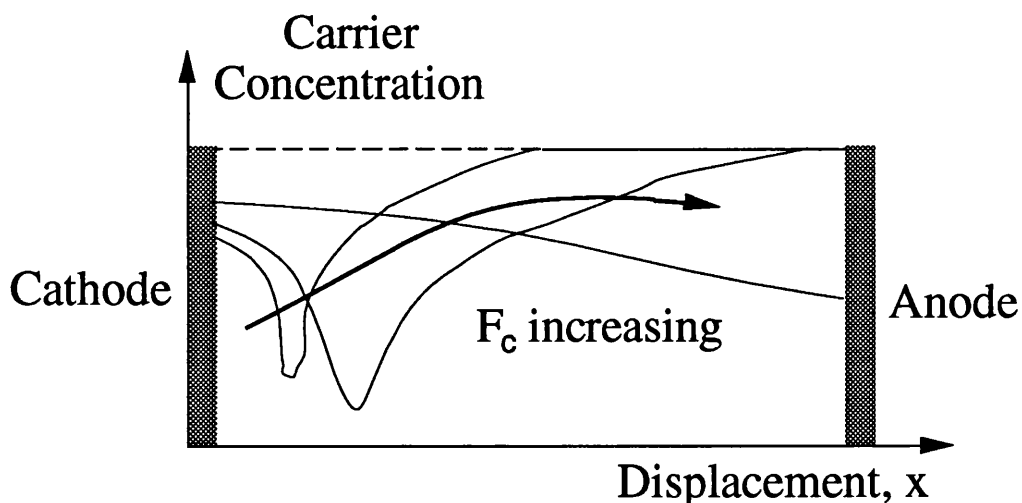


Figure 2.8 :- Spatial variation of carrier concentration

In the original mathematical analysis of the macroscopic space-charge dynamics of domain propagation [18] [33] [34] (circa early 1960s) **perfect cathode conditions** were assumed.

Subsequently, it emerged that this simplified representation of the dynamics did not predict all of the experimentally observed device behaviour.

### 2.4.1 Imperfect Cathode Boundary Conditions

In 1963 Gunn made the original experimental observations of what is now termed the “Gunn” effect. However, even at this rudimentary stage, these observations of current-time and voltage-displacement properties of a super-threshold GaAs sample suggested the formation of a **static depletion layer**. This was contrary to the domain formation hypotheses proposed by Hilsum and Ridley & Watkins in 1961 and 1962 [26] [27] respectively. It was not until H. Kroemer’s publication in 1968 that an explanation for this phenomena was offered. A reconciliation of theory and experiment was provided in terms of a **control characteristic**.

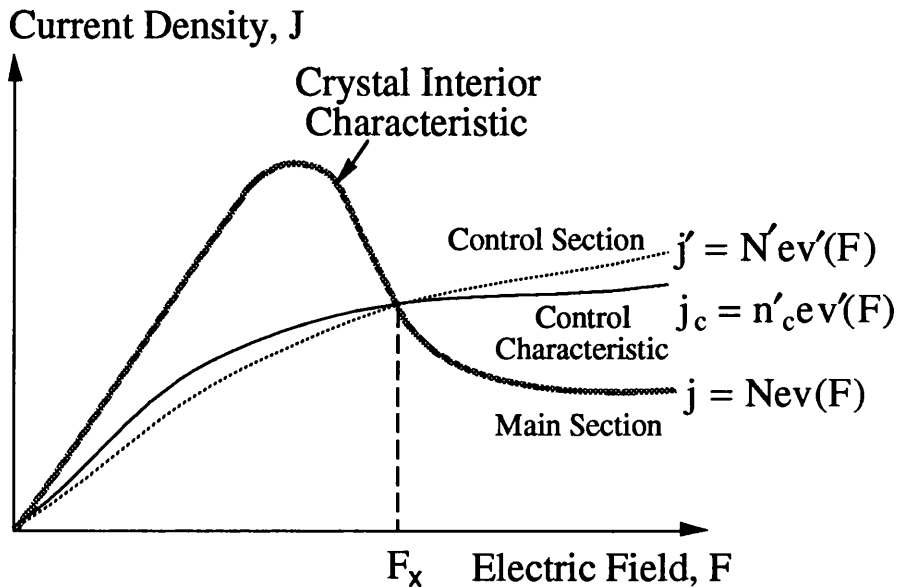


**Figure 2.9 :- Control characteristic concept**

Consider initially the GaAs region, physically confined between the cathode and anode of a simple oscillator, to be constituted of a **main region** and a **control region**.{Figure 2.7} The main region supports a familiar velocity-field characteristic, with saturation at higher fields corresponding to the onset of electron transfer {Figure 2.9}. The control region has a **control characteristic** which is unique to the cathode-semiconductor interface.

This characteristic may be arbitrary, but will commonly resemble that shown in Figure 2.9 due to the presence of an annealed "ohmic" contact. The width of region over which this profile applies may be narrow, but sufficient to limit the operation of the device.

Initially, the control section is regarded as a thin resistive layer, the bulk of the crystal being the main section, and the interface between the two as the **control plane**. At any field point, except the crossover field  $F_x$ , the natural current density in the two sections is dissimilar. This leads to an initial **static depletion region** for fields below  $F_x$ , and hypothetically a **static accumulation region** for fields above  $F_x$ . The latter case is not normally possible since the internal field can only reach  $F_x$  in long samples with the application of an infinite bias voltage. Shorter samples may achieve above-crossover fields in certain circumstances.

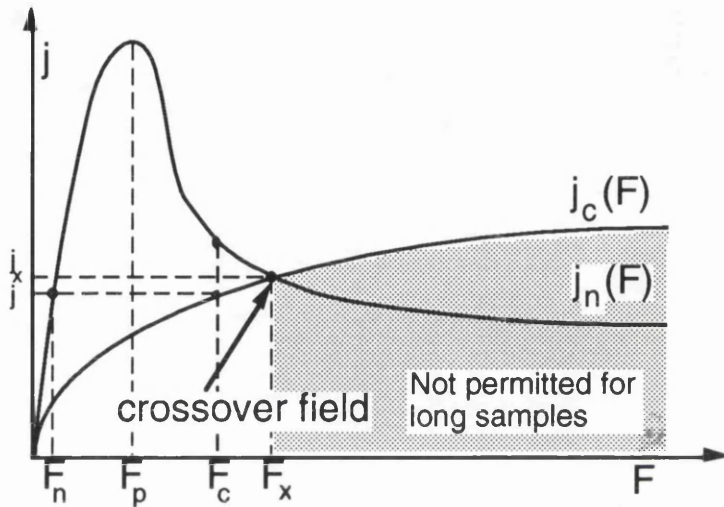


**Figure 2.10 :- Crossover field concept**

It was further assumed that the control section did not support negative differential mobility, and provided a higher low-field resistivity than the bulk semiconductor beyond it. This was represented by the simple current density relations :-

$$j_n = env(F) \quad \text{and} \quad j'_n = env'(F) \quad \text{--- (2.1)}$$

Their functional variation is illustrated in Figure 2.10, with a crossover at  $F_x$  as mentioned previously. In those regions of the sample where there is an absence of space charge,  $j_n$  and  $j'_n$  were equivalent to the local current density-field characteristics. Ordinarily, space charge distributions will exist, in which the local current density differs from that prescribed by the neutral characteristics. Current continuity in these regions required that :-

$$env(F) = env'(F) = \text{const} \tan t = j \quad \text{--- (2.2)}$$

and this valid also across the control plane. If we assume there are no discontinuities due to interface states, dielectric constants and heterojunction band-edges, then the control field,  $F_c$  will be continuous also across this plane. It followed that :-

$$en_c v(F) = e n'_c v'_c(F_c) \Rightarrow n_c - N = - \frac{j_n(F_c) - e n'_c v'_c(F_c)}{ev(F)} \quad \text{----- (2.3)}$$

where  $n_c$  and  $n'_c$  are the electron densities in the sections immediately adjacent to the control plane. Equation (2.3) demonstrated that electrical **neutrality** could only be achieved on both of sides of the control plane if the field at the control plane was  $F_x$ . Hence, if the field  $F_c$  at the control plane was less than  $F_x$  then this could only be satisfied by either **accumulation** in the control section or **depletion** in the main section. A combination of both may result. These space-charge layers are regarded as the **primary nucleation layers**. By similar reasoning, if the field at the control plane is in excess of  $F_x$ , then an initial **accumulation layer** would form inside the upstream main section.

The extent of the depletion/accumulation, in the immediate vicinity of the control plane on the main-section side, was functionally dependent upon the difference between the neutral characteristic and the quantity :-

$$j_c(F_c) = e n'_c v'_c(F_c) \quad \text{----- (2.4)}$$

In accordance with equation (2.3) it could be stated that :-

$$n_c - N = - \frac{j_n(F_c) - j_c(F_c)}{ev(F_c)} \quad \text{----- (2.5)}$$

where  $j_c(F_c)$  was regarded as the **control characteristic**. In general terms, the control characteristic can reside anywhere relative to the two neutral characteristics, but its most probable displacement would be between them as shown. The exact profile is determined by crystalline conditions before and after annealing processes, and hence may be highly sensitive to sample quality. In certain circumstances space-charge formation in the control section is limited or negligible, in which case the control characteristic coincides with the neutral equivalent. The crossover field would remain unperturbed.

A consequence of this depletion is a field enhancement at the control plane. This field increase may be insufficient to surpass the crossover field and hence fail to initiate a **secondary accumulation layer**. It is most probable that this will result in a **static depletion layer** and **cathode fall** similar to that originally observed by Gunn.

Kroemer demonstrated [19] [20] that crystal behaviour was governed by the magnitude of the NL product, with the following inequalities, where  $\sigma_x$  was the control region conductivity at  $F_x$ ,  $\sigma_c$  the conductivity of the control characteristic, and  $\sigma_-$  the negative conductance of the main section :-

$$NL \ll \frac{2 \epsilon F_x \sigma_x}{e \sigma_c - \sigma_-} \Rightarrow G_x = \frac{\sigma_c}{L} \quad \text{\{saturation\}} \quad \text{----- (2.6)}$$

$$NL \gg \frac{2eF_x}{e} \frac{\sigma_x}{\sigma_c - \sigma_-} \Rightarrow G_x = \frac{\sigma_c \sigma_x}{L(\sigma_c - \sigma_-)} \frac{2eF_x}{eNL} \ll \frac{\sigma_c}{L} \text{ ----- (2.7)}$$

For lower NL products, the conductance mimics the shape of the control characteristic. For much larger NL product values, the conductance is demonstrated to saturate, and confirmed that  $NL > 10^{12} \text{ cm}^{-2}$  for "Gunn" oscillations to be supported. The position of, and gradient at, the intersection exclusively determines device activity, irrespective of the physical phenomena by which a control characteristic originates. For natural functional control characteristics, there are three general properties attributable to it :- (1) the presence or absence of a portion of negative conductivity in the control characteristic itself. This is incidental in determining the possibility of static negative conductance ; (2) the intersection point (crossover field) between the control characteristic and the neutral crystal interior characteristic, if one exists. The further the crossover field is away from the inter-valley transfer threshold, the greater the departure of device behaviour from orthodox "Gunn" oscillations ; (3) the gradient of the control characteristic at the intersection point, which is incidental in determining the internal status of the crystal.

Two "physically distinct" parameter contributions were [45] identified for field (F), carrier concentration (n) and crystal impedance (Z) i.e. (i) a space-charge plasma wave element and (ii) a time-independent uniform element. The space charge contribution was seen to be proportional to :-

$$\sigma_c - \sigma = j_c \left[ \frac{\sigma_c}{j_c} - \frac{\sigma_-}{j_n} \right] = j_c \frac{d}{dF} \left( \ln \left[ \frac{j_c}{j_n} \right] \right)_{F=F_c} \text{ ----- (2.8)}$$

Expression (2.8) indicated that in the imposed limit,  $F_c \rightarrow F_x$ , it is proportional to the difference in gradients at the crossover field (intersection point). This expression vanishes in the condition that the control characteristic is a scaled version of the main neutral interior characteristic, i.e. :-

$$j_o(F) = \gamma \cdot j_n(F) \text{ ----- (2.9)}$$

In the case of near parallel control characteristics, no crossover point occurred, where the neutral interior characteristic had a flat-valley portion. Two limiting cases could then be isolated i.e. :-

(1) the parallel control characteristic case, quantified by expression (2.9), and the absence of space charge waves ; (2) the steep control characteristic case, quantified by the following criteria :-

$$\sigma_c \gg |\sigma_-| \text{ and } \sigma_c \gg \omega \epsilon \text{ ----- (2.10)}$$

and the dominance of space-charge waves.

## Chapter 3

### Theory of Modulation in Transferred Electron Devices

In previous publications [13] [14] [15], observations of modulation have been attributed to the passage of a disturbance in an n-GaAs sample. The elevated electric field and carrier accumulation associated with the disturbance were cited as the sources of these modulation events. The following combination of mechanisms were suggested (Figure 3.1) :-

- [A] **Franz-Keldysh Electroabsorption ;**
- [B] **Pöckels effect (Linear electro-optic effect) ;**
- [C] **Free carrier absorption ;**
- [D] **Depression of the refractive index due to a high-density charged plasma.**

Mechanisms [A] and [B] lead naturally to amplitude modulation (AM), while [C] and [D] modify the refractive index leading to frequency / phase modulation (FM / PM). Phase modulation may be converted to amplitude modulation with cross polarizers in a fixed experimental arrangement (Figure 3.2). A brief discussion of the principles governing each mechanism follows.

#### 3.1 Franz-Keldysh Electroabsorption

GaAs exhibits the electro-absorption effect, which leads to coherent electro-optic behaviour. The absorption characteristic (absorption coefficient versus e.g. incident photon wavelength) shown in Figure 3.3 defines a natural statistical limit for absorption, or an **absorption edge**. This limit is functionally related to the effective band-gap separation at any point in space, or value of electric field. The presence of intense electric fields modifies the band-gap, and hence perturbs the level of absorption by shifting the absorption edge. At a particular wavelength of incident optical radiation, the level of absorption increases with increasing electric field. Hence, a propagating dipole significantly perturbs the absorption characteristics in the locality of the disturbance only. For photons with energy close to that of the band-gap, the absorption coefficient,  $\alpha$ , depends significantly on the difference between the photon energy and the band-gap,  $E_g$ . This sensitivity results from the high gradient of the absorption curve at the band-edge. This is characteristic of direct band-gap materials such as gallium arsenide and indium phosphide.

# Origin of Modulation phenomena in Dipole disturbances

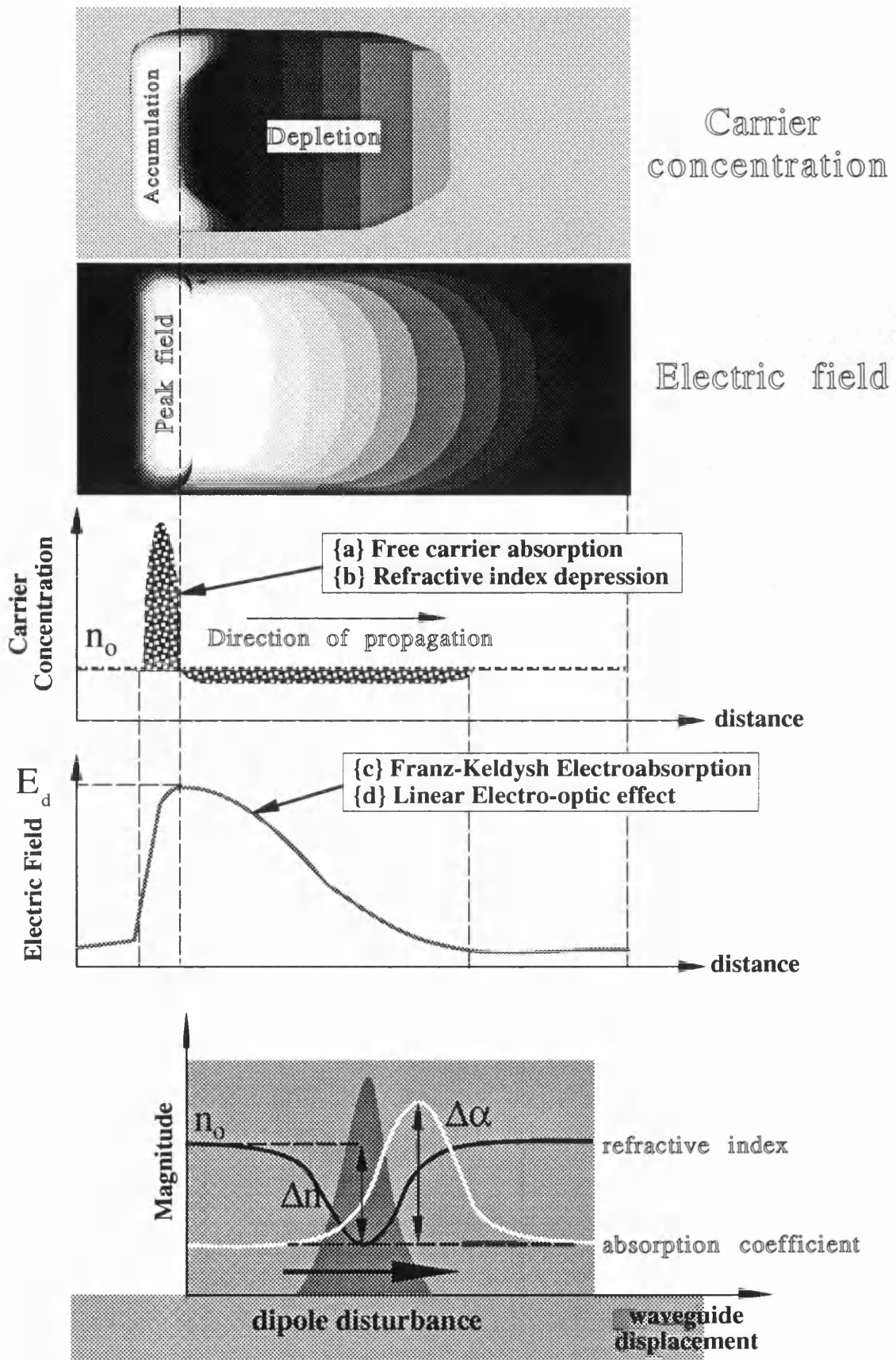
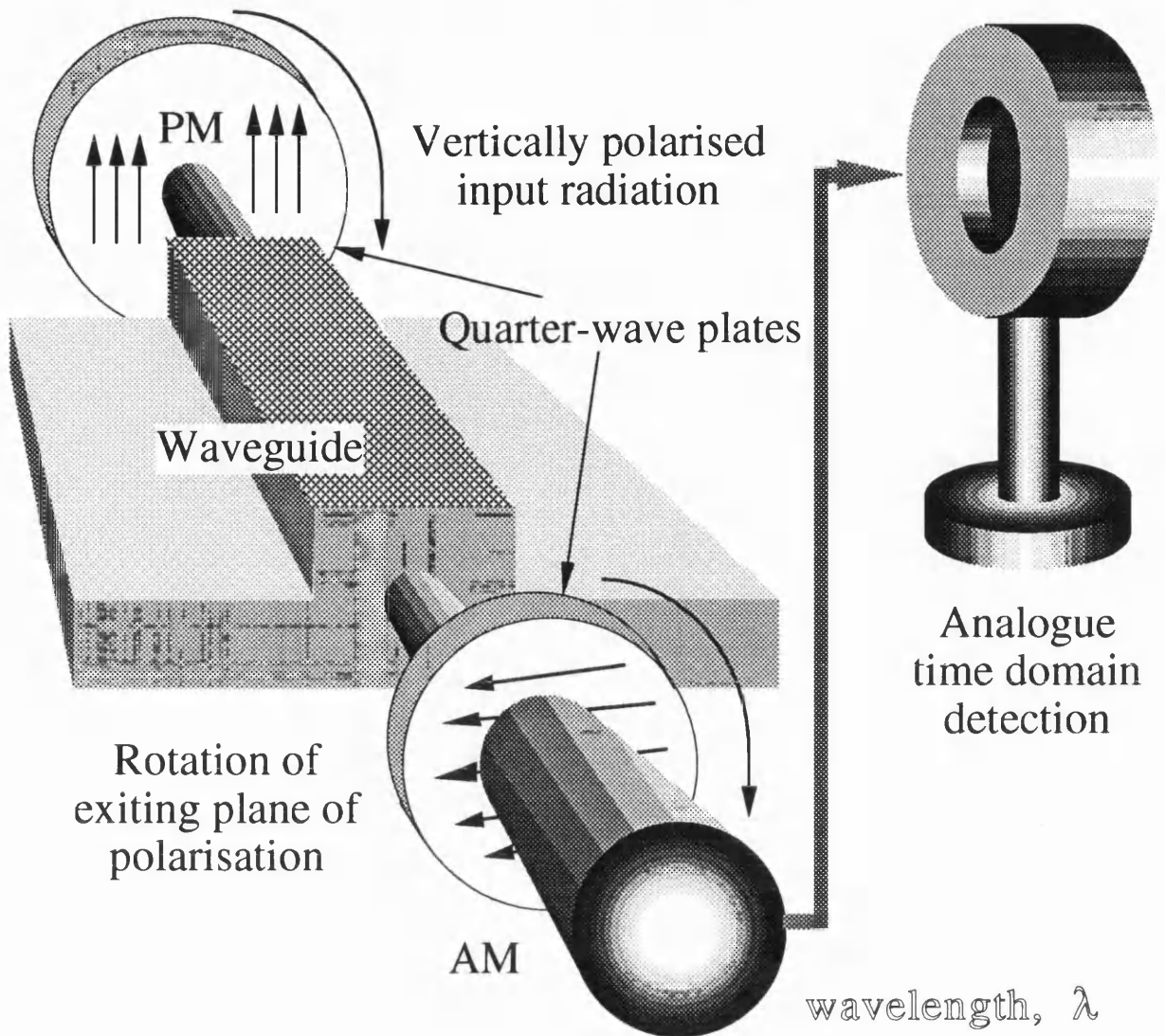


Figure 3.1

## Conversion of Phase Modulation into Amplitude Modulation



Dimensions reference for retardation calculations in vertical devices

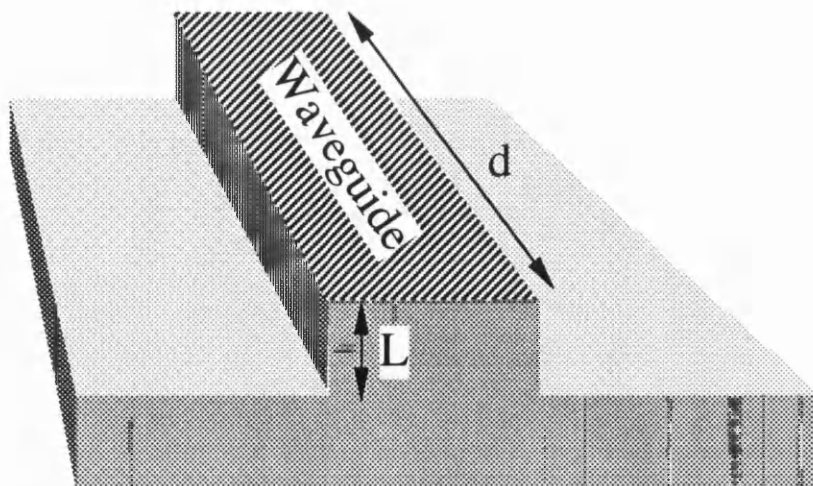
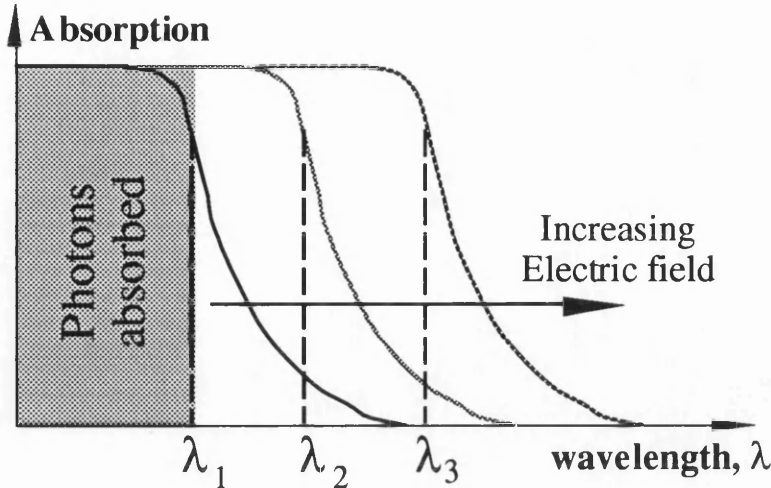


Figure 3.2

## Typical Absorption characteristic



**Figure 3.3 :- Absorption characteristic of direct bandgap materials**

Electro-absorption is enhanced if the energy of the incident photons is close to that of the natural band-gap of the material that it irradiates. Application of intense electric fields initiates band-bending, and critically shifts the absorption edge, causing strong absorption of the photons. This effectively broadens the possible density of states of electrons in the conduction band. The probability of an electron residing in the conduction band becomes finite with the application of intense electric fields. The absorption edge is shifted to longer wavelengths, reducing the effective band-gap, leading to the following :-

$$\Delta E = \frac{3}{2} \sqrt[3]{\frac{(ehE)^2}{m^*}} \quad \text{where} \quad \hbar = \frac{h}{2\pi}$$

$e = 1.6021892 \times 10^{-19} \text{ C}$  ;  $E = \text{applied electric field}$   
 $h = 6.626176 \times 10^{-34} \text{ Js}$  ;  $m^* = \text{electron effective mass} \dots (3.1)$

### **3.2 Free Carrier Effects -Absorption and Refractive Index Depression**

Charge density plasmas are constituted from a high density of free carriers. These carriers are responsible for intraband absorption, where a photon surrenders its energy to the charge carrier with which it interacts. The imparted energy induces promotion of free electrons in the conduction band, and by analogy, holes in the valence band [8].

The mechanics of the intraband absorption process may be analysed with electromagnetic theory, in which a time periodic electric field vector,  $E_0 e^{j\omega t}$ , is imposed upon the distribution. A simple

differential equation governing the motion of an electron residing in the conduction band could be derived with mass  $\times$  acceleration and damping factor contributions to the general force vector function.

Hence, for an arbitrary displacement  $x$ , and damping factor  $g$ , it could be stated that :-

$$m^* \frac{d^2 x}{dt^2} + m^* g \frac{dx}{dt} = -eE_0 e^{j\omega t} \quad \dots (3.2)$$

The general solution to this ordinary differential equation could be given as follows :-

$$x = \frac{\left[ \frac{e}{E_0 m^*} \right]}{\omega^2 - j\omega g} e^{j\omega t} \quad \dots (3.3)$$

The general expression for the dielectric constant in an arbitrary material was such that :-

$$k = \frac{\epsilon}{\epsilon_0} = 1 + \frac{P}{\epsilon_0 E} = 1 + \frac{P_0}{\epsilon_0 E} + \frac{P_1}{\epsilon_0 E} \quad \dots (3.4)$$

where  $P$  = polarisation in the media =  $P_0 + P_1$  in which  $P_0$  is the polarisation in the absence of free carriers.  $P_1$  is the modification to the overall polarisation due to electron shift when subjected to an arbitrary electric field and where  $N$  is the carrier concentration. Expressions (3.3) and (3.4) could be combined and simplified to yield :-

$$P_1 = -Ne \frac{dx}{dt} \Rightarrow k = n_0^2 + \frac{P_1}{\epsilon_0 E} = n_0^2 - \frac{\left[ \frac{e}{\epsilon_0 m^*} \right]}{\omega^2 - j\omega g} \quad \dots (3.5)$$

The real and imaginary parts of the dielectric constant could be separated as in the following :-

$$k_r = n_0^2 - \frac{\left[ \frac{Ne^2}{\epsilon_0 m^*} \right]}{\omega^2 + g^2} ; \quad k_i = \frac{g \left[ \frac{Ne^2}{\epsilon_0 m^*} \right]}{\omega^2 + g^2} \quad \dots (3.6)$$

The steady state distribution implies that  $d^2x / dt^2 = 0$ , thus the differential equation becomes :-

$$m^* g \frac{dx}{dt} = eE \Rightarrow g = \frac{e}{m^*} \frac{E}{\left[ \frac{dx}{dt} \right]} = \frac{e}{m^* \mu_e} \quad \dots (3.7)$$

Substituting standard values for the constants i.e.  $e = 1.6021892 \times 10^{-19}$  C,  $\mu_e = 8000$  cm<sup>2</sup>V<sup>-1</sup>s<sup>-1</sup> and  $m_r^*$  in GaAs  $\approx 0.0632 m_e$ , generated a value of  $g \approx 3.45 \times 10^{12}$  s<sup>-1</sup> for the damping constant. For material operation at optical frequencies of the order of  $\omega \approx 10^{15}$  s<sup>-1</sup>, the real and imaginary parts of the dielectric constant could be approximated as :-

$$k_r = n_0^2 - \frac{Ne^2}{\epsilon_0 m^* \omega^2} ; \quad k_i = \frac{gNe^2}{\epsilon_0 m^* \omega^2} = \frac{Ne^3}{(m^*)^2 \epsilon_0 \mu_e} \quad \dots (3.8)$$

In addition, the free carrier absorption coefficient,  $\alpha_{fc}$ , by definition is related to the imaginary [8] part of the dielectric constant  $k_i$ , such that :-

$$\alpha_{FC} = \frac{\Lambda k_1}{n} \dots (3.9)$$

where  $\Lambda$  = magnitude of the wavevector =  $\omega / c$  ;  $n$  = refractive index,  $c = f \lambda$  ;  $\lambda$  = free space wavelength ;  $\omega = 2\pi f$  ;  $f$  = frequency of photonic oscillation where  $E = hf$ . Hence :-

$$\alpha_{FC} = \frac{\Lambda}{n} \frac{Ne^3}{(m^*)^2 \epsilon_o \mu_e} = \frac{Ne^3}{(m^*)^2 \epsilon_o \omega^2 \mu_e c} = \frac{Ne^3 \lambda_o^2}{4\pi^2 (m^*)^2 \epsilon_o \mu_e c^3} \dots (3.10)$$

Equation (3.8) could be rewritten :-

$$k_r = n_o^2 - \Delta n^2 \quad \text{where} \quad \Delta n^2 = 2n_o \Delta n = - \frac{Ne^2}{m^* \epsilon_o \omega^2} \dots (3.11)$$

The change in refractive index due to a charge carrier plasma in which  $\Delta n^2 = 2n_o \Delta n$ , is given by analogy [8] :-

$$\Delta n = - \frac{Ne^2}{2n_o m^* \epsilon_o \omega^2} = - \frac{Ne^2 \lambda_o^2}{8\pi^2 n_o m^* \epsilon_o c^2} \dots (3.12)$$

The negative sign indicates that the presence of free carriers depresses the refractive index, assisted by intraband absorption. Hence, limited confinement is offered by charge plasma and doping disparities. Expression in (3.12) could be employed to calculate the relative index depressions due to doping disparities. The  $\Delta n$  refractive index modification was relative to the index value in the bulk with no deliberate Si dopants. Each donor atom liberates an electron that acts as a free carrier, and participates in intraband absorption and index depression. Since doping appears in both the active region and the substrate of a wafer structure, index depression occurs on both sides of their mutual interface. The greater doping in substrates leads to a relatively greater index depression in this region, hence generating limited total internal reflection and optical field confinement. An expression for the refractive index disparity incurred at the active region ( $n^-$ ) - substrate ( $n^{++}$ ) interface in devices of interest could be given from the following :-

$$\Delta n_{\text{active region}} = - \frac{N_{\text{act}} e^2 \lambda_o^2}{8\pi^2 n_o m^* \epsilon_o c^2} ; \quad \Delta n_{\text{substrate}} = - \frac{N_{\text{sub}} e^2 \lambda_o^2}{8\pi^2 n_o m^* \epsilon_o c^2} \dots (3.13)$$

$$\Rightarrow \Delta n = \Delta n_{\text{substrate}} - \Delta n_{\text{active region}} = - \frac{[N_{\text{sub}} - N_{\text{act}}] e^2 \lambda_o^2}{8\pi^2 n_o m^* \epsilon_o c^2} \dots (3.14)$$

The doping requirements of transferred electron devices suggests that  $N_{\text{act}} \ll N_{\text{sub}}$ , implying that an approximate expression for the net refractive index depression could be stated as :-

$$\Delta n \approx \Delta n_{\text{substrate}} = - \frac{N_{\text{sub}} e^2 \lambda_o^2}{8 \pi^2 n_o m^* \epsilon_o c^2} \quad \text{where} \quad N_{\text{sub}} = 10^{24} \text{ m}^{-3} \quad \text{--- (3.15)}$$

The doping level of the substrate was standardised at  $10^{18} \text{ cm}^{-3}$ , while other parameters such as  $\epsilon_o (n_o) m^*$  and  $\lambda_o$  could be considered as constants in GaAs samples. For operation at  $\lambda_o = 1.15 \mu\text{m}$ ,  $m^* = 0.0632 m_e$ , where  $m_e = 9.109534 \times 10^{-31} \text{ kg}$ , the overall expression could be reduced to that dependent upon either  $\lambda_o$ ,  $N_{\text{sub}} - N_{\text{act}}$  or both such that :-

$$\Delta n[\lambda_o] = 2.06 \times 10^{-3} \lambda_o^2 \quad \text{for} \quad \lambda_o \text{ in } \mu\text{m} \quad \text{--- (3.16)}$$

### **3.3 The Linear Electro-optic Effect**

The Linear Electro-optic Effect, or Pöckels effect, can only be observed in crystals without a centre of symmetry. To characterise or quantify this effect, the optical refractive index ellipsoid equality is introduced as follows :-

$$\frac{x^2}{n_x^2} + \frac{y^2}{n_y^2} + \frac{z^2}{n_z^2} = 1 \quad \text{--- (3.17)}$$

where  $n_x$ ,  $n_y$  and  $n_z$  are the indices in the three principle directions. These correspond to the crystallographic axes of zinc blende crystal types, such as GaAs, InP etc. The unity condition is met with zero electric field applied. In GaAs,  $n_x = n_y = n_z = n_o$ , hence leading to :-

$$\frac{x^2 + y^2 + z^2}{n_o^2} = 1 \quad \text{--- (3.18)}$$

The application of an electric field, with components in any of the principle axes,  $E(n_x, n_y, n_z)$ , induces modifications to  $1/n_x^2$ ,  $1/n_y^2$  and  $1/n_z^2$ . Extra terms could be introduced as follows :-

$$\left(\frac{1}{n^2}\right)_1 x^2 + \left(\frac{1}{n^2}\right)_2 y^2 + \left(\frac{1}{n^2}\right)_3 z^2 + 2\left(\frac{1}{n^2}\right)_4 yz + 2\left(\frac{1}{n^2}\right)_5 xz + 2\left(\frac{1}{n^2}\right)_6 xy = 1 \quad \text{--- (3.19)}$$

In the absence of an electric field ( $E = 0$ ) :-

$$\left(\frac{1}{n^2}\right)_1 \equiv \frac{1}{n_x^2}; \quad \left(\frac{1}{n^2}\right)_2 \equiv \frac{1}{n_y^2}; \quad \left(\frac{1}{n^2}\right)_3 \equiv \frac{1}{n_z^2}; \quad \left(\frac{1}{n^2}\right)_4 = \left(\frac{1}{n^2}\right)_5 = \left(\frac{1}{n^2}\right)_6 = 0 \quad \text{--- (3.20)}$$

Modifications to these coefficients  $(1/n^2)_i$ , for  $i = 1, 2, \dots, 6$  due to  $E$  is given by :-

$$\Delta\left(\frac{1}{n^2}\right)_i = \sum_{j=1}^3 r_{ij} E_j \quad \text{where} \quad x = 1, \quad y = 2, \quad z = 3 \quad \text{--- (3.21)}$$

Expression (3.21) is a compressed version of the Electro-optic tensor, giving a  $6 \times 3$  matrix of  $r_{ij}$  matrix elements, which can be derived from symmetry considerations [46]. For GaAs, and other zinc

sulphide lattice materials, this matrix can be reduced to three non-equivalent non-zero terms. Hence  $r_{63}$

$$= r_{52} = r_{41}.$$

$$\Delta \left[ \frac{1}{n^2} \right]_i = \begin{bmatrix} \Delta \left[ \frac{1}{n^2} \right]_1 \\ \Delta \left[ \frac{1}{n^2} \right]_2 \\ \Delta \left[ \frac{1}{n^2} \right]_3 \\ \Delta \left[ \frac{1}{n^2} \right]_4 \\ \Delta \left[ \frac{1}{n^2} \right]_5 \\ \Delta \left[ \frac{1}{n^2} \right]_6 \end{bmatrix} = \begin{bmatrix} r_{11} & r_{12} & r_{13} \\ r_{21} & r_{22} & r_{23} \\ r_{31} & r_{32} & r_{33} \\ r_{41} & r_{42} & r_{43} \\ r_{51} & r_{52} & r_{53} \\ r_{61} & r_{62} & r_{63} \end{bmatrix} \cdot \begin{bmatrix} E_1 \\ E_2 \\ E_3 \end{bmatrix} \Rightarrow \begin{bmatrix} 0 & 0 & 0 \\ 0 & 0 & 0 \\ 0 & 0 & 0 \\ r_{41} & 0 & 0 \\ 0 & r_{52} & 0 \\ 0 & 0 & r_{63} \end{bmatrix}_{\text{GaAs}} \cdot \begin{bmatrix} E_1 \\ E_2 \\ E_3 \end{bmatrix} \quad \text{--- (3.22)}$$

Recalling equation (3.19), and employing :-

$$\left[ \frac{1}{n^2} \right]_1 = \left[ \frac{1}{n^2} \right]_2 = \left[ \frac{1}{n^2} \right]_3 = \frac{1}{n_o^2} \quad \text{--- (3.23)}$$

the index ellipsoid is deformed with an applied electric field leading to :-

$$\frac{x^2 + y^2 + z^2}{n_o^2} + 2r_{41}[E_x yz + E_y xz + E_z xy] = 1 \quad \text{--- (3.24)}$$

A new co-ordinate system  $x', y', z'$  could then be introduced, in which the directions of the new system may be determined through rotation of the original  $x, y, z$  system to coincide with those in

(3.24) :-

$$\frac{x'^2}{n_x'^2} + \frac{y'^2}{n_y'^2} + \frac{z'^2}{n_z'^2} = 1 \quad \text{and} \quad \begin{bmatrix} x \\ y \\ z \end{bmatrix} = \begin{bmatrix} \alpha_1 & \beta_1 & \gamma_1 \\ \alpha_2 & \beta_2 & \gamma_2 \\ \alpha_3 & \beta_3 & \gamma_3 \end{bmatrix} \begin{bmatrix} x' \\ y' \\ z' \end{bmatrix} \quad \text{--- (3.25)}$$

where  $n_x', n_y', n_z'$  = principle indices under electric field tension

$\alpha_1, \beta_1, \gamma_1$  = direction cosines relating  $x, y, z$  to  $x', y', z'$

Roots could be found to the discriminant [43] of the following, hence generating  $n_x', n_y', n_z'$ :-

$$\begin{vmatrix} \frac{1}{n_o^2} - \eta & r_{41}E_x & r_{41}E_y \\ r_{41}E_z & \frac{1}{n_o^2} - \eta & r_{41}E_x \\ r_{41}E_y & r_{41}E_x & \frac{1}{n_o^2} - \eta \end{vmatrix} = 0 \quad \text{--- (3.26)}$$

Field directions normal to the  $\langle 100 \rangle$ ,  $\langle 011 \rangle$  and  $\langle 111 \rangle$  crystallographic planes in zinc sulphide lattice crystals are employed in material characterisation. Modifications to the refractive

indices and associated phase retardations, for these crystal directions, are provided in the table of Figure 3.4. With the natural cleavage planes of GaAs lying in the  $\langle 011 \rangle$  direction, and wafer growth misoriented  $2^\circ$  from  $\langle 100 \rangle$ , the directions of disturbance propagation in planar and vertical TEDs are as shown in Figure 3.5.

	$E \perp \langle 100 \rangle$	$E \perp \langle 011 \rangle$
Applied Field	$E_x = E_y = 0,$ $E_z = E$	$E_x = E_y = \frac{E}{\sqrt{2}}, E_z = 0$
$n'_x$	$n_o + \frac{1}{2}n_o^3r_{41}E$	$n_o + \frac{1}{2}n_o^3r_{41}E$
$n'_y$	$n_o - \frac{1}{2}n_o^3r_{41}E$	$n_o - \frac{1}{2}n_o^3r_{41}E$
$n'_z$	$n_o$	$n_o$
Phase difference, $\Gamma$	$\Gamma[100] = \frac{2\pi}{\lambda}n_o^3r_{41}V$ $\Gamma[001] = \Gamma[00\bar{1}] = 0$ $\Gamma[011] = \frac{\pi L}{\lambda d}n_o^3r_{41}V$	$\Gamma[100] = 0$ $\Gamma[011] = 0$ $\Gamma[0\bar{1}1] = \frac{2\pi L}{\lambda d}n_o^3r_{41}V$

$L$  = thickness of crystal in direction of applied electric field

$d$  = thickness of crystal in direction of optical propagation

**Figure 3.4 :- Phase retardations and index modifications with LEO effect**

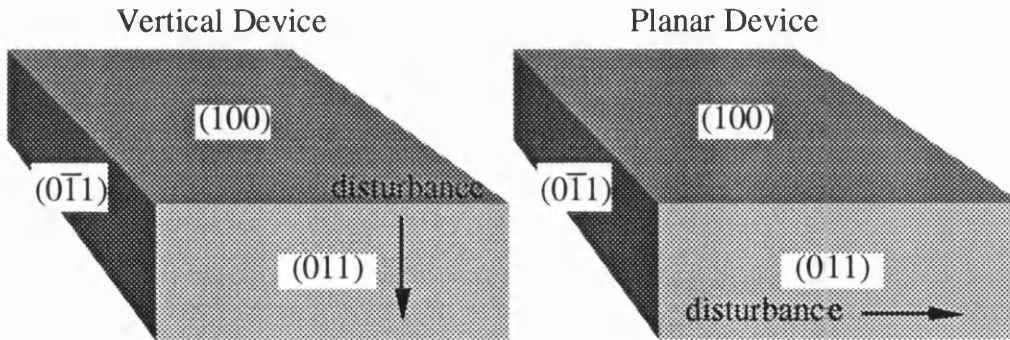


**Figure 3.5 :- Direction of disturbance propagation in TEDs**

For devices with a vertical orientation, optical radiation undergoes a positive phase shift relative to the phase with which it enters the crystal, while planar devices lead to a negative phase shift. The table also demonstrates that no phase shifts occur in the  $\langle 011 \rangle$  direction, in contrast to the  $\langle 0\bar{1}1 \rangle$  orientation in planar devices.

### **3.4 Estimation of Modulation Depths**

The theory of the electro-optic effect [8] demonstrates that the modulation depth can be obtained from experimental or theoretical values of the phase retardation,  $\Gamma$ , through the following :-

$$\eta_{EO} = \frac{I_{EO}}{I_o} = \sin^2 \left[ \frac{1}{2} \Gamma \right] = \sin^2 \left[ \left[ \frac{\pi}{2\lambda} \right] n_o^3 r_{41} E_{dom} L \right] \quad \text{where } E_{dom} = \text{peak dipole field} \quad \dots (3.27)$$

Experimental assessments of modulation depth could be made by employing the general principle of cross and parallel polarisers as shown in Figure 3.2. Calculations could also be performed with the assistance of Yariv's methods [8] for estimating the refractive index,  $n_o$ , of an unperturbed crystal. An expression for  $n_o$  in terms of incident wavelength and aluminium fraction was defined as follows (Figure 3.10) :-

$$n_o(x, \lambda) = \sqrt{10.9 - 2.92x + \frac{0.9751}{(\lambda^2 - \alpha) - \beta\lambda^2}}; \quad \dots (3.28)$$

$$\alpha = 0.30386 - 0.105x \quad \text{for } x > 0.36; \quad \lambda \text{ in } \mu\text{m}$$

$$\alpha = 0.52886 - 0.735x \quad \text{for } x < 0.36; \quad \beta = 2.437 \times 10^{-3} [1 + 1.413x] \quad \dots (3.29)$$

Combining expressions (3.27) and (3.28), the modulation depth due to the linear electro-optic effect was calculated at an assortment of peak dipole fields, wavelengths and ribs lengths, with  $r_{41} = 1.2 \times 10^{-12} \text{ mV}^{-1}$ ,  $x = 0$  (i.e. GaAs). These variations were shown in Figures 3.6, 3.7, 3.8 and 3.9.

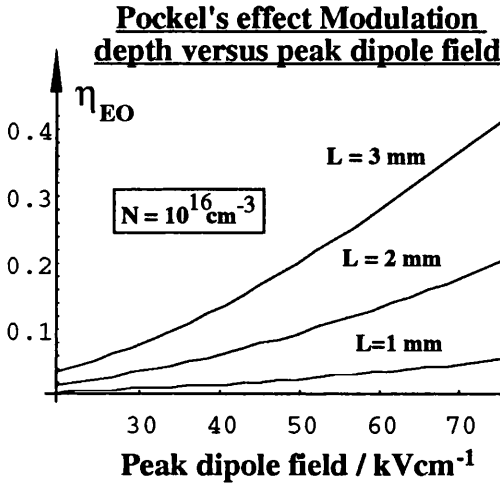


Figure 3.6

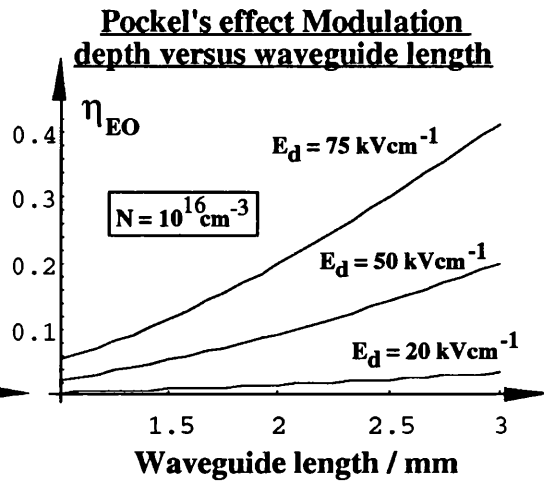


Figure 3.7

The projected modulation depth for the Linear electro-optic effect was shown to increase sharply with peak domain field in particular, with a similar sensitivity to waveguide length. The decrease in depth with increasing wavelength of incident radiation was determined through the base refractive index. Maximum modulation depths were demonstrated to be of the order of 40 % with the parameter ranges used.

In a similar manner, the modulation depths due to Franz-Keldysh and free carrier absorption, and high density charged plasma contributions were calculated, with the assistance of expressions

(3.1), (3.10) and (3.12). The absorption coefficients generated by calculations were used to imply modulation depths by noting that :-

$$\eta_{EA} = \frac{I_o - I_{EA}}{I_o} = 1 - e^{-\Delta\alpha_{EA}L}; \quad \eta_{FC} = 1 - e^{-\Delta\alpha_{FC}L}; \quad \eta_{FC} = \sin^2 \left[ \frac{N e^2 \lambda_o L}{16 \pi d n_o m^* \epsilon_o c^2} \right] \quad (3.30)$$

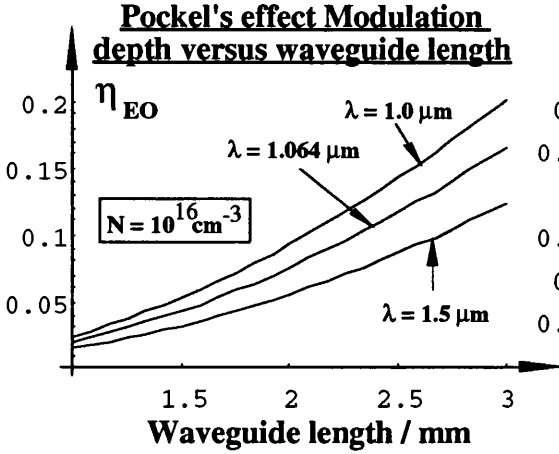


Figure 3.8

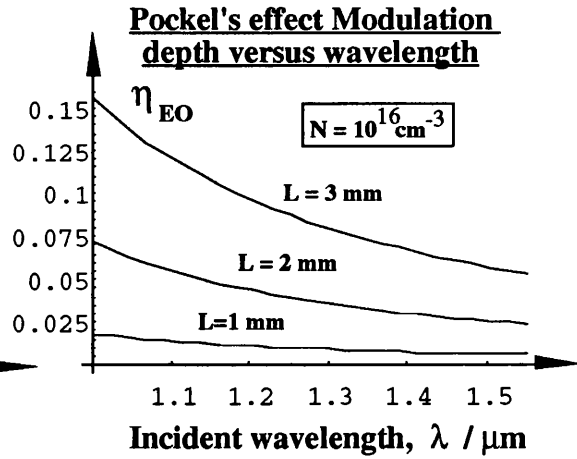


Figure 3.9

Variations of the estimated modulation depth due to free carrier plasma index depression were given in Figures 3.11, 3.12 and 3.13. The depth was observed to decrease with increasing waveguide length and increase with increasing rib height and incident wavelength. Maximum modulation depths of the order of 4 % were suggested by the calculations.

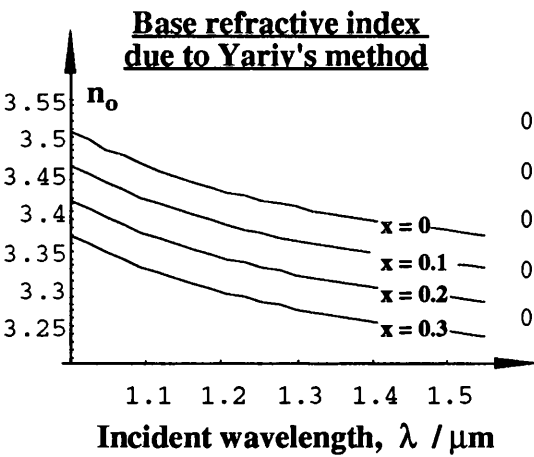


Figure 3.10

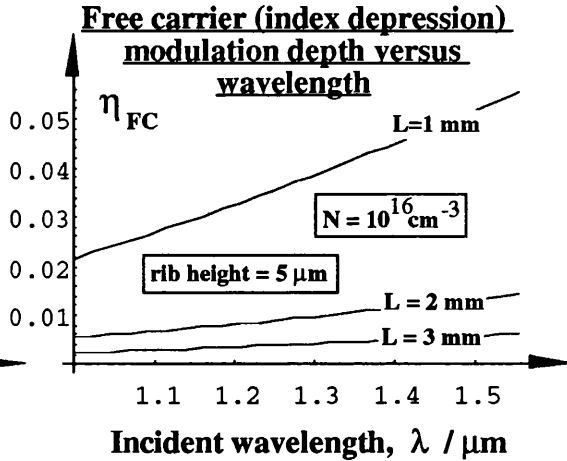


Figure 3.11

Further to this, the influence of absorption processes were evaluated with similar parameter values. Modulation depths resulting from free carrier absorption were given in Figures 3.14 and 3.15, and were observed to increase with both wavelength and background doping. The general depth, no more than 0.3 %, was three orders of magnitude below that afforded by Pöckels effect (Linear electro-optic effect) in the same circumstances.

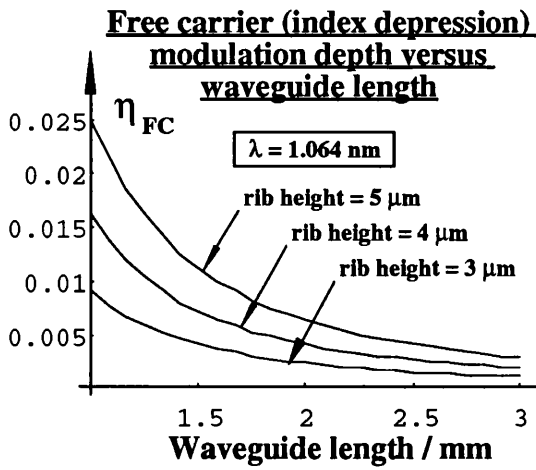


Figure 3.12

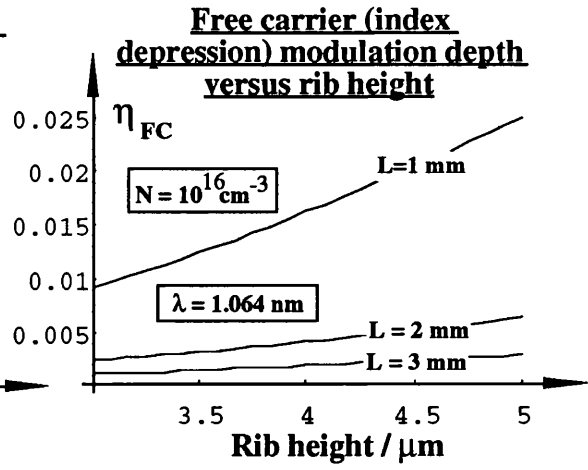


Figure 3.13

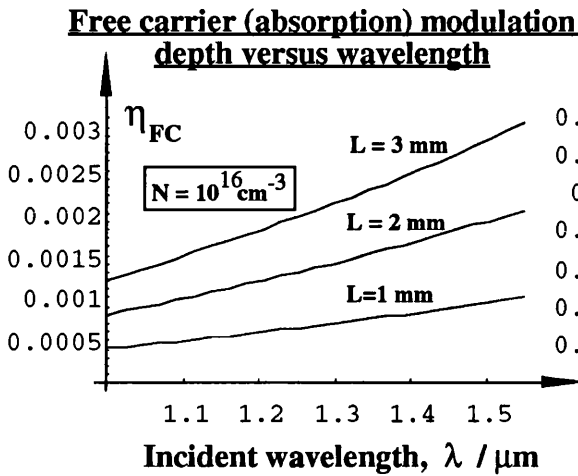


Figure 3.14

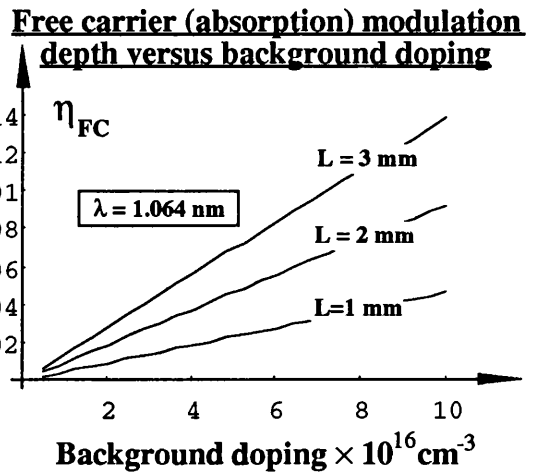


Figure 3.15

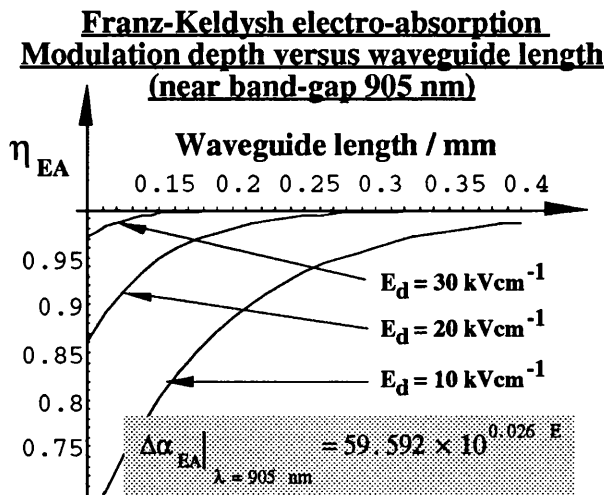


Figure 3.16

Equivalent calculations for the modulation depth due to Franz-Keldysh electro-absorption were limited to near band-gap wavelengths, (i.e. 905 nm) since the absorption coefficient in GaAs was

negligible at wavelengths of 1.15  $\mu\text{m}$  and above. With radiation approaching the 890 nm GaAs band-edge, virtually complete (100 %) extinction was observed even with very short waveguide sections (Figure 3.16). The functional variation of absorption coefficient in GaAs at 905 nm with applied electric field was as given at the base of Figure 3.16.

### **3.5 Conclusions**

Theoretical calculations of the projected modulation depths due to the four optoelectronic phenomena cited by E. I. Gordon [44] were performed for standard vertical rib waveguide devices. Throughout these calculations, several idealised assumptions were made :-

(i) the whole volume of bulk crystal was at the peak dipole field, leading to overestimates of all the modulation indices ; (ii) the level of optoelectronic interaction remained constant along the whole length of the rib waveguide ; (iii) base refractive index values in bulk GaAs were generated by Yariv's function [8].

The deepest modulation at longer wavelengths resulted from Pöckel's effect (40 %max.), while free carrier contributions were minimal in comparison (4 % phase retardation, 0.3 % absorption). Accounting for the fact that the peak domain field is only achieved over a very restricted spatial region in the interaction site, the modulation depths expected in real devices were significantly below those predicted. The predicted total extinction ratio of >50 % was reduced by the limited average electric field value within the whole critical region of interaction. In particular, the requirement of modern optical fibre communication systems to operate at wavelengths as distant from the natural GaAs band-edge as 1.3  $\mu\text{m}$ , meant that Franz-Keldysh electro-absorption could not be exploited efficiently. All of the other phenomena were also seen to produce lower depths at longer wavelengths. The experimental observations of Cohen et al [11], Ohta et al [12] and Moreland et al [13] all confirmed that practical modulation indices were no more than 20 % in high speed TEDs. In addition, to achieve these depths, very long waveguide sections were required (e.g. 3 mm). As is demonstrated in Chapters 4 and 7, waveguide lengths are inhibited by the necessity to heatsink the device.

## Chapter 4

### Device Design and Fabrication

This chapter includes a discussion of the principles upon which devices were designed. A description of the fabrication procedure, featuring plasma dry-etching, is also provided. A range of fabrication parameters were varied as appropriate, while evaluations of refractive index depression, waveguide modal modelling and wafer design are given. Modal analysis of waveguiding ribs was performed using FWAVE III [47] and LWAVE [48] applications.

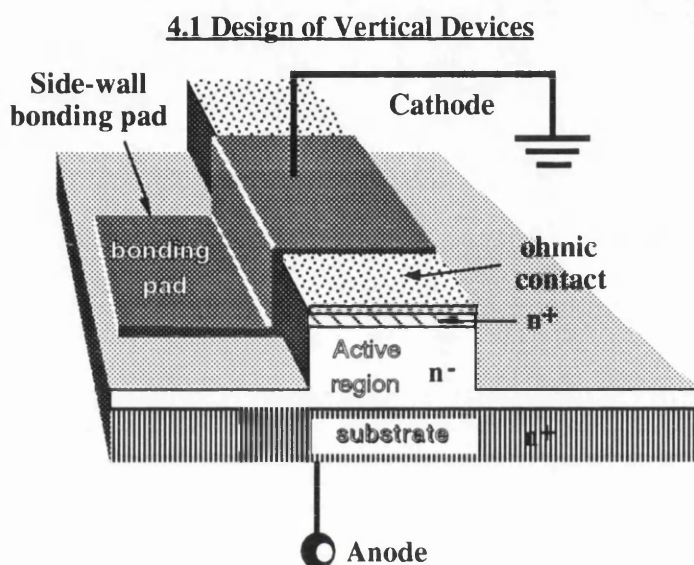


**Figure 4.1 :- Moreland vertical device design**

Moreland et al [13] [14] [15] reported coherent modulation at 1.15  $\mu\text{m}$  wavelength radiation in a device of the structure shown in Figure 4.1. A high-field disturbance was thought to provided this modulation. The merits of these integrated structures for optoelectronic devices have been well documented [4] [8]. The Moreland vertical device achieved electrical communication through a non-isolated side-wall Schottky bonding pad. Devices were fabricated from MOVPE wafer material from Sheffield University, which contained doping disparities and homojunctions exclusively. No attempt to depart from the customary  $n^+-n^-n^{++}$  active region format was made. Since this device structure was reported to generate modulation through dipole instabilities, it was replicated. Existing photolithographic mask plates were used in the process. Rib widths generated by these mask plates ranged from 2  $\mu\text{m}$  up to 15  $\mu\text{m}$ , with a standard length of 7 mm (7000  $\mu\text{m}$ ). For such a simple device, only plates defining rib and bonding pad were required for photolithography. After analysing the

# Non-ideal Features associated with inherited device design

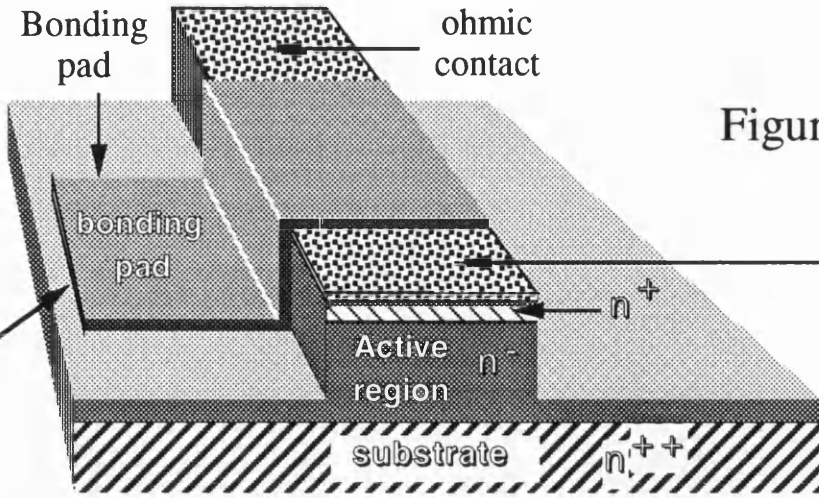


Figure 4.2

Non -ideal feature	Consequence for device operation
Side-wall bond pad	Lateral asymmetry of pre-threshold Electric field
Coincident rib-waveguide and cathode contact	Minimum dimensional requirements of physical waveguide increased device current capacity
Epitaxial-side cathode with substrate-side cathode	Substantial substrate thick nesses ( $>200 \mu\text{m}$ ) led to excessive thermal energy generation and series +ve resistance

# Attempted Engineering Solutions for vertical Implementation

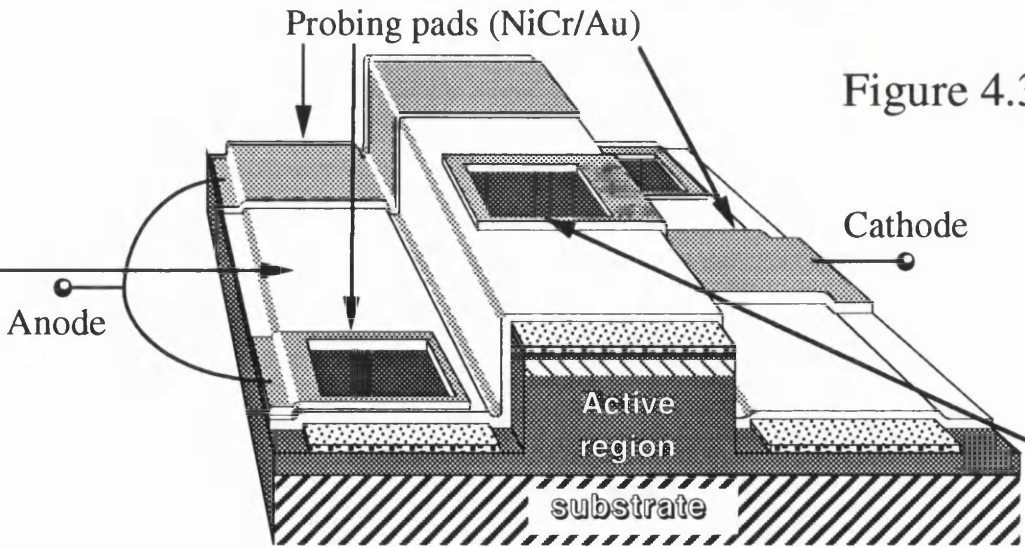
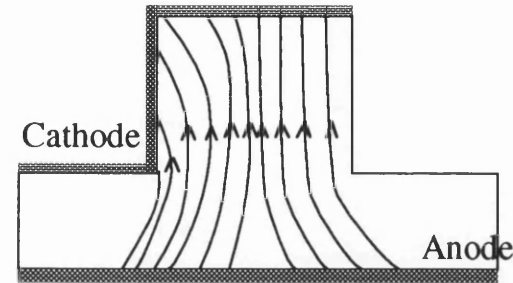


Figure 4.3

Attempted solution	Proposed Benefit
$\text{SiO}_2$ isolation layer with $\text{C}_2\text{F}_6$ -etched communicating windows	Elimination of side-wall nature of bonding pads. Surface communication possible
Reduced current - carrying channel in the lateral direction	Small, high-proximity etched windows define this reduced channel
Dual-anode reappropriated to epitaxial side	Substrate no longer supports current, hence reduces power dissipation and +ve series resistance

Moreland structure, many defects and non-ideal features were identified (Figures 4.2 and 4.3). A reappraisal of this device suggested a more appropriate device-form of the type shown in Figure 4.3.

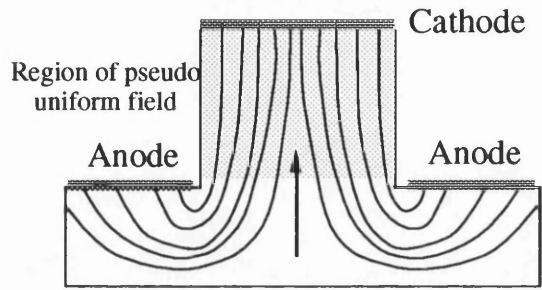
**Fundamental asymmetry of side wall bonding pad device**



Estimated electric field distribution

**Figure 4.4 (a) :- Asymmetrical field distribution in sidewall structure**

**Symmetrical field distribution in dual anode device**



Estimated electric field distribution

**Figure 4.4 (b) :- Symmetrical field in Dual-anode vertical device structure**

The thermal implications of the substrate were considered initially. Similar limitations have occurred with semiconductor lasers [7], and were solved through substrate thinning exclusively. Proposals to improve its thermal performance included the repositioning of the anode contact onto epitaxial side of the device. A symmetrical field distribution was achieved by separating the anode into two parts. One contact of the dual-anode was positioned either side of the central rib (with coincident cathode contact). The side-wall non-isolated bonding pad induced an asymmetric electric field profile within the active region, while surface states and imperfections acted as efficient carrier traps (Figures 4.4 (a) and 4.4 (b)).

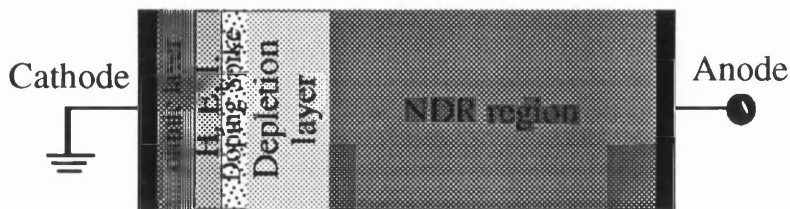


**Figure 4.5 :- Cathode features in vertical wafer devices**

Extra features were introduced next to the cathode contact to modify the pre-threshold electric field and / or carrier injection into the active region (Figure 4.5). In the Side-wall structure, a reverse bias Schottky contact {70 nm Ti : 300 nm Au} was used to provide limited electrical isolation. The revised structure did not employ rectification, but relied alternatively on electrical isolation through dielectric layers. The growth of epitaxial layers "fixes" the natural transit mode frequency in vertical

devices through the thickness of the active region layer. The  $10^7 \text{ cm s}^{-1}$  transit velocity of the disturbance leads to the simple relation for all GaAs transferred electron devices :-  $f_{\text{GHz}} L_{\mu\text{m}} \approx 100$

#### 4.1.2 Capacitance Considerations of Vertical devices

For a device operating in isolation, in the absence of an external resonant circuit, the natural resonant frequency was given by :-

$$f_{\text{nat}} = \frac{1}{2\pi\sqrt{LC}} \dots\dots (4.1)$$

where L and C represent the natural device inductance and capacitance of the device itself. To operate the device in a basic D.C. environment with negligible external resonances, the inductance and capacitance of the device was minimised.

Ordinarily, the inductance of the device resulted from bond-wires used to electrically communicate with the device. The magnitude of the inductance was determined by the loop areas generated by bond-wires. Small loop areas and tight bond-wires minimised the added inductance and its limiting effect upon the natural resonant frequency.

The main contribution to device capacitance came from metallised overlaps in parallel plate form. Large area overlaps could be identified in both the side-wall and revised structures. Their magnitude significantly limited the upper frequency. In A.C. conditions, or in a state of internal RF self excitation, the parallel plate capacitance could be stated as in equation 4.2, where x is the amount of substrate removed by thinning,  $\epsilon$  is the dielectric permittivity and A is the area of overlap (Figure 4.6):-

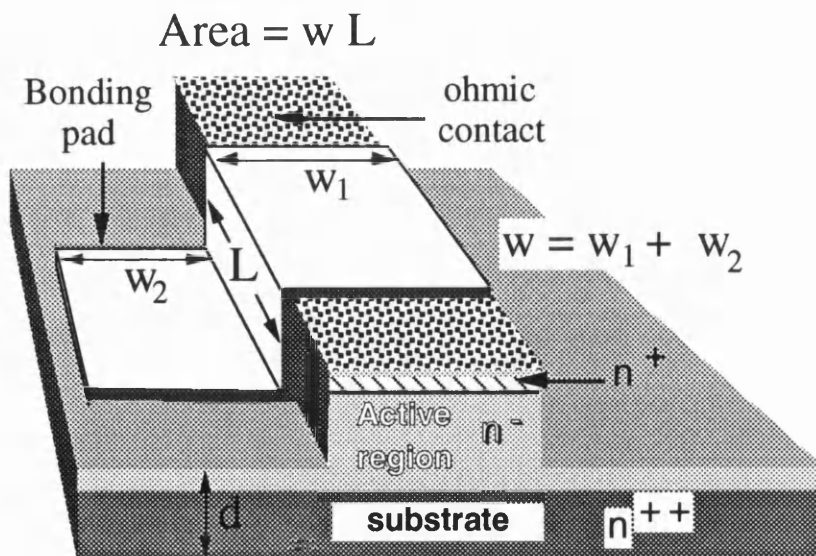


**Figure 4.6 :- Overlap capacitance in side-wall devices**

$$C_{\text{thinned}} = \frac{\epsilon_{\text{GaAs}} w L}{450 \mu\text{m} - x} \quad \text{---- (4.2)}$$

This is plotted in Figure 4.7. For 6000  $\mu\text{m}$  length and 600  $\mu\text{m}$  width, a side-wall device with a thinned 100  $\mu\text{m}$  substrate yields a capacitance of over 4 pF.

### Overlap Capacitance for "Side-wall" structure (1 mm bonding pad width)

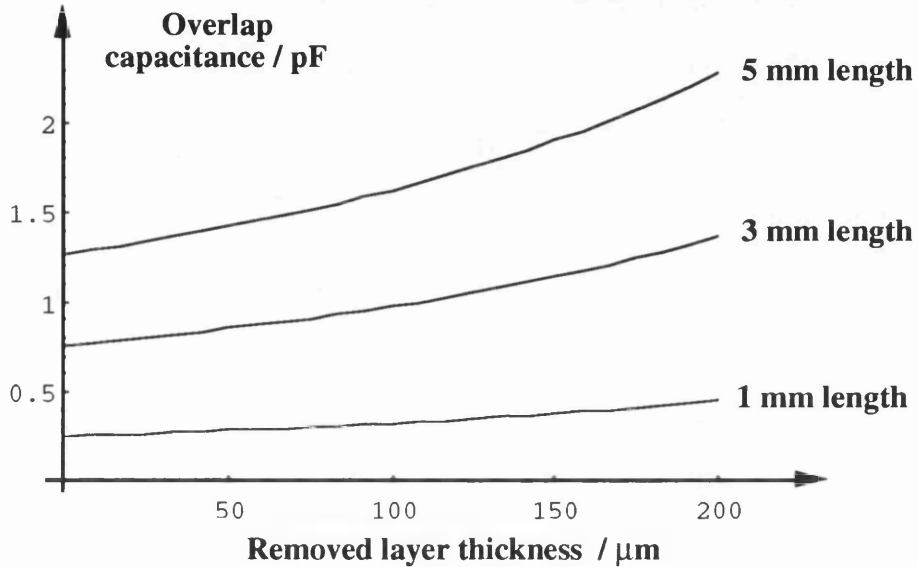


Figure 4.7

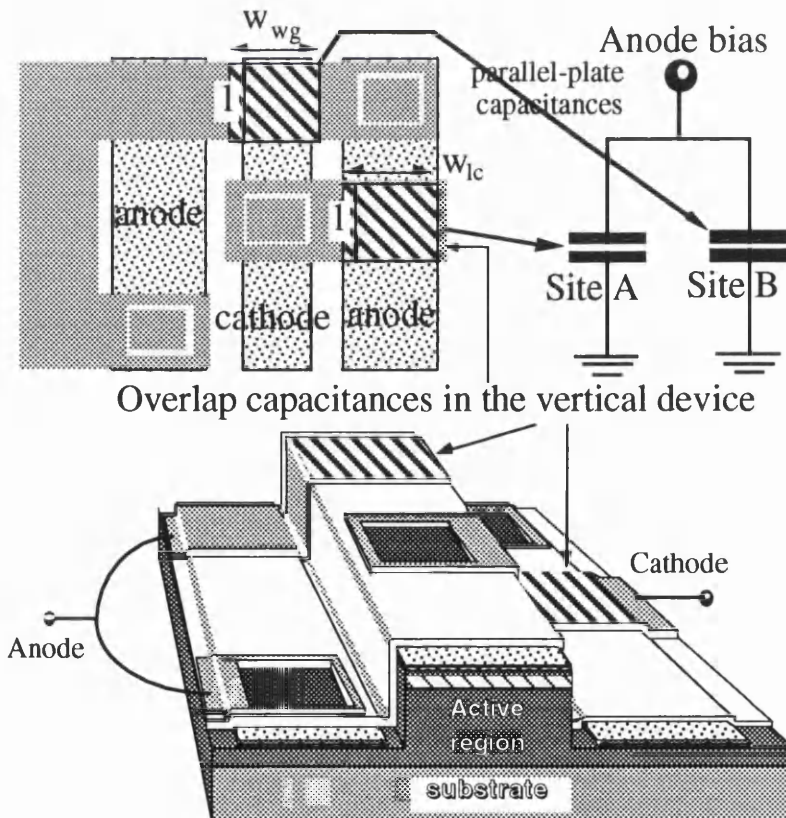
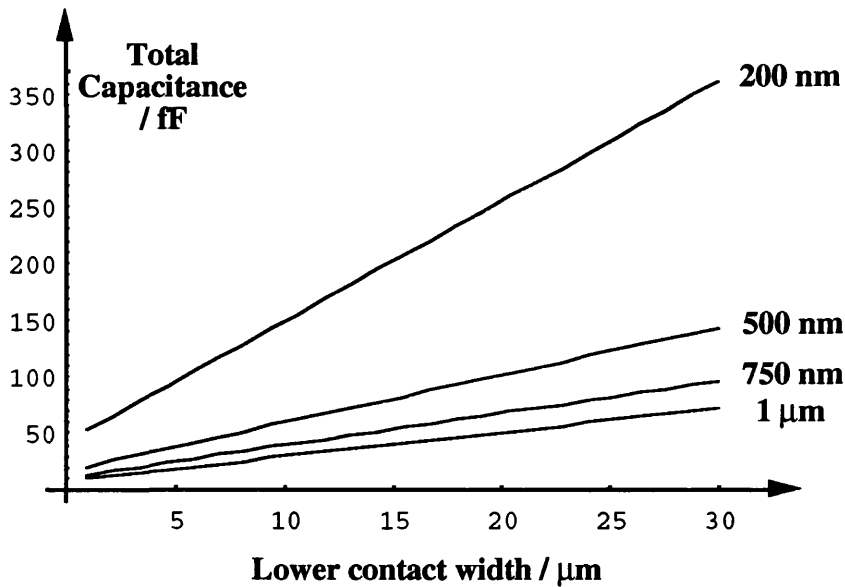


Figure 4.8 :- Dynamic "parallel-plate" capacitances

**Total Capacitance of Revised vertical Structure, varying with lower contact width for various values of dielectric thickness**



**Figure 4.9**

**Total Capacitance of Revised vertical Structure, varying with dielectric thickness for various values of lower contact width**

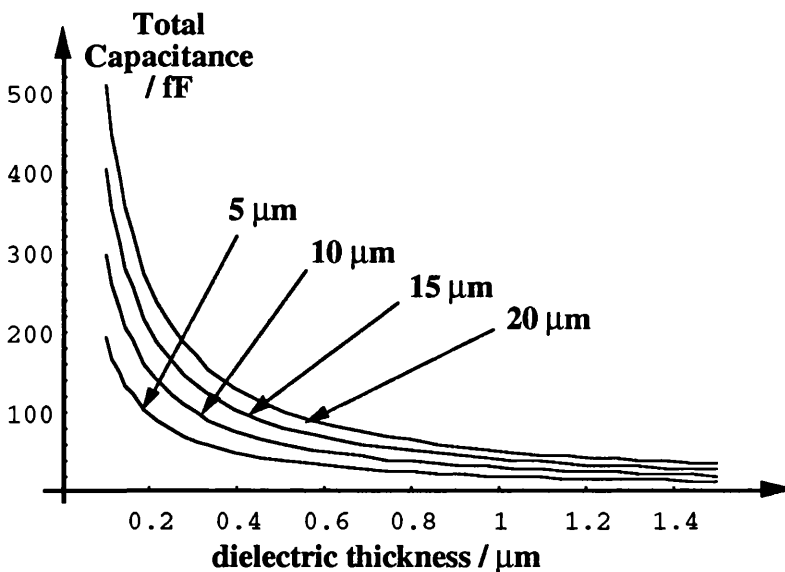


**Figure 4.10**

The revised device generated dynamic capacitances from bonding pad digit and ohmic contacts overlaps with the silica insulating layer. The same voltage was dropped across both metal-dioxide-metal combinations, leading to a simple parallel configuration (Figure 4.8). The total device capacitance (neglecting interdigital coupling effects at high frequency) could be stated as :-

$$C_{wg} = \frac{\epsilon_{SiO_2} L w_{wg}}{d_{SiO_2}} ; C_{lc} = \frac{\epsilon_{SiO_2} L w_{lc}}{d_{SiO_2}} \Rightarrow C_{total} = \frac{\epsilon_{SiO_2} L}{d_{SiO_2}} \{ w_{wg} + w_{lc} \} \quad \text{--- (4.4)}$$

Figures 4.9 and 4.10 described the variation of the total capacitance with the width of the lower contact and dielectric thickness respectively. An increase in the dielectric thickness had the desired effect of reducing the total capacitance.

### Natural resonant frequency variation with capacitance (for values of inductance) of series LC network for a vertical device

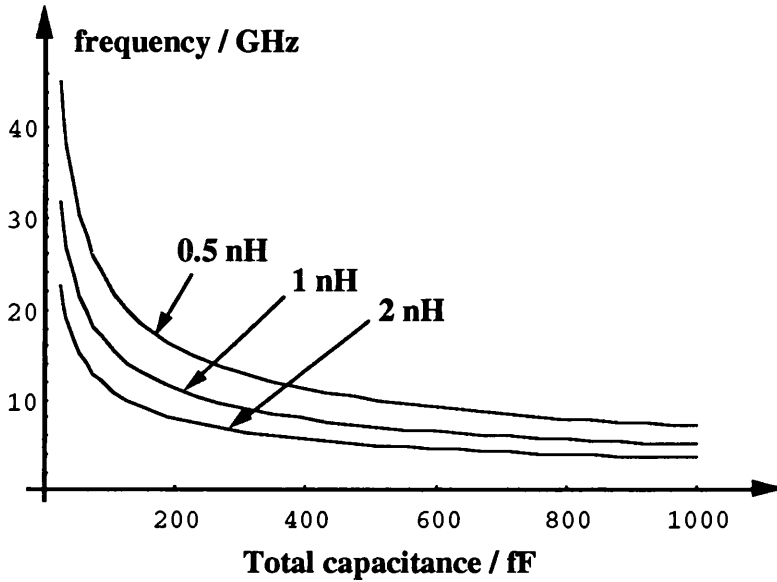


**Figure 4.11**

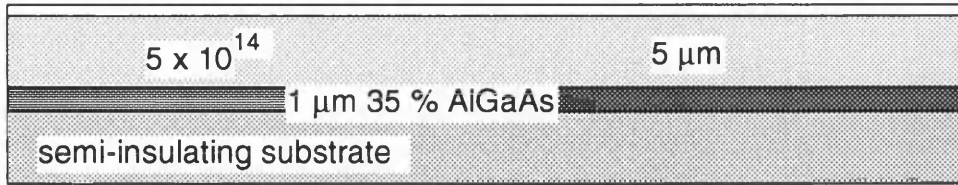
The natural resonant frequency was evaluated through the assumption that 1 nH inductance was present from external contributions, and plotted in Figure 4.11. For 40 GHz oscillatory operation, the product of inductance and capacitance was such that  $LC < 1.583 \times 10^{-23} \text{ HF}$  which for 1 nH inductance implies a maximum capacitance of 0.158 pF. Transferred electron oscillations required that the active region n-type doping, and the active region effective length should be such that [19] [20]  $n_o L > 10^{12} \text{ cm}^{-2}$  for genuine Transit mode operation. Certain groups [23] [24] have determined that fully-matured and saturated disturbances do not form in samples with propagation zones of less than 10  $\mu\text{m}$ . Attention was directed towards the physical dimensions of devices. Consider a waveguide of length,  $L_{wg}$  and width,  $w_{wg}$ . A simple expression for the current drawn at threshold could be given as :-

$$I_{th} = n_o e \mu L_{wg} w_{wg} E_{th} \quad \text{--- (4.5)}$$

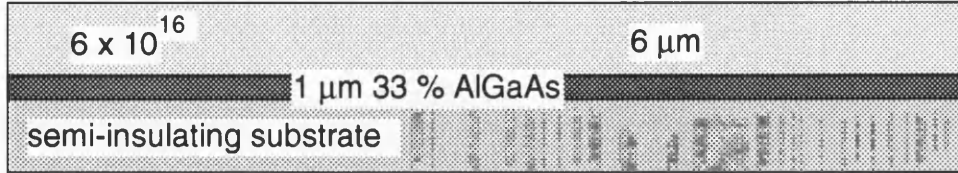
(a) Wafers for planar devices

A297

$10^{18}$  100 nm

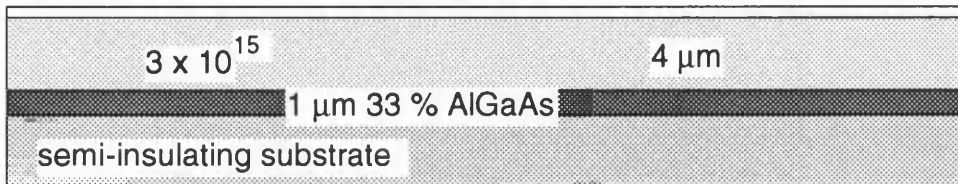


A455



B157

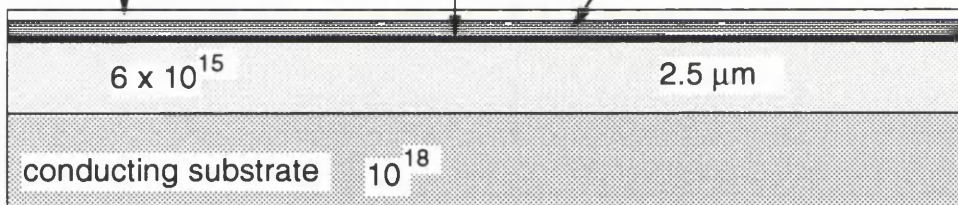
$10^{18}$  200 nm



(b) Wafers for vertical devices

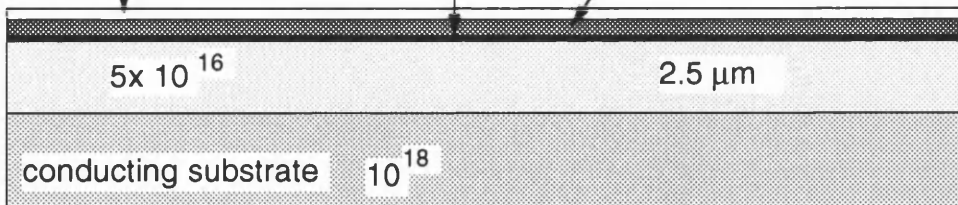
B115

$10^{18}$  200 nm  $3 \times 10^{18}$  doping spike 50 nm 50 nm 0-30 % AlGaAs



B148

$10^{18}$  200 nm  $>5 \times 10^{18}$  doping spike 40 nm 100 nm 0-30 % AlGaAs



A746

$10^{18}$  200 nm  $>5 \times 10^{18}$  doping spike 40 nm

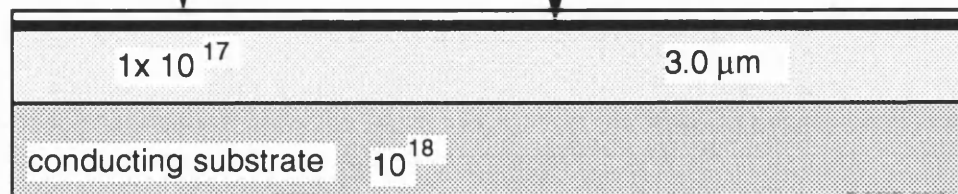


Figure 4.12

# Hot Electron Injector Mechanism

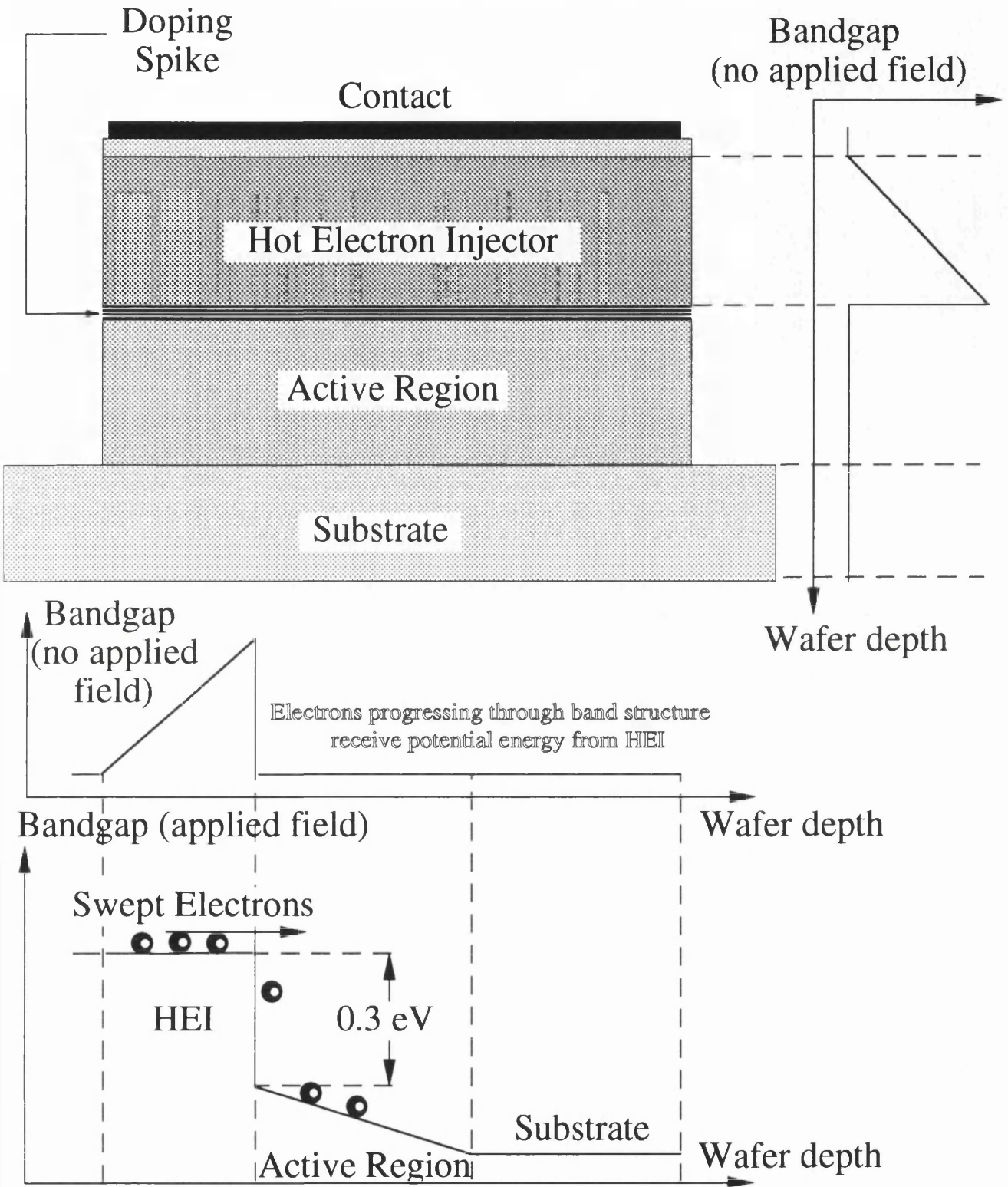


Figure 4.13

where the threshold field,  $E_{th}$ , was taken to be  $3200 \text{ Vcm}^{-1}$  in gallium arsenide. If an arbitrary 1 Amp current limitation at threshold was imposed, this implied the inequality :-

$$L_{wg} w_{wg} = \frac{I_{th}}{n_o e \mu E_{th}} \Rightarrow L_{wg} w_{wg} (\text{cm}) < \frac{2.438 \times 10^{11}}{n_o (\text{cm}^{-3})} \text{ ---- (4.6)}$$

Subsequently, the fundamental operating frequency could be taken as :-

$$f = \frac{v_{dis}}{h_{ar}} \Rightarrow f_{\text{GHz}} h_{ar} \approx 100 ; n_o h_{ar} > 10^{12} \text{ cm}^{-2} \Rightarrow n_o \frac{10^7}{f} > 10^{12} \text{ cm}^{-2} \text{ ---- (4.7)}$$

where  $v_{dis}$  is the velocity of the disturbance. Several wafers were designed in view of these engineering requirements. All material was grown by the MBE facility at the University of Glasgow. Wafers suitable for both vertical and planar devices were grown separately (Figure 4.12).

An important feature beyond the doping spike was the so called "hot electron injector". It consisted of a graded AlGaAs layer, varying in fraction from 0 % to 30 % at the Hot Electron Injector (HEI) - doping spike interface (Figure 4.13). The linear grading of the AlGaAs layer generated a similar grading of the bandgap within this layer. The theoretical and practical merits of a HEI-incorporated transferred electron device were reported by Kelly, Couch and Spooner [16] [17] in 1990.

#### 4.2 Design of Planar Devices

A planar implementation, of the form of Figure 4.14, was considered additionally. Its primary virtue was its simplicity, with disturbance development occurring in the plane of epitaxial growth (perpendicular to the direction of crystal growth).

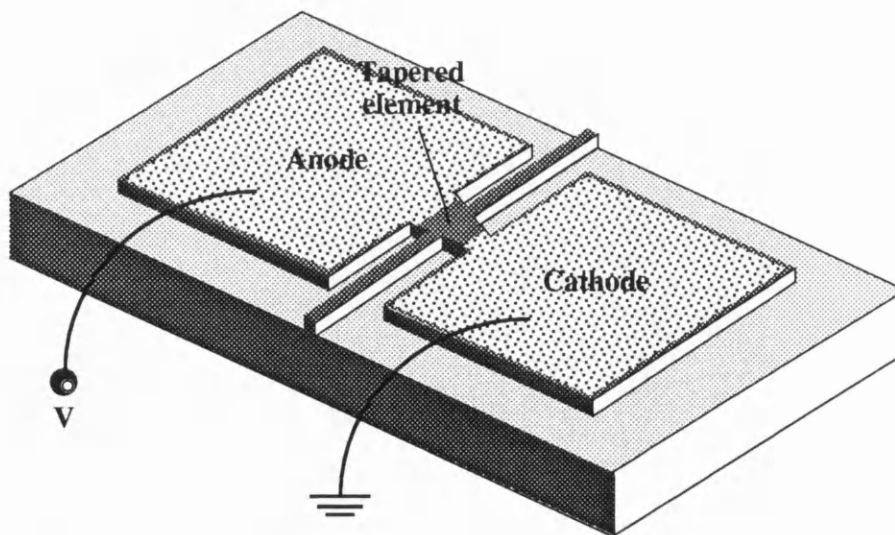


**Figure 4.14 :- Planar implementation of the waveguide device**

Wafers for planar devices were of greater simplicity, with the lateral nature of the devices only requiring (1) semi-insulating substrate, (2) optical confinement layer i.e. lattice matched bulk undoped AlGaAs (33 %), (3) active region n-type GaAs layer, (4) ohmic contact layer.

Since no vertical conduction was required, semi-insulating substrates, in addition to a 1  $\mu\text{m}$  AlGaAs layer, provided confinement of conduction. The AlGaAs layer naturally confined optical radiation in the vertical direction. This was due to the refractive index depression afforded by greater band gap materials. The conduction channel was a standard Si-doped n-type GaAs layer, 4 - 6  $\mu\text{m}$  deep, with doping generally lower than its vertical wafer equivalent. Planar devices had larger intercontact separations and propagation zones.

Typical dimensions for planar devices (tapered and non-tapered, Chapter 5) were 15  $\mu\text{m}$  - 50  $\mu\text{m}$  channel widths and 4  $\mu\text{m}$  - 6  $\mu\text{m}$  depths for conduction channels. A standardised 4  $\mu\text{m}$  wide integrated rib waveguide of arbitrary length was included.

### 4.3 Comparison between Vertical and Planar Devices

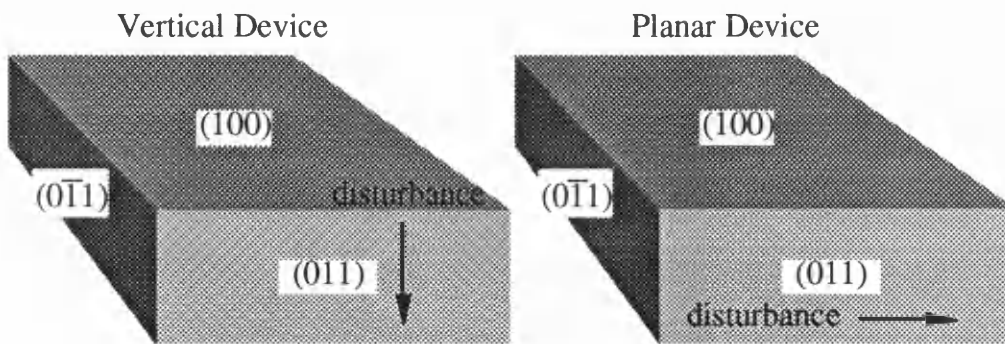


**Figure 4.15 :- Direction of disturbance propagation**

Disturbance propagation was orthogonal to the direction of propagation of the optical radiation in both cases (Figure 4.15). A specific volume of overlap (interaction) between the carrier accumulation / electric field content of the disturbance, and the optical field is created in both geometries.

Many influential disparities existed between the vertical and planar device implementations, and are summarised in the table of Figure 4.16. In addition to the definition of the active region conduction channel and incorporated rib waveguide, only a minimal number of further fabrication procedures were required for planar devices. This emphasised one of its primary virtues when compared with the vertical device previously described i.e. its simplicity of design.

(a) Vertical Devices	(b) Planar Devices
Transit-mode frequency can be determined at the wafer design and growth stage, and is therefore unalterable	Operating frequency can be determined by contact separation during the fabrication stage
Epitaxial growth by MBE permits the inclusion of homo- or heterojunctions as an integral part of the structure e.g. graded AlGaAs hot electron injector, doping spikes	No heterojunctions are immediately possible, and homojunctions only achievable using e.g. ion implantation, which is an extra fabrication complication
The dielectric layer and successive mask alignments required to provide bonding pads for electrical access gives rise to a fabrication process of greater complexity	Only one mask alignment, ohmic contact evaporation and etching process required, hence there is a naturally higher yield.
Waveguide and ohmic contact are of the same geometrical dimensions, hence leading to difficult area-optical confinement compromise	Waveguide and conducting channel are not directly coincident, allowing a longer waveguide, and lower area contact
Inclusion of a physical waveguide (i.e rib) does not introduce a significant electric field discontinuity in the active region. Disturbances will not be inadvertently collapsed at the rib-substrate interface	The rib introduces a <b>lateral</b> discontinuity into the active region, hence providing a possible virtual-anode point in the structure where the disturbance may prematurely collapse.

**Figure 4.16 :- Comparison between planar and vertical devices**

#### 4.4 Fabrication Process

The fabrication of complete vertical and planar devices included the definition of a rib waveguide, ohmic contact deposition, silica deposition, plasma etching and bonding pad evaporation.

##### 4.4.1 Silicon Tetrachloride Dry-etching of GaAs / AlGaAs

Four primary processes, ionisation, recombination, excitation and relaxation through electron and ion-ion impact (Figure 4.17), participate in sustaining plasmas [49] [50] [51]. The main disparity between wet and dry-etching is the physical nature of the etching environment [52] [53] [54] [55].

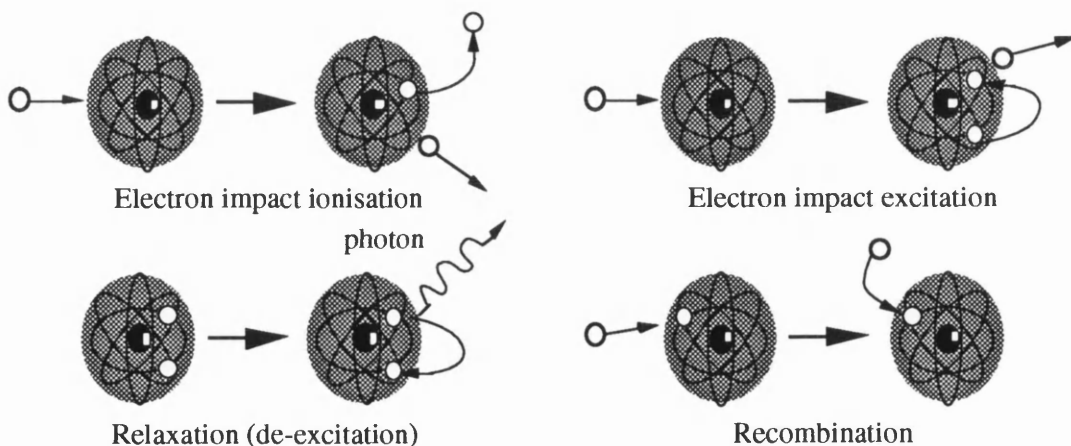


**Figure 4.17 :- Fundamental Collision processes**

Wet etching results from the low energy reactions between reagents and material through natural diffusion in a liquid phase media [52] [54]. It is often fundamentally limited by this diffusion. Dry-etching is ostensibly a combination of physical ion bombardment and surface chemical reactivity at higher energies.

Impact dissociation [49] [50] [51] is critical in the creation of the species responsible for surface reactions. It may be simultaneously accompanied by ionisation, such that the parent molecule is dissociated and ionised in a single collision event. This yields an appropriate species for surface reactivity. Impact dissociation participates in the sustenance of silicon tetrachloride (SiCl<sub>4</sub>)-based plasmas. The etching species are positively-charged ions, such that they may be accelerated through the dark space and strike the surface while it acts as an effective cathode (Figure 4.18). The products of these surface reactions must be fundamentally volatile for the molecule to be removed from the surface and enter the plasma. Both of these criteria are satisfied by several plasma products of SiCl<sub>4</sub>, in combination with the gallium, aluminium and arsenic of the target substrate.

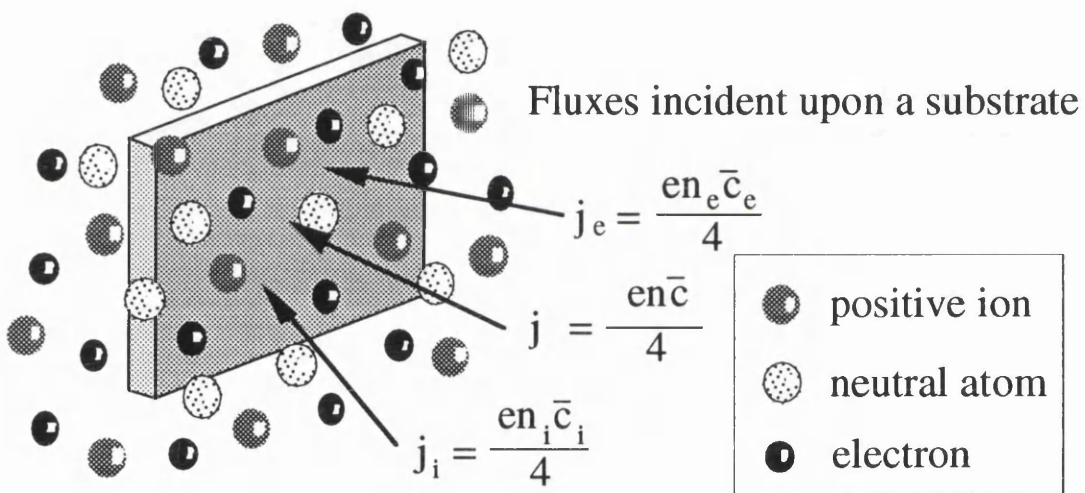
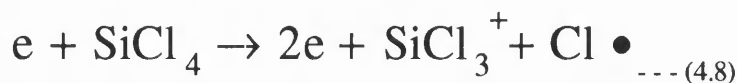
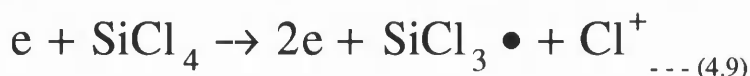


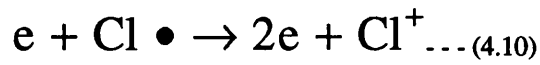
**Figure 4.18 :- Substrate bombardment in a plasma**

The generation of two important species, the silicon trichloride ion, SiCl<sub>3</sub><sup>+</sup>, and the chlorine ion, Cl<sup>+</sup>, can be achieved by impact ionisation-dissociation with electrons :-

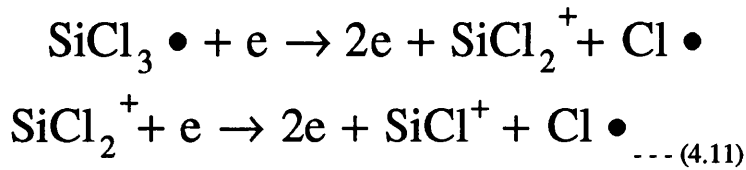


An ion and a chlorine free-radical resulted from this collision. The free chlorine radical may be further ionised in a separate collision, or by direct collision with a SiCl<sub>4</sub> molecule :-





Virtually any impact-event generated species could exist directly, or as intermediates, in high RF power plasma environments. However, when the electronegativity of chlorine, and silicon's affinity for it are considered, it significantly reduces the populations and probabilities of existence of certain species. The mono- and dichlorides of silicon ( $\text{SiCl}$  and  $\text{SiCl}_2$ ), in either neutral or ionised form, do exist in limited populations. They are generally removed by further recombination with free chlorine radicals to yield the volatile and stable  $\text{SiCl}_4$ . Existing neutrals or ions could be involved in impact events such that :-



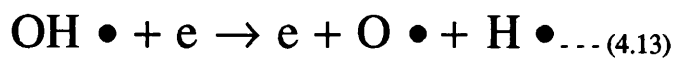
It is also possible for the residual species  $\text{SiCl}_2^+$  and  $\text{SiCl}^+$  to act as reactive ions if incident upon the the substrate surface (target wafer). The exact products of reaction at the surface of the GaAs / AlGaAs sample cannot be determined definitely. It is known from optical emission spectroscopy experimentation (OES) [56] [57] that  $\text{SiCl}_2^+$  and  $\text{Cl}^+$  are the predominate etching species in the GaAs / AlGaAs in  $\text{SiCl}_4$  system. Once incident upon the surface, they encounter gallium, arsenic, and/or aluminium atoms bound in a crystal lattice. The most probable intermediates are the mono and trichlorides of gallium ( $\text{GaCl}$ ,  $\text{GaCl}_2$ ) and arsenic ( $\text{AsCl}$ ,  $\text{AsCl}_2$ ). The volatility of the intermediate by-product allows them to depart from their lattice sites and be drawn into the plasma. It is almost certain that the  $\text{GaCl}$ ,  $\text{AsCl}$  and  $\text{AsCl}_2$  intermediates, whilst in the plasma, combine with free chlorine radicals or ions to yield stable and volatile  $\text{GaCl}_3$  and  $\text{AsCl}_3$  molecules in the plasma. They will mostly remain as neutrals in the effluent and be removed when the plasma gases are refreshed. Further ionisations of these etched reaction products will occur, however, leading to the appending of these molecules to the walls of the fixtures in the chamber.

#### **4.4.2 Chamber Contamination**

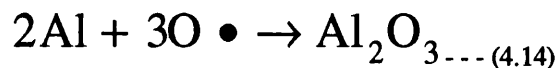
The preceding discussion concentrated on the basic chemistry of reactions and impact events of pure silicon tetrachloride plasmas. No attention was paid to the possibility of stray gases or molecules being present in the chamber in addition to  $\text{SiCl}_4$ . These could be regarded as contaminants with respect to the main processes. The reality is, through breaching of seals and closures, practical

forms of reactor suffer from leaks and venting inadequacies. It is therefore expected that once the chamber has been lowered and sealed, and evacuated to very low pressures, traces of atmospheric gases (e.g. nitrogen, oxygen, water vapour etc.) remain in addition to the intended etchant gas. In a similar manner to that incurred by the SiCl<sub>4</sub>, impact ionisation and dissociation of these spurious gases occurs in the plasma. These generate a variety of free radicals, ions and molecular derivatives. It is also possible that traces of oxygen could be present due to its use as a clean-up or purging gas during the venting procedures of the chamber.

Oxygen and hydrogen, as separate and highly reactive free radicals, could result from impact dissociation (and additional ionisation) of contaminating water molecules :-



The electronegativity of oxygen, combined with the relative stability of many oxides and oxygenated species, lead to the formation of molecular combinations with Ga, As, Si etc. The probability and populations of some molecular derivatives are below the recognition thresholds of optical emission spectroscopy detection experiments [56]. The main implication of oxygen radicals and ions is the formation of very stable aluminium oxide (Al<sub>2</sub>O<sub>3</sub>). These occur at lattice sites in AlGaAs layers where aluminium atoms are accumulated. The stability of Al<sub>2</sub>O<sub>3</sub> at the surface renders the site inert to any further reactions. Hence, it remains as a resistant isolated region at the surface. Reactive ion etching is prevented at these points on the AlGaAs layer surface.



#### **4.4.3 Reactive Ion etching**

Reactive ion etching exploits the bombardment of the substrate with positively charged ions to etch through it via surface chemical reactivity. The instantaneous chemical by-products of the reaction are then swept away into the plasma as volatile free molecules. The waste molecules are extracted from the chamber, and the chamber gases replenished through the systems cyclic pumping and venting system. Many forms of reactor have been used for ion bombardment processes [58] [59]. The most favoured version for reactive ion etching is the diode format (Figure 4.19). Reactive ion

etching in the low pressure diode (10 mtorr - 150 mtorr) is performed with the target wafer arranged on the grounded electrode of the system.

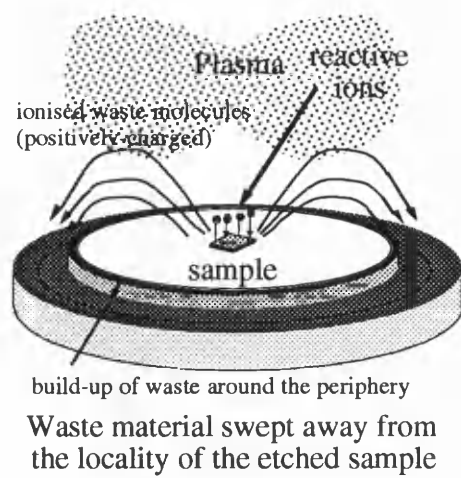
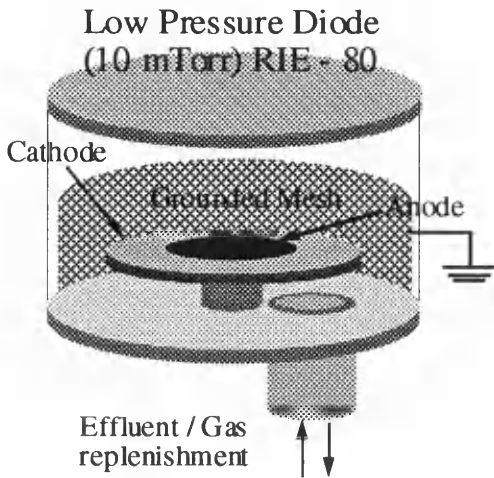


**Figure 4.19 :- RIE80 etching apparatus**

**Figure 4.20 :- Quartz plate activity**

Nichrome (90 % Ni : 10 % Cr) was considered to be appropriate as the etch mask [60] [61] since it offered significant levels of surface adherence, and a small crystalline grain size. This allowed for very high resolution pattern definition. These metals were inert to the silicon tetrachloride ( $\text{SiCl}_4$ ) plasma. Dry-etching mask preparation was as follows :-

(1) Samples of the intended wafer material were cleaved into standardised shapes and sizes ; (2) The next procedure was to remove particles and chemical agents from the surface (i.e. grease etc.). Each sample was individually placed in a plastic beaker, and immersed in 10 ml. of (a) trichloroethane (III), (b) methanol and (c) acetone in turn. These sample beakers were placed in an ultrasonic bath and agitated for five minutes ;

(2) Photoresist (S1400-17 or S1400-31) was spun onto the sample, with optional primer. Spin-times varied between 40 - 60 seconds, at 4000 rpm. Once spun, the sample was baked at 90 °C for 30 minutes standard.

(3) Samples were exposed to ultra-violet radiation on a contact printer at 26 Amps bulb current for three minutes standard. An original electron-beam written chrome mask plate (2 1/2") was used. Shipley's developer solution was used to develop the patterns in photoresist in a 1 : 1 ratio with water for 60 - 75 seconds [61] [62] [63]. Over-development caused degradation of the resist pattern edges. These perturbations (Figure 4.21) were induced by developing spuriously exposed resist resulting from vibration during the three minute overall exposure.

Serrated edge in definition mask transfers to etched pattern

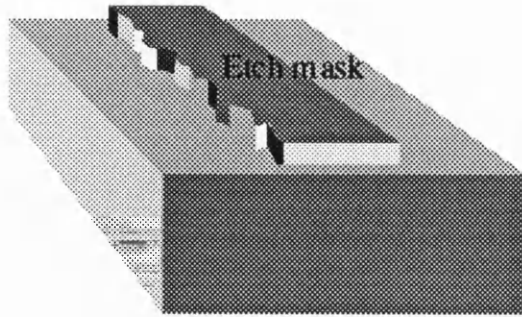


Figure 4.21 :- Serrated feature edges

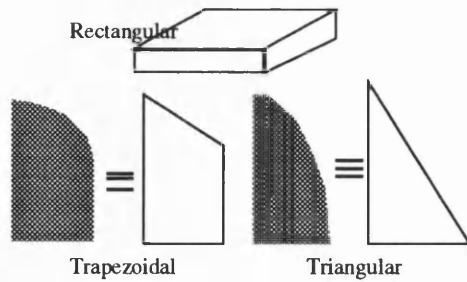


Figure 4.22 :- Shape approximation

(4) The next major procedure was to evaporate a layer of Nichrome to form the etch mask. A standard evacuated chamber "bell-jar" style evaporator was used to manually evaporate the layers (Figure 4.23).

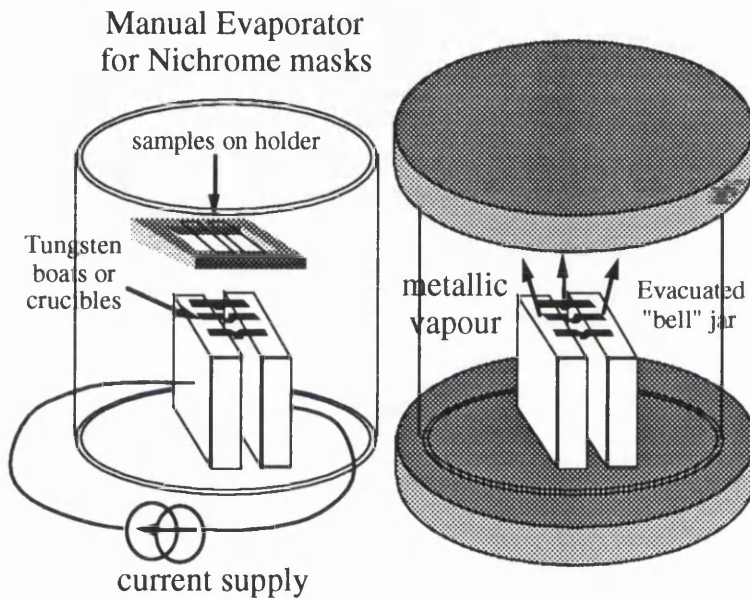
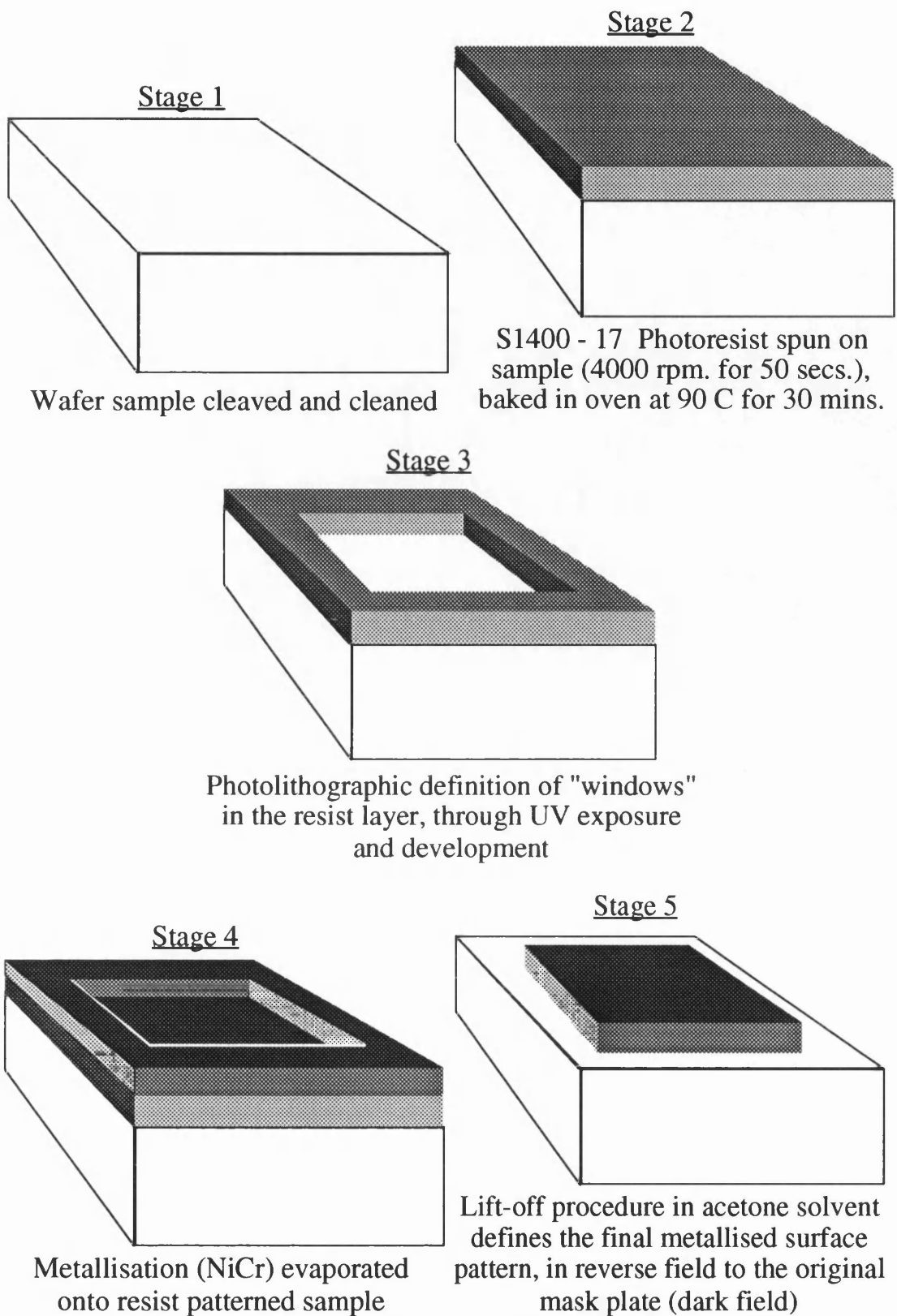


Figure 4.23 :- Manually-operated "Bell-jar" evaporator

(5) The "lift-off" process was performed in acetone solvent. This pattern definition process is summarised in Figure 4.24 [64];

(6) The sample, with 50 nm Nichrome etch mask, was placed in the dry-etching apparatus (RIE 80) and etched in an 13.56 MHz RF-excited silicon tetrachloride plasma. Gas flow rate and cooling temperature were standardised at moderate values throughout, at 9 sccms and 40 °C respectively. Typical pressures achieved in this low-pressure diode system were of the order 10-15 mtorr. The most fundamental parameters influencing etch depth (through an averaged etch rate) were RF power and etching time.



**Figure 4.24 :- Metallised mask definition with "lift off"**

The areas of individual samples were assessed, with peripheral pieces approximated as either triangles or trapeziums where appropriate (Figure 4.22). The total active wafer area per run in the RIE 80 chamber was then determined. A variety of etch runs were performed with the RIE 80 reactive ion

etching apparatus. Observations of visible discolouration, striations associated with mask attack, waste deposition or surface grass formation were made. "Mirror" finishes, i.e. very clean etch floors, were characteristic of high quality runs. For samples with relatively perturbation-free etch floors, the "Talystep" apparatus (Rank, Taylor & Hobson) was used to analyse the etch depth. For specimens with non-ideal etch floors, scanning electron microscopy was required to make an estimation of the etch depth. A simple time-averaged value for the etch-rate per run was evaluated using :-

$$\text{Etch rate (nm min}^{-1}\text{)} = \frac{\text{Etch depth (nm)}}{\text{Etch time (min)}} \dots (4.15)$$

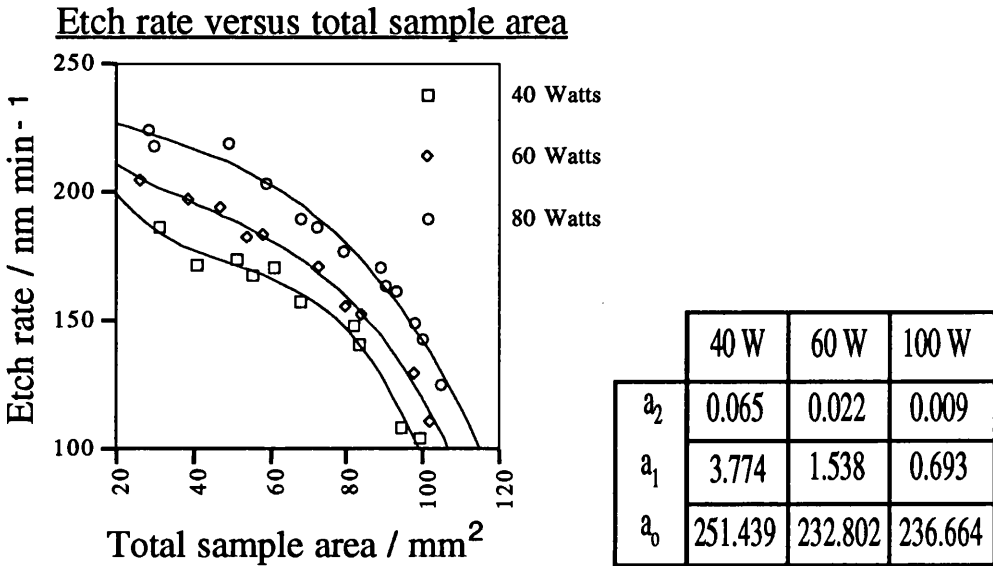


**Figure 4.25 :- Etch rate versus total sample area data**

The results for three separate RF powers, 40 W (low), 60 W (medium) and 80 W (medium-high), are shown in Figure 4.25. Data from the samples suggested the same fundamental functional variation for the etch rate-sample area dependency i.e :-

$$\text{Etch rate} = a_0 - a_1 A + a_2 A^2 \dots (4.16)$$

where  $a_0$ ,  $a_1$  and  $a_2$  are all positive constants, and  $A$  represents the total wafer area in the chamber during a particular etch run. It took the form of an inverted quadratic, {near linearity}. The rate of decrease of the first etch rate derivative (with area) increased in magnitude with area according to :-

$$\frac{d(\text{ER})}{dA} = -a_1 + 2a_2 A \dots (4.17)$$

The curves were shifted upwards {i.e higher etch rate} as the base RF power was increased. The appropriate values for constants, and associated Pearson's product-moment quadratic correlation

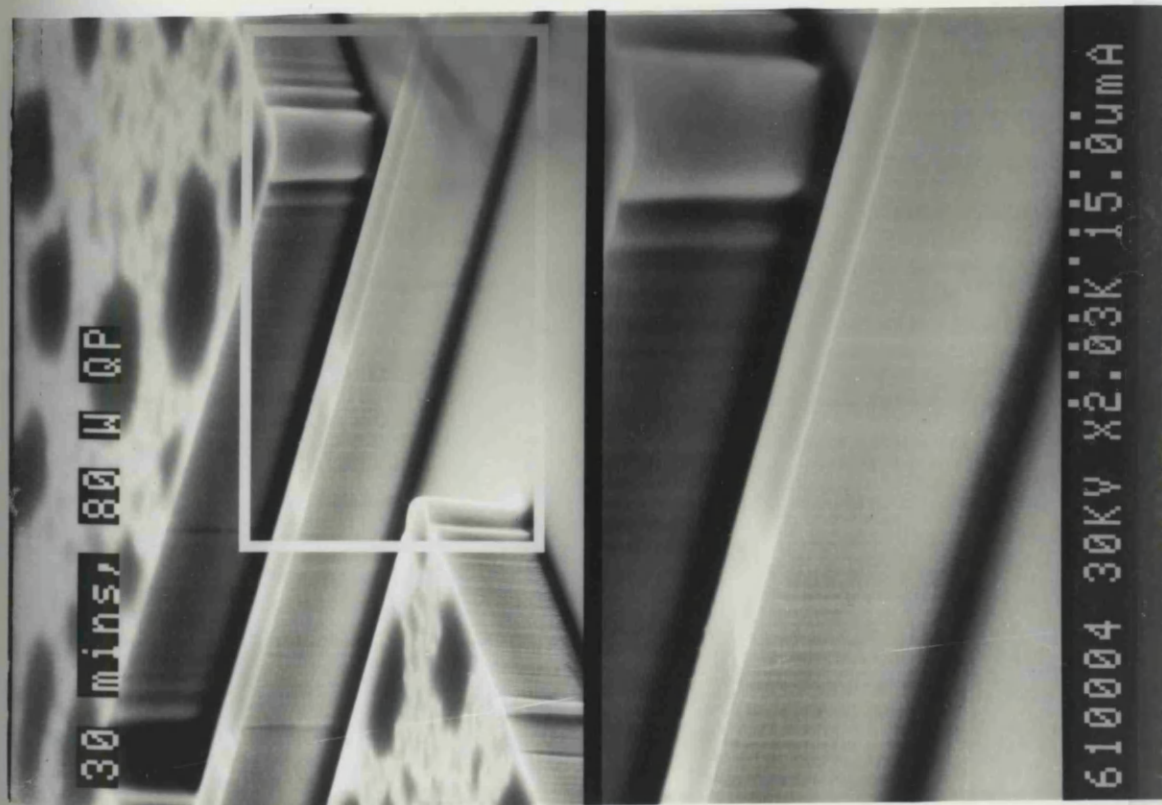
coefficients for the data, are given in the table of Figure 4.25. The reduction in the effective etch rate with increasing substrate area is known as the loading effect, and has been observed and identified in other material - plasma gas combinations, e.g. SiO<sub>2</sub> in CF<sub>4</sub> and Si in O<sub>2</sub> / CF<sub>4</sub> [65].

#### **4.4.4 Photographic Assessment of Etch Quality :- Quartz plate assisted etching**

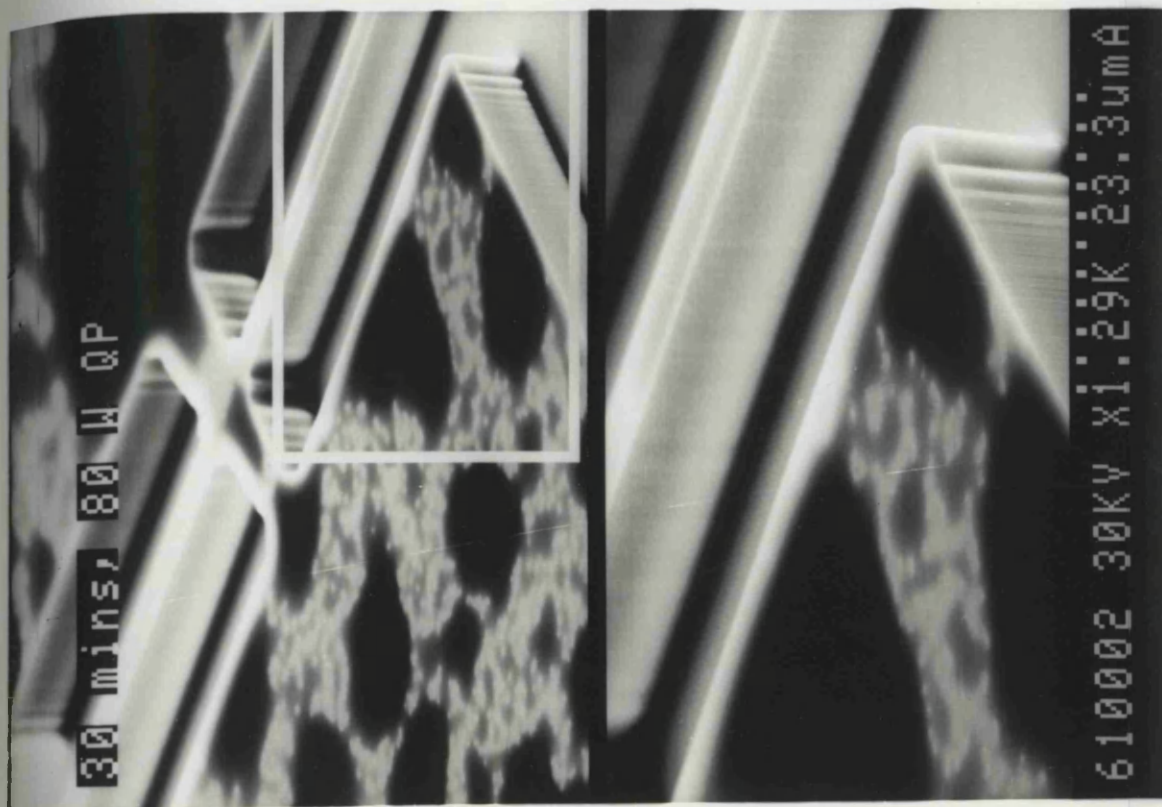
A reactive ion etching process was regarded as having produced a "quality" result if it exhibited the three following characteristics :- (1) Low perturbation density, or "smoothness" of feature walls ; (2) Vertical etch walls, derived by the fundamental directionality (anisotropy) of the etching mechanism ; (3) Cleanliness and uniformity of etch floor (normal to the ion bombardment direction).

To improve the overall quality of etched specimens, a "quartz" (SiO<sub>2</sub> / SiBO<sub>3</sub> glass) plate was placed over the electrodes of the diode reactor. It was approximately 4 mm thick and 20 cm diameter. A significant portion of the electrode plates were disguised by it (Figure 4.20). An array of samples were distributed at the centre of the plate, i.e at the geometrical centre axis of the plasma itself. Consider initially the etched samples shown in Photographs 1 and 2. A thirty-minute, 80 Watt quartz-plate etch run was standard. High quality walls (very high verticality and low perturbation densities) were produced over large expanses of the defined feature - the rib in particular. Coupled with this wall quality, was a virtually blemish-free and "grassless" etch floor. There was a complete absence of etch resistance. A notable feature of these etched samples was the severe attack of the Nichrome etch mask. The dark nebulous patches on the mask surfaces were probably the result of localised reactions of the Nichrome with reactive ion species from the plasma. A primary culprit would have been the Cl<sup>+</sup> ion, forming either NiCl<sub>2</sub>, CrCl<sub>3</sub>, or both in situ at the surface. If these patches were due to deposits directly from the plasma, then it might be expected that similar deposits would appear elsewhere, and not exclusively on the mask. Further, the samples emerged with golden-brown masks, indicating the natural colour chemistry of transition element salts. It was also important to note the experimentally deep 8 μm etches achieved in these samples, using wafer material B157 (Figure 4.12) in particular. When compared to maximum etches of 3-4 μm, 8 μm represented an influential increase in etching possibilities. These depths were normally the preserve of wet etching techniques [52] [53].

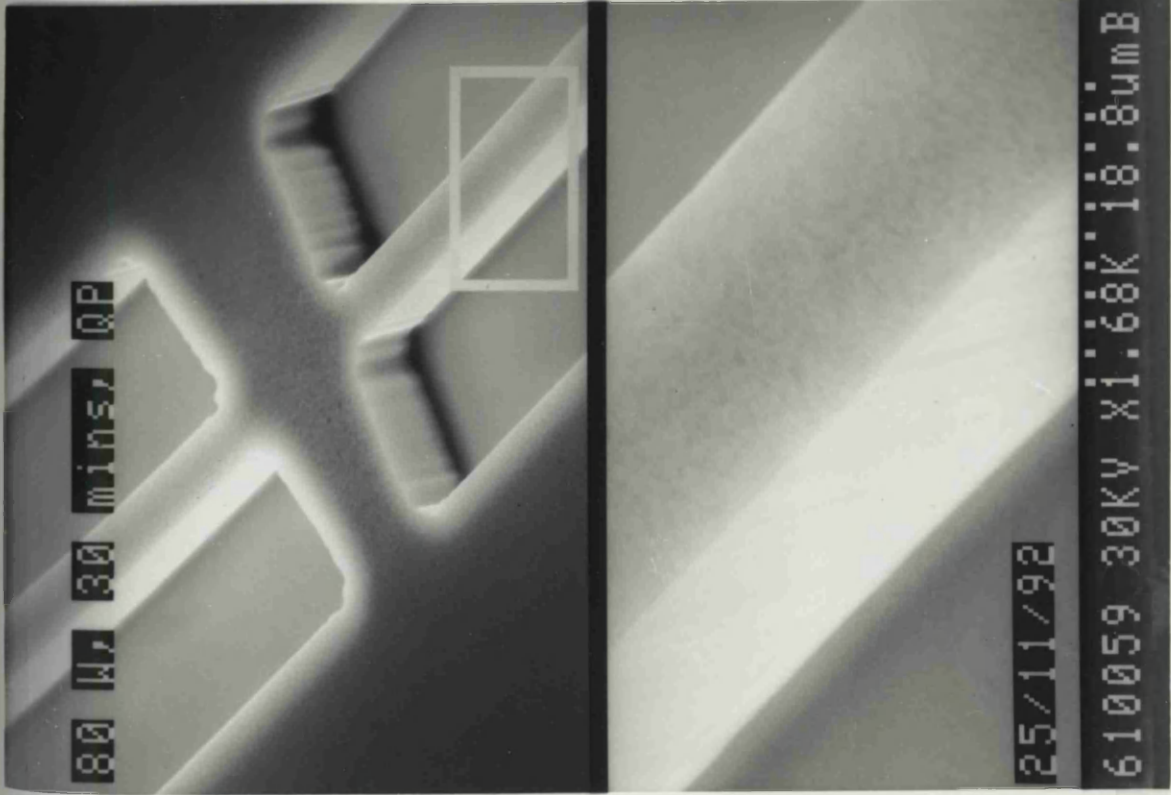
Photographs 3 and 4 demonstrated further the improved etch depths possible with quartz plates. However, on these two occasions no significant mask attack was encountered, while similar



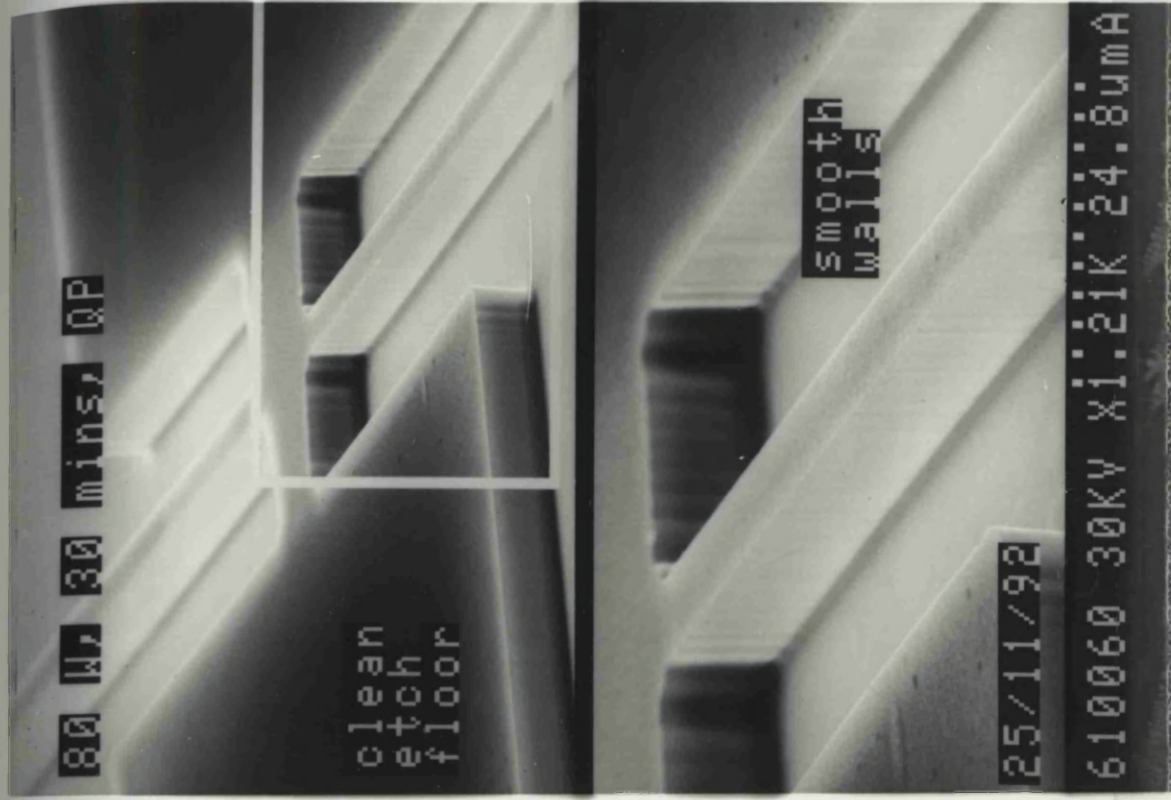
Photograph 1 :- High quality deep etch (8  $\mu$ m) obtained with a quartz plate (mask attack)



Photograph 2 :- see opposite



Photograph 3 :- Very clean etch floors, with high verticality and smooth walls



Photograph 4 :- see opposite

Bi-tapered device with  
high-quality rib

18/09/92

610006 30KV X2.50K 12.0um

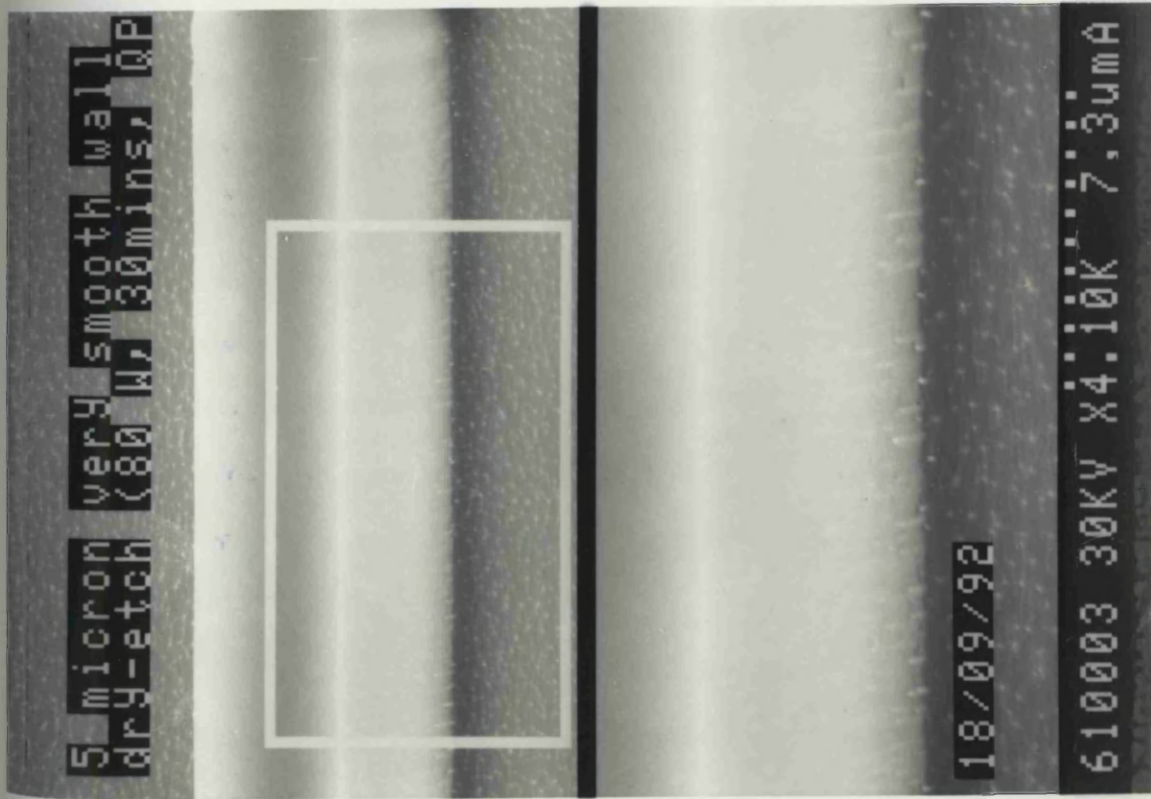
Photograph 5 :-  
A visible line near the base of the etched  
feature (4  $\mu\text{m}$  down) signified the GaAs /  
AlGaAs junction

5 micron very smooth wall  
dry-etch (80 W, 30mins, QP

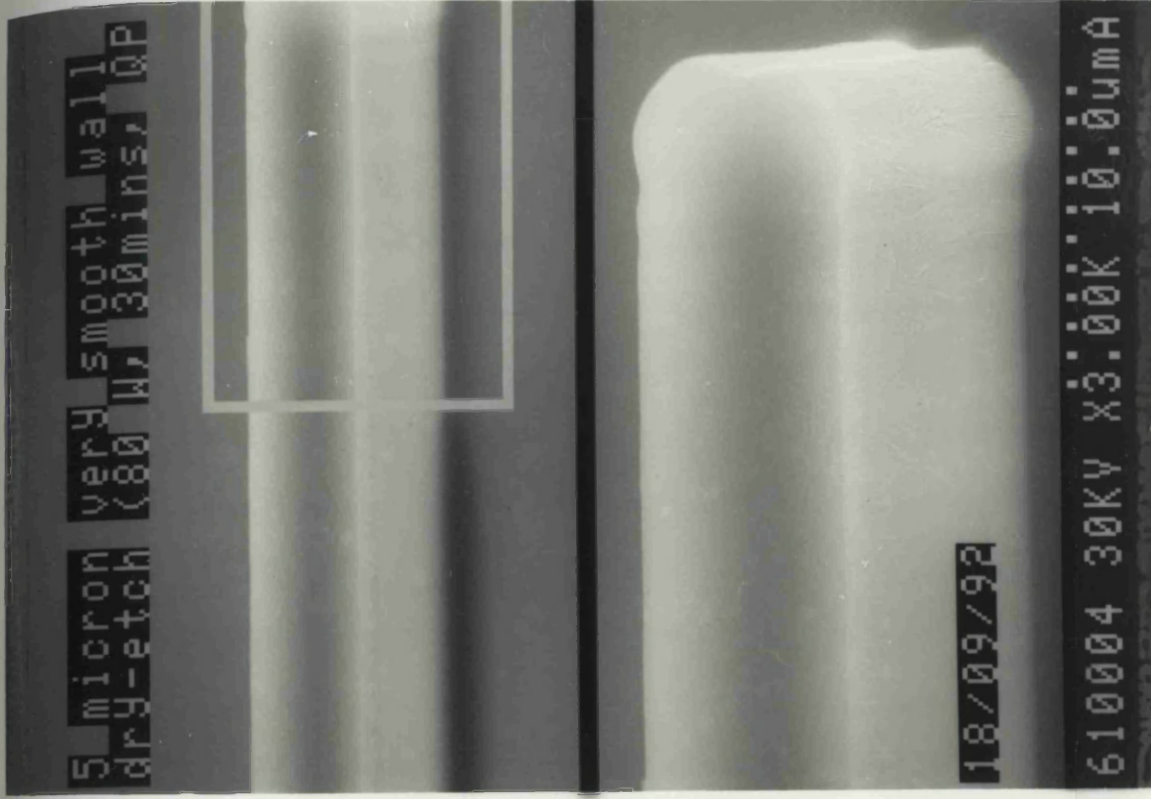
18/09/92

610005 30KV X700 43umB

Photograph 6 :-  
A further example of low perturbation  
densities and clean etch floors



**Photograph 7 :-**  
 A depreciation of etch quality and speckled etch floor revealed the original epitaxial-substrate interface



**Photograph 8 :-**  
 Very smooth wall feature, with blemishless etch floor and high verticality

wall and etch floor quality prevailed. In these cases, the 1  $\mu\text{m}$  bulk layer of  $\text{Al}_{0.33}\text{Ga}_{0.67}\text{As}$  was encountered without any incidence whatsoever, i.e. no  $\text{Al}_2\text{O}_3$  formations were present. This suggested that no oxygen free radicals were present, or they did not significantly oxidise the aluminum if they were. The features etched in Photographs 1, 2, 3 and 4 all displayed point diffraction effects at corners and junctions. These were symptoms of the lack of close contact between chrome plate and resist-spun sample during exposure. This was caused by the excess resist build-up at the edges of the chip.

Photographs 5 and 6 contained further examples of device fabrication from silicon-doped n type GaAs /  $\text{Al}_{0.33}\text{Ga}_{0.67}\text{As}$  wafer material from B157. These 5  $\mu\text{m}$  deep structures illustrated the almost molecularly perfect and uniform etch floors attainable with quartz plate assisted etching. The walls of the structure were also highly uniform, with only very fine "waterfall" features present. In addition, a further feature in Photograph 5 was the definite parallel etch line near the base of the mesa, approximately 4  $\mu\text{m}$  from the surface. This line signified a sudden depreciation in etch wall quality. It corresponded to the region of the GaAs / AlGaAs layer interface, a fact which was considered in conjunction with Photographs 7 and 8. The wall quality and verticality of the etched features in these two images represented the best and definitive quality achieved with GaAs / AlGaAs in silicon tetrachloride. Virtually no "ribbing" of the walls was visible anywhere upon the defined structures. This was combined with the near mirror-finished etch floors. Accurate Talystep etch depth determination revealed that the sample in Photograph 7 was etched to a depth of 5.2  $\mu\text{m}$ , while that in Photograph 8 to a depth of 4.9  $\mu\text{m}$ . This was perhaps reflected in the dissimilarity of the etch floors in these two cases. The first was slightly speckled in nature and would have reached the original pre-epitaxial wafer, while the second remained unperturbed. The epitaxial growth layer would not have been surpassed in the second case. In a similar manner to that of Photograph 5, a change in wall quality appeared after approximately 4  $\mu\text{m}$  of GaAs had been removed. This phenomena occurred on many subsequent occasions, in entirely separate runs with the same B157 wafer material. The differences in total etch depths between the samples in Photographs 1 - 8, all etched with the standardised parameters of 80 Watts for 30 minutes, were due to the loading effect.

#### 4.4.5 General Aspects

Figure 4.26 gives a schematic summary of the possible errors and ideal requirements of a reactive ion etch. The possibility of very deep etches of GaAs / AlGaAs in  $\text{SiCl}_4$  were explored by

# Etching error Schematic

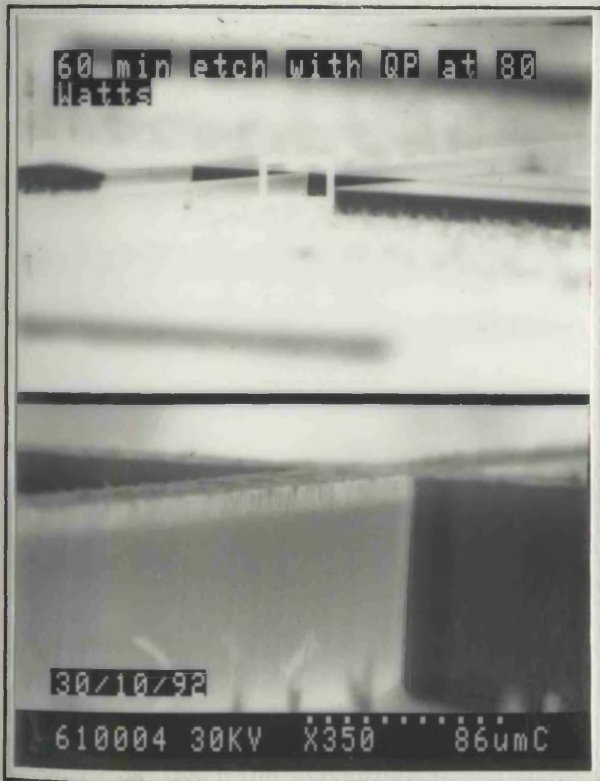
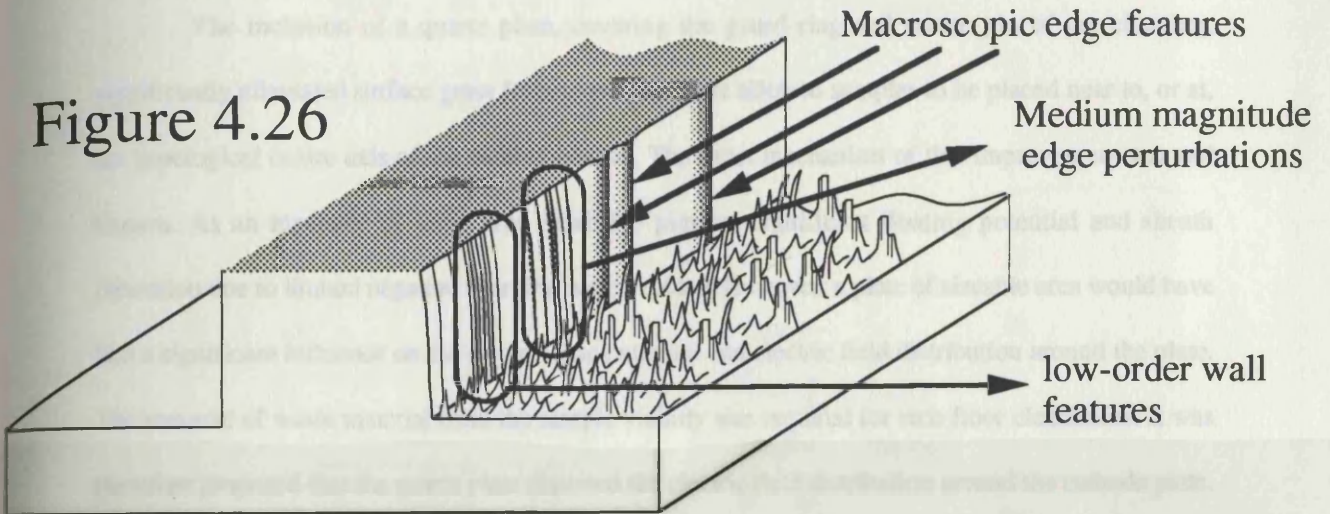
## Ideality

- (1) Smooth walls
- (2) High verticality
- (3) Clean etch floor

## Reality

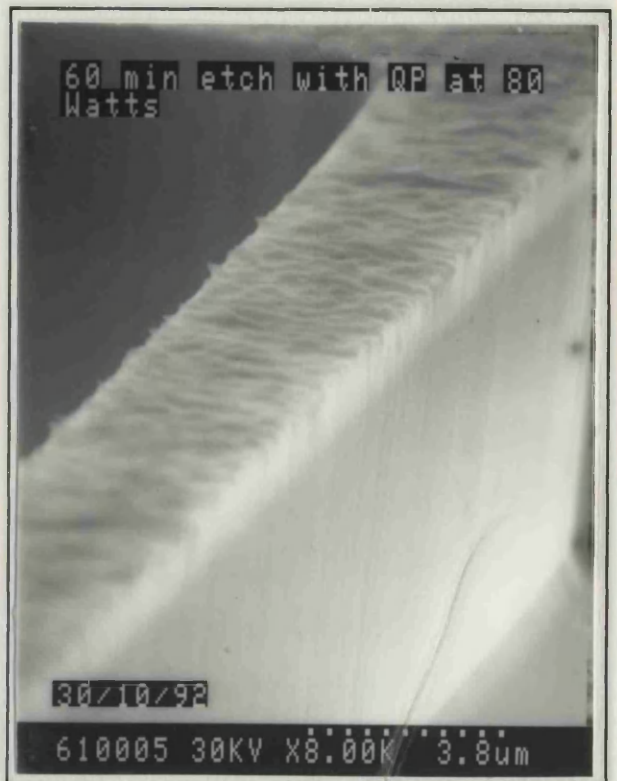
- (1) Rough walls
- (2) anisotropic etch profiles
- (3) grassy etch floors

Figure 4.26



Photograph 9

Very deep 11  $\mu\text{m}$  etch in GaAs with chamfering effect



Photograph 10

Mask attack is clearly evident after 60 mins exposure

pursuing 60 minute, 80 Watt quartz plate assisted etches. The results of this were shown in Photographs 9 and 10. From the SEM images, etch depths of the order of 11  $\mu\text{m}$  were estimated for these structures (beyond the range of the Talystep). The unprecedented length of etching exposure eventually caused lateral erosion of the mask edges. This yielded the "chamfered" derived etch profile. Despite this, high quality etching was sustained even at these extended depths, while the mask exhibited signs of attack.

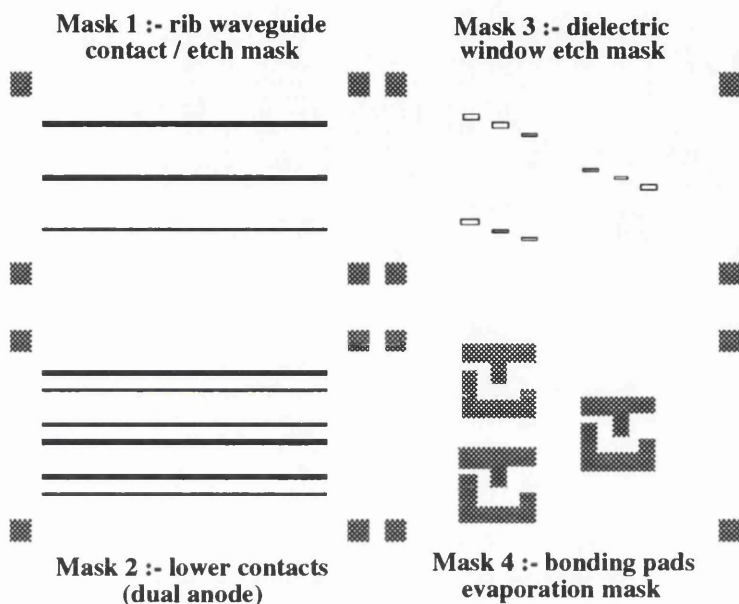
The inclusion of a quartz plate, covering the guard ring and centre pin of the chamber, significantly alleviated surface grass formation. This plate allowed samples to be placed near to, or at, the topological centre axis of the etching plasma. The exact mechanism of this improvement was not known. As an insulator of large area in an RF plasma, significant floating potential and sheath formation due to limited negative charging were avoided. However, a plate of sizeable area would have had a significant influence on the electrostatic potential and electric field distribution around the plate. The removal of waste material from the sample vicinity was required for etch floor cleanliness. It was therefore proposed that the quartz plate distorted the electric field distribution around the cathode plate. Pernicious ionised species were removed from the sample surface. Simultaneously, there must be the continuous bombardment of the target substrate with positive ions. This could be reconciled if the waste material was negatively charged in the plasma. Dark waste was observed around the circumference of the plate after several quartz plate etch runs had taken place (Figure 4.20). This was regarded as active waste removal induced by the quartz plate. The trajectory of exiting waste molecules was affected such that redeposition on the sample surface was avoided.

#### **4.5 Fabrication of Vertical Devices**

(1) The cathode ohmic contact was defined by first opening up an appropriate window in a surface spun resist through photolithography. The sample was cleaned using trichloroethane III, methanol, acetone and rinsed in isopropylalcohol (IPA) or RO water. Once blown dry, S1400-31 resist was spun for 60 seconds at 4000 rpm to yield a uniform 1.8  $\mu\text{m}$  resist layer. An electron beam lithographically written chrome plate (2 1/2" square) (Figure 4.27), was used in conjunction with the contact printer to perform UV exposure of the resist in the normal way. The sample was developed in Shipley's developing solution, (in an equal proportion with water). Acetone was employed to develop

the lift off metal pattern, followed by plasma-ashing in an oxygen plasma for a standard 60 second period. The standard "Mikeohm" ohmic contact recipe was evaporated in conjunction with the Plassys evaporator. The recipe is contained in the table of Figure 4.28. Once evaporated, the rib-shaped cathode contact was exploited as an inert etch mask for SiCl<sub>4</sub> plasma-etching.

Approximate schematic of Mask set  
for Dual-anode vertical device



Not shown to proportion

**Figure 4.27 :- Photolithographic mask set for dual anode device**

Actual Silica deposited thickness  
versus intended thickness

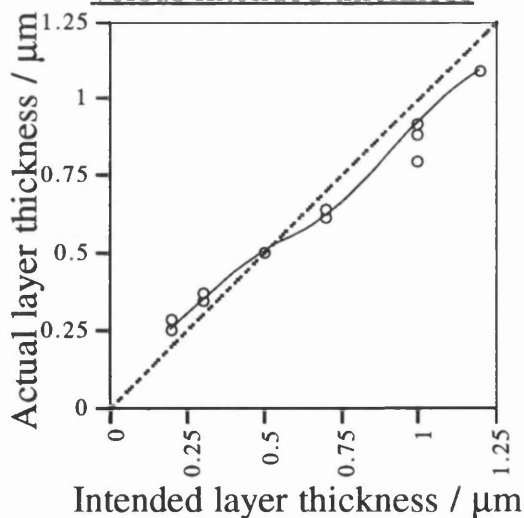


**Figure 4.29:- Silica deposition data**

	Metallisation	Thickness	Rate of evaporation
(1)	Nickel (Ni)	2 nm	0.15 nm s <sup>-1</sup>
(2)	Gold (Au)	14 nm	0.40 nm s <sup>-1</sup>
(3)	Germanium (Ge)	14 nm	0.85 nm s <sup>-1</sup>
(4)	Nickel (Ni)	11 nm	0.30 nm s <sup>-1</sup>
(5)	Gold (Au)	>200 nm	0.75 nm s <sup>-1</sup>

**Figure 4.28 :- "Mikeohm" recipe**

## Vertical modulator structure :

(2) Dual anode contacts were applied. Thicker resist layers were required to minimise the height differential between the top surface of the rib and the etch floor. The mask aligner was used to develop lower contact window patterns, with 15 sec. UV exposure and Shipley's developer.

(3) Plasma ashing of the sample surface was followed by a standard "Mikeohm" ohmic contact recipe evaporation. Lift-off was performed in acetone solution. The next stage was to anneal the cathode and anode contacts using the "rapid thermal annealer (RTA)" or strip annealer. Annealing was performed at 390 °C for 60 seconds, the general annealing conditions for the "Mikeohm" recipe. No attempt was made to vary these conditions in vertical devices.

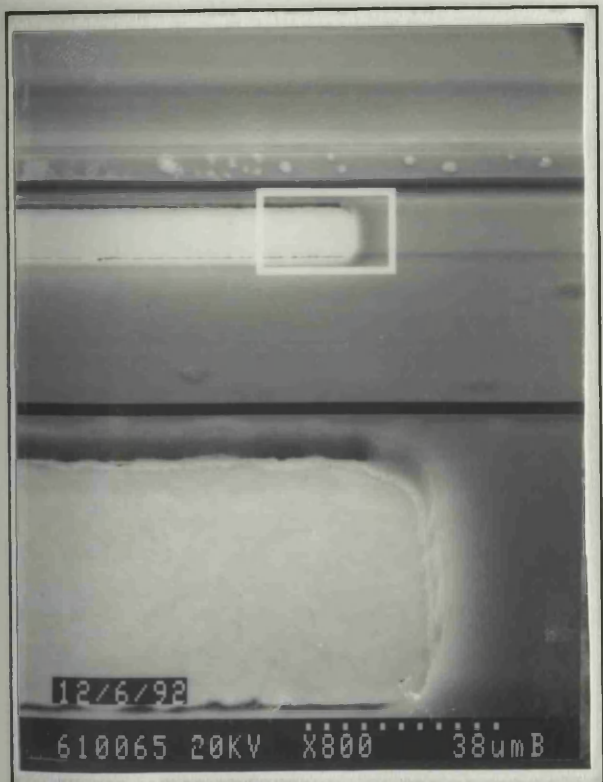
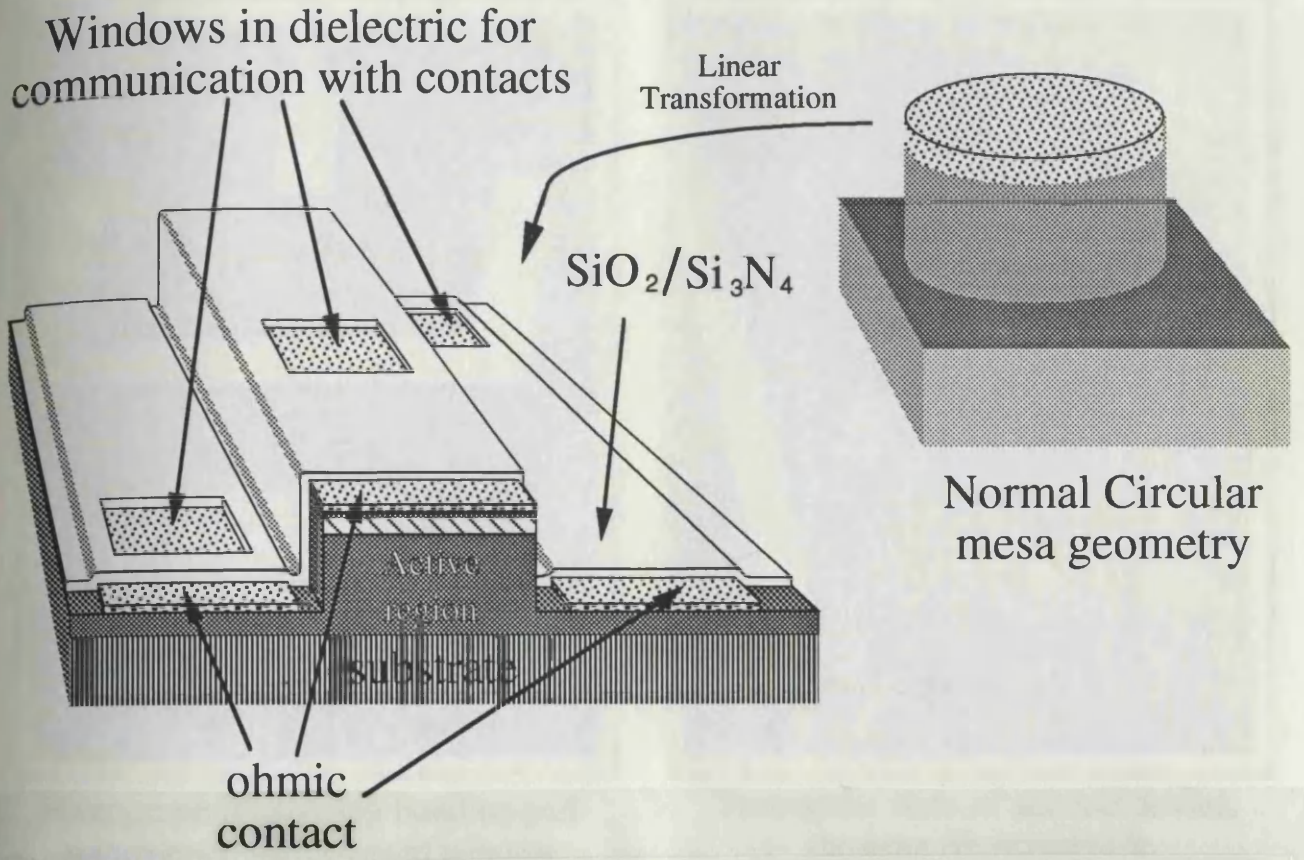
(4) An 800 nm isolation layer of silicon dioxide was deposited. The device capacitance was dependent upon the absolute layer thickness of SiO<sub>2</sub> i.e. the thicker the layer, the lower the capacitance. Figure 4.29 describes the variation between the intended layer thickness, and that eventually acquired in the chamber. The graph clearly shows that with the original silica deposition plant, lower thicknesses were consistently over-deposited, while higher thicknesses were under deposited. The construction of a dual anode device is shown in the photographs of Figures 4.30[a] and 4.30[b].

(5) Electrical access windows were defined by photolithography, using AZ4620A resist. In contrast to SiCl<sub>4</sub> etching of GaAs, the etching of silicon dioxide required the use of a photoresist etch mask. The etchant was the fluorocarbon compound C<sub>2</sub>F<sub>6</sub> (hexafluoroethane). The primary etching species in the process were probably the F<sup>+</sup> and C<sub>2</sub>F<sub>5</sub><sup>+</sup> ions, which bombarded the silica surface and reacted with either Si or oxygen. Etch rates in this system were comparatively low i.e. 500 Å (50 nm) per minute. A ferric plate and the mask aligner were used to define these windows in the resist, with UV exposure times elevated to 30 seconds. Development times were similarly increased due to the thickness of the layer. Photolithography difficulties were always present with resists such as AZ4620A.

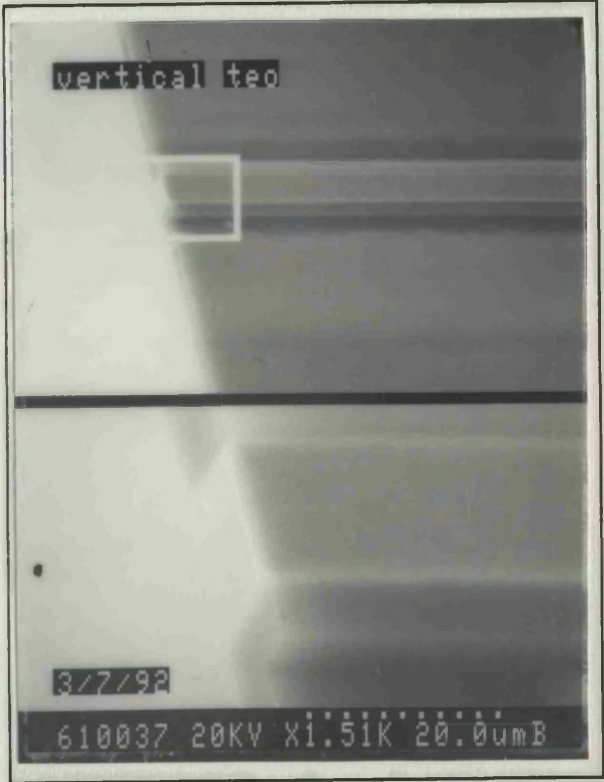
(6) The resist mask was removed in acetone solvent, followed by I.P.A. Bonding pad windows were defined with AZ4620A at 6000 rpm for 60 seconds (4.0 µm). The Plassys evaporator was used to evaporate the bonding pad combination of Nichrome (50 nm) and gold (250 - 300 nm).

(7) Waveguide devices, with clean and uniform facets, were cleaved with 1.0 - 1.5 mm by 4 µm waveguides, and unthinned substrates.

# Vertical modulator structure : Electrical Isolation and windows



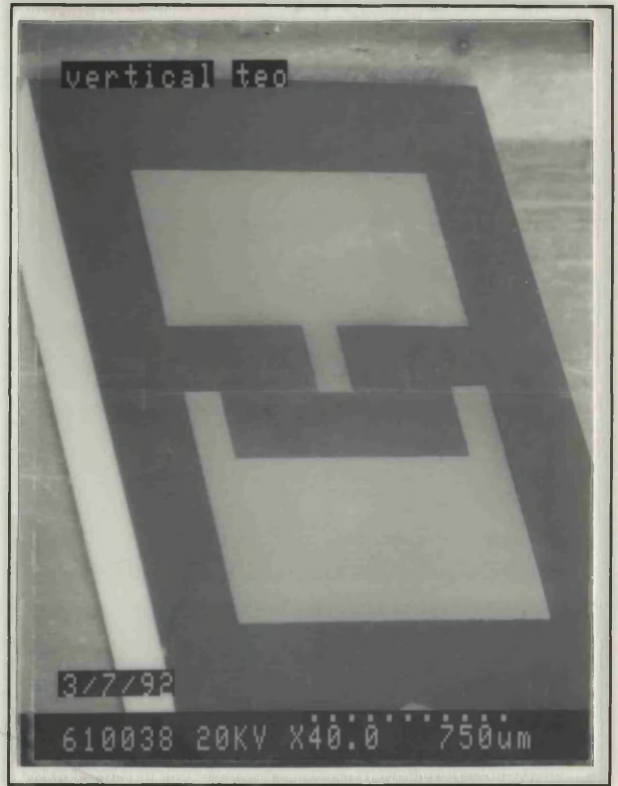
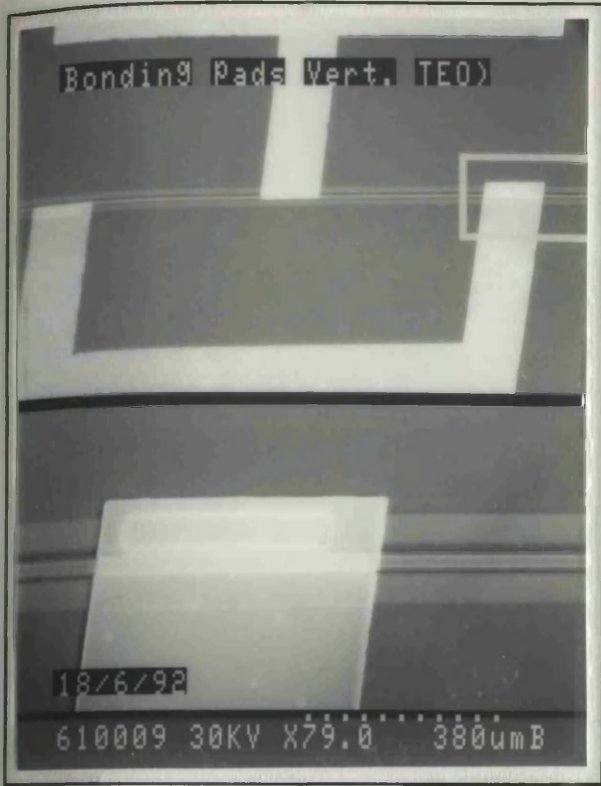
Photograph illustrating the position of etched windows relative to the contact



Photograph demonstrating the relative thickness of the post-etched  $\text{SiO}_2$

Figure 4.30(a)

# Vertical modulator structure : Bonding pads



Photograph illustrating bonding pad coincidence with opened window

Panoramic view of vertical device, showing rib waveguide

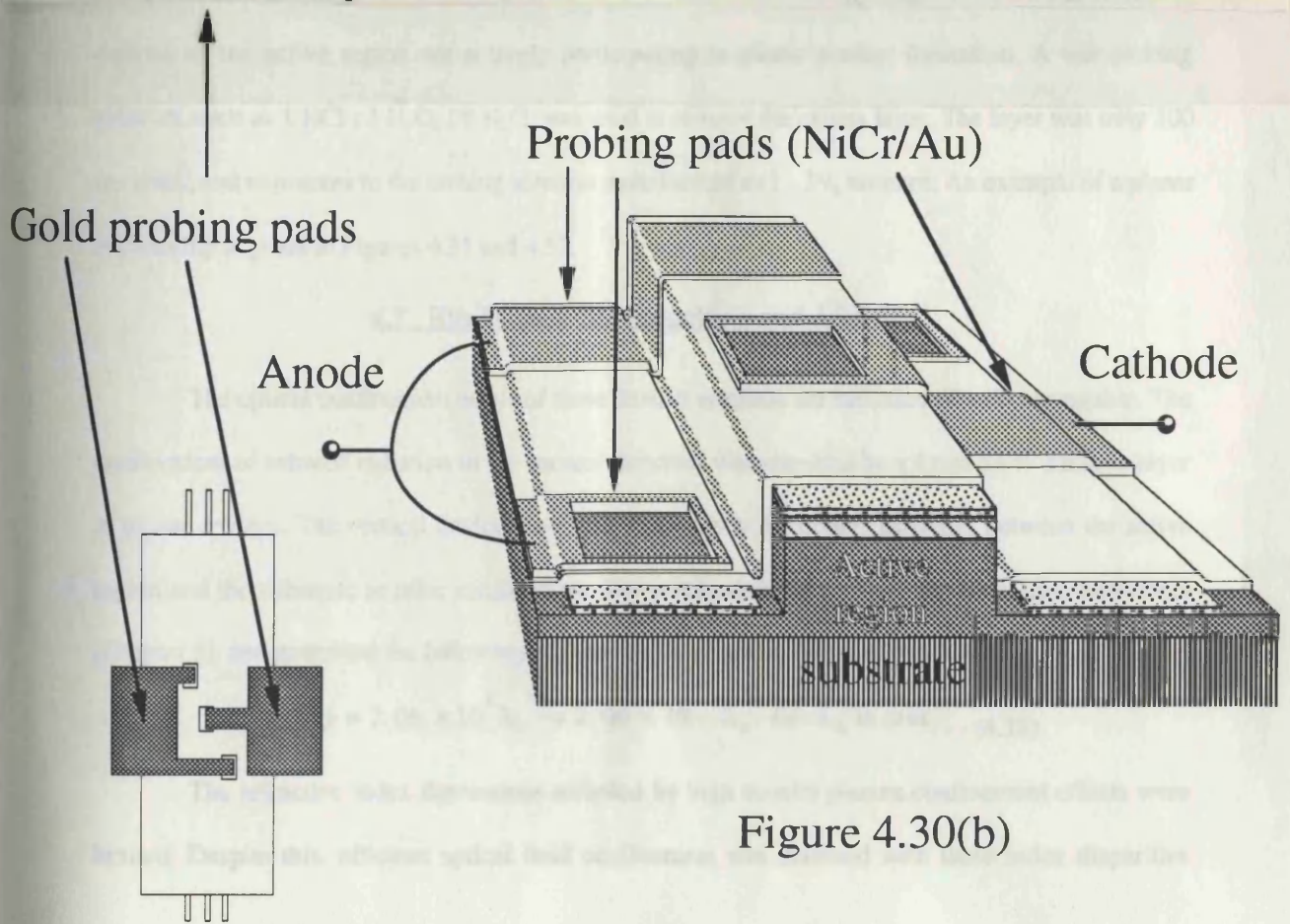


Figure 4.30(b)

## **4.6 Fabrication of planar devices**

After plasma dry-etching, the following steps were required to complete a planar device :-

(1) Removal of the Nichrome etch mask in aqueous solution. The initial reagent used was hydrochloric acid in a 4 HCl : 1 H<sub>2</sub>O proportion with water. Alternative solvents such as (SO<sub>4</sub><sup>2-</sup>) sulphuric acid, were used in aqueous solution to completely remove mask traces. Samples from the barrel asher treated with 1 HCl : 4 H<sub>2</sub>O solution for 30 seconds to remove oxides.

(2) S1400-31 resist was spun at 4000 rpm for 40 seconds, ferric oxide contact pattern plate aligned to the sample and UV exposed as routine. Development of the resist defined the ohmic contact windows.

(3) Recipes for contact metallisations were subject to modifications. The absence of cathode boundary features like hot electron injectors and doping spikes meant that the cathode boundary conditions could only be imposed by alterations to composition and annealing conditions. Fast interstitial diffusant species such as nickel (and to some extent germanium) were expected to penetrate into the active region.

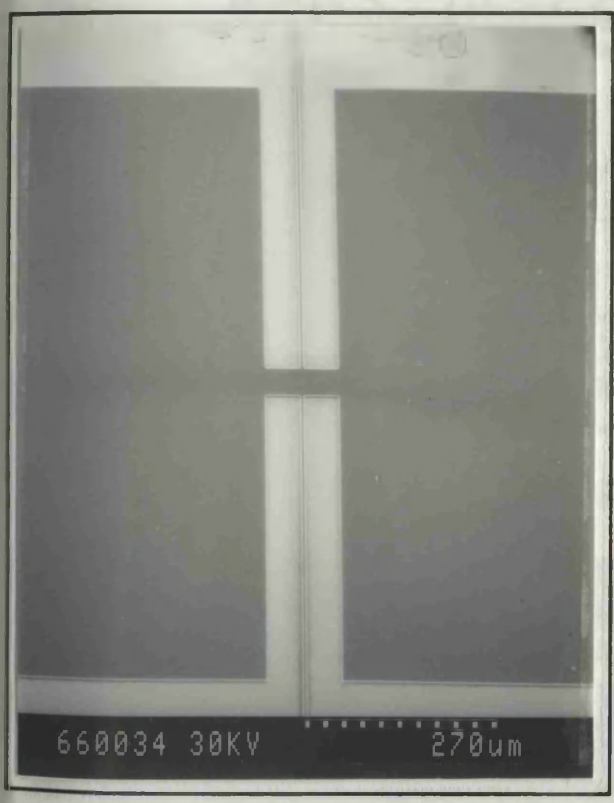
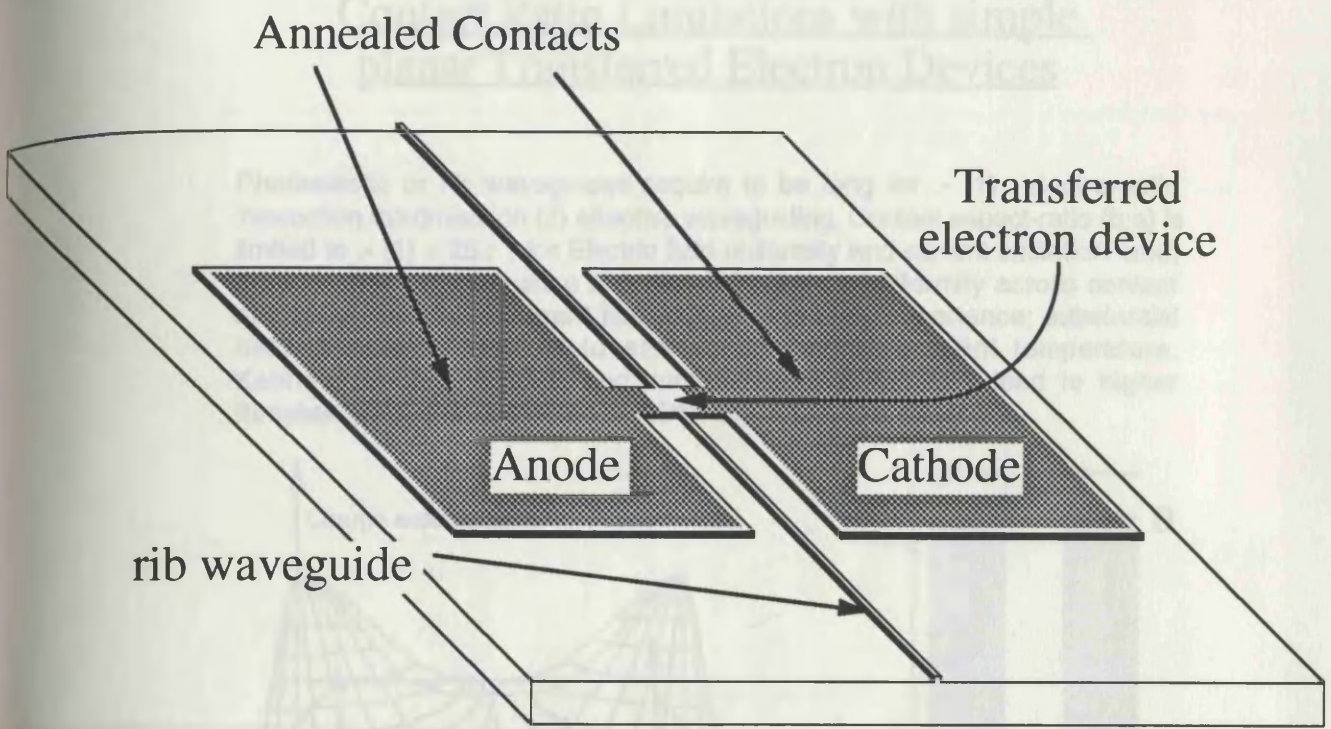
(4) The final procedure was to remove the highly-doped n-type ohmic contact layer in those regions of the active region not actively participating in ohmic contact formation. A wet etching solution, such as 1 HCl : 1 H<sub>2</sub>O<sub>2</sub> : 9 H<sub>2</sub>O, was used to remove the excess layer. The layer was only 100 nm thick, and exposures to the etching solution were limited to 1 - 1½ minutes. An example of a planar device chip is given in Figures 4.31 and 4.32.

## **4.7 Rib Waveguide Modelling and Analysis**

The optical confinement needs of these devices required the inclusion of a rib waveguide. The confinement of infrared radiation in the vertical direction was provided by a 1 µm 33 % AlGaAs layer in planar devices. The vertical device, however, relied upon the doping disparity between the active region and the substrate to offer confinement. The mechanism for this was the Moss-Burstein effect [Chapter 3], and generated the following refractive index change, for wavelength λ<sub>0</sub> :-

$$\Delta n(\lambda_0) = 2.06 \times 10^9 \lambda_0^{-2} \rightarrow 2.06 \times 10^{-3} \lambda_0^{-2} \text{ for } \lambda_0 \text{ in } \mu\text{m} \quad \dots (4.18)$$

The refractive index depressions afforded by high density plasma confinement effects were limited. Despite this, efficient optical field confinement was obtained with these index disparities



Typical Non-tapered Planar device {large geometry}

Three possibilities :-

- [1] Convex saturation
- [2] Concave saturation
- [3] Sharp discontinuities

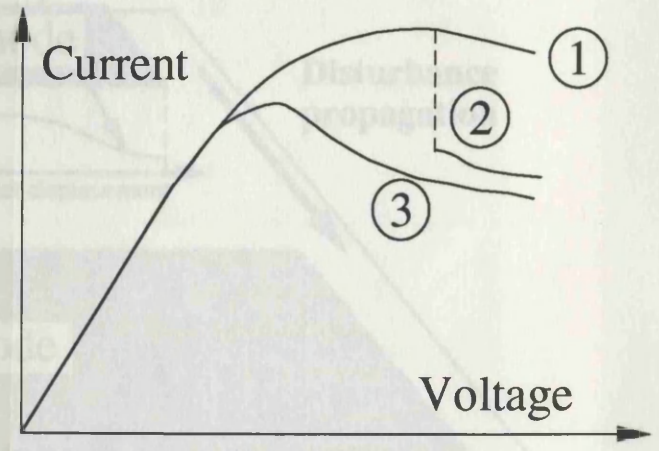


Figure 4.32

Figure 4.32

## Contact Ratio Limitations with simple planar Transferred Electron Devices

Photoelastic or rib waveguides require to be long for :- (1) electro-optic interaction maximisation (2) effective waveguiding. Contact aspect-ratio ( $b:a$ ) is limited to :- (1)  $< 25 : 1$  for Electric field uniformity and current limitation and; (2)  $< 5 : 1$  for maintenance of lattice temperature uniformity across contact nucleation interface. Current limitation is of primary importance; substantial heat dissipation required to achieve operational ambient temperature. Kennedy pre-amplification and control region status may lead to higher threshold fields than expected or NON- OSCILLATION states

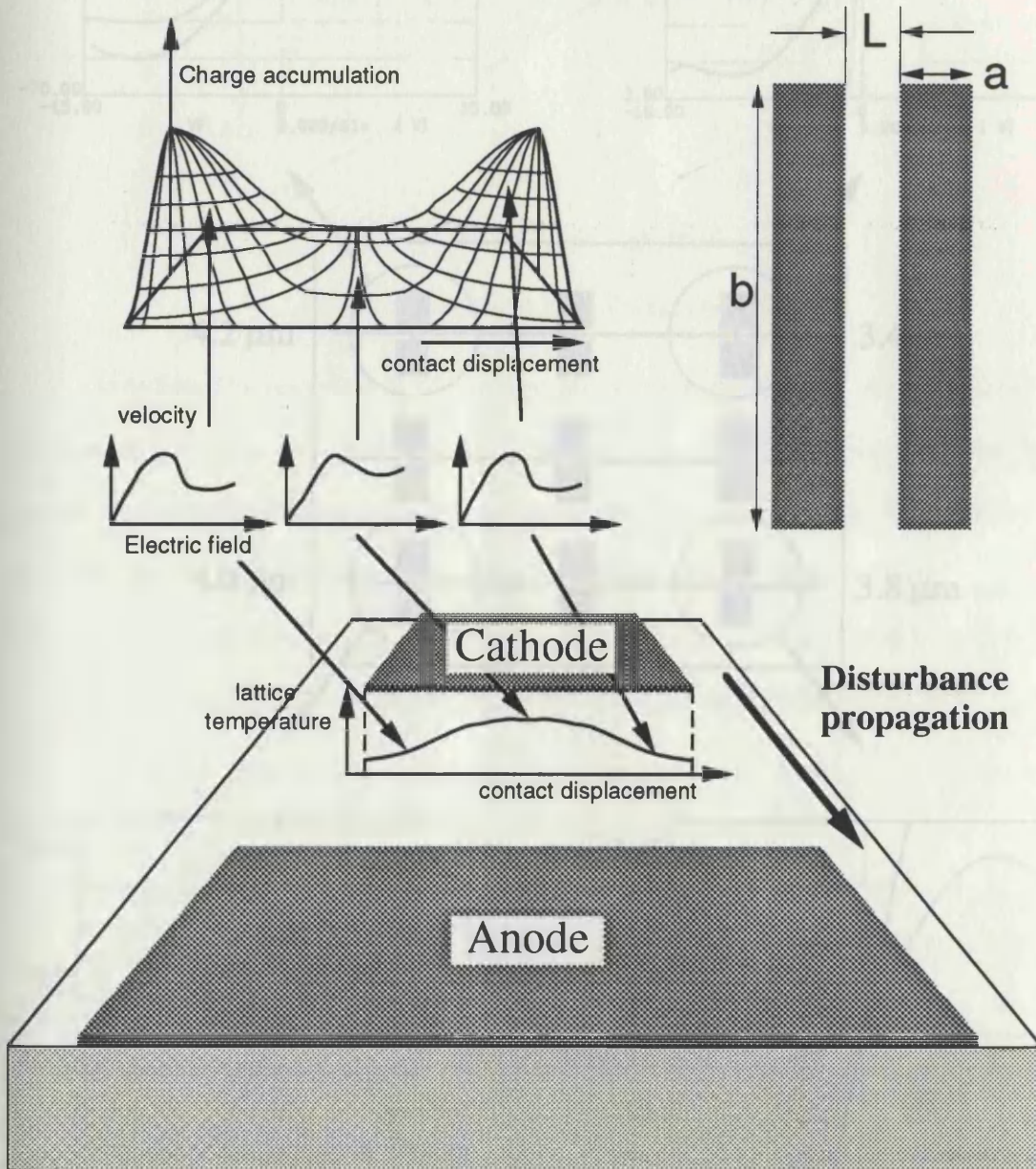
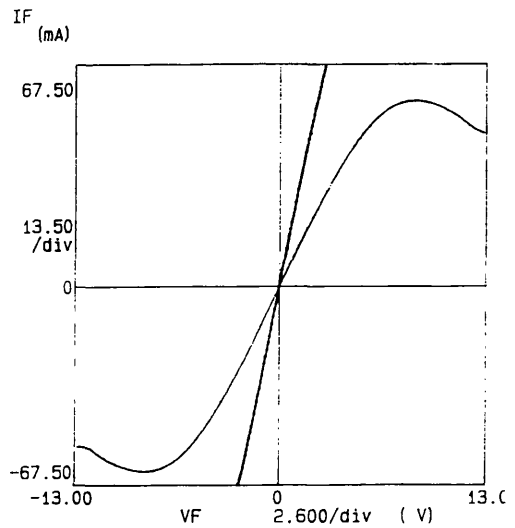
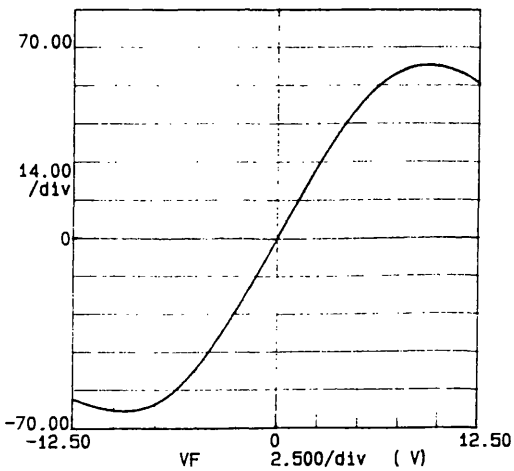
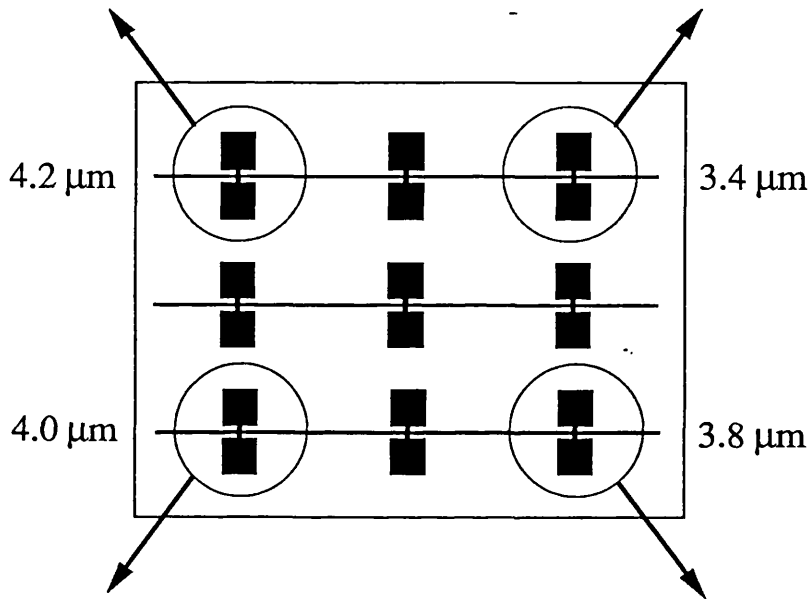
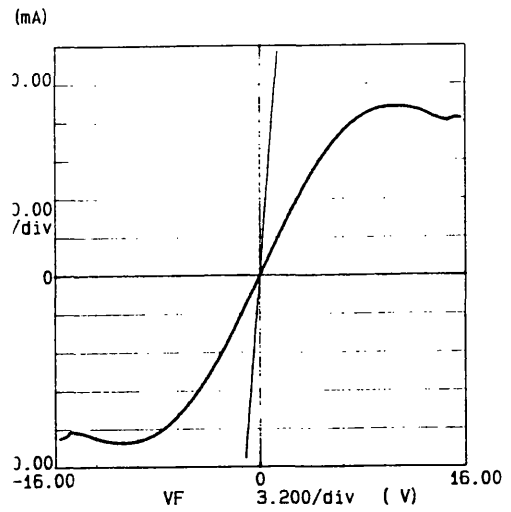
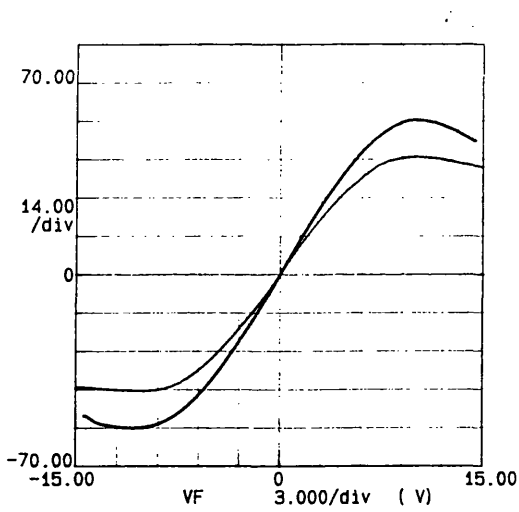


Figure 4.32

# Variation of I-V characteristics of planar devices

One fabrication run generates 9 separate devices. The figures shown indicate Talystep-measured etch depths across the single sample.



(Figure 4.33). In cases where the depth of the etched rib corresponded accurately to the depth of the active region substrate interface, confinement was most efficient.

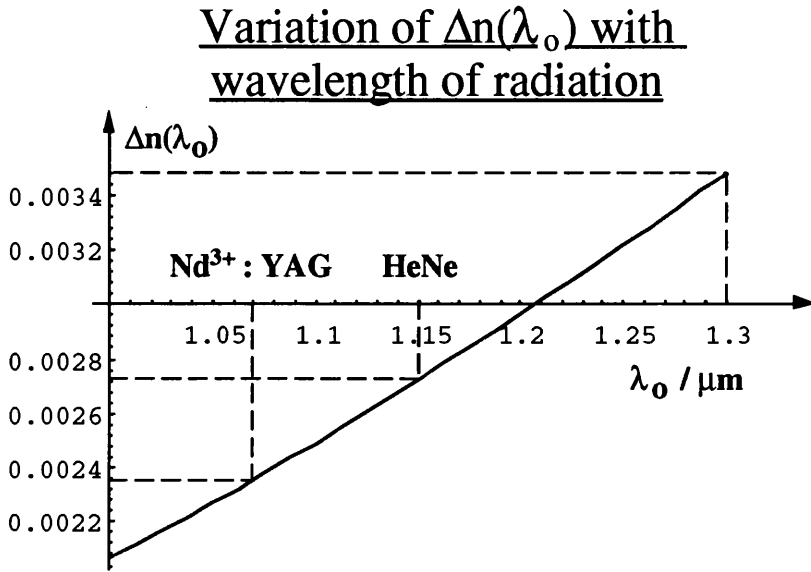


**Figure 4.33 :- Yariv's method**

#### 4.7.1 Calculation of the Base Refractive index

As indicated by expression (4.18), the depression of the refractive index was proportional to the square of the absolute wavelength of the incident radiation. Additionally, the depression was inversely proportional to the magnitude of the refractive index value in the material in the absence of free carriers,  $n_0$ . The general refractive index value is dependent upon the following factors :-

- (1) The presence of substitutional atoms of different elements leading to tertiary or quaternary alloys with the bi-valent material, and the proportion or x fraction of the atoms in e.g.  $Al_xGa_{1-x}As$  or  $Al_xGa_{1-x}As_yP_{1-y}$  ;
- (2) The wavelength of the propagating radiation ;
- (3) The doping concentration, N, deliberately (or otherwise) introduced into the material.

The base refractive index,  $n_0(x, \lambda)$ , presented by  $Al_xGa_{1-x}As$  material, could be calculated using many differing approaches [2] [3] [66]. One such method of estimation was due to Yariv. Ilegems and Pearson [67] quoted the following expression for the refractive index in the absence of free carriers,  $n_0(x, \lambda)$  (Figure 4.34) :-

$$n_0(x, \lambda) = \sqrt{10.9 - 2.92x + \frac{0.9751}{(\lambda^2 - \alpha) - \beta\lambda^2}} ; \quad \dots (4.19)$$

$$\alpha = 0.30386 - 0.105x \text{ for } x > 0.36 ; \quad \lambda \text{ in } \mu\text{m}$$

$$\alpha = 0.52886 - 0.735x \text{ for } x < 0.36 ; \quad \beta = 2.437 \times 10^{-3} [1 + 1.413x]$$

The variation of the Yariv's refractive index function is given in Figure 4.34.

Base refractive index for  $\text{Al}_x\text{Ga}_{1-x}\text{As}$   
due to Yariv's method

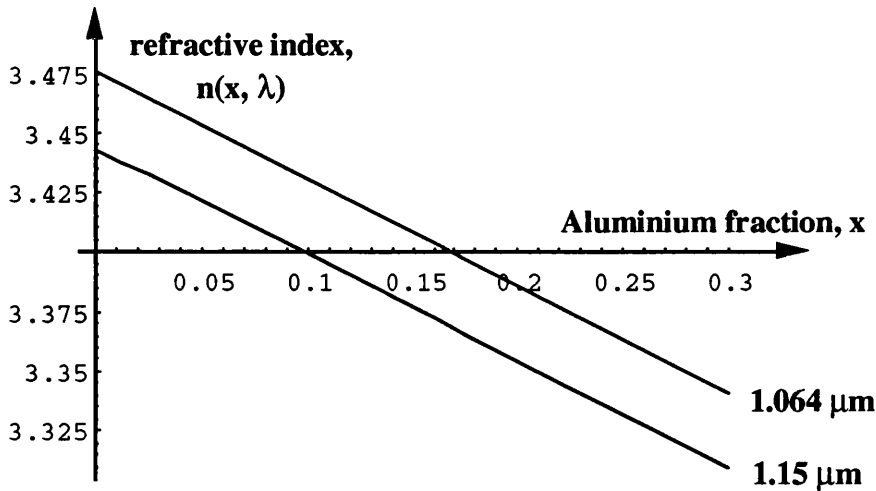


**Figure 4.34**

4.7.2 FWave III Output for Device designs

The FWAVE [47] [48] group of application programs, running on Apple Macintosh computer systems, were used to model the multi-moded behaviour of waveguides. They were able to numerically deduce or estimate the electromagnetic field distributions within specific rib geometries. Data relating to rib depth, width, layer structure of the wafer and its refractive index distribution were all required as a standard input set. Both horizontal (transverse electric, TE) and vertical (transverse magnetic, TM) field components, found by numerical solution at finite difference mesh boundaries, could be plotted within the geometry. In general, the larger the number of iterations allowed to converge to a solution, the more accurate the final solution obtained for a particular mode. Typical number of iterations used varied from 100 to 250 depending on the narrowness of layers, and proximity of refractive index values between these layers. The methods and functions of Yariv [66] and Adachi [2] were employed to estimate refractive index values for insertion into the FWAVE III [47] program. Information relating to both planar and vertical wafers was introduced into the program separately. The output of the program, for the typical vertical wafer B115, is displayed in Figures 4.35 and 4.36. An assortment of parameter values at the two discrete wavelengths 1.064 μm and 1.15 μm were used. With a standardised rib width of 4 μm, it was shown at 1.064 μm to support more than one mode (i.e. multi-moded) at the rib depth of 2.5 μm. The standard 0 - 30 % graded AlGaAs layer was modelled as six layers with discretely stepped refractive index. The optical field was observed to

Typical vertical wafer (B115) @ 1.064  $\mu\text{m}$

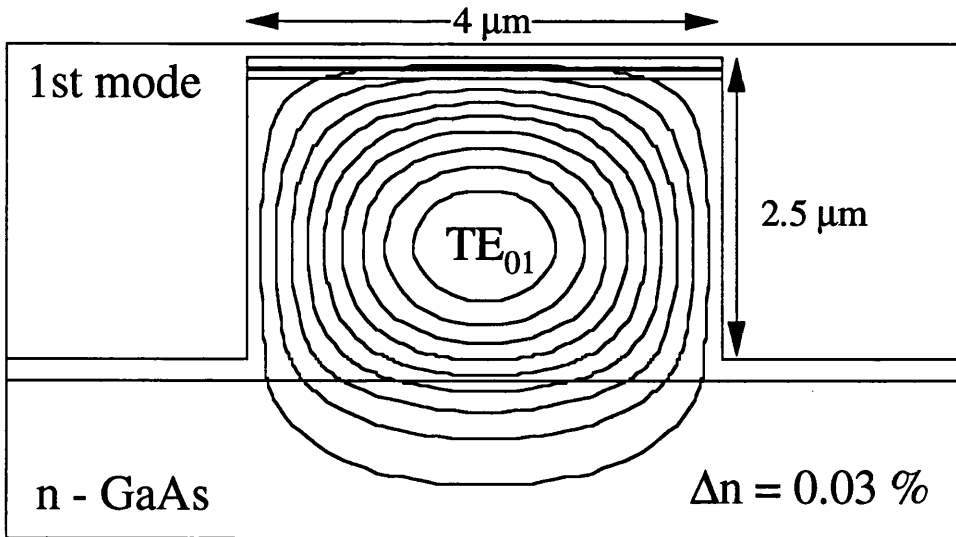


Figure 4.35(a)

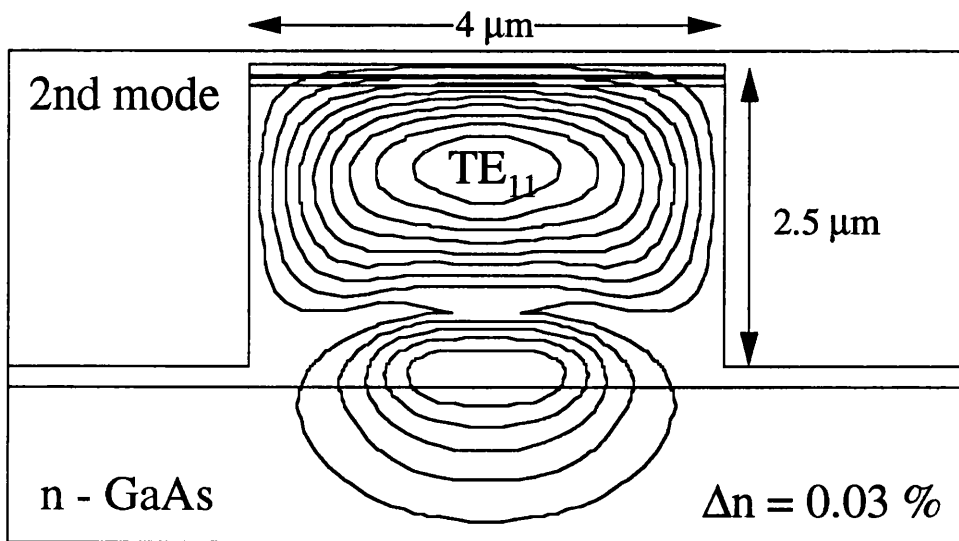


Figure 4.35(b)

Typical vertical wafer (B115) @ 1.15  $\mu\text{m}$

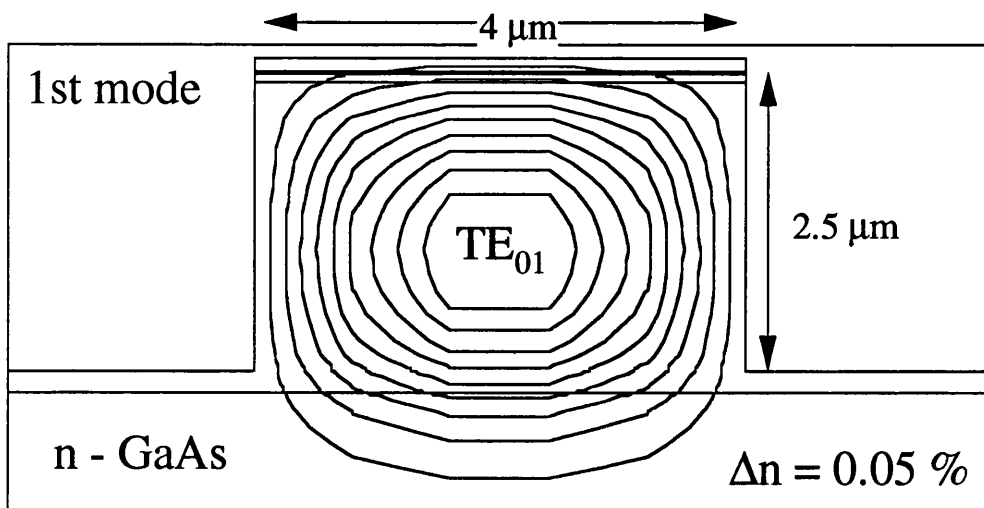


Figure 4.36(a)

Typical vertical wafer (B115) @ 1.15  $\mu\text{m}$

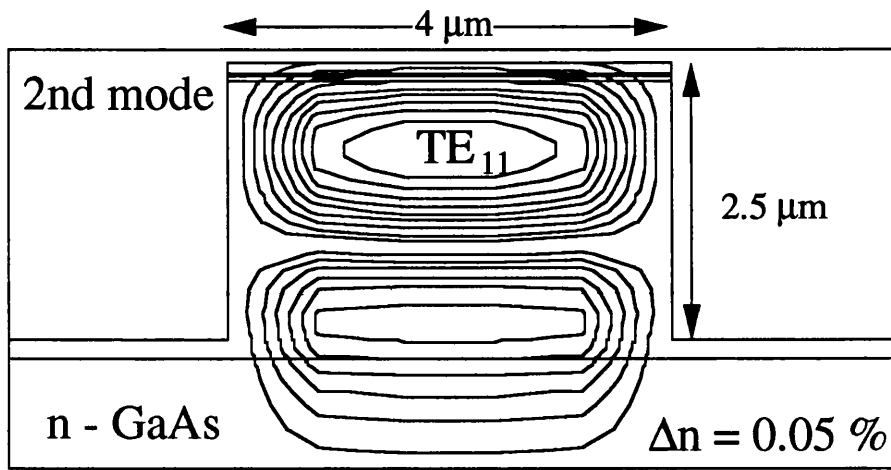


Figure 4.36(b)

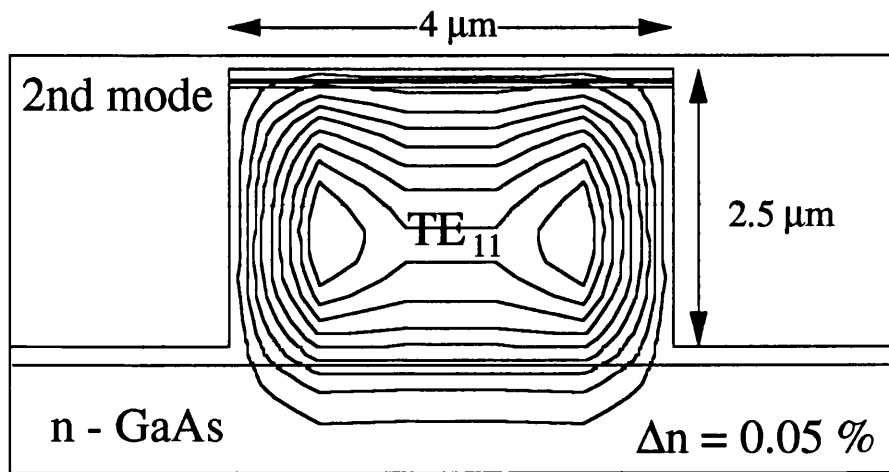


Figure 4.36(c)

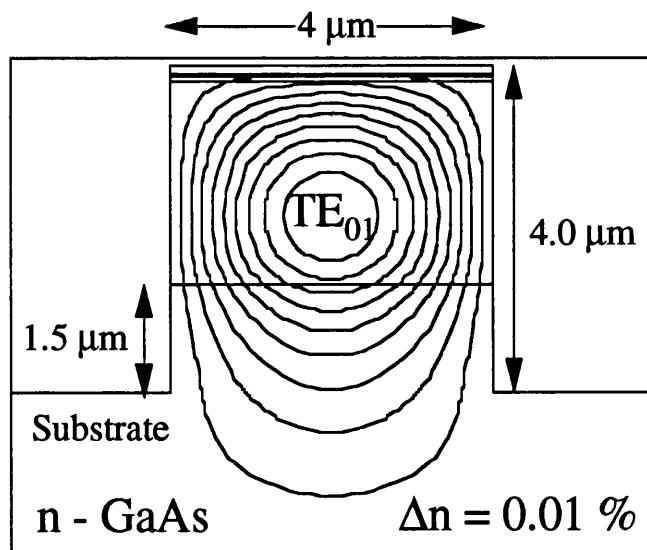


Figure 4.36(d)

Wafers B157, B234, @ 1.064  $\mu\text{m}$

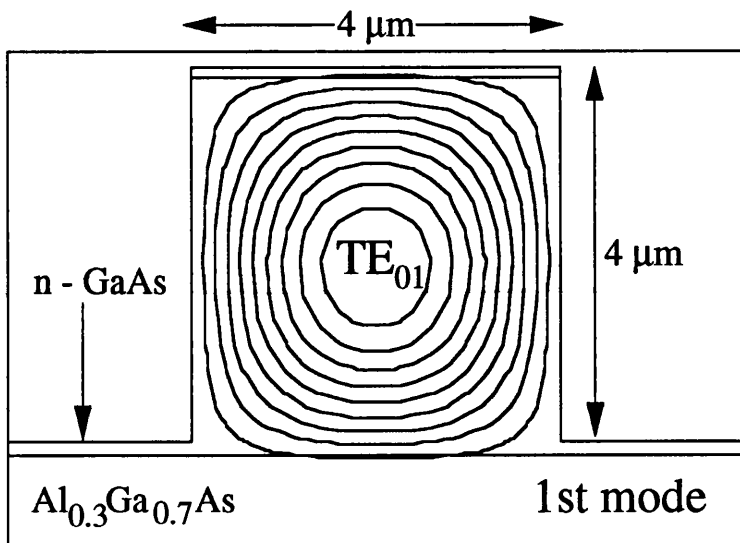


Figure 4.37(a)

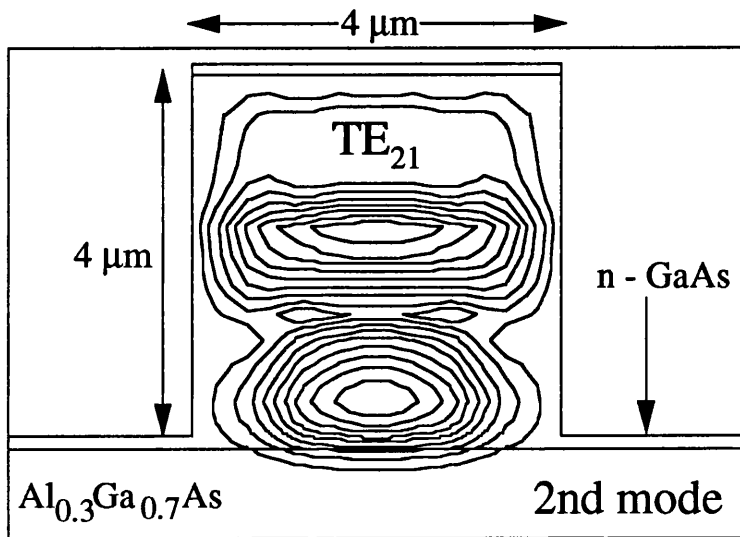


Figure 4.37(b)

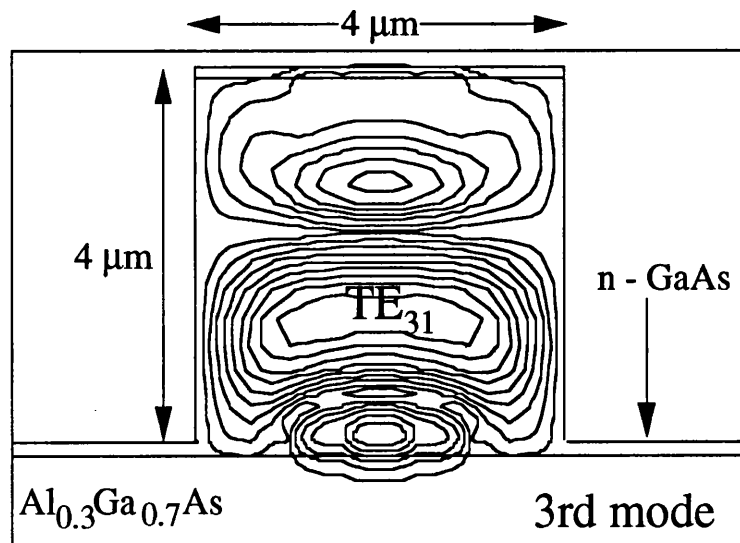


Figure 4.37(c)

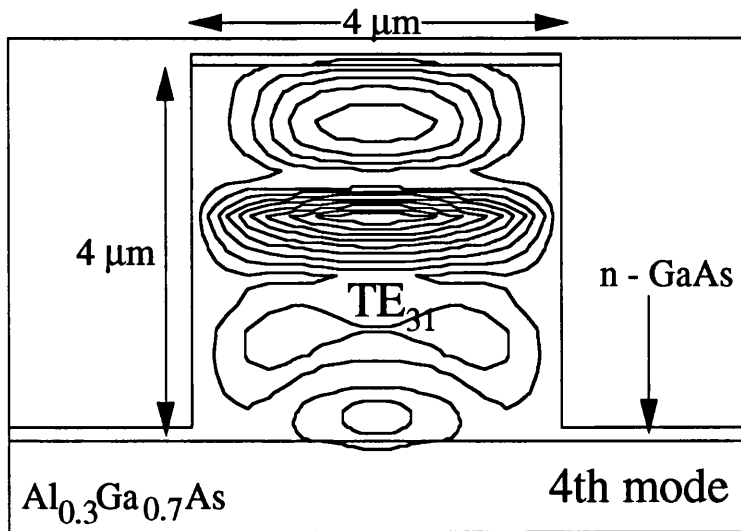


Figure 4.37(d)

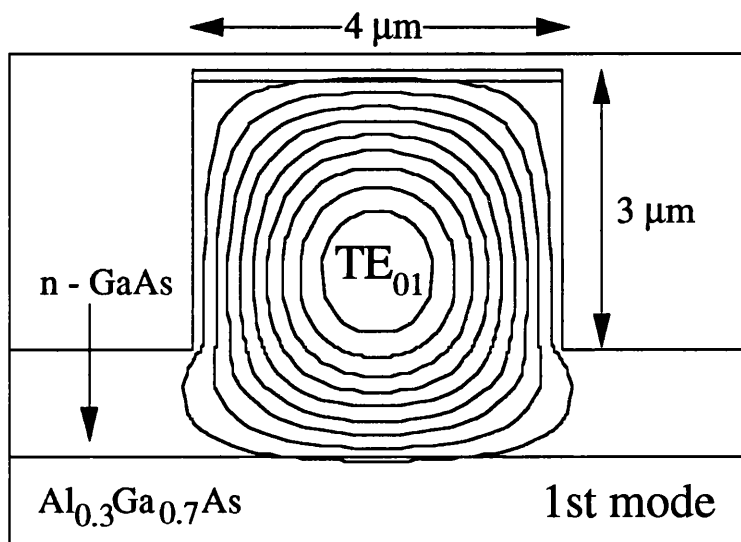


Figure 4.37(e)

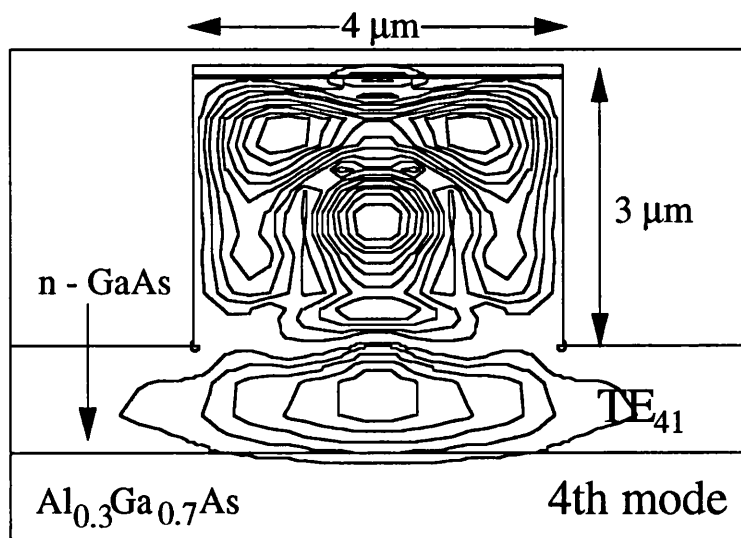


Figure 4.37(f)

penetrate this layer, and be confined ostensibly by the physical rib itself in the upper vertical direction. The depression of the refractive index at the lower boundary was exploited to provide moderate confinement. However, the 0.03 % to 0.05 % refractive index depression afforded by the active region-substrate interface allowed non-negligible optical power leakage. A majority of the incident optical power could be concentrated in the rib by increasing its depth. This did not however, guarantee the greatest optoelectronic interaction. The vertical nature of these devices prevented the inclusion of an AlGaAs layer at the base of the active region (c.f. planar devices). At 1.15  $\mu\text{m}$  wavelength, double moded waveguiding for TE modes was also supported (Figure 4.36(b) and (c)), with similar levels of confinement.

Modelling of planar wafers (e.g. B157) was performed, with the field distributions (TE modes) shown in Figure 4.37. Confinement levels were considerably improved by including a 1  $\mu\text{m}$  33 % AlGaAs confinement layer. Greater guiding efficiency and more compact modal profiles were to be expected in planar devices. 4  $\mu\text{m}$  deep waveguides were used as routine, creating symmetrical and uniform field profiles. Reducing the rib depth (e.g. to 2.0  $\mu\text{m}$ ) generated unnecessary lateral spreading of the optical field in lower regions of the n-GaAs layer (Figure 4.37(e) & (f)). The added depth, however, was responsible for the very multi-moded nature of these waveguides. A 4  $\mu\text{m} \times 4 \mu\text{m}$  waveguide facet was considered necessary for efficient radiation coupling and de-coupling.

#### 4.8 Conclusions

It was concluded, from the benefits of reduced thermal power dissipation and field-symmetry within the device, that a reappraisal of the original side-wall structure (vertical device) was justified. A more reliable device design was proposed, with an order of magnitude reduction in the natural capacitance. The fabrication viability of this structure was demonstrated, and the inclusion of the dielectric isolation layer justified. Modelling of the optical field distributions in the standardised 4  $\mu\text{m}$  rib waveguides indicated that limited multi-moded activity was likely. Despite this, the necessity to obtain a sizeable power throughput of optical radiation meant that rib widths were maintained at 4  $\mu\text{m}$ . The simplicity of the planar device was confirmed by its fabrication. The merits and de-merits of the vertical and planar implementations were considered, with both designs justifiable for different reasons. Physical discontinuities were maintained in the designs to confine optical radiation. Both

structures were optimised (within engineering limitations) for the primary purpose of achieving and observing modulation, if this was possible.

The areas of overlap generated by the original mask designs for the side-wall device were significant, with maximum overlap areas due to the blanket contact up to  $360,000 (\mu\text{m})^2$ . In the context of a semiconductor RF microwave device, this represented an area of unprecedented magnitude. Maximum capacitances were of the order of 0.924 pF with these areas. The natural capacitance was increased by the substrate thinning made necessary by the thermal dissipation requirements, and was assessed in the context of a combination with inductances. Inductances in the range 1-10 nH were possible with average multi-bond wire arrangements. Capacitance values for digit widths of 20  $\mu\text{m}$ , with contact and waveguide widths of 10  $\mu\text{m}$  and 4  $\mu\text{m}$  respectively, were in the range 600 - 800 fF (0.6 - 0.8 pF). This was an order of magnitude improvement on the side-wall structure device, and was another justification for the reappraisal of the Moreland structure.

High wall smoothness and verticality of ribs and mesas could be obtained through careful mask preparation. The active intervention of the quartz plate lead to devices with clean etch floors, and with unprecedented depths. This was normally the preserve of wet etching techniques. Square or rectangular waveguide profiles were achieved with ease due to the inherent directionality of the etching process, and absence of lateral etching of the mask.

The loading effect for quartz plate reactive ion etches was demonstrated and functionally quantified. The physical limitations of practical plasma etching apparatus (RIE 80) could be seen through the presence of oxygen radicals, leading to "AlGaAs grass".

## Chapter 5

### Theoretical Analysis of the Graded Area Device

#### 5.1 DC Current - voltage characteristic of a Graded Device

The DC current-voltage characteristic is of fundamental interest in the analysis of a graded-area element. In the first instance, it may indicate predominant modes of operation of a device, and also confirms assumptions made in theoretical modelling.

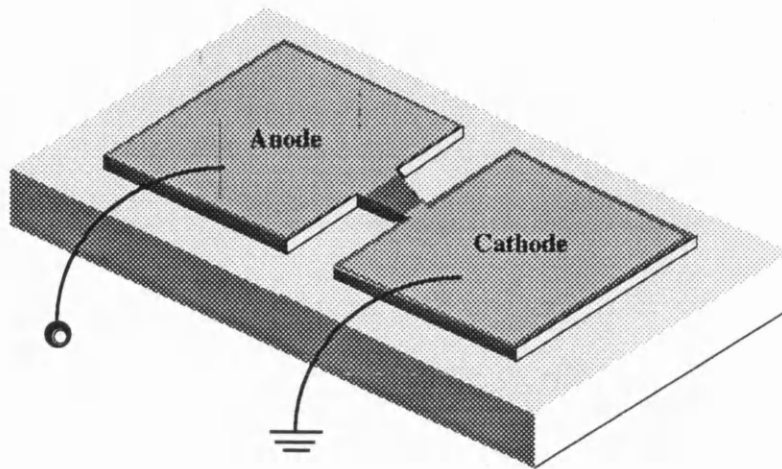
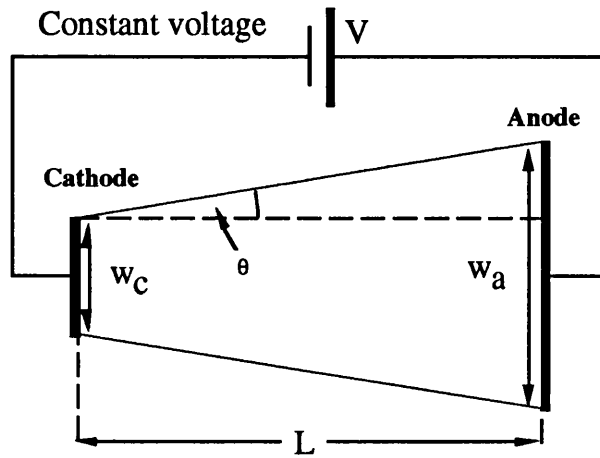


Figure 5.1 :- Tapered planar device

It was necessary to clarify the distinction between the current density - field relationship, and that between the total elemental current and the external terminal voltage. In effect, the total current flowing between the cathode and anode was a **global summation** of the **instantaneous** current density - area product between the spatial limits of the active region. In addition, since the electric field was a spatially - dependent function, then it followed that there was no immediate relationship between electric field and applied voltage. Further, the displacements in field and space of maxima and / or saturation events exhibited in the J - F characteristic were not directly transferred to DC I - V traces. The I - V trace function was evaluated analytically, with approximations for the velocity-field relation, and by adopting the determined electric field distribution. The derivation was performed in four discrete steps as follows :- (1) Determination of the spatial sub-threshold electric field distribution for the tapered element; (2) Derivation of the dependence of the **characteristic decay length**,  $\delta$ , upon the applied voltage at the terminals, and subsequent substitution for  $\delta$  in the result of (4). (3) Development of a suitable current density (velocity)-field relation, and deduction of a function relating it to spatial coordinates ; (4) Integration of this function with respect to displacement (as derived from the spatial dependence of the cross-sectional area).

**5.1.1 Determination of Electric field variation**



$$w(x) = w_c \left( 1 + \frac{x}{L} \left[ \frac{w_a}{w_c} - 1 \right] \right)$$

$$\tan \theta = \frac{w_a - w_c}{2L} \Rightarrow w(x) = w_c + 2x \tan \theta$$

**Figure 5.2 :- Constant voltage condition for tapered active region**

Consider the graded device shown in Figure 5.2. The term "graded" refers to the tapered active region width, which when coupled to the standard depth of the element, generates a device with a graded or tapered area. The functionally varying area of the device induces a similar spatial variation of Electric field. If the standard depth of the element is  $h$ , then the area of the active region varied as follows :-

$$A(x) = h \cdot w(x) = hw_c \left( 1 + \frac{x}{L} \left[ \frac{w_a}{w_c} - 1 \right] \right) = A(1 + Bx) \rightarrow A = hw_c ; B = \frac{1}{L} \left[ \frac{w_a}{w_c} - 1 \right] \quad (5.1)$$

This functional variation was used in the derivation of functions for a **Linearly-graded physically tapered** device. Under normal circumstances, for a uniform cross-sectional area device with uniform background doping ( $n_0$ ), the Electric field varies **linearly**, decreasing in magnitude for **n** type doped areas, and increasing in regions where the doping is **p** type. These variations in the magnitude of electric field comply with the **1-D Poisson's equation** as follows -

$$\frac{\partial E}{\partial x} = \frac{e}{\epsilon} [n(x) - n_0] \Rightarrow E(x) = \int \frac{e}{\epsilon} (-n_0) dx = E(0) - \frac{en_0}{\epsilon} x \quad (5.2)$$

where a solution for  $n = \text{constant}$ ,  $n(x) = 0$  has been sought. Equation (5.2) is applicable to all situations where there is doping present, and must be coupled with the space-charge transit requirements of **conduction (drift) current, diffusion current and Maxwellian displacement current** for an element with an applied bias. In certain circumstances, one or other of these components of the total current may be ignored as negligible.

### 5.1.2 The Spatial Variation of Electric Field

Initially, it was assumed that the current (sum of the total current density-area product contributions) remained constant throughout the spatial extent of the element. If this was not so, and current was larger or smaller than that in other areas, this would lead directly to regions of **accumulation** and / or **depletion** to re-establish electrical **neutrality** within the element. This disparity would then remain as a permanent feature in the device for all fields - this is not the case. With this criteria, the variation of the field within the device must accommodate both the requirements of the **conduction, diffusion and displacement current densities, and the tapered area function.**

Consider the expression for the total current density in an arbitrary conducting element with an applied terminal voltage :-

$$J(x) = n e \mu E(x) - eD \frac{\partial n}{\partial x} + \epsilon \frac{\partial E(t)}{\partial t} \approx n e \mu E(x) - eD \frac{\partial n}{\partial x} \dots \dots (5.3)$$

where the three components are due to conduction, diffusion and displacement respectively. For time invariant conditions, the time derivative of field could be ignored. Reconsidering (5.3), where doping could be an arbitrary function of x [n(x)], then it could be asserted that :-

$$\frac{\partial E}{\partial x} = \frac{e}{\epsilon} [n(x) - n_o] \Rightarrow n(x) = n_o + \frac{\epsilon}{e} \frac{\partial E}{\partial x} \dots (5.4)$$

The expression for n[x] was then substituted into equation (5.4), leading to :-

$$J(x) = \left( n_o + \frac{\epsilon}{e} \frac{\partial E}{\partial x} \right) e \mu E(x) - eD \frac{\partial}{\partial x} \left( n_o + \frac{\epsilon}{e} \frac{\partial E}{\partial x} \right) = n_o e \mu E(x) + \mu \epsilon E(x) \frac{\partial E}{\partial x} - eD \frac{\partial^2 E}{\partial x^2} \dots (5.5)$$

If the average current was defined as  $I_{av}$ , then a functional variation for the total current density could be extracted as :-

$$J(x) = \frac{I_{av}}{hw_c \left( 1 + \frac{x}{L} \left[ \frac{w_a}{w_c} - 1 \right] \right)} \rightarrow \frac{A}{(1 + Bx)} ; A \equiv \frac{I_{av}}{hw_c} = J_c ; B \equiv \left[ \frac{w_a - w_c}{Lw_c} \right] \dots (5.6)$$

To solve for the electric field variation that satisfies both (5.5) and (5.6), they were initially equated in (5.7), and then an exponential variation of the form of equation (5.8) assumed :-

$$n_o e \mu E(x) + \mu \epsilon E(x) \frac{\partial E(x)}{\partial x} - eD \frac{\partial^2 E(x)}{\partial x^2} = \frac{A}{(1 + Bx)} \dots (5.7)$$

$$E[x] = E_c e^{mx} \quad \text{where} \quad E_c \equiv \text{cathode field} \dots (5.8)$$

If  $\sigma_0 = n_o e \mu$ , then equation (5.7) could be expanded and reduced to yield the following :-

$$\gamma_0 e^{mx} + \gamma_1 e^{2mx} \equiv A(1 + Bx)^{-1} \rightarrow \gamma_0 = [\sigma_0 - \epsilon Dm^2]E_c; \gamma_1 = m\mu\epsilon E_c^2 \quad \text{--- (5.9)}$$

The next step was to obtain an expression independent of  $x$  for the exponential constant  $m$ . This was performed by the expansion of the LHS and RHS of (5.9) using **Maclaurin's Theorem** and the **Binomial theorem** respectively. The inherent validity of the derivation is limited by the range of valid values for the binomial expansion of (5.9). This expansion required that :-

$$|Bx| < 1 \Rightarrow \left| \frac{x}{L} \left( \frac{w_a}{w_c} - 1 \right) \right|_{x=L} = \left| \frac{w_a}{w_c} - 1 \right| < 1 \Rightarrow w_a < 2w_c \Rightarrow \theta < 45^\circ$$

This implied that the analysis was only valid for taper angles less than  $45^\circ$ . This did not provide an extreme limitation in the use of the function. The series were evaluated up to and including the terms in  $x^0$  and  $x^1$ , generating :-

$$\underbrace{\gamma_0 \left( 1 + mx + \frac{m^2 x^2}{2!} + \dots \right)}_{\text{LEFT HAND SIDE}} + \underbrace{\gamma_1 \left( 1 + 2mx + \frac{4m^2 x^2}{2!} + \dots \right)}_{\text{RIGHT HAND SIDE}} \equiv A \left( 1 - Bx + \frac{(-1)(-2)}{2!} x^2 + \dots \right) \quad \text{--- (5.10)}$$

The relationship between the constants  $\gamma_0$  and  $\gamma_1$ , and the exponential constant  $m$ , was then obtained by simply equating coefficients in  $x^0$  and  $x^1$ , resulting in expression (5.11) as follows :-

$$\gamma_0 + \gamma_1 \equiv A; \quad m[\gamma_0 + 2\gamma_1] \equiv -AB \quad \text{--- (5.11)}$$

Hence, the exponential decay of electric field could be written as in expression (5.12), where the concept of the **characteristic decay length**,  $\delta$  had been introduced such that :-

$$m \equiv -\frac{1}{\delta} \Rightarrow E[x] = E_c e^{mx} \rightarrow E[x] = E_c e^{-\frac{x}{\delta}} \quad \text{--- (5.12)}$$

The spatial dependency of current density was incorporated by including both simultaneous equations. Rearranging yielded the following quadratic in  $m$ , with accompanying solutions :-

$$m^2 + \frac{A}{\mu\epsilon E_c^2} m + \frac{AB}{\mu\epsilon E_c^2} = 0 \Rightarrow m = -\frac{1}{2} \left[ \frac{A}{\mu\epsilon E_c^2} \pm \sqrt{\left\{ \frac{A}{\mu\epsilon E_c^2} \right\}^2 - \frac{4AB}{\mu\epsilon E_c^2}} \right] \quad \text{--- (5.13)}$$

Factorising (5.13) generated the following :-

$$m = -\frac{1}{2} \left( \frac{A}{\mu\epsilon E_c^2} \right) \left[ 1 + \sqrt{1 - \left( \frac{4\mu\epsilon B}{A} \right) E_c^2} \right] \Rightarrow \delta[E_c^2] = \frac{\chi_0 E_c^2}{\left[ 1 + \sqrt{1 - \chi_1 E_c^2} \right]}$$

$$\chi_0 = \left( \frac{2\mu\epsilon}{A} \right); \quad \chi_1 = \left( \frac{4\mu\epsilon B}{A} \right) \quad \text{--- (5.14)}$$

The characteristic decay length had a dependency upon the value of the field at the cathode (i.e.  $E[x=0] = E_c$ ), and a fundamental variation with absolute temperature in the device. Figure 5.3 illustrated

the variation of  $\delta$  in the  $E_c$ - $n_0$  plane, while Figure 5.4 demonstrated the exponential decay of the field in the device.

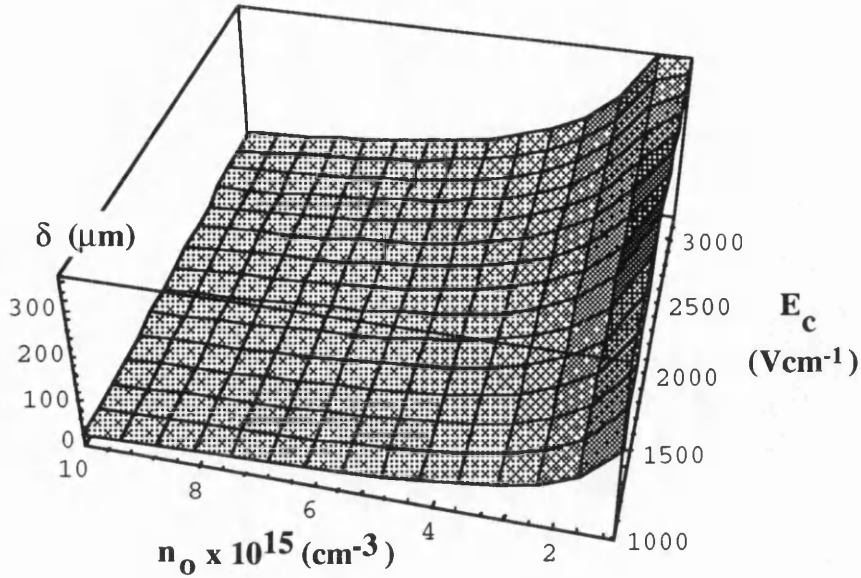


**Figure 5.3 :- Variation of characteristic decay length**

Spatial Decay of Electric Field for various values of doping

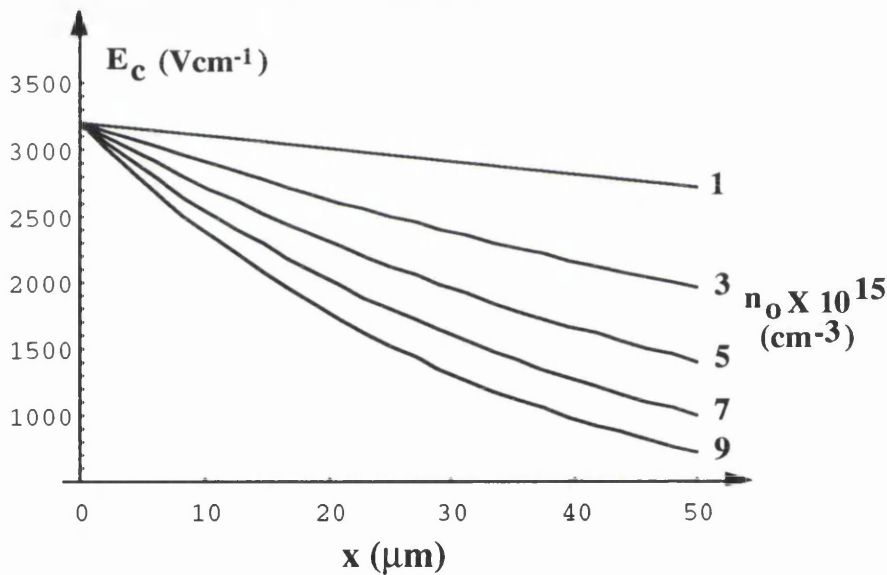


**Figure 5.4 :- Exponential decay of electric field (fixed cathode value)**

As the background doping increased, the rate of decay increased. In order to maintain constant current, the current density had to fall with increasing  $x$  - this was reflected in the fall in electric field. Rearranging expression (5.14), the cathode field could be determined in terms of the characteristic decay length as follows :-

$$2\chi_o \left[ \frac{1}{\delta} - B \right] = \frac{\chi_o^2}{\delta^2} E_c^2 \Rightarrow E_c[\delta] = \sqrt{\frac{2\delta}{\chi_o} [1 - B\delta]} = \sqrt{\frac{J_{ci} \delta}{\mu\epsilon} \left[ 1 - \frac{2}{w_c} \delta \tan \theta \right]} \dots (5.15)$$

where the constant  $A = J_{ci}$ , the average current density at the cathode injecting interface. The electric field distribution in a sub-threshold active region, with validity criteria, could be stated as :-

$$E_c[x, \delta] = \sqrt{\frac{J_{ci} \delta}{\mu \epsilon} \left[ 1 - \frac{2}{w_c} \delta \tan \theta \right]} e^{-\frac{x}{\delta}} \quad \text{where} \quad \delta < \frac{w_c}{2} \cot \theta \quad \dots (5.16)$$

### Variation of Electric field for spatially -dependent current density with displacement (for various $\delta$ )

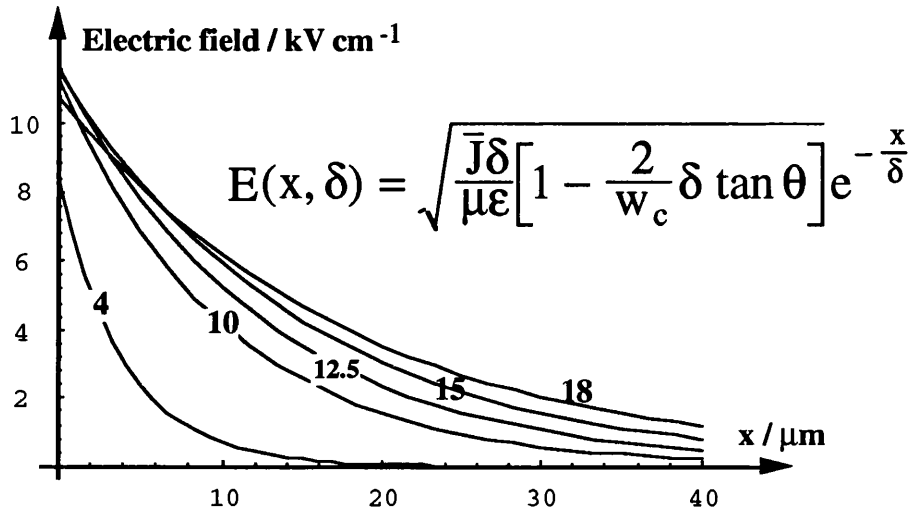


Figure 5.5

### Variation of Cathode field with $\delta$

$$E_c(x, \delta) = \sqrt{\frac{J \delta}{\mu \epsilon} \left[ 1 - \frac{2}{w_c} \delta \tan \theta \right]}$$

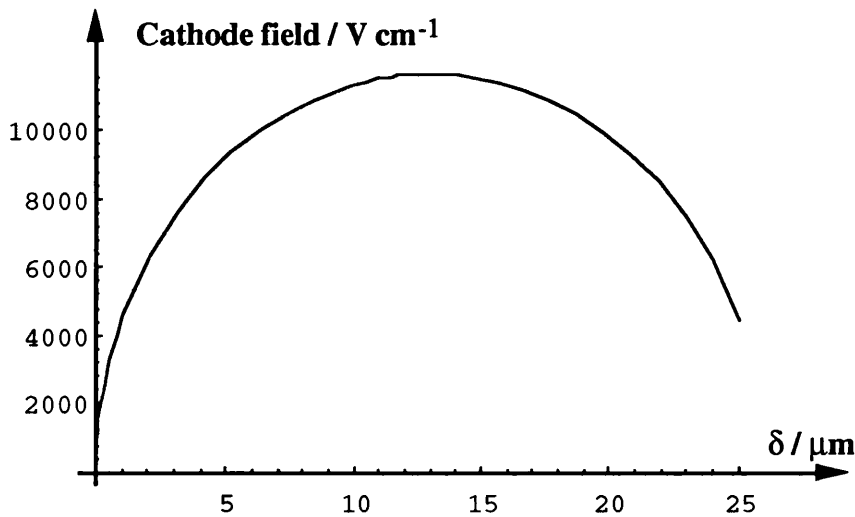
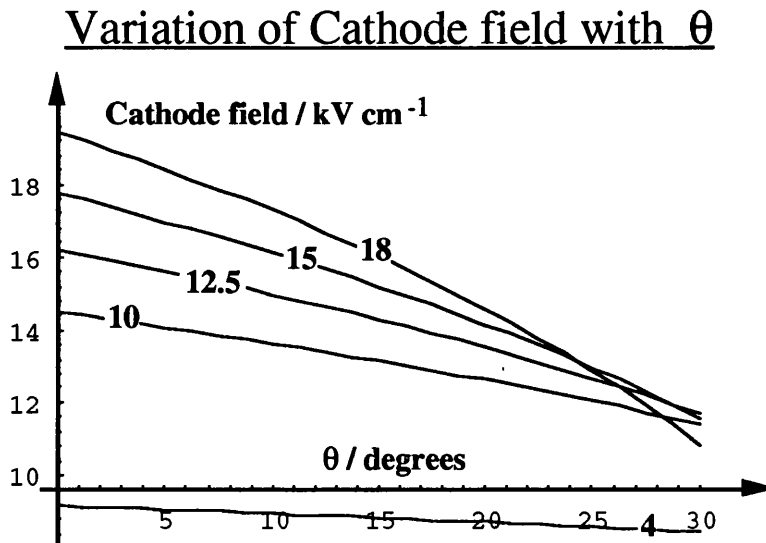


Figure 5.6

The variation of the electric field distribution with displacement, at various values of the decay length, is given in Figure 5.5. The area beneath the curve increased in a general sense, by virtue of the

increase in cathode field combined with a increase in the decay constant (slower decay) with increasing terminal voltage. The variation of the cathode field with  $\delta$ , where  $J = n_0 e \mu_e E$ ,  $w_c = 30 \mu\text{m}$ ,  $\theta = 30^\circ$ ,  $E = 500 \text{ V cm}^{-1}$ , is given in Figure 5.6. An initial increase in the cathode field was followed by a maxima, and a subsequent decline in the cathode field beyond it, as dictated by the inverted quadratic nature of the cathode field-decay length function.



**Figure 5.7**

The variation of the cathode field distribution with the angle of taper, at various values of the decay length, is given in Figure 5.7. A general decrease in the cathode field value was experienced with increasing gradient of taper within the element.

### **5.2 Functional relationship between Decay-length and Voltage**

As indicated, the characteristic decay length was defined in terms of standard semiconductor theory constants and cathode boundary field. The latter parameter was to prove important in establishing a complete description of the voltage-decay length relation. The functional variation of the characteristic decay length with applied voltage was intuitive, i.e. the decay constant increased with increasing voltage. This was to be expected since the tapering of the electric field would have to be more gradual, coupled with a general increase in the cathode field to accommodate the increase in area under the field-displacement function. The functional variation of the decay length with voltage could be simplified. Substantial variations in characteristic decay constants, cathode field values and current-voltage characteristics in tapered devices were possible.

If only the first of the simultaneous equations in expression (5.11) had been used in the development of an expression for the characteristic decay length, this would have been equivalent to

assuming a constant current density distribution in the element. This criteria had been adopted in other discussions of the nature of functional bulk elements (Shoji [68], 1967). However, in the DC constant voltage environment, this would have implied that greater current entered the device through the anode than departed from it via the cathode, i.e. there was a net arrival of positive charge. Translating from conventional current flow into electron terms, this implied additionally that the bulk of the device had to undergo depletion in order to accommodate this. A net displacement of charge occurred per unit time from the device to the source.

The mathematical derivation was pursued with expression (5.16) as the initial step. The total applied voltage to the element was determined through :-

$$\begin{aligned} \frac{\partial \Phi}{\partial x} = E[x] &\Rightarrow \Phi = \int_{\Phi_c}^{\Phi_a} d\Phi = \int_0^L E[x] dx = \int_0^L \sqrt{\frac{J_{ci} \delta}{\mu \epsilon} \left[ 1 - 2 \frac{\delta}{w_c} \tan \theta \right]} e^{-\frac{x}{\delta}} dx \\ &= \sqrt{\frac{J_{ci} \delta}{\mu \epsilon} \left[ 1 - 2 \frac{\delta}{w_c} \tan \theta \right]} \delta \left[ 1 - e^{-\frac{L}{\delta}} \right] \Rightarrow \Phi \approx \sqrt{\frac{J_{ci} \delta}{\mu \epsilon} \left[ 1 - 2 \frac{\delta}{w_c} \tan \theta \right]} L \left[ 1 - \frac{L}{2\delta} \right] \dots (5.17) \end{aligned}$$

Expression (5.17) was squared and expanded, leading to a cubic equation in  $\delta$  with the voltage-dependent coefficients as shown :-

$$\left[ \frac{2}{w_c} \tan \theta \right] \delta^3 + \left[ 1 + \frac{2L}{w_c} \tan \theta \right] \delta^2 + \left[ \frac{\mu \epsilon}{L^2 J_{ci}} \Phi^2 - \left( L + \frac{2L^2}{4w_c} \tan \theta \right) \right] \delta + \frac{L^2}{4} = 0 \dots (5.18)$$

The pursuit of an analytical solution to the decay constant-voltage (and hence current-voltage) relationship meant that the  $\delta^3$  factor of the cubic equation had to be discarded for ease of computation. This inherently induced error, which was intuitively identified in the final roots of the quadratic equation as follows :-

$$\begin{aligned} a_3 \delta^3 + a_2 \delta^2 + a_1 \delta + a_0 &\equiv a_0 \delta^2 + a_5 \delta + a_4 ; \\ \text{if } a_3 \neq 0 &\Rightarrow \{ \delta - [\delta_1 + \text{Error}] \} \{ \delta - [\delta_2 + \text{Error}] \} = 0 \end{aligned}$$

An approximate root to the quadratic equation from (5.18) was determined, which was of the form :-

$$\begin{aligned} \left[ 1 + \frac{2L}{w_c} \tan \theta \right] \delta^2 + \left[ \frac{\mu \epsilon}{L^2 J_{ci}} \Phi^2 - \left( L + \frac{2L^2}{4w_c} \tan \theta \right) \right] \delta + \frac{L^2}{4} = 0 &\Rightarrow \\ |\delta[\Phi]| = \frac{\beta \Phi^2 - \left( L + \frac{L^2}{4} \alpha \right)}{2(1 + \alpha L)} \left\{ 1 + \sqrt{1 - \frac{(1 + \alpha L)L^2}{\left[ \beta \Phi^2 - \left( L + \frac{L^2}{4} \alpha \right) \right]^2}} \right\} ; &\alpha = \frac{2}{w_c} \tan \theta ; \beta = \frac{\mu \epsilon}{L^2 J_{ci}} \end{aligned} \dots (5.19)$$

where the error was isolated and the expression simplified as follows :-

$$|\delta[\Phi]| = \frac{\eta \beta \Phi^2}{2(1 + \alpha L)} \left\{ 1 + \sqrt{1 - \frac{(1 + \alpha L)L^2}{[\eta \beta \Phi^2]^2}} \right\} + \text{Error} \dots (5.20)$$

Further simplification was achieved by noting of the tendency to unity of the second factor. In addition, a scaling factor was incorporated into expression (5.20), to accommodate the error due to curtailing the cubic function, and compound injection conditions. It also served a future curve-fitting role between theoretical and real data in current-voltage traces and otherwise. The final averaged formulae describing the variation between the decay constant and the applied terminal voltage was as follows :-

$$\left\{ 1 + \sqrt{1 - \frac{(1 + \alpha L)L^2}{[\eta\beta\Phi^2]^2}} \right\} \rightarrow 1 \Rightarrow \delta[\Phi] \approx \frac{\eta\beta\Phi^2}{2 \left[ 1 + \frac{2L}{w_c} \tan \theta \right]} \dots (5.21)$$

Figure 5.8 illustrated the evaluated variation of the decay constant with terminal voltage.

### Variation of decay length with applied terminal voltage (for values of scaling constant, $\eta$ )

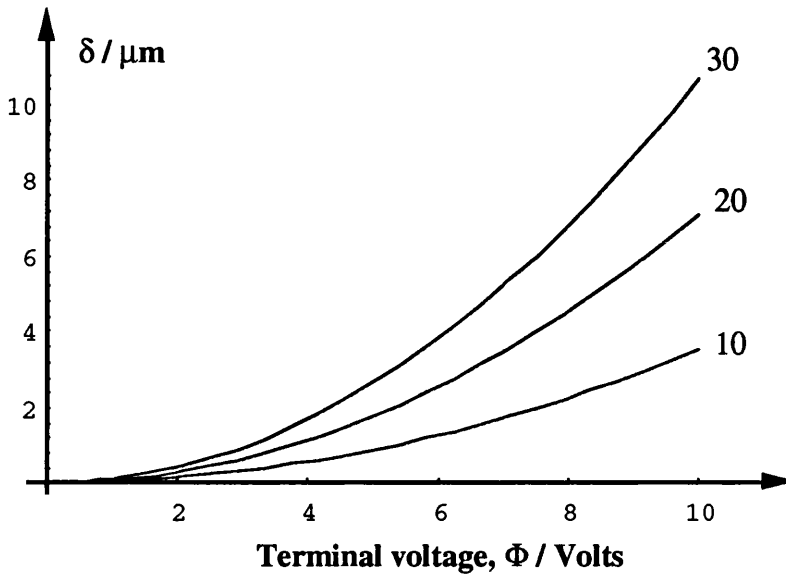


**Figure 5.8**

#### 5.4 Functional dependence of Current with Voltage

With an effective decay length-voltage function, the overall variation of the electric field distribution with voltage could be obtained. An equivalent expression was then derived for the current density varying with applied terminal voltage, yielding global current flow with spatial integration. As stated in the introduction, total current flowing, assumed constant as most appropriate, was a global integral of the all the current density - area contributions within the active region of the device. The total current flowing in the element could be evaluated through the following :-

$$I = \frac{\int_{A[0]}^{A[L]} J(A) dA}{\int_{A[0]}^{A[L]} dA} = \frac{\int_{A[0]}^{A[L]} J(A) dA}{A[L] - A[0]} \rightarrow \frac{\frac{h}{L}(w_a - w_c) \int_0^L J(x) dx}{\frac{h}{L}(w_a - w_c)} \rightarrow \frac{1}{L} \int_0^L J(x) dx \dots (5.22)$$

where the following area variation with x had been asserted and substituted :-

$$A(x) = A(1 + Bx) \Rightarrow dA \equiv ABdx \quad \rightarrow \quad dA \equiv hw_c \left[ \frac{w_a - w_c}{Lw_c} \right] = \frac{h}{L}(w_a - w_c) dx$$

A functional variation of current density with the spatial variable was obtained simply and directly from the drift current contribution taken in isolation [essential physics was lost by omitting diffusion current] i.e. :-

$$J(x) = n_o e \mu E(x) \quad \rightarrow \quad n_o e \mu E_c e^{-\frac{x}{\delta[\Phi]}} \quad \text{----- (5.23)}$$

After integration, the expression derived previously for the relationship between the decay length and voltage was inserted into (5.24), and rationalised and simplified. The developed expression included  $G_a$ , and two curve-fitting coefficients  $\eta_o$  and  $\eta_1$ .  $G_a$  was equivalent to the scaled conductance of a non-tapered device with the width of the anode. This indicated that a tapered device should be considered as a device with crystal removed, as opposed to a narrow device with crystal added. In accordance with (5.22), the current was given by :-

$$\begin{aligned} I(\Phi) &= \frac{n_o e \mu}{L} \sqrt{\frac{J_{ci} \delta[\Phi]}{\mu \epsilon} \left[ 1 - 2 \frac{\delta[\Phi]}{w_c} \tan \theta \right]} \int_0^L e^{-\frac{x}{\delta[\Phi]}} dx \\ &= \frac{n_o e \mu h w_a}{2} \sqrt{\frac{\eta \Phi^2 \left[ 1 - 2 \frac{\delta[\Phi]}{w_c} \tan \theta \right]}{2L^2 \left[ 1 + 2 \frac{L}{w_c} \tan \theta \right]}} \left[ 1 - e^{-\frac{L}{\delta[\Phi]}} \right] \quad \text{---- (5.24)} \end{aligned}$$

$$\Rightarrow I(\Phi) = G_a \eta_o \Phi \left[ 1 - e^{-\frac{L}{\delta[\Phi]}} \right] \sqrt{\frac{\left[ 1 + \left( 2 \frac{L}{w_c} - \frac{\eta_1 \beta \Phi^2}{w_c} \right) \tan \theta \right]}{\left[ 1 + 2 \frac{L}{w_c} \tan \theta \right]^2}} \quad \text{where} \quad G_a = \frac{n_o e \mu h w_a}{2\sqrt{2}L}$$

Equation (5.24) for device terminal current was separated into three fundamental function types, each with its own contribution to the overall profile of the current - voltage characteristic. These were as follows :-

$$I(\Phi) = F_1[\Phi] \cdot F_2[\Phi] \cdot F_3[\Phi] \quad \text{--- (5.25)}$$

### Function 1

### Function 2

### Decay length

$$F_1[\Phi] = \frac{n_o e \mu h w_a}{2\sqrt{2}L} \eta_o \Phi = G_a \eta_o \Phi; \quad F_2[\Phi] = \left[ 1 - e^{-\frac{L}{\delta[\Phi, \eta_2]}} \right]; \quad \delta[\Phi, \eta_2] \approx \frac{\eta_2 \beta \Phi^2}{2 \left[ 1 + 2 \frac{L}{w_c} \tan \theta \right]}$$

### Function 3

$$F_3[\Phi, \eta_1] = \sqrt{\frac{\left[ 1 + \left( 2 \frac{L}{w_c} - \frac{\eta_1 \beta \Phi^2}{w_c} \right) \tan \theta \right]}{\left[ 1 + 2 \frac{L}{w_c} \tan \theta \right]^2}} \quad \text{--- (5.26)}$$

### Cathode field versus voltage

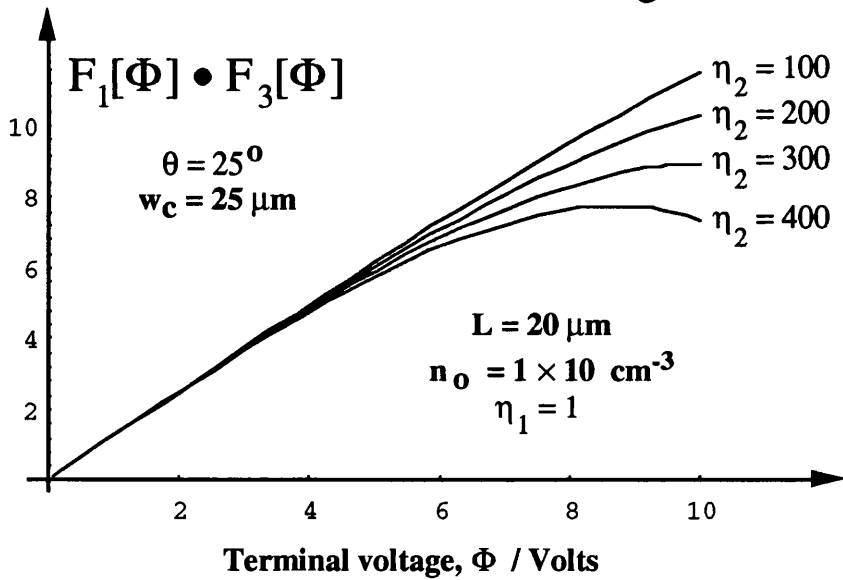


Figure 5.9

### Function 2 versus voltage

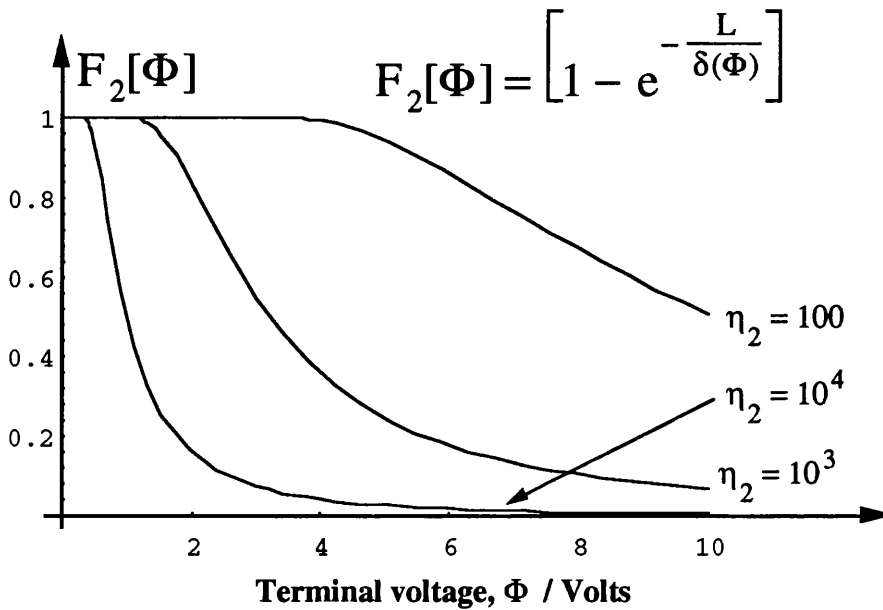
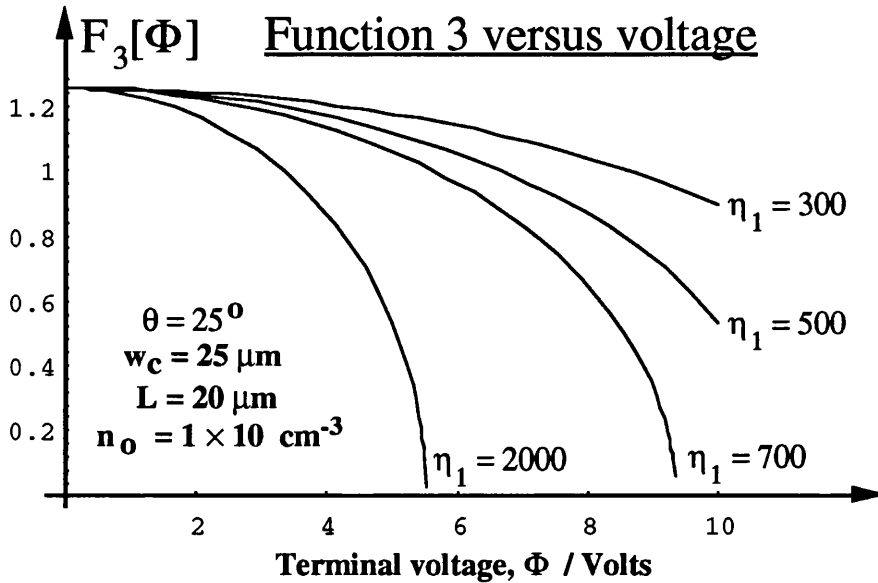


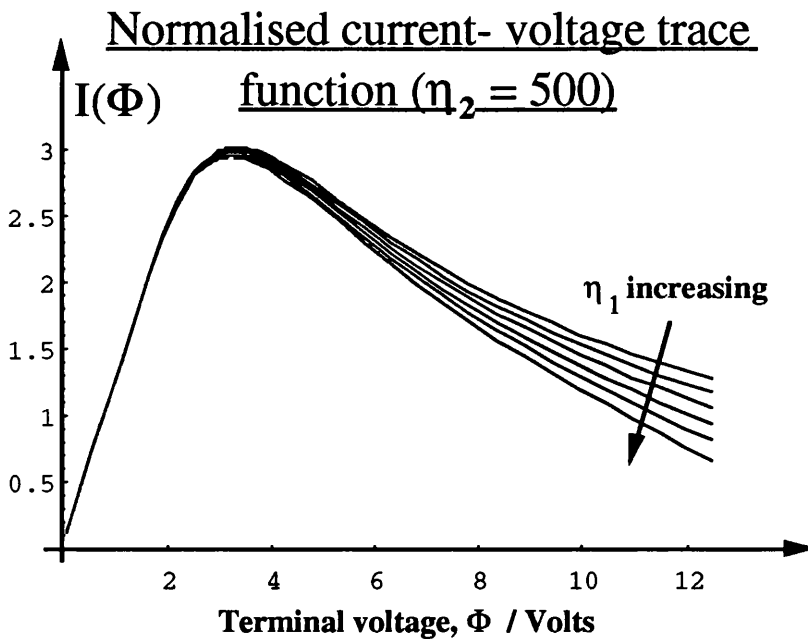
Figure 5.10

Figure 5.9 illustrated the variation of the cathode field ( $E_c$ ), or  $F_1[\Phi].F_3[\Phi]$ , with voltage, characterising the initial linear ohmic increase in current from the origin at lower voltages. The first rudiments of saturation were also evident for medium to higher voltages. Figure 5.10 exhibited the variation of the  $F_2[\Phi]$  function, seen as a unitary multiplier which decreased in a concave exponential manner. It also showed enhanced sensitivity to the values of the control parameter variables such as  $\eta_2$ , due to dependence upon the  $\delta[\Phi]$  factor. Whereas Function 1 provided the linear ohmic increase at lower voltages, Function 2 generated initial saturation at medium voltages and Function 3 implied further

saturation at higher voltages. Figure 5.11 illustrated the variation of the  $F_3[\Phi]$  in isolation, hence clarifying its contribution to the overall form. Combining these three functions, through multiplication, a final normalised current-voltage trace function could be plotted as in Figure 5.12, which encapsulated all of the influences of these three functions.



**Figure 5.11**



**Figure 5.12**

The concave nature of the saturation was evident at lower values of the  $\eta_1$  control parameter, i.e. the rate of fall of current diminished with increasing voltage. However, the influence upon the trace of the second control parameter ( $\eta_2$ ) was more immediately apparent in the group of curves in Figure 5.13, where it has been incremented.  $\eta_2$  determined the shape of the current-voltage profile, as opposed

to the scaling / shaping role performed by the primary control parameter,  $\eta_1$ . For complete curve-fitting and modification, a third separate control parameter (scaling only),  $\eta_o$ , was incorporated. It was observed from Figure 5.13 that as  $\eta_2$  decreased, the shape of the profile changed from concave saturation to simple convex saturation with low rate of change. It was characterised by the absence of a well-defined threshold voltage for this saturation, and notably higher peak currents than for those curves with concave saturation.

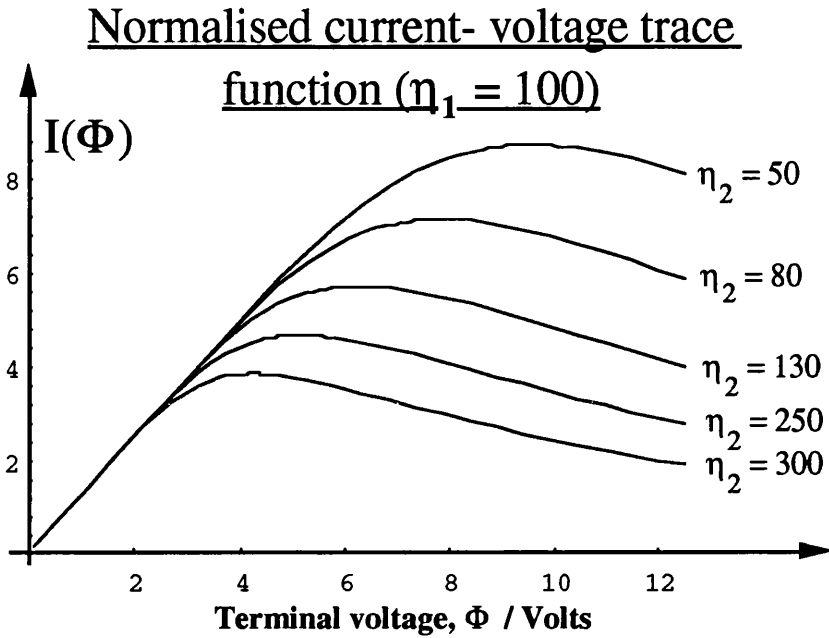


**Figure 5.13**

This sensitivity to the relative values of the control parameters within the function derived, could be exploited to match the theoretical form to real current-voltage traces. The transformation of the type of profile in particular suggested that some form of empirically-derived function could be determined for prediction of the control parameter values. This is discussed further in Chapter 6.

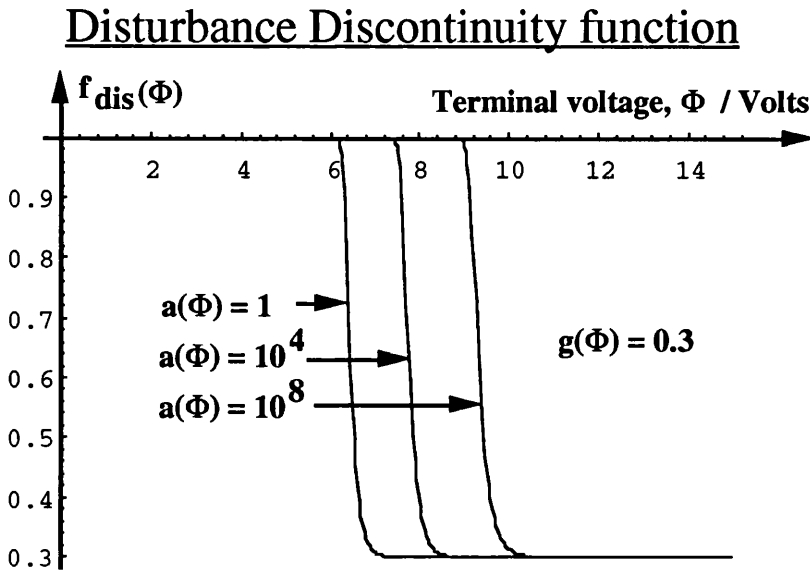
### 5.5 Disturbance Saturation Function

Further to the current-voltage function, profound current discontinuities, signifying the onset of disturbance formation, could be inserted arbitrarily into the trace by multiplying by an appropriate function. One such function was of the form shown in equation (5.27) :-

$$f(\Phi) = g(\Phi) \left[ 1 + a(\Phi) e^{-\left(\frac{\Phi_s}{\Phi}\right)^{100}} \right] + [1 - g(\Phi)] \dots (5.27)$$

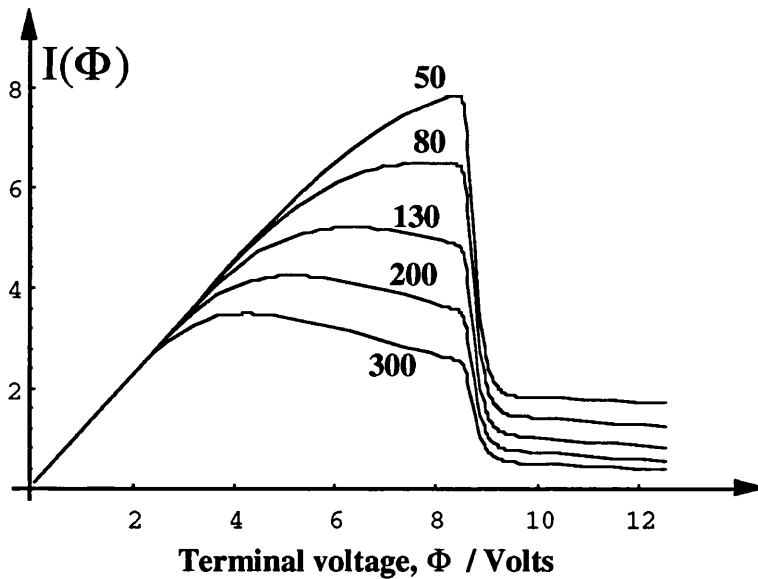
The intermediate functions  $f(\Phi)$  and  $g(\Phi)$  could be determined by through extrapolation with data from practical devices. Arbitrary relationships between the discontinuity and fabrication parameters

could be derived, and predictive worth extracted from expression (5.27). For a constant  $a(\Phi) = 1, 10^4, 10^8$ , the variation of this multiplication function was as shown in Figure 5.14.



**Normalised current- voltage trace function (for various values of  $r_2$ )**

$$I(\Phi) = F_1[\Phi] \cdot F_2[\Phi] \cdot F_3[\Phi] F_{dis}[\Phi]$$



A net fall in average current was superposed upon the whole trace by multiplying the current-voltage expression with the discontinuity function (Figure 5.15), modelling dipole disturbance formation. Figures 5.16 and 5.17 demonstrated further variations of the full function with the discontinuity incorporated. They illustrated the modification of the discontinuity threshold with the

value of  $\Phi_{th}$ , where it was shown that these two values did not correspond directly. A threshold of  $\Phi_{th} = 4$  Volts gave a discontinuity at 5.5 Volts on the actual trace.

Normalised current- voltage trace function (for various values of  $\Phi_{th}$ )

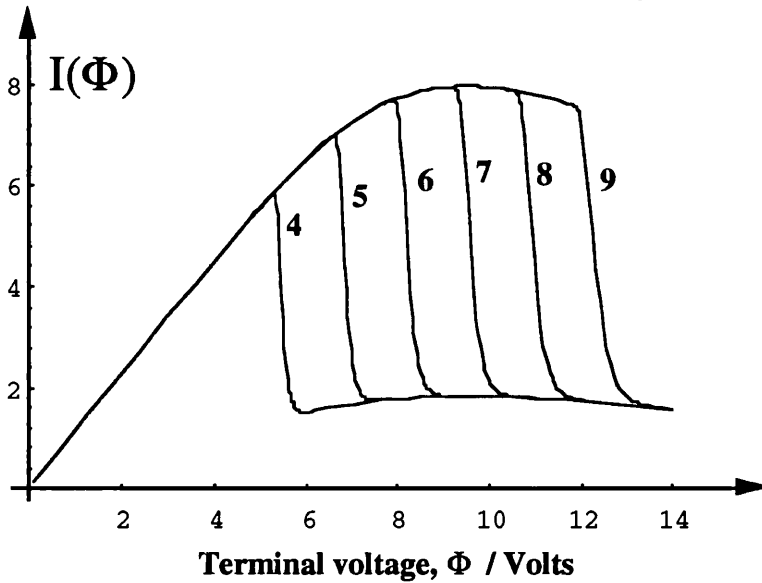


Figure 5.16

Normalised current- voltage trace function

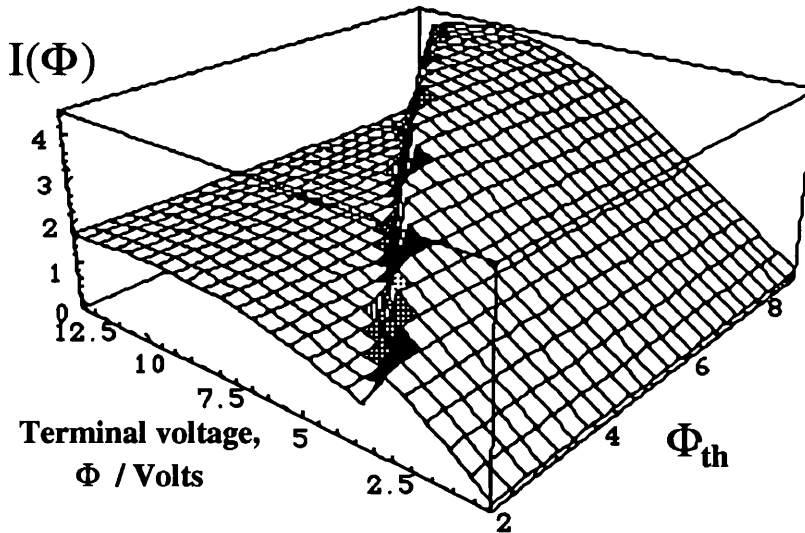
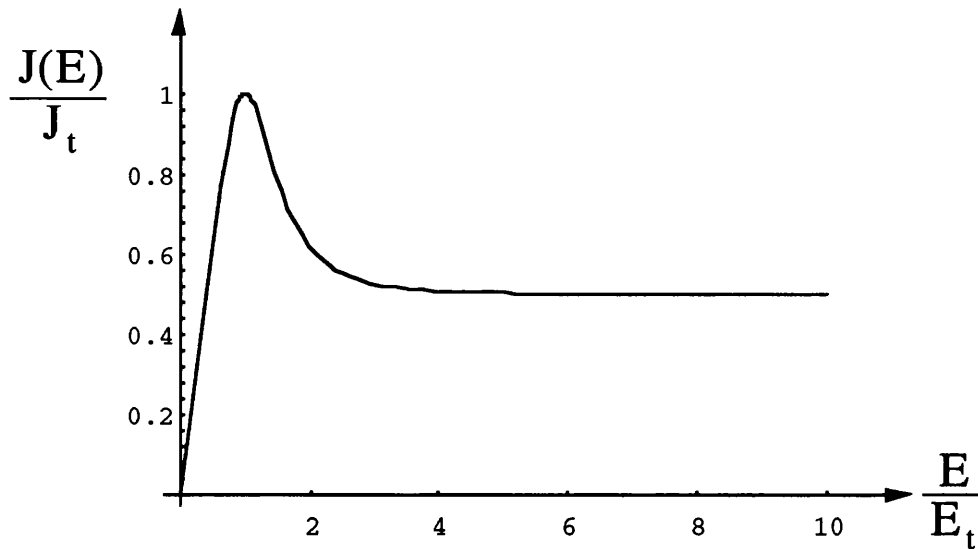


Figure 5.17

5.6 Superposition of Intervalley Transfer upon the Current -Voltage Function

The transferred electron phenomena does not automatically lead to matured spatio-temporal structures. Only under specific cathode boundary conditions can dipoles develop from monopoles, and satisfy criteria necessary for space-charge growth and propagation. The implications of intervalley transfer could be incorporated with an appropriate transition function for the voltage variable.



**Figure 5.18 :- Altukhov et al function (1978)**

Consider initially the normalised current-density-electric field function derived by Altukhov et al [69] (1978) :-

$$\frac{J}{J_{th}} = \frac{1}{2} \left[ \left( \frac{E}{E_{th}} \right)^5 + 5 \left( \frac{E}{E_{th}} \right) \right] \left[ \left( \frac{|E|}{E_{th}} \right)^5 + 2 \right]^{-1} \quad \text{---- (5.28)}$$

Its variation is shown in Figure 5.18. The function characterised the threshold nature of the fall in current-density with electric field, and provided flat saturation at fields greatly in excess of the threshold field. This formed the basis of a voltage transformation function encapsulating the transferred electron phenomena. The fall in average mobility due to inter-valley transfer was regarded as equivalent to a fall in carrier velocity through a reduction in bias electric field ( $E^*$ ) at a displacement in the active region.

$$J^* = nev(E^*) = ne \mu E^* \rightarrow ne \mu \left[ \frac{\Phi \{ \Phi^* \}}{L} \right] \quad \text{---- (5.29)}$$

The threshold / saturation nature was preserved by assuming a constant mobility, and transferring the field-dependence to the bias voltage,  $\Phi$ . In this manner, a voltage multiplier function,  $\Phi_{IVT}$ , itself a function of voltage,  $f_{IVT}[\Phi]$ , was implied such that :-

$$f_{IVT}[\Phi] = \frac{1}{2} \left\{ \frac{\left( \frac{\Phi}{\Phi_{th}} \right)^5 + 5 \left( \frac{\Phi}{\Phi_{th}} \right)}{\left( \frac{|\Phi|}{\Phi_{th}} \right)^5 + 2} \right\} \Rightarrow \Phi \rightarrow \Phi \frac{f_{IVT}[\Phi]}{\left( \frac{\Phi}{\Phi_{th}} \right)} \rightarrow \frac{\Phi}{2} \left\{ \frac{\left( \frac{\Phi}{\Phi_{th}} \right)^4 + 5}{\left( \frac{|\Phi|}{\Phi_{th}} \right)^5 + 2} \right\} \quad \text{---- (5.30)}$$

The variation of the bias field multiplier with applied voltage, at various values of the threshold field, is shown in Figure 5.19. The parameters used for Figure 5.17 previously were employed for these calculations.

## Bias Field Multiplier Function

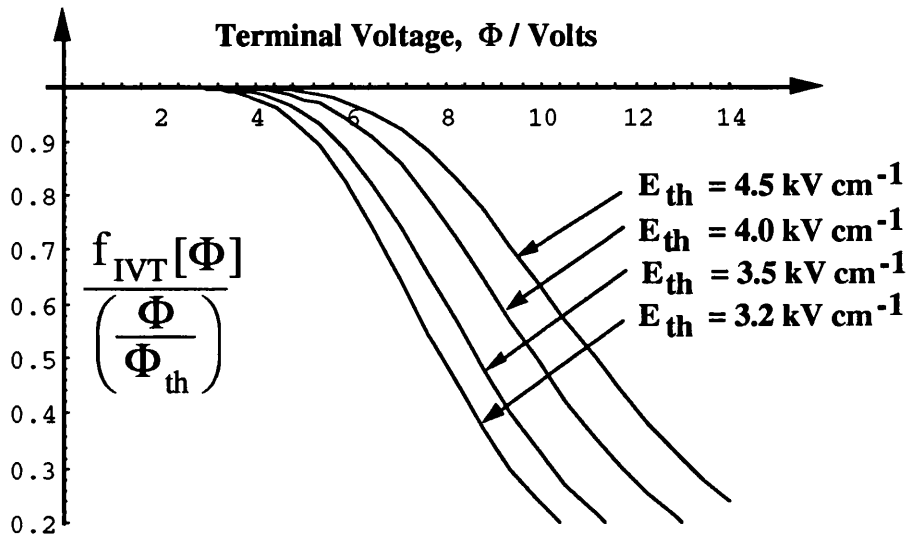


**Figure 5.19**

With this voltage transformation in effect, the theoretical current-voltage function could be rewritten as in expression (5.31). A critical comparison between theory curves, generated with and without superposition of the transferred electron phenomena, is shown in Figure 5.20.

$$I[\Phi] = G_a \eta_o \frac{\Phi}{2} \left\{ \frac{\left(\frac{\Phi}{\Phi_{th}}\right)^4 + 5}{\left(\frac{|\Phi|}{\Phi_{th}}\right)^5 + 2} \right\} \sqrt{\frac{1 + \left[ 2 \frac{L}{w_c} - \frac{\eta_1 \beta \Phi^2}{4 w_c} \left\{ \frac{\left(\frac{\Phi}{\Phi_{th}}\right)^4 + 5}{\left(\frac{|\Phi|}{\Phi_{th}}\right)^5 + 2} \right\} \tan \theta \right]^2}{\left[ 1 + 2 \frac{L}{w_c} \tan \theta \right]^2}} \left[ 1 - e^{-\frac{2L \left[ 1 + 2 \frac{L}{w_c} \tan \theta \right]}{\eta_1 \beta \Phi_{VT}^2}} \right] \quad (5.31)$$

## Comparison of Theory functions with and without the superposition of the Transferred Electron Phenomena

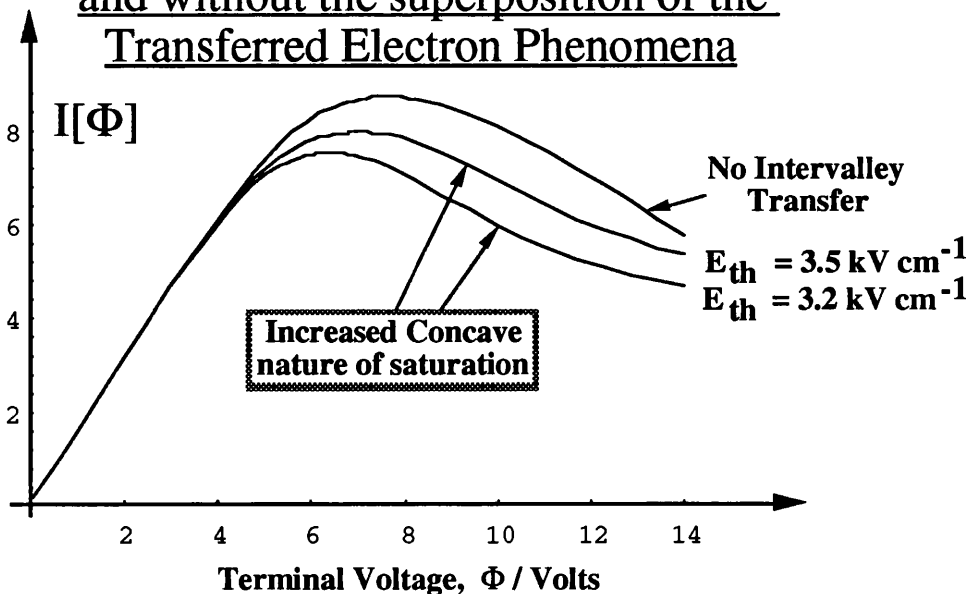


**Figure 5.20**

Primary observations included :- (1) a reduction of peak current with the introduction of inter-valley transfer ; (2) the shifting of the turning point field to a value approaching the imposed threshold for inter-valley transfer ; (3) a significant increase in the concave nature (and rate of fall) of the post-peak saturation. The rate of fall increased with the value of threshold field / voltage.

### 5.7 Disturbance Growth in a Tapered (graded area) device

In the analysis of an orthodox constant area element [19] [70], the growth of an initial field and / or carrier concentration disturbance was demonstrated, and determined as being exponential in nature. A similar analysis for the graded area element was pursued, with the main dissimilarity being the inability to assume a uniform sub-threshold electric field environment. Consider initially the unperturbed electric field distribution in a graded area element to be of the exponential decay form previously derived, where  $E_c$  = the field at the **virtual cathode** point i.e. :-

$$E[x] = E_c e^{-\frac{x}{\delta}} = \frac{\Phi}{L} \sqrt{1 - \frac{\beta_{ci} \Phi^2}{w_c} \left\{ \frac{\tan \theta}{1 + 2 \frac{L}{w_c} \tan \theta} \right\}} e^{-\frac{2x \left[ 1 + 2 \frac{L}{w_c} \tan \theta \right]}{\eta_i \beta_{ci} \Phi^2}} \quad \text{---- (5.32)}$$

The decay in field indicated that the current density was not constant in the device. The instantaneous first and second derivatives of carrier concentration and electric field were spatially dependent prior to the development of a critical disturbance. Consider two separate displacements,  $x_1$  and  $x_2$ , within the active region of the element, to be either side of a secondary imposed field and / or doping perturbation. Subsequently, it could be stated that :-

$$\frac{E[x_1]}{E[x_2]} \equiv \frac{\left( \frac{\partial E[x_1]}{\partial x} \right)}{\left( \frac{\partial E[x_2]}{\partial x} \right)} \equiv \frac{\left( \frac{\partial^2 E[x_1]}{\partial x^2} \right)}{\left( \frac{\partial^2 E[x_2]}{\partial x^2} \right)} \Rightarrow \frac{\partial E[x_2]}{\partial x} = \frac{E[x_2]}{E[x_1]} \frac{\partial E[x_1]}{\partial x} ; \frac{\partial^2 E[x_2]}{\partial x^2} = \frac{E[x_2]}{E[x_1]} \frac{\partial^2 E[x_1]}{\partial x^2} \quad \text{---- (5.33)}$$

The relations of expression (5.33) were direct results of the exponential nature of the sub-threshold electric field. To progress, the expression for total current density was reconsidered. Maxwellian displacement current was retained, since it embodied the time dependence of the electric field within the device. This time dependent component revealed the periodicity of transit time effects. By applying a 1-D Poisson's equation in this region, an expression for  $n[x]$  was derived and substituted into the current density expression. Consider :-

$$n[x] = n_o + \frac{\epsilon}{e} \frac{\partial E[x]}{\partial x} \Rightarrow J[x] = n[x] e \mu E[x] - eD \frac{\partial n[x]}{\partial x} + \epsilon \frac{\partial E[x, t]}{\partial t}$$

$$\rightarrow \frac{J[x]}{\epsilon} = \frac{n_o e \mu}{\epsilon} E[x] + \mu E[x] \frac{\partial E[x]}{\partial x} - D \frac{\partial^2 E[x]}{\partial x^2} + \frac{\partial E[x, t]}{\partial t} \quad \text{--- (5.34)}$$

It was necessary to evaluate this expression at the two arbitrary displacements in the active region,  $x_1$  and  $x_2$ , considered previously. The subsequent expressions could then be equated and a difference expression determined as follows :-

$$\begin{aligned} J[x_1] &\rightarrow J_1; \quad J[x_2] \rightarrow J_2; \quad E[x_1] \rightarrow E_1; \quad E[x_2] \rightarrow E_2 \\ \frac{J_1}{\epsilon} &= \frac{n_o e \mu}{\epsilon} E_1 + \mu E_1 \frac{\partial E_1}{\partial x} - D \frac{\partial^2 E_1}{\partial x^2} + \frac{\partial E_1}{\partial t}; \quad \frac{J_2}{\epsilon} = \frac{n_o e \mu}{\epsilon} E_2 + \mu E_2 \frac{\partial E_2}{\partial x} - D \frac{\partial^2 E_2}{\partial x^2} + \frac{\partial E_2}{\partial t} \\ \Rightarrow \left[ \frac{J_1 - J_2}{\epsilon} \right] &= \frac{n_o e \mu}{\epsilon} [E_1 - E_2] + \frac{\partial}{\partial t} [E_1 - E_2] + \mu \left( E_1 \frac{\partial E_1}{\partial x} - E_2 \frac{\partial E_2}{\partial x} \right) - D \left( \frac{\partial^2 E_1}{\partial x^2} - \frac{\partial^2 E_2}{\partial x^2} \right) \quad \text{--- (5.35)} \end{aligned}$$

To rationalise the difference expression in (5.35), it was necessary to recall the relations defined for the first and second partial derivatives quoted in expression (5.33). It could be asserted that :-

$$\left[ \frac{J_1 - J_2}{\epsilon} \right] = \frac{n_o e \mu}{\epsilon} [E_1 - E_2] + \frac{\partial}{\partial t} [E_1 - E_2] + \mu \left( \frac{E_1^2 - E_2^2}{E_1} \right) \frac{\partial E_1}{\partial x} - D \left( \frac{E_1 - E_2}{E_1} \right) \frac{\partial^2 E_1}{\partial x^2} \quad \text{--- (5.36)}$$

The particular case of the exponential decay of electric field with the spatial variable permitted simple expressions for the actual first and second partial derivatives of electric field, with respect to  $x$ , to be derived. Thus :-

$$\begin{aligned} \frac{\partial E_1}{\partial x} &= -\frac{1}{\delta} E_1; \quad \frac{\partial^2 E_1}{\partial x^2} = \frac{1}{\delta^2} E_1; \quad \text{if } E_1 \approx E_2 \Rightarrow E_1^2 - E_2^2 \approx 2E_1[E_1 - E_2] \\ \Rightarrow \left[ \frac{J_1 - J_2}{\epsilon} \right] &= \frac{n_o e \mu}{\epsilon} [E_1 - E_2] + \frac{\partial}{\partial t} [E_1 - E_2] - \frac{2\mu E_1 [E_1 - E_2]}{\delta} - \frac{D [E_1 - E_2]}{\delta^2} \quad \text{--- (5.37)} \end{aligned}$$

The difference expression,  $(E_1 - E_2)$ , was factorised from expression (5.37) and further reduced :-

$$\begin{aligned} \frac{\partial}{\partial t} [E_1 - E_2] &= \left[ \frac{J_1 - J_2}{\epsilon} \right] - \left( \left[ \frac{n_o e \mu}{\epsilon} \right] - \frac{2\mu E_1 e^{-\frac{x}{\delta}}}{\delta} - \frac{D}{\delta^2} \right) [E_1 - E_2] \\ \rightarrow \frac{\partial}{\partial t} [E_1 - E_2] &= - \left( \frac{1}{\tau_{\text{taper}}} \right) [E_1 - E_2] + \left[ \frac{J_1 - J_2}{\epsilon} \right] \quad \text{--- (5.38)} \end{aligned}$$

The remaining stage in the deduction was to integrate both sides of (5.38) with respect to  $x$ , over the limits  $x_o - w/2$  and  $x_o + w/2$ , where  $x_o$  was deemed to be the phenomenological centre of the arbitrary disturbance, and  $w$  the width of the perturbed region ( Figure 5.21). The spatial integral of  $(E_1 - E_2)$  across the extent of the perturbation is, by definition, an expression for the net **Voltage** content of the disturbance. This concept could then be used to establish the time variance associated with the **magnitude** of this perturbation. Thus :-

$$\frac{d}{dt} \int_{x_o - \frac{w}{2}}^{x_o + \frac{w}{2}} [E_1 - E_2] dx = \int_{x_o - \frac{w}{2}}^{x_o + \frac{w}{2}} \left[ \frac{J_1 - J_2}{\epsilon} \right] dx - \left( \frac{1}{\tau_{\text{taper}}} \right) \int_{x_o - \frac{w}{2}}^{x_o + \frac{w}{2}} [E_1 - E_2] dx \quad \text{---- (5.39)}$$

$$\Rightarrow \frac{d\Phi_d}{dt} = - \frac{\Phi_d}{\tau_{\text{taper}}} + \int_{x_o - \frac{w}{2}}^{x_o + \frac{w}{2}} \left[ \frac{J_1 - J_2}{\epsilon} \right] dx \quad \text{where} \quad \tau_{\text{taper}} = \left( \frac{1}{\tau_{\text{nt}}} - \frac{1}{\tau_{\text{corr}}} \right) \quad \text{---- (5.40a)}$$

$$\tau_{\text{nt}} = \frac{\epsilon}{n_o e \mu} ; \quad \tau_{\text{corr}} = \delta \left( 2\mu E_c e^{-\frac{L}{2\delta}} - \frac{D}{\delta} \right)^{-1} \quad \text{---- (5.40b)}$$

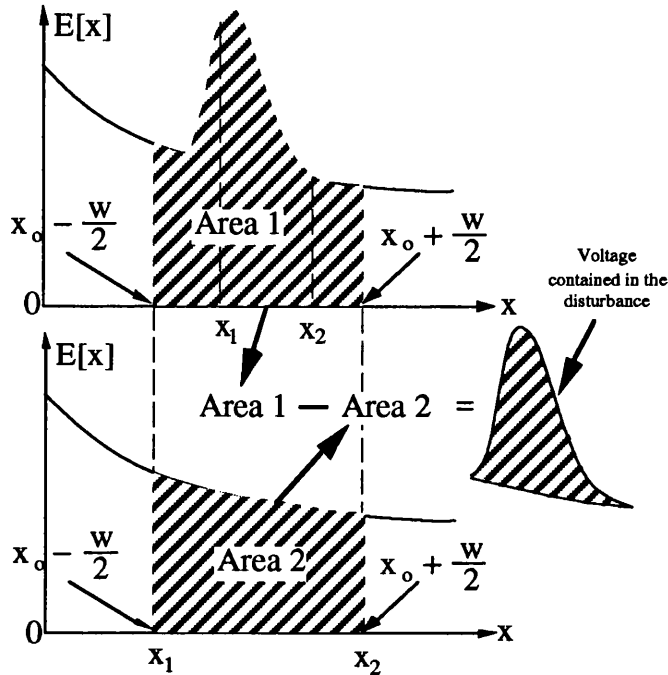


Figure A

Figure 5.21 :- Voltage content of an arbitrary disturbance

This process introduced the concept of the **characteristic time constant**  $\tau_{\text{taper}}$ , which governs the temporal evolution or spatial growth of any instability or disturbance in the region. If the taper in the device was gradual, and the initial disturbance small, then expression (5.40) simplified, with the formal solution to this first order ordinary differential equation being that of an exponential decay / growth as indicated :-

$$J_1 \rightarrow J_2 \Rightarrow \int_{x_o - \frac{w}{2}}^{x_o + \frac{w}{2}} \left[ \frac{J_1 - J_2}{\epsilon} \right] dx \rightarrow 0 \Rightarrow \frac{d\Phi_d}{dt} = - \frac{\Phi_d}{\tau_{\text{taper}}} \Rightarrow \Phi_d(t) = \Phi_d \Big|_{t=0} e^{-\frac{t}{\tau_{\text{taper}}}} \quad \text{--- (5.41)}$$

The characteristic time constant  $\tau_{\text{taper}}$ , was dissociated into two constituents, i.e. that time constant governing growth in an ungraded device, and a further **correction** time constant introduced by the tapered nature of the active region. For normal operating devices with typical parameters (e.g.  $n_o = 10^{15} - 10^{16} \text{ cm}^{-3}$ ), for satisfaction of nl product criteria and others, it was found that :-

$$\tau_{\text{taper}} = \frac{1}{\mu \left( \frac{n_o e}{\epsilon} - \frac{1}{\delta} \left[ 2E_c e^{-\frac{L}{2\delta}} - \frac{kT}{e\delta} \right] \right)}; \text{ if } \frac{n_o e}{\epsilon} \gg \frac{1}{\delta} \left[ 2E_c e^{-\frac{L}{2\delta}} - \frac{kT}{e\delta} \right] \Rightarrow \tau_{\text{taper}} \approx \frac{\epsilon}{n_o e \mu} \equiv \tau_{\text{nt}}$$

----- (5.42)

Area grading, increasing from cathode to anode, modified the characteristic time constant governing the growth of an arbitrary disturbance in the active region. It also implicitly indicated that **Transit mode** operation was sustainable in such a device. Expression (5.42) indicated that ordinarily the time constant in the graded (tapered) device approached that for a non-graded element. The magnitude of the corrective time constant induced by grading was comparatively large, and would not have any significant implications in one transit time-period (which was appreciably smaller).

### 5.8 Fundamental voltage dependency of transit distance (frequency)

Previously, it was implicitly assumed that the background field must remain above some critical value to sustain a self-organised disturbance. Below this value, the disturbance would not survive to the natural collapsing point (i.e anode). Subsequently, the spatial limit within the active region that this critical value of field,  $E_s$ , was reached could then be termed the **virtual anode point** (Figure 5.23). This was a direct consequence of the exponentially decaying field. It was considered to be that field at which insufficient inter-valley transfer took place to provide net NDM within the active region.

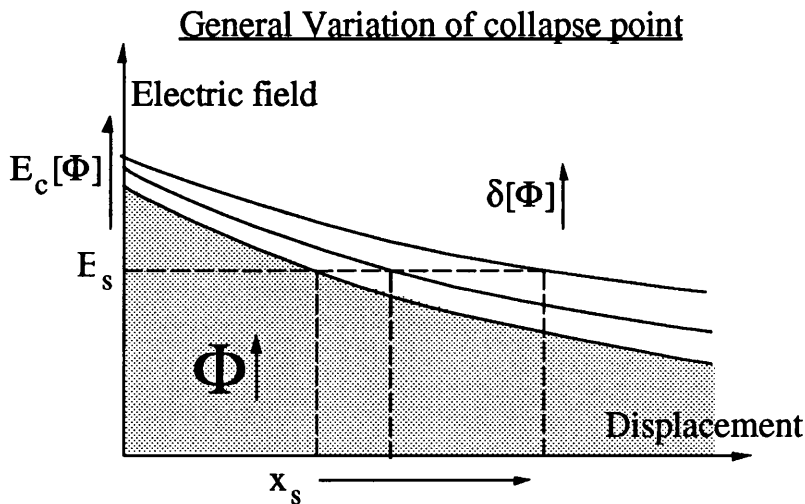


**Figure 5.23 :- Virtual Anode point**

Area grading had the effect of inducing a form of primitive voltage-controlled oscillation frequency. The exact functional dependence was complicated by the variability of the cathode field. It was permitted to vary such that net voltage criteria were satisfied. To analyse this dependency, the following was considered :-

$$E(0) = E_s \Rightarrow E_c[\Phi] e^{-\frac{x_s}{\delta[\Phi]}} \rightarrow x_s = \delta[\Phi] \ln \left[ \frac{E_c[\Phi]}{E_s} \right] \dots \dots (5.43)$$

A simple expression for the net oscillation frequency in the device was derived from expression (5.43), introducing the fundamental voltage dependence of this frequency :-

$$f[\Phi] = \frac{v_{dis}}{\delta[\Phi] \cdot \ln \left[ \frac{E_c[\Phi]}{E_s} \right]}; \quad \delta[\Phi] = \frac{\beta_{ci} \Phi^2}{2 \left[ 1 + 2 \frac{L}{w_c} \tan \theta \right]} \dots \dots (5.44)$$

where the electric field,  $E[x, \Phi]$ , had the form defined previously :-

$$E[x] = E_c e^{-\frac{x}{\delta}} = \frac{\Phi}{L} \sqrt{1 - \frac{\beta_{ci} \Phi^2}{w_c} \left\{ \frac{\tan \theta}{1 + 2 \frac{L}{w_c} \tan \theta} \right\}} e^{-\frac{2x \left[ 1 + 2 \frac{L}{w_c} \tan \theta \right]}{\eta_i \beta_{ci} \Phi^2}} \dots \dots (5.45)$$

Substituting expression (5.45) into that for frequency in (5.44) and rearranging, yielded the following complex voltage relation, evaluated at  $\Phi = \Phi_0$  :-

$$f[\Phi_0] = \left\{ \ln \left[ \frac{\Phi_0}{LE_s} \sqrt{1 - \frac{\beta_{ci} \Phi_0^2}{w_c} \left\{ \frac{\tan \theta}{1 + 2 \frac{L}{w_c} \tan \theta} \right\}} \right] \right\}^{-1} \frac{\beta_{ci} \Phi_0^2}{2 v_{dis} \left[ 1 + 2 \frac{L}{w_c} \tan \theta \right]} \dots \dots (5.46)$$

To evaluate the change in frequency expected from the graded element when a small perturbation of the terminal voltage is applied to the device, the total derivative of the frequency function with respect to  $\Phi$  was required. If the changes are small enough, then a simple approximation for the frequency change, using the first derivative of frequency (expression 5.44), could be made such that :-

$$\frac{df[\Phi]}{d\Phi} \rightarrow \frac{(f + \Delta f) - f}{(\Phi + \Delta\Phi) - \Phi} \approx \frac{\Delta f}{\Delta\Phi} \Rightarrow \Delta f \approx \frac{df[\Phi]}{d\Phi} \Delta\Phi$$

$$\frac{df[\Phi]}{d\Phi} = - \left[ \frac{2}{\Phi^3} \ln \left\{ \frac{E_c[\Phi]}{E_s} \right\} + \frac{1}{\Phi^2 E_c[\Phi]} \frac{dE_c[\Phi]}{d\Phi} \right] \left( \ln \left\{ \frac{E_c[\Phi]}{E_s} \right\} \right)^{-2} \dots \dots (5.47)$$

The Global terminal voltage,  $\Phi$ , accommodated the total voltage drop incurred across the three identifiable regions / entities in the sample. These were (a) the voltage drop across the statutory depletion layer,  $\Phi_{dep}$ ; (b) the voltage dropped across the unperturbed background electric field {NDR} region,  $\Phi_0$ ; (c) the voltage content of any arbitrary disturbance (assumed small),  $\Phi_{dis}$ . For constant voltage operation (Figure 5.24), the total sum of these potential drops must be constant such that :-

$$\Phi = \Phi_{dep} + \Phi_{dis} + \Phi_0 \dots \dots (5.48)$$

where from expression (5.43) it could be stated further that :-

$$\Phi_{dis} = \hat{\Phi}_{dis} e^{\frac{t}{\tau_{taper}}} \rightarrow \hat{\Phi}_{dis} e^{\frac{\mu_{NDR} L_{NDR}}{v_{dis}} \left( \frac{n_o e}{\epsilon} - \frac{1}{\delta[\Phi]} \left[ 2E_c[\Phi] e^{-\frac{L_{NDR}}{2\delta[\Phi]}} + \frac{kT}{e\delta[\Phi]} \right] \right)} \quad \text{--- (5.49)}$$

### Disturbance Development in Tapered devices with Exponentially-decaying field

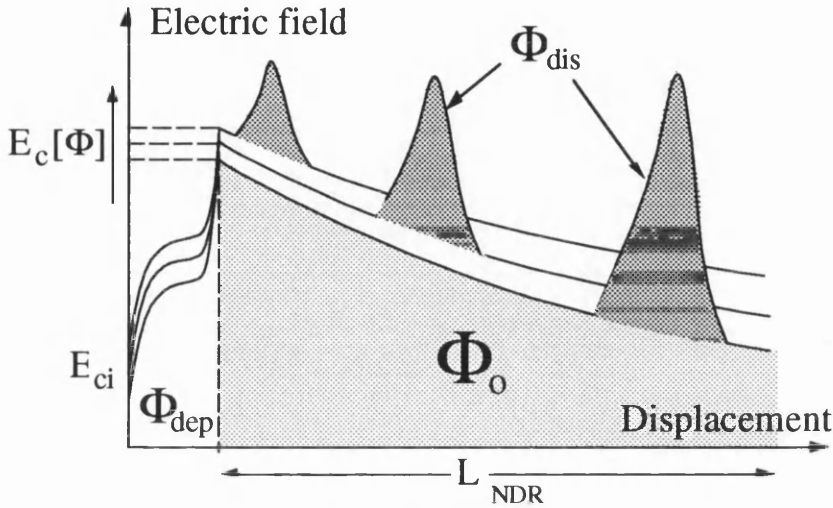


**Figure 5.24**

With the expression for disturbance voltage content given in (5.49), the overall frequency relation with voltage was reduced to the following :-

$$f[\Phi] = \frac{\left( \frac{2v_{dis} \left[ 1 + 2\frac{L}{w_c} \tan \theta \right]}{\beta_{ci} \left[ \Phi - \hat{\Phi}_{dis} e^{\frac{\mu_{NDR} L_{NDR}}{v_{dis}} \left( \frac{n_o e}{\epsilon} - \frac{1}{\delta[\Phi]} \left[ 2E_c[\Phi] e^{-\frac{L_{NDR}}{2\delta[\Phi]}} + \frac{kT}{e\delta[\Phi]} \right] \right)} - \Phi_{dep} \right]^2} \right)}{\ln \left[ \frac{\Phi - \hat{\Phi}_{dis} e^{\frac{t}{\tau_{taper}}} - \Phi_{dep}}{LE_s} \right]} \sqrt{1 - \frac{\beta_{ci} \left( \Phi - \hat{\Phi}_{dis} e^{\frac{t}{\tau_{taper}}} - \Phi_{dep} \right)}{w_c \left\{ \frac{1 + 2\frac{L}{w_c} \tan \theta}{\tan \theta} \right\}}} } \quad \text{--- (5.50)}$$

The natural **limiting linewidth** of spectral peaks, due to oscillation, is determined by noise signals generated by the resistive fraction of the device, such that **Johnson Noise** dominates, in accordance with (Figure 5.25) :-

$$\Delta f_{Noise} \approx \frac{df[\Phi_o]}{d\Phi} \sqrt{kTR^+ f[\Phi_o]} \quad \text{--- (5.51)}$$

Shoji [68] demonstrated experimentally that the fundamental oscillation frequency in practical tapered TEDs reduced with increasing terminal voltage (Figure 5.24). The exponential decay of the background electric field distribution theoretically predicted accommodates these observations. All of the factors in expression (5.50) are positive, indicating that the rate of change of frequency is negative with

increasing voltage. Evaluations of the frequency expressions above also lead to decreasing frequency with increasing voltage, hence confirming the observations of Shoji [68] and others. A similar voltage dependency of fundamental frequency has been observed with non-tapered devices. This corresponds to the case of near-linearity and high characteristic decay lengths. The same principles could be demonstrated to be equally valid in all these cases, since the electric field is never perfectly uniform or flat in doped active regions.

### Example of Spectral Voltage Dependence of Tapered Devices

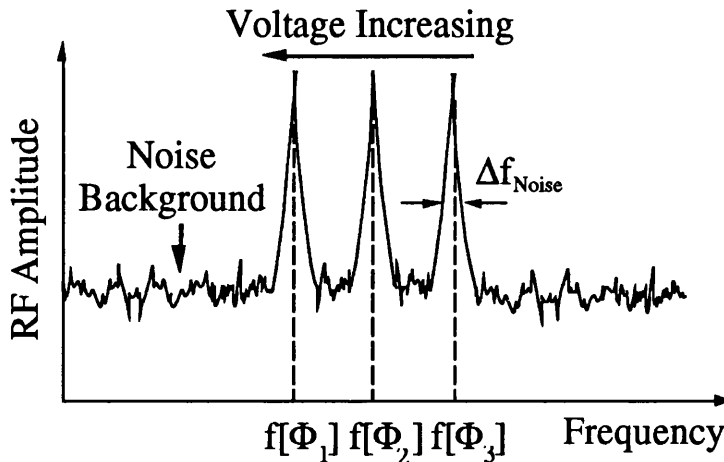


**Figure 5.25**

### 5.9 Conclusions

An expression for the electric field distribution, within tapered and non-tapered n-GaAs elements, was derived from fundamental principles. The field variation was shown to decay exponentially for tapered elements, with the concept of the characteristic decay length being introduced. By initially assuming that no spatio-temporal structures were present, a formula for the D.C. current-voltage variation in such elements was derived. The presence of disturbances in carrier concentration /electric field were superposed upon the trace through either corrections to the voltage for momentum space transfer, or by the discontinuity multiplier. This multiplier was an arbitrary function of the appropriate form necessary to generate a controlled-sharp discontinuity associated with dipole formation. However, it was possible to relate this discontinuity function to the predicted time-rate of change of voltage exterior to a growing disturbance.

The final  $I-\Phi$  function was shown to be constituted of three essential multiplied factors. The first accommodated the initial linear increase in current at lower fields ( $< 1 \text{ kVcm}^{-1}$ ). The second quantified the direct influence of the tapered nature of the conducting region, and the third generated the natural

## Kilburn's Theoretical Current-Voltage Function (Full Solution)

$$\begin{aligned}
 I[\Phi] &= \frac{n_o e \mu_{\text{NDR}} h w_a}{2\sqrt{2}L} \eta_o \Phi \left[ \frac{\left(\frac{\Phi}{\Phi_{\text{IVT}}}\right)^5 + 5\left(\frac{\Phi}{\Phi_{\text{IVT}}}\right)}{\left(\frac{\Phi}{\Phi_{\text{IVT}}}\right)^5 + 2} \right] \\
 1 - \left\{ 1 - \frac{\hat{Q}_{\text{dis}} e^{\frac{\mu_{\text{NDR}} v_{\text{dis}}}{L} \left[ \frac{n_o e}{\epsilon} - \frac{1}{\delta[\Phi]} \left( 2E_c[\Phi] e^{-\frac{L}{2\delta[\Phi]}} - \frac{kT}{e\delta[\Phi]} \right) \right]}}{F_1[\Phi] \cdot F_2[\Phi] \cdot F_3[\Phi]} \right\} e^{-\left(\frac{\Phi_x}{\Phi}\right)^{100}} \\
 &\left\{ \mu_{\text{NDR}} \left[ \frac{n_o e}{\epsilon} - \frac{1}{\delta[\Phi]} \left( 2E_c[\Phi] e^{-\frac{L}{2\delta[\Phi]}} - \frac{kT}{e\delta[\Phi]} \right) \right] \right\} \\
 \times &\left\{ \frac{1 + \left[ \frac{2\frac{L}{w_c} - \frac{\eta \left[ \left(\frac{\Phi}{\Phi_{\text{IVT}}}\right)^5 + 5\left(\frac{\Phi}{\Phi_{\text{IVT}}}\right) \right]^2}{\left(\frac{\Phi}{\Phi_{\text{IVT}}}\right)^5 + 2} \beta_{\text{ci}} \Phi^2}{w_c} \right] \tan \theta}{1 + 2\frac{L}{w_c} \tan \theta} \right\} \\
 \times &\left[ 1 - \text{Exp} \left( - \frac{2L \left[ 1 + 2\frac{L}{w_c} \tan \theta \right]}{\eta \beta_{\text{ci}} \left[ \frac{\left(\frac{\Phi}{\Phi_{\text{IVT}}}\right)^5 + 5\left(\frac{\Phi}{\Phi_{\text{IVT}}}\right) \right]^2}{\left(\frac{\Phi}{\Phi_{\text{IVT}}}\right)^5 + 2} \Phi^2} \right) \right]
 \end{aligned}$$

The following Phenomena have been incorporated :-

- (1) Kroemer's crossover field concept ;
- (2) Momentum-space intervalley transfer ;
- (3) Spatio-temporal Growth determination of dipole discontinuity depth ;
- (4) Time constant correction due to tapered active region.

Figure 5.27

"concave" saturation observed in elements of this type at higher fields ( $> 3 \text{ kVcm}^{-1}$ ). The function suggested that "concave" saturation was a natural result of the exponential decay of the electric field within the active region. This saturation was reinforced by the introduction of real-time intervalley transfer, ordinarily expected in devices operating in hybrid modes (i.e. in the absence of sharp discontinuities from dipoles). It was also possible to accommodate Kroemer's crossover field principle (Chapter 2 [19] [20]) directly in the discontinuity multiplier, through the threshold voltage for activity,  $\Phi_{th}$ .

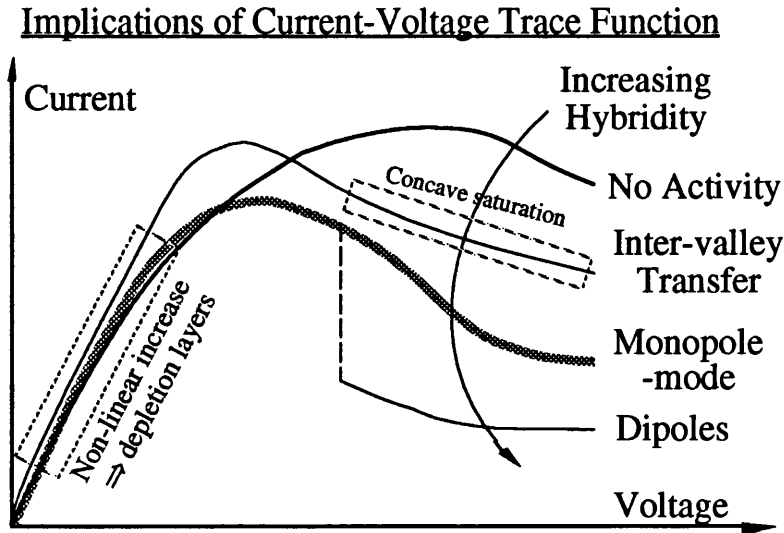


Figure 5.26 provides a schematic summary of the implications of current-voltage traces, as indicated by the function derived (Full function Figure 5.27). Purely convex saturation implied no transfer activity of the electron bulk, saturation occurred as a consequence of the exponentially decaying electric field. The emergence of significant concave saturation was indicative of momentum-space transfer, and in some cases plasma waves or propagating monopoles [19]. Sharp discontinuities signified dipole formation at cross-over field dictated bias fields (terminal voltages). Finally, it was concluded that the derived current-voltage function, and the constant current criteria imposed in its derivation, were of significant predictive worth. The proximity of its functional output was employed in a comparison with real data, whereby the significance of the dimensionless  $\eta$  coefficients was revealed.

# Chapter 6

## Device Analysis and Experimentation

This chapter details analysis and experimentation intended to assess the possibility of oscillation (and hence modulation) in fabricated devices. Through this analysis, the benefits of structural modifications were observed. The influence of the cathode boundary conditions in planar devices was investigated using the **theoretical current-voltage function**. It concurred with the hypotheses of Kroemer [20] and others [21] [22] [71] [72] (Chapter 2).

### 6.1 D.C. Current - Voltage traces in Transferred Electron Devices

It has been acknowledged by many researchers, that current-voltage profiles indicate the presence of dipole disturbances, and associated oscillatory behaviour. The appearance of these disturbances was regarded by Hakki [73], Foyt and McWhorter [74], Kroemer [19], Kowalsky et al [75] and others, as the instigating factor in either the sharp or gradual fall in mean current at the terminals observable in the current voltage traces. The fall in mean current flowing in the element was attributed to the consumption of voltage, and the reduction of the electric field exterior to the disturbance. Analysis of their qualitative content was sought by Bakanas (1991) [76], Kostylev (1978) et al [75], Altukhov (1978) et al [69] amongst others, and most recently Bonilla and Higuera (1992) [21] [22], and Usanov et al (1992) [78]. Their assessment was based on incidences of correlation between operating regime and trace-form. In 1978, Kostylev et al [77] introduced the notion of a "good" diode as one where the current-voltage trace increased ohmically (linearly) until it met with a sudden but smooth decrease in mean current and subsequent saturation.

In 1978, electrical instability in semiconductors with NDC due to simultaneous heating of electrons by static and alternating electric fields was studied by Altukhov et al [69]. The work of the group concentrated on the effects of static and microwave fields on the appearance of coherent disturbances, and the modes in which they predominate. They noted that the threshold value of static voltage, at which propagating dipoles appeared, was dependent upon the regime used to connect the sample to the source of microwave power. The relevance of microwave-biassed operation for the accessing of Limited Space Charge Accumulation (LSA) mode [79] [80] [81] in these devices was assessed. This was performed in view of the suppression of dipole disturbance oscillations observed by

previous researchers under the same circumstances, (Hashizume and Kataoka [82], 1970). Altukhov et al [69] used mathematical modelling and calculations to confirm that spontaneous interspersant oscillations occurred, rendering LSA mode unachievable in these samples. The current-voltage characteristic for static fields was almost identical in form (i.e. linear ohmic portion, curved section due to stationary states, current fall with dipole disturbance formation) to that derived experimentally by Kostylev et al [77] and others. Substantial and abrupt current saturations were observed by Kowalsky and Schlachetzki in 1983 in experimental  $\text{In}_{0.53}\text{Ga}_{0.47}\text{As}$  [75], in addition to that measured by Takeda et al [83] and Zhao et al [84]. Modern research into current-voltage trace relevance was provided by Usanov et al [79], and the extensive non-linear dynamic system approach used by Bonilla and Higuera [21] [22], both in 1991. Usanov et al recognised the role of these traces in indicating modes of operation.

Bonilla and Higuera [21] [22] verified previous simplified hypotheses. They considered "Stationary states, stability and boundary conditions in finite GaAs samples", followed by oscillatory states in long samples. Their analysis was derived from a two-independent variable non-linear dynamic system approach to the internal semiconductor dynamics. They constructed a detailed phase portrait of the system with the spatial rate of change of electric field versus electric field. The second paper in the series dealt with the evolution of stationary and steady states, and the formation of oscillatory disturbances in "long" n-GaAs samples. The role of the "ohmic" contacts was assessed. Normalised transport equations were used to analyse stationary states and travelling waves, and the influence of the cathode contact resistivity. As was the case with classic works [18] [19] [33] [34], the shape of the dipole disturbance was formulated by Bonilla and Higuera. A second type of propagating wave, a monopole, was revealed by numerical simulations. The charge dipoles were solitary waves of permanent form and constant velocity. Pure Kroemer-type [19] accumulation layers (monopoles) were also suggested.

In addition to this, the resistivity of the ohmic contact interior regions influenced the operation of the device. Numerical calculations indicated that some critical value of contact resistivity existed, above which fully-matured dipole disturbances predominated. In contrast, monopoles formed in the sample where contact resistivities were below this critical value (low resistivity). It was demonstrated that two-layer dipoles propagated at a constant velocity, while monopoles travelled with a variant velocity. All of the criteria defined by Kroemer [19] and Shaw et al [43] for nucleation at the cathode

were met by the numerical transport equations used by Bonilla and Higuera. The resistivity values of the cathode ohmic contacts were observed to generate the non-uniform pre-threshold electric field characterising "imperfect" cathode boundary conditions.

## 6.2 Practical DC Current-voltage Characteristics

For planar devices (Figure 6.1), with contacts in the same epitaxial plane, the annealing conditions were assumed to be identical for both contacts. The same series resistance was appropriated to each of these contacts. An estimate of the electrical resistance of the bulk could be obtained by approximating the active region n-GaAs crystal as a standard cuboid of known dimensions (Figure 6.2). For a region of length  $a$ , width  $b$  and depth  $c$ , the volume of the region was simply  $abc$ , the cross-sectional area  $bc$ , such that the resistance could be evaluated as follows :-

$$R = \frac{\rho L}{A} = \frac{L}{\sigma A} \equiv \frac{a}{n_o e \mu_e bc} \text{ ---- (6.1)}$$

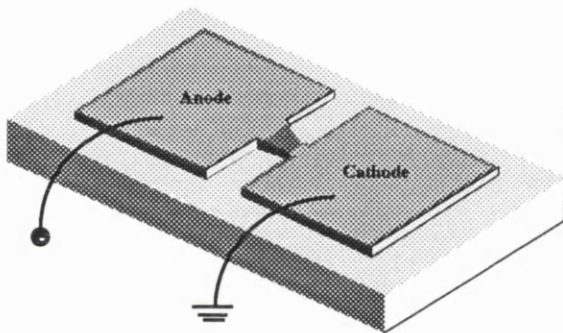


**Figure 6.1 :- Typical planar device**

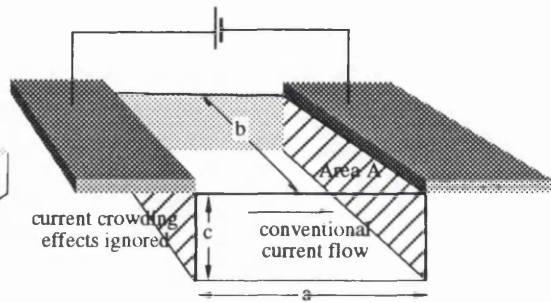


**Figure 6.2 :- Resistance estimation**

The influence of charge crowding effects in the vicinity of the contacts, and the sizeable discontinuity due to the waveguide intersection, were ignored in the first instance. Several wafers, A297, B157 and B230, were grown to fabricate planar devices. Common device dimensions were 20  $\mu\text{m}$  intercontact separation, 50  $\mu\text{m}$  contact width (for earlier planar devices) and wafer layer depths 4 - 6  $\mu\text{m}$ . The latter two dimensions were fixed for a particular mask design set, with only the intercontact separations being varied between devices. DC current-voltage traces, swept at a variety of rates and number of constituent points, were obtained with a Hewlett-Packard HP4145A sweep analyzer. The main objective of these traces was to assess the opportunity for coherent oscillations in the devices. Both charge monopoles and dipoles, as indicated by Bonilla and Higuera [21] [22] and others, were possible. Profiles indicating dipole disturbance propagation varied from sharp vertical discontinuities, to gradual ("concave") falls in mean current beyond some threshold.

Optimum conditions for low resistivity annealing were 390 °C for 60 seconds with a 10 second rise time. Ohmic contact formation was to standard layers doped at  $10^{18} \text{ cm}^{-3}$  with silicon donors to generate n-type material. The exact role of the nickel atoms in the gold-germanium eutectic formation was not known in detail, and remained a candidate for modification in the recipe.

Profiles 1, 2 and 3 depicted the subtle variations observed with modified annealing conditions, while retaining the layer thickness prescribed by the "Mikeohm" recipe for all these samples. Combinations of lower temperature and longer duration, or higher temperature and shorter duration were used to anneal the samples. Intermediate values of temperature and duration were assessed in addition. The devices shown typified those obtained with devices of their specific parameters (physical dimensions and annealing conditions). Further information was extracted from in excess of 20 fabrication runs as shown (30-50 devices per chip). These included peak power dissipated with low-field ohmic resistance (Figure 6.3) and the low-field ohmic resistance versus peak current (Figure 6.4).

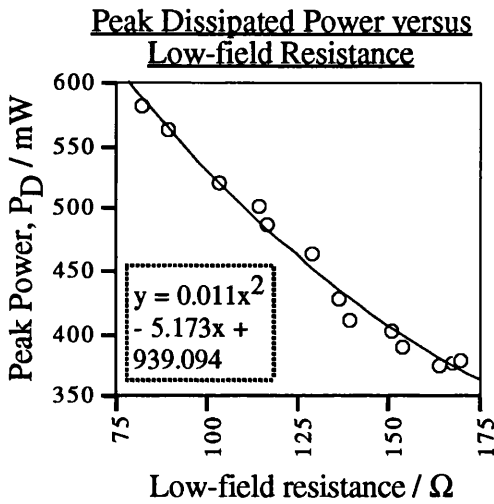


**Figure 6.3**

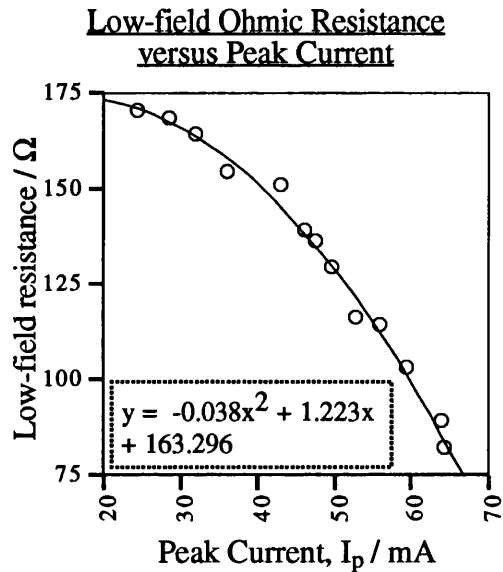
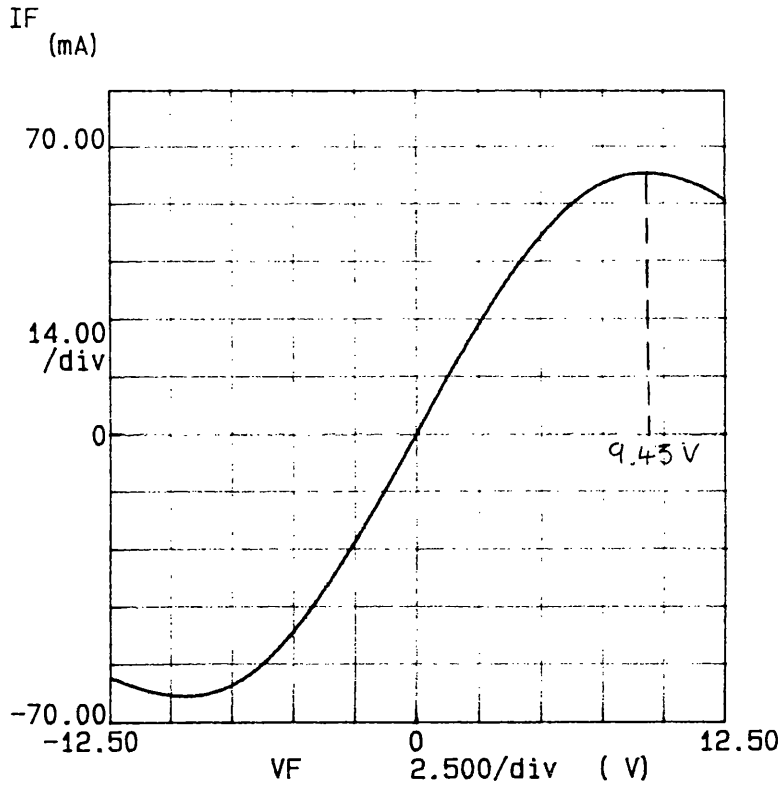


**Figure 6.4**

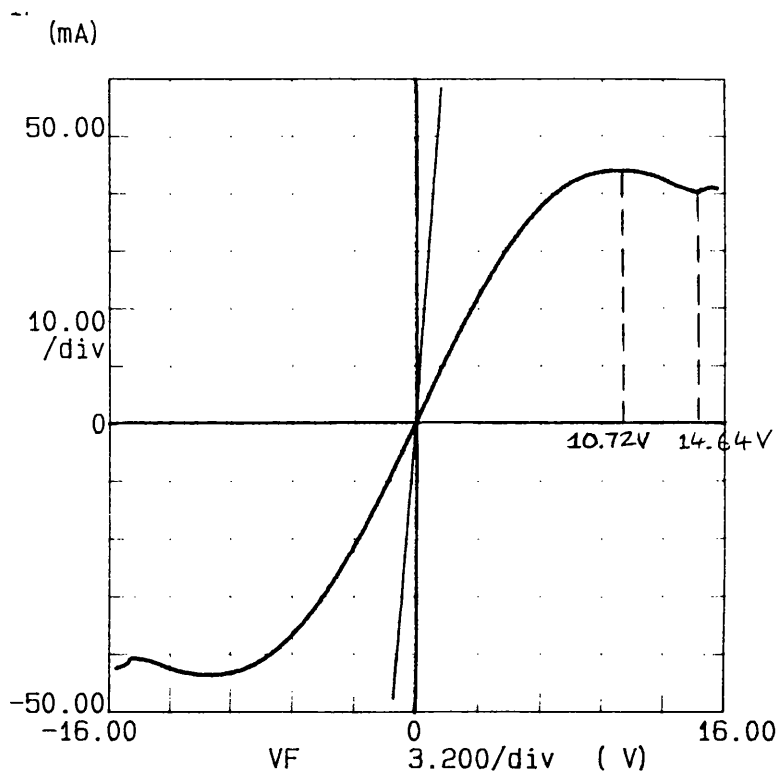
Curve 1 (375 °C for 60 secs) was characterised by gradual saturation, which was not accompanied by any secondary changes in terminal current. This suggested that no oscillatory behaviour occurred prior to breakdown of the contacts. For Type A devices (Figure 6.5), the higher annealing temperature coupled with a longer duration of annealing was deemed unsuitable for encouraging the injection conditions necessary for dipole disturbances. The gradual saturation in current was due to the field taper in the active region.

Typical trace for Type A device : 60 secs. @ 360 °C



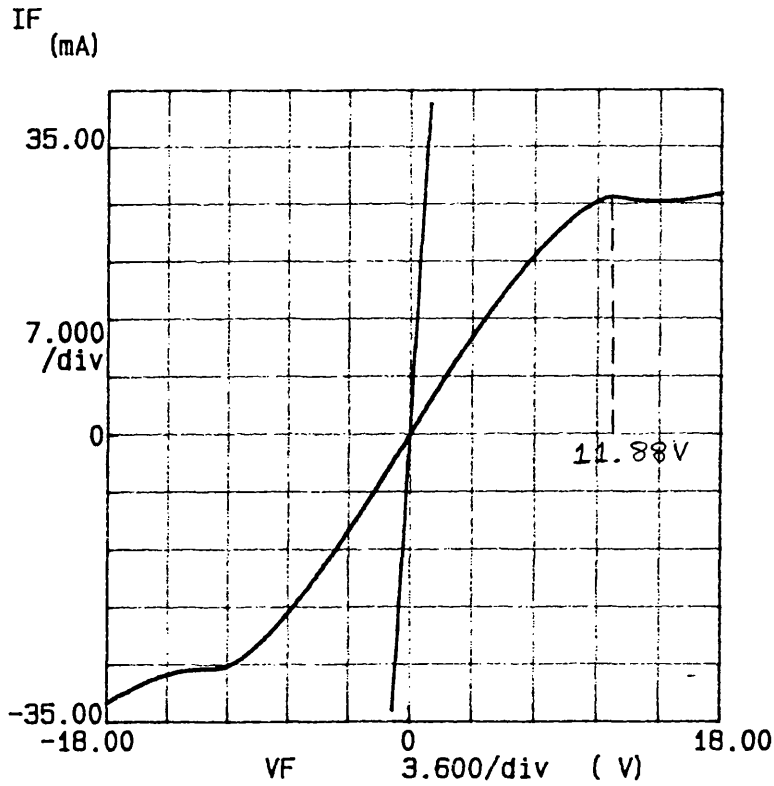
Curve 1 :- convex trace with "no activity"

Typical trace for Type B device : 45 secs. @ 375 °C



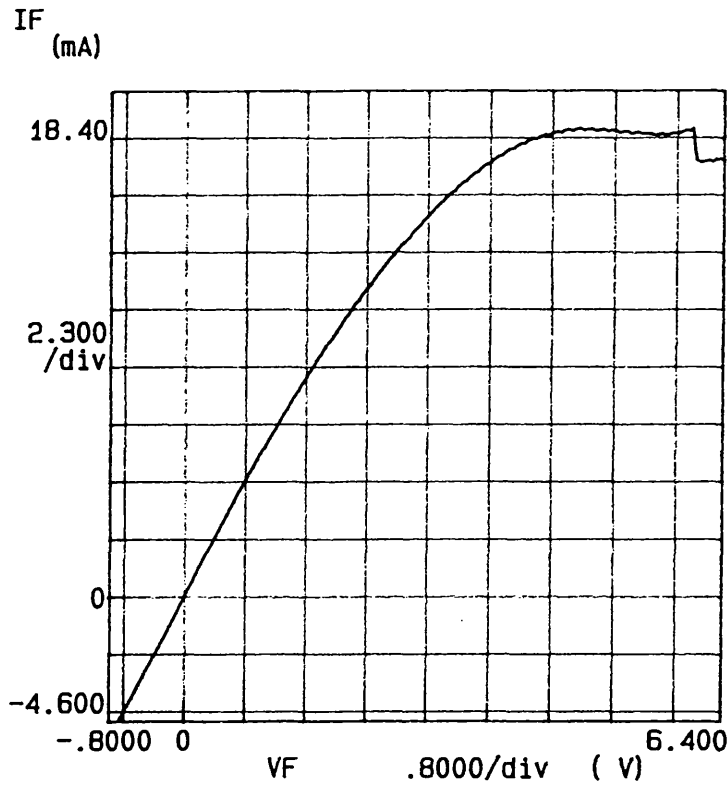
Curve 2 :- small inflexions appear in curves

Typical trace for Type C device : 30 secs. @ 390 °C



Curve 3 :- inverted current recovery

Sharp discontinuities in traces for Type C annealing



Curve 4 :- Discontinuity at approximately 3.2 kVcm<sup>-1</sup>

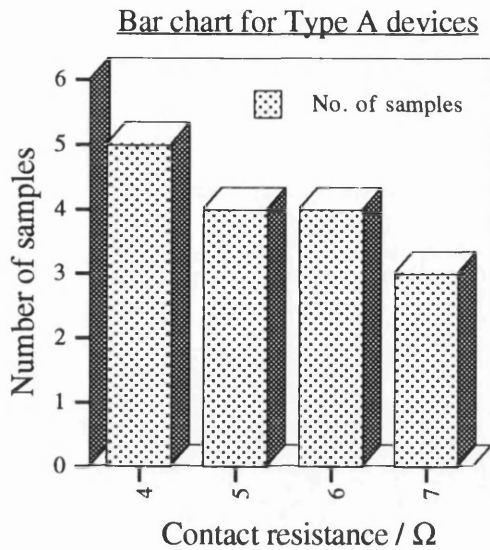


**Figure 6.5**

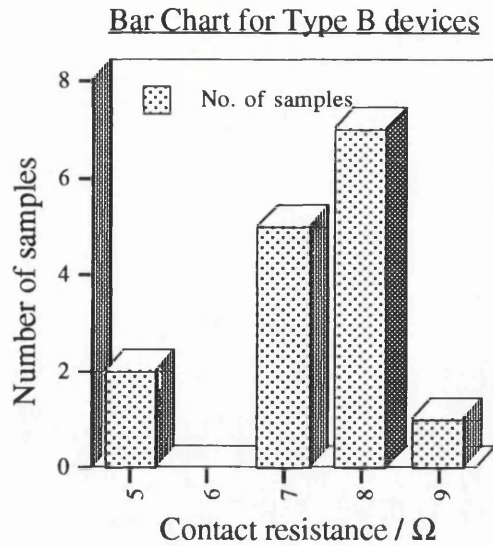


**Figure 6.6**

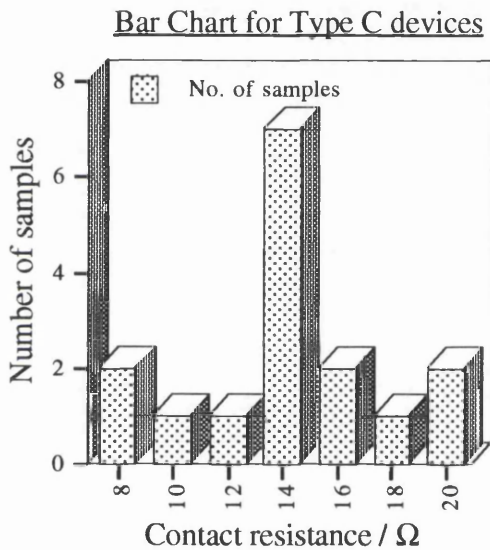


**Figure 6.7**

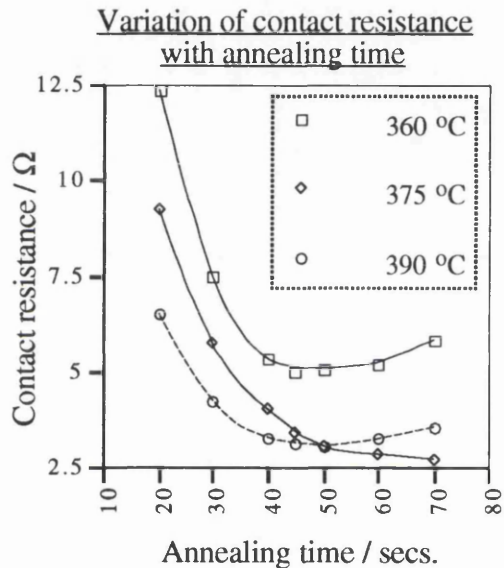
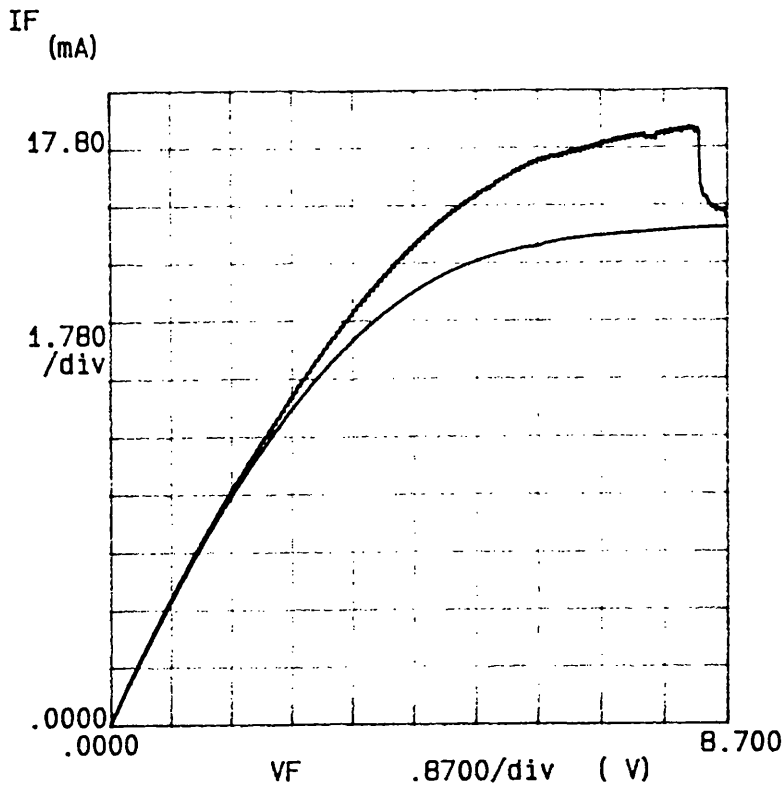


**Figure 6.8**

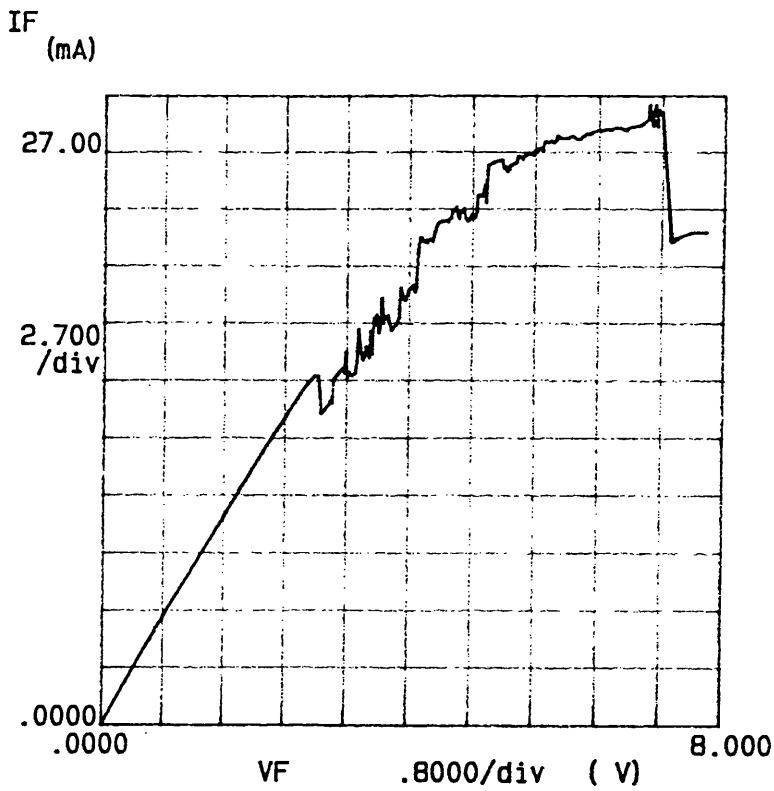
Curve 2 revealed inflexion and mean current recovery prior to the avalanching limit. This fell into the category of moderate annealing duration (i.e Type B :- 375 °C for 45 seconds). Differences in current capacity indicated either greater series resistance (Figure 6.6), or the inhibition of injection of free carriers at the cathode interface. In all of these devices, activity in the current voltage traces occurred in the proximity of the breakdown field which limited their usefulness.

Distinct changes occurred in the Type C (390 °C and 30 secs.) device of Curve 3 (Figure 6.7). A concave section emerged in the trace once the field had surpassed a defined threshold. This form of saturation was notable not only for its concave nature, but additionally for the limited current recovery

# Sharp discontinuities in traces for Type C annealing



Curve 5 :- more pronounced discontinuity at higher field



Curve 6 :- a further variation with contact composition

for even higher fields. A minima was consequently defined in this non-linear section. Device modelling performed by Bonilla and Higuera [21] [22] and others indicated that curve sections of this type signified the formation of unitary layers (Gunn layer) or monopoles. No other form of spatio-temporal structure has been shown to produce mean current sections of this type, and hence it was assumed that devices of Type C generated monopoles. Since these devices approached more closely dipole nucleation, these annealing conditions were adopted with the established contact metal recipe. Device dimensions and current densities were large for Type A, B and C devices. A process of miniaturisation was undertaken to improve the thermal performance of devices.

Figures 6.5, 6.6 and 6.7 compared a selection of planar devices conforming with the three defined types A, B and C. Average values of individual contact resistances due to each type were as follows :-

**TYPE A : 4.6  $\Omega$                       TYPE B : 8.3  $\Omega$                       TYPE C : 11.5  $\Omega$**

Further to the analysis of devices with these fixed annealing conditions, contact resistances were analysed for samples of fixed geometry and variant annealing temperature and time. The results of these experimental variations were shown in Figure 6.8. The contact resistance reduced with increasing annealing time, with a minima defined around the standard 60 seconds. This general trend was supported by Type A and B devices, with temperatures of annealing 375 °C and 390 °C respectively.

While series contact resistances for the low temperature variation (360 °C) were much higher than the other two curves, resistance values for 375 °C annealings fell below those at the higher temperature for longer annealing times. With geometric modifications and reduced thermal dissipation, abrupt changes in mean terminal current were achieved with minimised active region cross-sections. Type C annealing parameters were used in the preparation of the samples shown in Curves 4, 5 and 6. Considering Curve 4 initially, a small concave inflexion was followed by an abrupt discontinuity at approximately 6.4 Volts. This corresponded to a field value slightly in excess of 3.2 kVcm<sup>-1</sup> for this 20  $\mu$ m sample, and hence conformed accurately to the threshold electric field for inter-valley transfer. When compared to Curve 5, for an identical 20  $\mu$ m wide device, the mean current discontinuity occurred at a greater electric field value, (4.35 kVcm<sup>-1</sup>). This was reconciled using a crossover field and control characteristic concept. The devices in Curves 4 and 5 differed in their contact metal ratios. 14 Au : 20 Ge : 15 Ni was used in place of the 14 Au : 14 Ge : 11 Ni standard ratio in the Mikeohm

recipe. In addition to the shift of the threshold for the discontinuity (dipole), the depth of the discontinuity was increased. Similar trends were observed for several device samples fabricated in the process. Varying the germanium content in particular had a significant influence upon this discontinuity displacement (field). Figure 6.9 illustrated the variation in the threshold field with the germanium content for fixed values of nickel fraction. The gold layers (14 nm and 200 nm) remained unmodified throughout. Abrupt discontinuities were visible below and above particular germanium fractions. At 15 nm Ni fraction, the variation included a defined maxima, while the equivalent curve for 20 nm Ni fraction did not exhibit a maxima in the range considered. Increasing the germanium thickness, while maintaining the Ni proportion, modified the ternary phase alloy population in the sub-surface contact layers. The ratio of GaAs to Ni<sub>2</sub>GeAs to Ni and Ge in the region was modified in this manner. A further example of many is shown in Curve 6. Increasing the proportion of germanium in the recipe had the secondary effect of enhancing the population of unalloyed germanium atoms penetrating into the active region. The increase in germanium content induced abrupt discontinuities associated with dipole disturbance formation.

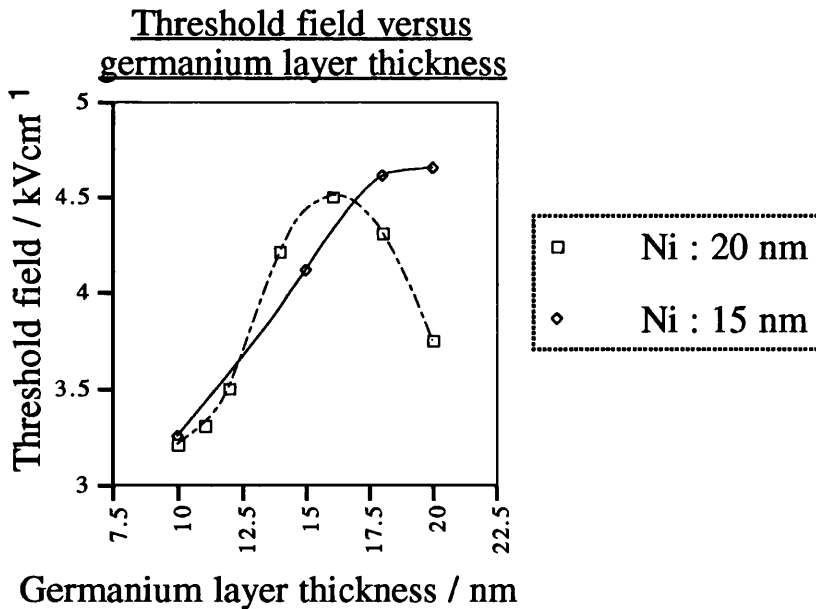


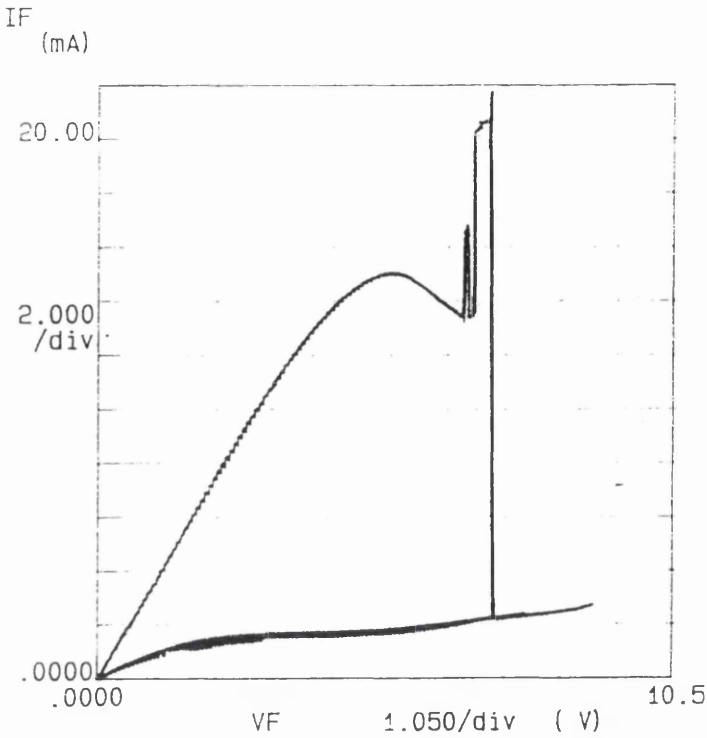
**Figure 6.9**

### **6.3 Waveguide Distortion and Thermal Runaway**

Many of the devices fabricated suffered from uncontrollable thermal runaway (and avalanching) [85] [86] [87]. Subsequently, premature burnout became a continuous detracting characteristic of both planar and vertical devices. Figure 6.10, in conjunction with the SEM images

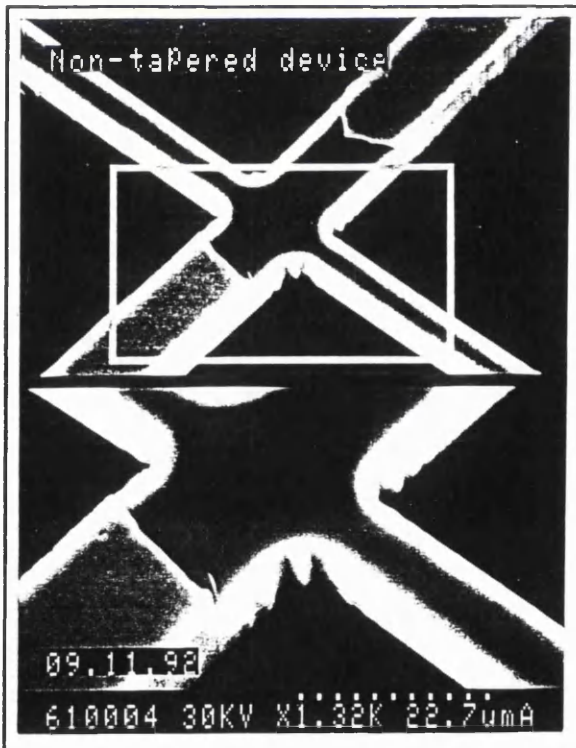
# "Burnout" of planar devices

400°C FOR 30 SEC



Fall in mean current at the terminals is characteristic of the onset of oscillations. The second trace indicates the partial removal of the mesa crystal after thermal destruction

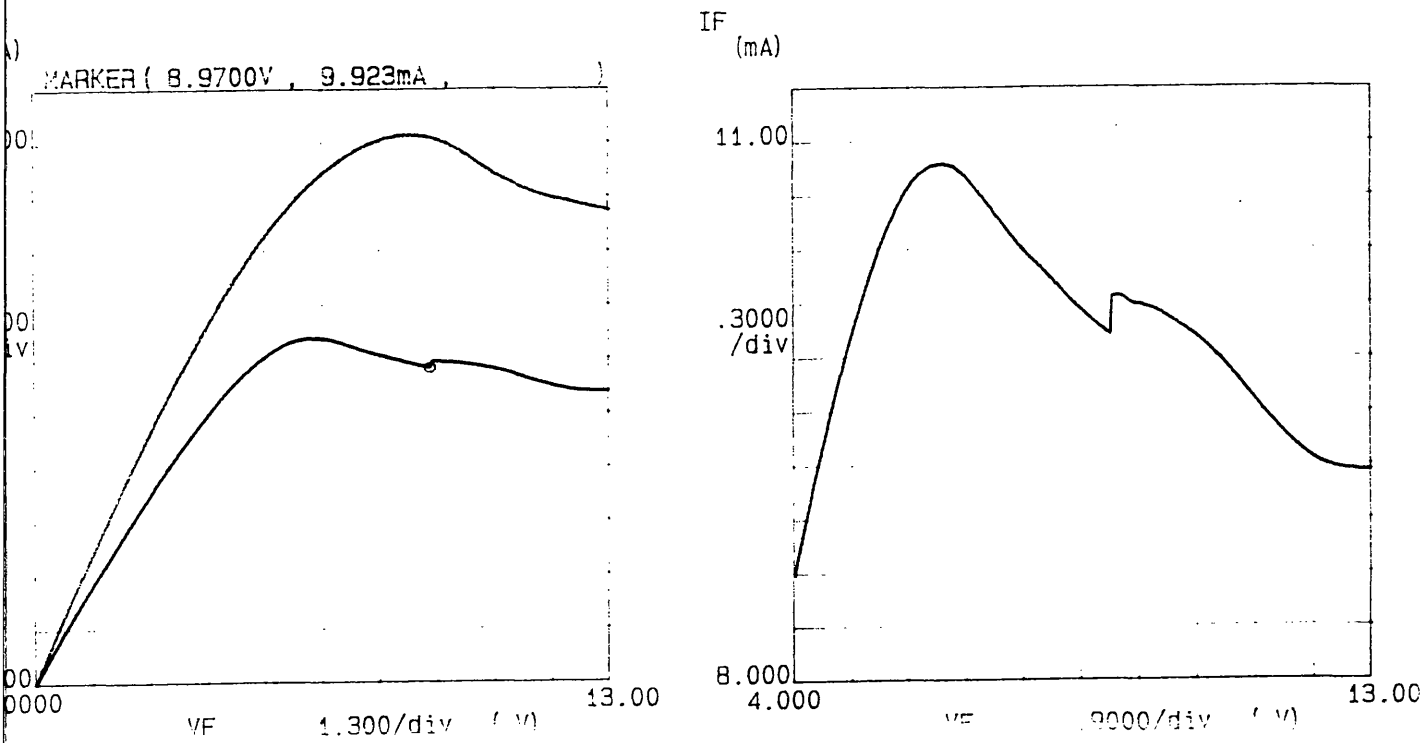
Figure 6.10



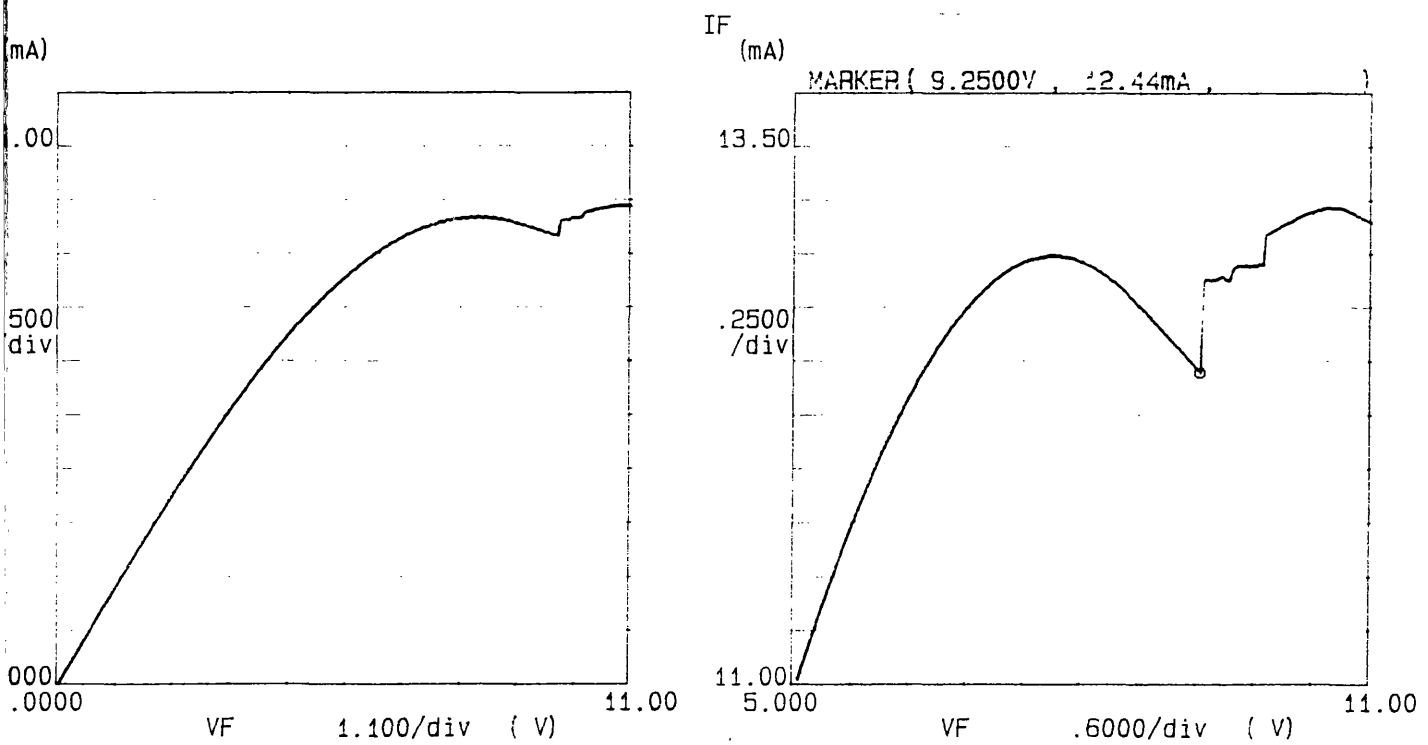
Device before and after oscillation-initiated burnout

# Evidence of Current-Voltage trace Distortion in Planar-geometry Devices

## Figure 6.11



### Two conducting segments



### Three conducting segments

shown, illustrated :- (i) the formation of an instantaneous current filament (ii) the massive fall in mean current (dipole formation) and (iii) destruction by thermal waves. This was typical of a significant proportion of reduced dimension samples.

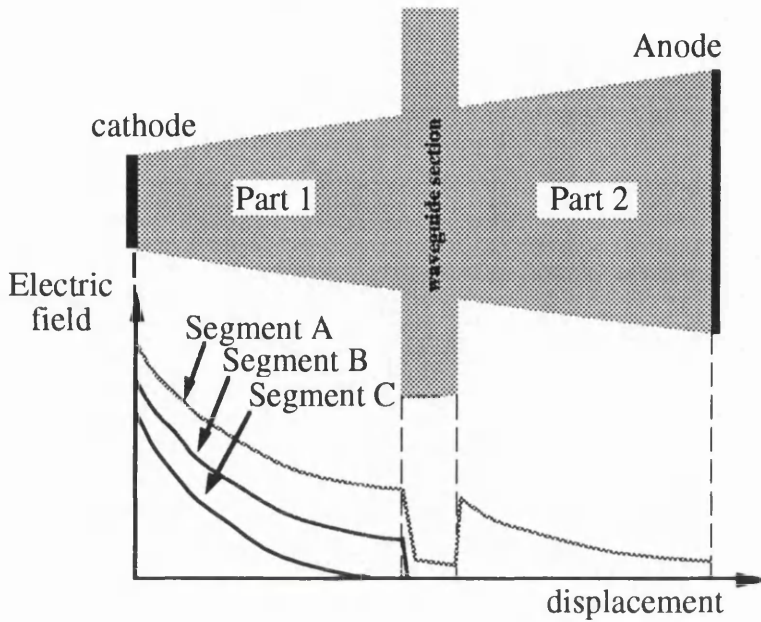


**Figure 6.12 :- Successive conducting portions in a tapered device**

The presence of rib waveguide intersections with the active region of planar devices resulted in a sudden change in cross-sectional area at their junction. The effects of the discontinuity upon the current voltage trace was shown in Figure 6.11. The waveguide presence distorted the internal electric field distribution, generating sharp increases and "dislocations" in these traces. Figure 6.12 provided a conjectured schematic view of the influence of the rib waveguide, which was unequivocally detrimental. The active region could be separated into three segments, pre-determined by physical geometry discontinuities in the device. With voltage increasing from low to higher values, the electric field became non-zero in an increasing length or proportion of the device. At the instant the evanescent field reaches a physical discontinuity, the terminal current rose sharply as further segments of the active region were "activated". In some circumstances, either the first (tapered), plus the second (waveguide) and / or third (tapered) partitioned regions were activated in the device at a particular value of terminal voltage. The first of the traces shown in Figure 6.11 demonstrated all three regions conducting successively with increasing terminal voltage. The second illustrated the case where only two portions carried drift current, the remainder of the carrier transport was through diffusion to the anode. The large cross-sectional area of the waveguide section caused a significant fall in the electric field in this

region. Its influence was only observed when the electric field reached the exiting physical discontinuity (i.e. the junction of rib and the anode side tapered region).

#### **6.4 Comparison between Current-voltage trace Functions and Real data - Curve fitting**

In Chapter 5, a theoretical derivation of a current - voltage trace function was given, which was applicable to tapered and non-tapered devices. Three coefficients ( $\eta_0$ ,  $\eta_1$ ,  $\eta_2$ ) were introduced for the purposes of shaping and scaling of the function. They could be determined through a systematic comparison with current-voltage data derived from measured traces from fabricated devices. To relate these coefficients to practical fabrication parameters (e.g. annealing conditions, germanium / nickel fraction), further manipulation of this function was required.

##### **6.4.1 Evaluation of the Electric Field value at the Curve Maxima**

By evaluating the first derivative of the I- $\Phi$  function with respect to voltage, and equating the resultant expression to zero, the value of voltage at the turning point (curve maxima) was determined. Recalling the I- $\Phi$  function, with the discontinuity multiplier omitted, the first derivative was found as in the following :-

$$I(\Phi) \rightarrow F_1[\Phi] \cdot F_2[\Phi] = G_a \eta_0 \Phi \left( 1 - e^{-\frac{L}{\delta[\eta_2, \Phi]}} \right) \quad \dots (6.2)$$

leading to an expression for the derivative of I[ $\Phi$ ] :-

$$\frac{dI[\Phi]}{d\Phi} = G_a \eta_0 \left\{ 1 - \left[ 1 + \frac{\Pi L}{\eta_2 \Phi^2} \right] e^{-\frac{L}{\delta[\eta_2, \Phi]}} \right\}; \quad \Pi = \frac{4}{\beta} \left[ 1 + 2 \frac{L}{w_c} \tan \theta \right]; \quad \beta = \frac{\mu \epsilon}{n_{ci} e \mu_{ci} F_{ci} L^2} \quad \dots (6.3)$$

Equating to zero yielded :-

$$\frac{dI[\Phi]}{d\Phi} = 0 \Rightarrow e^{\frac{L}{\delta[\eta_2, \Phi]}} = \left\{ 1 + \frac{L}{\delta[\eta_2, \Phi]} + \frac{L^2}{2! \delta^2[\eta_2, \Phi]} + \dots \right\} = \left[ 1 + \frac{\Pi L}{\eta_2 \Phi^2} \right] \quad \dots (6.4)$$

Substituting for the decay constant generated the following, where  $\Phi_{tp}$  represented the turning point voltage, i.e. the voltage at which peak current flowed, such that :-

$$\delta[\eta_2, \Phi] = \frac{2\eta_2 \Phi^2}{\Pi} \Rightarrow \frac{\Pi L}{2\eta_2 \Phi^2} + \frac{\Pi^2 L^2}{8\eta_2^2 \Phi^2} = \frac{\Pi L}{\eta_2 \Phi^2}$$

$$\Rightarrow \Phi_{tp}[\eta_2, \theta] = \sqrt{\frac{\Pi L}{4\eta_2}} = \sqrt{\frac{\left[ 1 + 2 \frac{L}{w_c} \tan \theta \right] L^3 n_{ci} e \mu_{ci} F_{ci}}{\mu \epsilon \eta_2}}$$

The constant  $\beta$  was defined in terms of the injected cathode current density. In previous discussions it had been illustrated that device behaviour was modified by the exact boundary conditions prevailing at the cathode injecting interface. The arguments of Kroemer [20] and others indicated that this current density was dissimilar to that presented to carriers in the interior crystal regions. Hence this current density factor was deemed to be an arbitrary function  $f_{\text{cath}}[x_{\text{Ge}}, x_{\text{Ni}}, T_a, \tau_a]$ , of one or more of the following parameters considered to influence the cathode boundary conditions :- (1) germanium fraction ; (2) nickel fraction ; (3) annealing temperature ; (4) annealing time. Subsequently,  $\beta$  and the voltage at peak current could be written as :-

$$\beta_{\text{cath}} [x_{\text{Ge}}, x_{\text{Ni}}, T_a, \tau_a] = \frac{\mu \epsilon}{L^2 f_{\text{cath}} [x_{\text{Ge}}, x_{\text{Ni}}, T_a, \tau_a]} \text{ ---- (6.5)}$$

$$\Rightarrow \Phi_{\text{tp}} [\eta_2, \theta] = \sqrt{\frac{\left[1 + 2 \frac{L}{w_c} \tan \theta\right] L^3 f_{\text{cath}}}{\mu \epsilon \eta_2}} \Rightarrow \eta_2 [x_{\text{Ge}}, x_{\text{Ni}}, T_a, \tau_a] = \frac{\left[1 + 2 \frac{L}{w_c} \tan \theta\right] L^3 f_{\text{cath}}}{\mu \epsilon \Phi_{\text{tp}}^2 [\eta_2, \theta]} \text{ ---- (6.6)}$$

### Variation of the second shaping coefficient

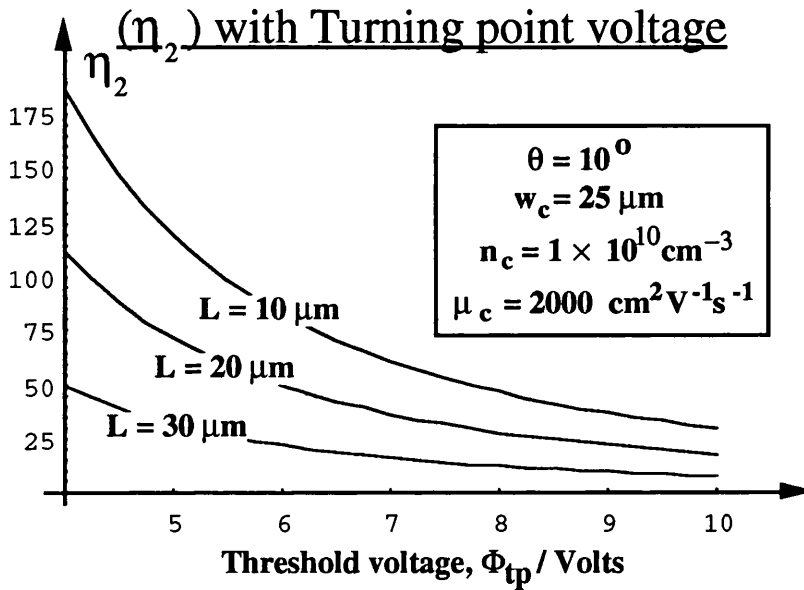


**Figure 6.13**

A means of relating the value of the  $\eta_2$  coefficient in the theoretical curve, to measured data from real  $I-\Phi$  curves, was now possible. For a particular sample, the taper angle and physical dimensions of the device were invariant. The transformation of the shape and magnitude of the  $I-\Phi$  curves of the measured devices was then functionally related to the four physical contact parameters listed above.

Transposition of equation (6.6) lead to an expression for the arbitrary cathode-dependency function,  $f_{\text{cath}}[\eta_2, \Phi_{\text{tp}}]$ , in terms of  $\eta_2$  and  $\Phi_{\text{tp}}$ . The voltage variable could be replaced by the "bias" field value  $E_{\text{tp}} = \Phi_{\text{tp}}/L$ , normalising the expression and allowing it to be related directly to data from real devices, yielding equation (6.7) :-

$$f_{\text{cath}}[\eta_2, E_{\text{tp}}] = \frac{\mu\epsilon\eta_2 E_{\text{tp}}^2}{\left[1 + 2\frac{L}{w_c} \tan\left(\frac{w_a - w_c}{2L}\right)\right]L} \dots (6.7)$$

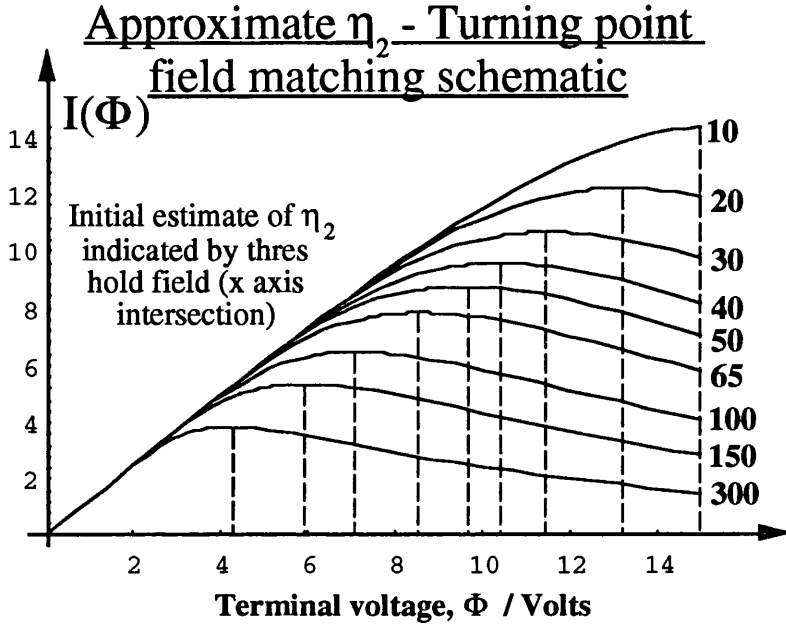


Figure 6.14

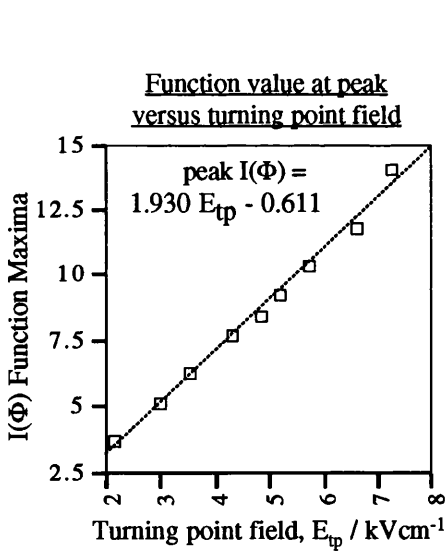


Figure 6.15

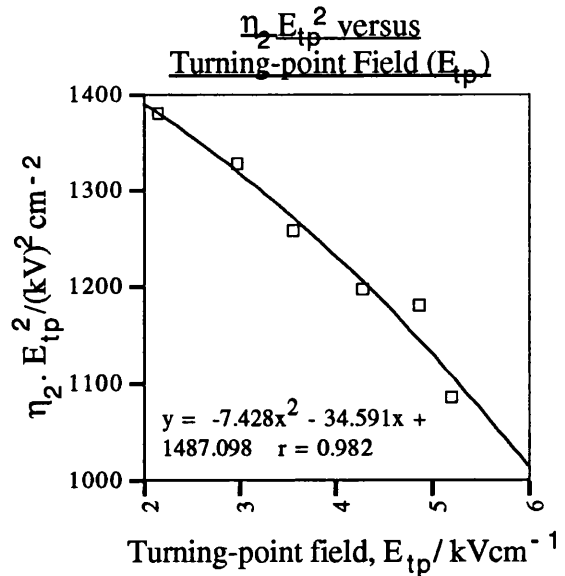
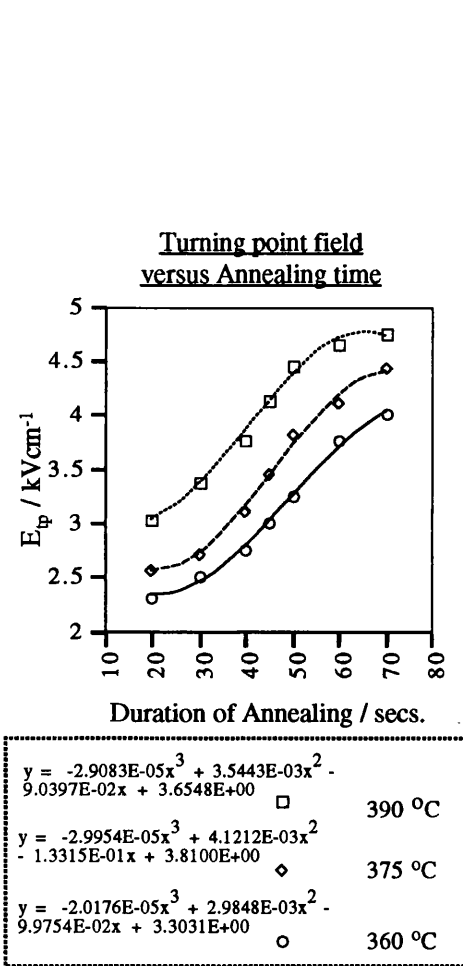


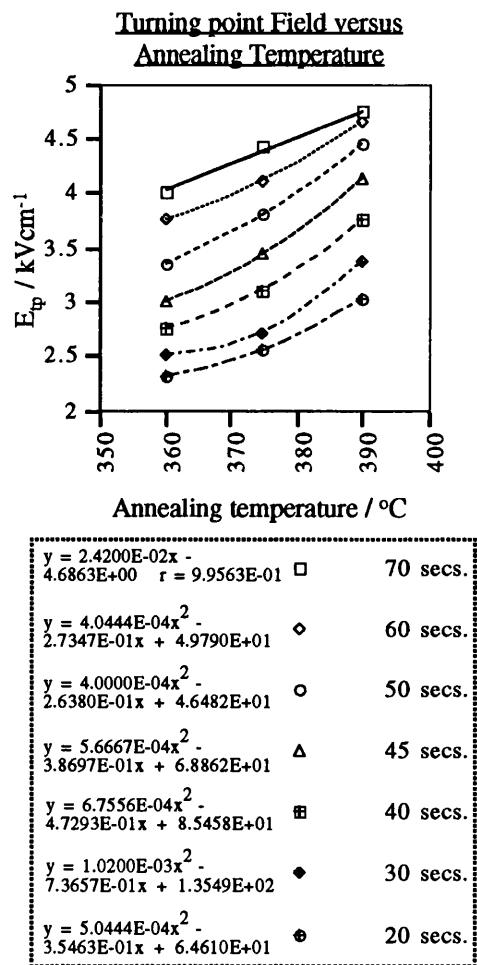
Figure 6.16

Figure 6.14 represented a curve family generated from discrete values of  $\eta_2$ , with low to medium values applicable to fabricated devices. Variations of the  $I(\Phi)$  function maxima (peak value) and  $\eta_2 E_{tp}^2$  with electric field at this maxima ( $E_{tp}$ ) were extracted from Figure 6.14 and plotted in Figures 6.15 and 6.16 respectively. The functional form of the curve in Figure 6.16 represented a scaled version of the cathode boundary function. The function maxima ( $I_p$ ) was shown to be unequivocally linearly dependent upon the turning point field,  $E_{tp}$ . A functional relation for  $f_{cm}[\eta_2, \Phi_{tp}]$  with  $E_{tp}$  was determined as follows :-

$$\left(\eta_2 E_{tp}^2\right)[T_a, \tau_a] = 1487.098 - 34.591 E_{tp}[T_a, \tau_a] - 7.428 E_{tp}^2 [T_a, \tau_a] \dots (6.8)$$



**Figure 6.17**



**Figure 6.18**

Similar turning point field ( $E_{tp}$ ) dependencies with annealing time and temperature were determined. For data to be valid for this purpose, samples fabricated with identical contact composition (i.e 15 % germanium and 20 % nickel by weight) were used to provide data profiles. Measurements were ordinarily extracted directly from the HP 4145A sweep analyser through the "marker" facility,

without curves being plotted. Each data point represented an average value of 200-250 individual devices. Figure 6.17 gave the variation of the turning point field with annealing time, for three separate annealing temperatures. The curves were functionally similar at these temperatures (almost parallel). The turning point field was observed to decrease with increasing annealing time, and bore similarities to the variation of contact resistance with annealing time. This suggested some level of correlation between contact resistance and  $E_{tp}$ . Similarly, the variation of  $E_{tp}$  with annealing temperature was plotted in Figure 6.18, with a family of curves generated at different annealing temperature. Polynomial expressions describing these variations with  $T_a$  and  $\tau_a$  were generated subsequently. A functional dependence, of the form of a general quadratic in  $T_a$ , was constructed from time dependent coefficients :-

$$E_{tp}[T_a, \tau_a] = a_2[\tau_a]T_a^2 + a_1[\tau_a]T_a + a_0[\tau_a] \dots (6.9)$$

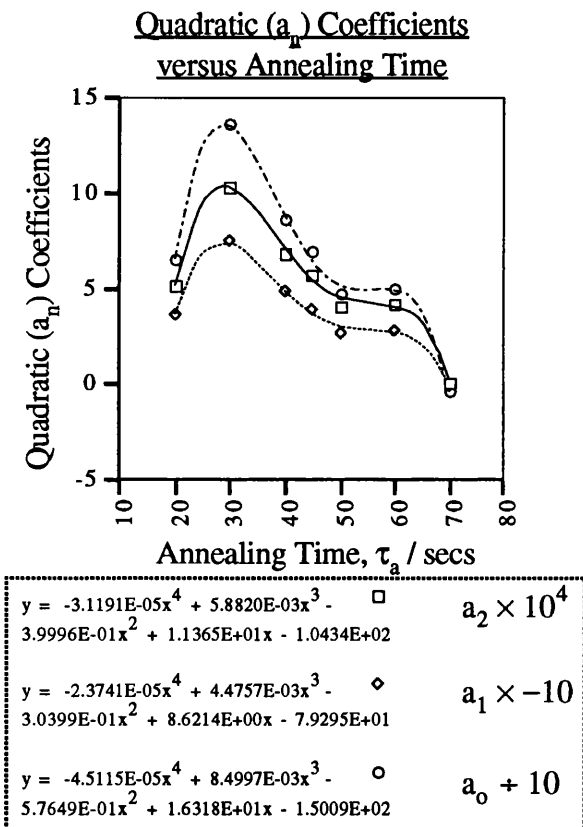


**Figure 6.19**

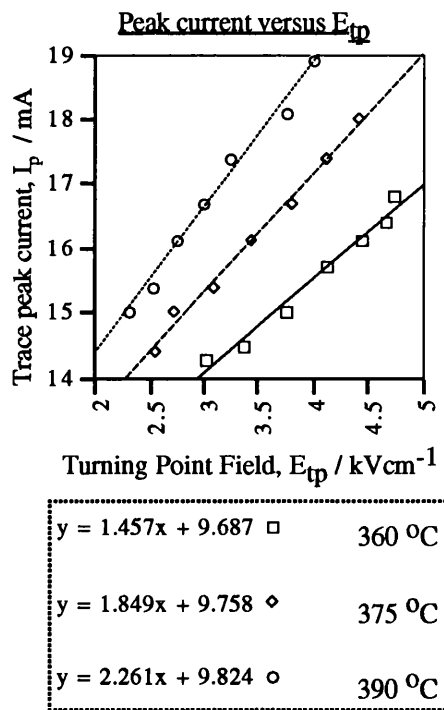


**Figure 6.20**

The general functional variation corresponding to these experimentally-derived curves, was that of a cubic polynomial in  $\tau_a$ . An overall calculative function, of considerable complexity, was derived for the dependence of  $E_{tp}$  with annealing temperature ( $T_a$ ) and time ( $\tau_a$ ), for the standardised contact composition of 15 % and 20 % germanium and nickel fraction respectively.

This  $E_{tp}$  function was inserted into equation (6.8) yielding the  $\eta_2$  coefficient dependency with annealing temperature and time, leading to a complex variation with these parameters.

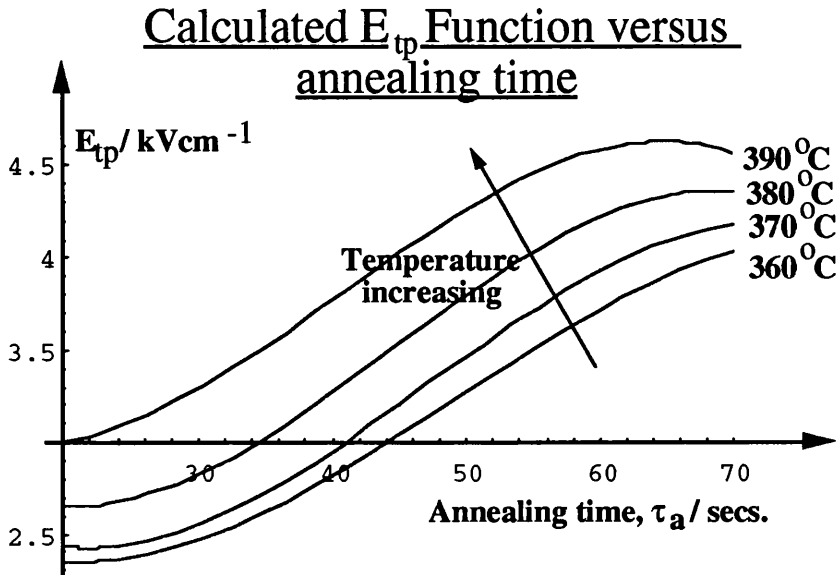


**Figure 6.21**

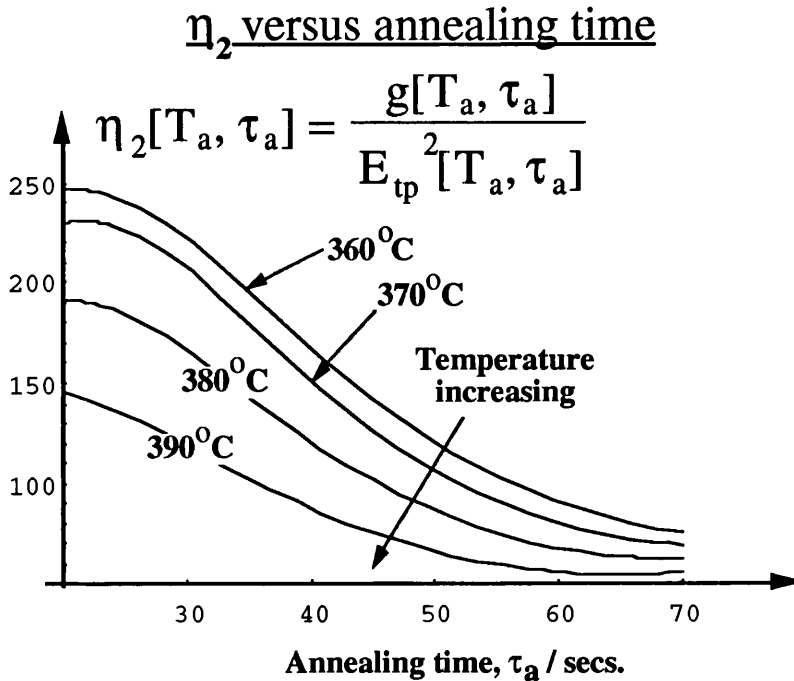


**Figure 6.22**

Before evaluating the  $\eta_2$  function for constant contact composition samples, the pre-defined

$f_{cath} [T_a, \tau_a]$  function was evaluated as follows :-

$$f_{cath} [T_a, \tau_a] = \frac{\mu \epsilon}{\left[ 1 + 2 \frac{L}{w_c} \tan \theta \right] L} \left[ \begin{array}{l} 1487.098 \\ - 34.591 \left\langle a_2 [\tau_a] T_a^2 + a_1 [\tau_a] T_a + a_0 [\tau_a] \right\rangle \\ - 7.428 \left\langle a_2 [\tau_a] T_a^2 + a_1 [\tau_a] T_a + a_0 [\tau_a] \right\rangle^2 \end{array} \right] \dots (6.10)$$

$$\eta_2[T_a, \tau_a] = \frac{\eta_2 E_{tp}^2[T_a, \tau_a]}{E_{tp}^2[T_a, \tau_a]} = \frac{\left[1 + 2 \frac{L}{w_c} \tan \left\{ \frac{w_a - w_c}{2L} \right\} \right] L}{\mu \epsilon} \cdot \frac{f_{cath}[T_a, \tau_a]}{E_{tp}^2[T_a, \tau_a]} \dots (6.11)$$

Curve families of constant temperature and time contours were plotted in Figures 6.22 and 6.23 respectively, where  $\eta_2 E_{tp}^2[T_a, \tau_a]$  was defined as in expression (6.8). In both cases,  $\eta_2$  was observed to decrease as annealing time and/or temperature were increased. This revealed the influence of the cathode boundary in real devices.

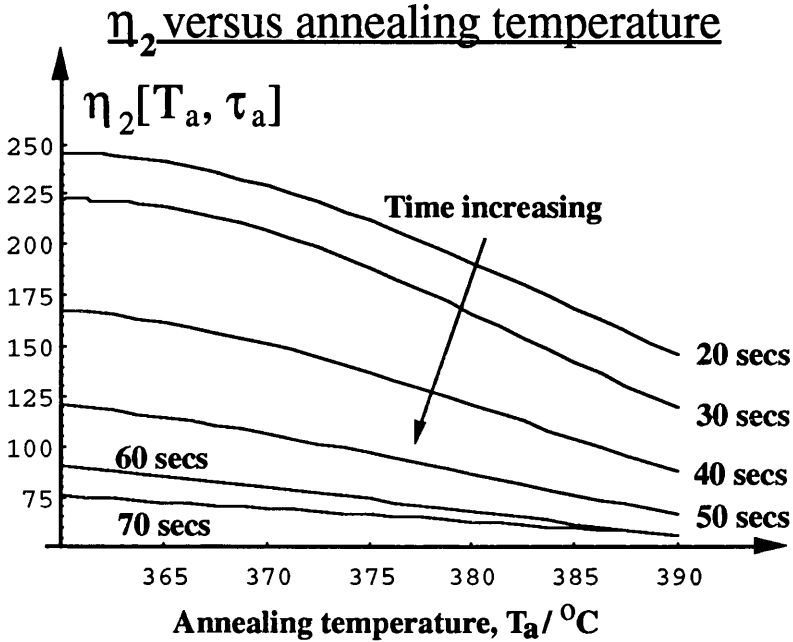


**Figure 6.23**

### **6.4.2 Functional Dependency for $\eta_0$**

An expression in terms of annealing temperature and time was derived for the scaling constant,  $\eta_0$ . Figure 6.20 showed the linear dependency of the peak current with  $E_{tp}$ , compiled from real device data at three experimental temperatures. Appropriate functions were generated and the variation of the gradients and constants of these functions plotted additionally against annealing temperature (Figure 6.24 and 6.25 respectively). The value of the maxima of the theoretical function  $I[\Phi]$  with  $E_{tp}$  was presented in Figure 6.15. This maxima ( $I[\Phi]_{max}$ ) had the linear variation :-

$$I[\Phi]_{max} = 1.93 E_{tp} - 0.611 \dots (6.12)$$

It could be stated further that :-

$$I_p[E_{tp}] = I[\Phi]_{max} \eta_0[E_{tp}] \cdot \frac{n_o e \mu_e h w_a}{2\sqrt{2} L} \Rightarrow \eta_0[E_{tp}] = \frac{2\sqrt{2} L}{n_o e \mu_e h w_a} \cdot \frac{I_p[E_{tp}]}{I[\Phi]_{max}} \dots (6.13)$$

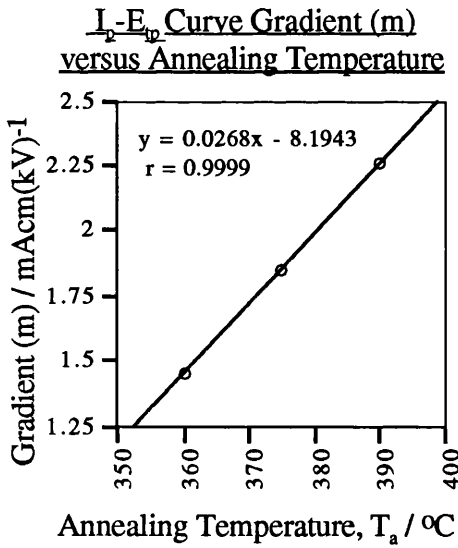


**Figure 6.24**

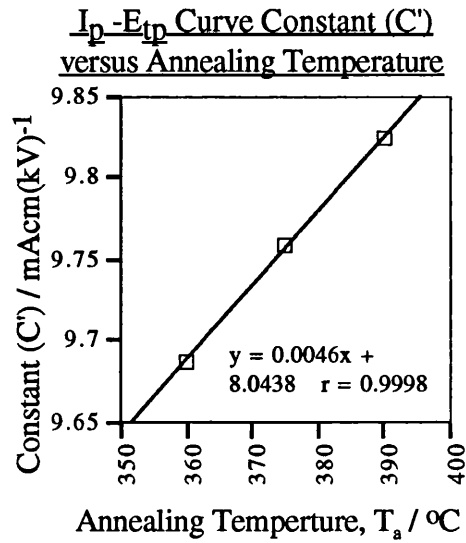


**Figure 6.25**

$\eta_o$  was determined in terms of the annealing temperature and time, such that :-

$$\eta_o [T_a, \tau_a] = \frac{2\sqrt{2}L}{n_o e \mu_e h w_a} \cdot \frac{mE_{tp}[T_a, \tau_a] + \hat{C}}{1.93 E_{tp}[T_a, \tau_a] - 0.611} = \frac{2\sqrt{2}L}{n_o e \mu_e h w_a} \cdot \frac{[0.0268 T_a - 8.1943] \cdot \left\{ a_2 [\tau_a] T_a^2 + a_1 [\tau_a] T_a + a_0 [\tau_a] \right\} + [0.0046 T_a + 8.0438]}{1.93 E_{tp}[T_a, \tau_a] - 0.611} \quad \text{---(6.14)}$$

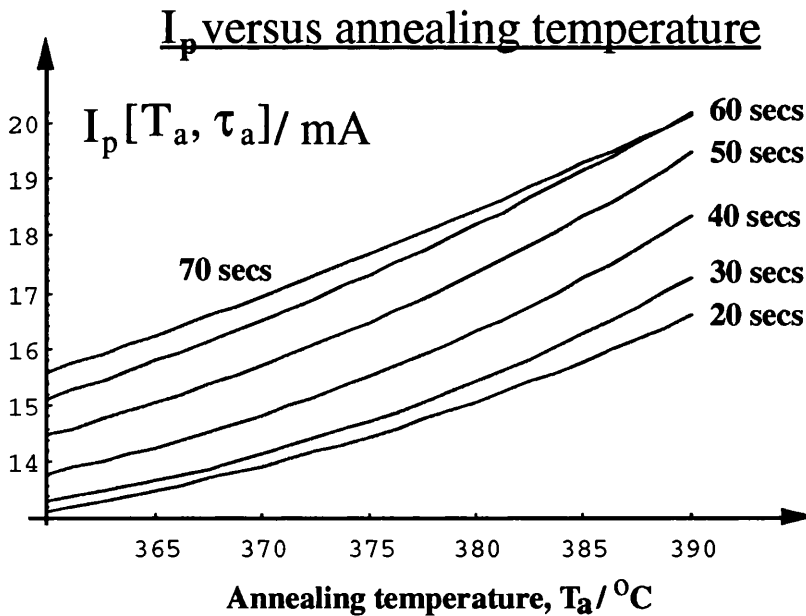


**Figure 6.26**

Superposing this function for  $I_p [T_a, \tau_a]$  upon that given for  $\eta_o$  in (6.14) above, the peak current value of the measured data could be correlated with, and compared to, the theoretical  $I[\Phi]$  function. The functional variations of  $I_p [T_a, \tau_a]$  with annealing temperature and time considered

separately were plotted in Figures 6.26 and 6.27 respectively. Additionally, the scaling constant was plotted as a function of annealing temperature and time. These variations were shown in Figures 6.28 and 6.29.

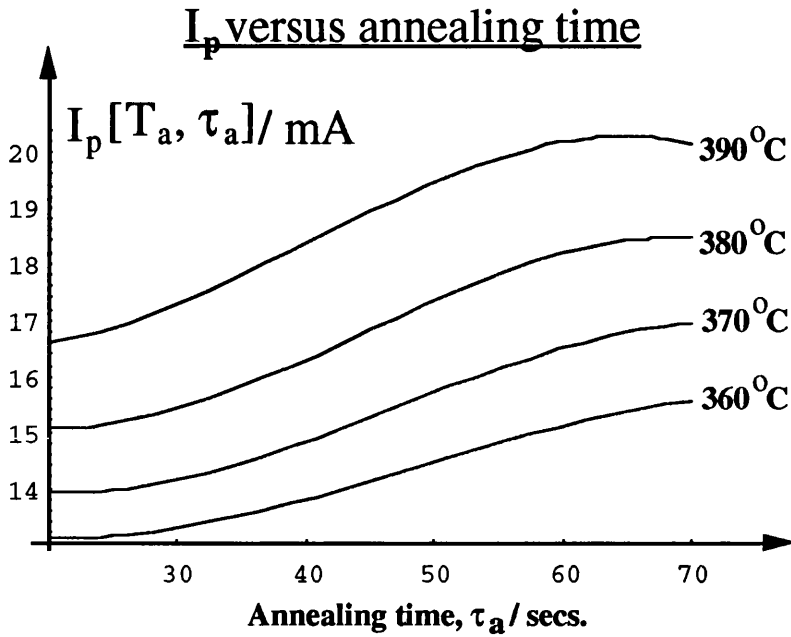


Figure 6.27

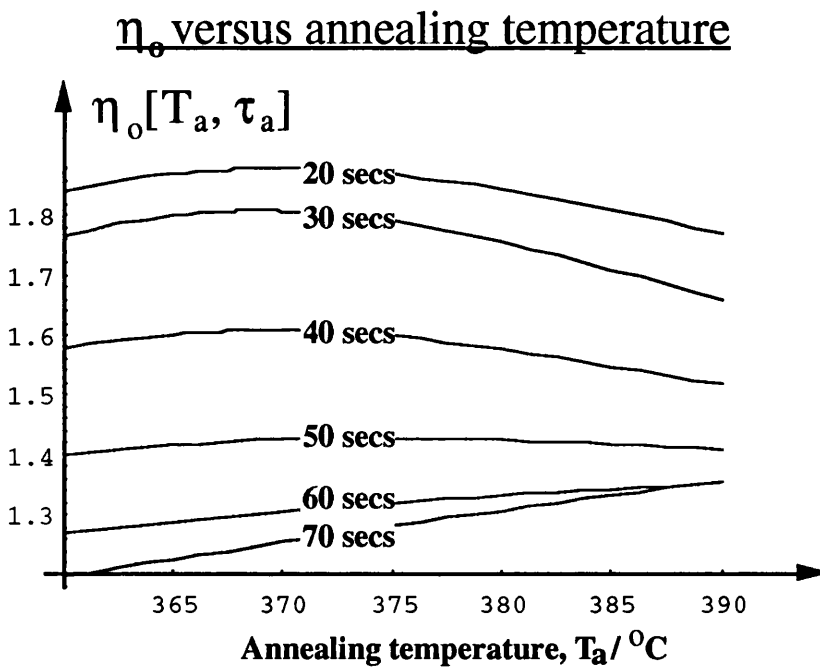
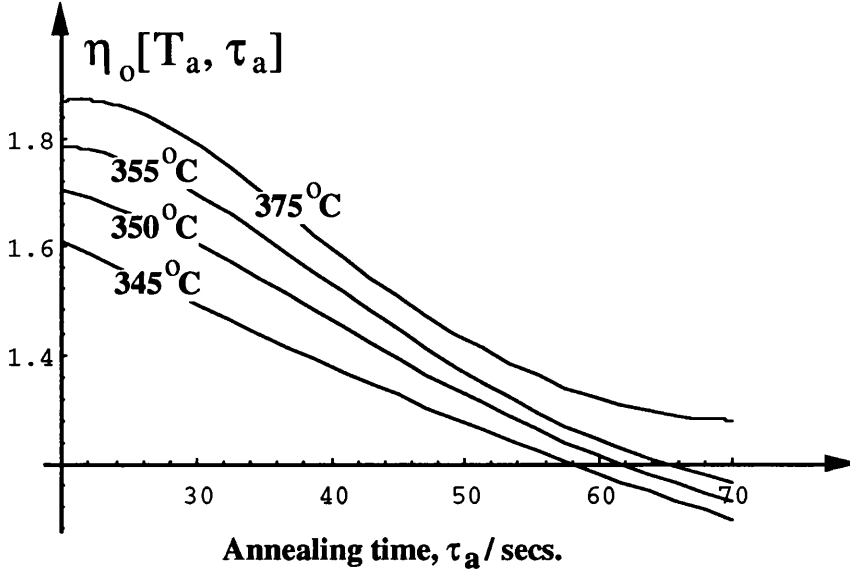


Figure 6.28

A chart relating the annealing conditions to the value of the achieved turning point field,  $E_{tp}[T_a, \tau_a]$  was plotted. In doing so, the chart could be used to predict intermediate combinations of annealing time and temperature necessary to generate a particular  $E_{tp}[T_a, \tau_a]$ .

## $\eta_o$ versus annealing time



**Figure 6.29**

This was achieved through an analytical solution (positive value) to the quadratic form of  $E_{tp}[T_a, \tau_a]$  in expression (6.9).  $T_a$  was calculated in terms of  $\tau_a$ , for constant values of  $E_{tp}[T_a, \tau_a]$ , generating a family of constant  $E_{tp}[T_a, \tau_a]$  contours or loci.  $T_a$  was given by :-

$$T_a[E_{tp}, \tau_a] = \frac{|a_1[\tau_a]|}{2a_2[\tau_a]} \left[ 1 + \sqrt{1 - \frac{4a_2[\tau_a][a_0[\tau_a] - E_{tp}]}{a_1^2[\tau_a]}} \right] \dots (6.15)$$

where the  $a_2$ ,  $a_1$  and  $a_0$  coefficients had the definition as shown at the base of Figure 6.19. The  $E_{tp}[T_a, \tau_a]$  loci were plotted at 0.5 kVcm<sup>-1</sup> incremented values, and displayed in Figure 6.30.

### **6.4.3 Disturbance Discontinuity and Real Data**

Relationships between coefficients  $\eta_2$  and  $\eta_o$  and annealing time and temperature were determined from measured data. Similarly, the displacement in voltage (or electric field) of a domain-initiated sharp trace discontinuity was related to nickel and germanium fraction (contact composition). The  $I(\Phi)$  discontinuity function,  $f_{dis}(\Phi)$ , introduced as expression (5.27), could be rewritten as :-

$$f_{dis}[\Phi] = 1 - g[\Phi]e^{-\left(\frac{\Phi_m}{\Phi}\right)^{100}} = 1 - g[\Phi]e^{-\left(\frac{L[0.03567 \Phi_{dis} - 0.00223]}{\Phi}\right)^{100}} \dots (6.16)$$

where  $L$  was the active region length in  $\mu\text{m}$ , and the voltage value at this discontinuity,  $\Phi_{dis}$  was related to  $\Phi_{th}$  through the linear equation :-

$$\Phi_{th} = L[0.03567 \Phi_{dis} - 0.00223] \dots (6.17)$$

# Annealing Temperature and Time selection Chart

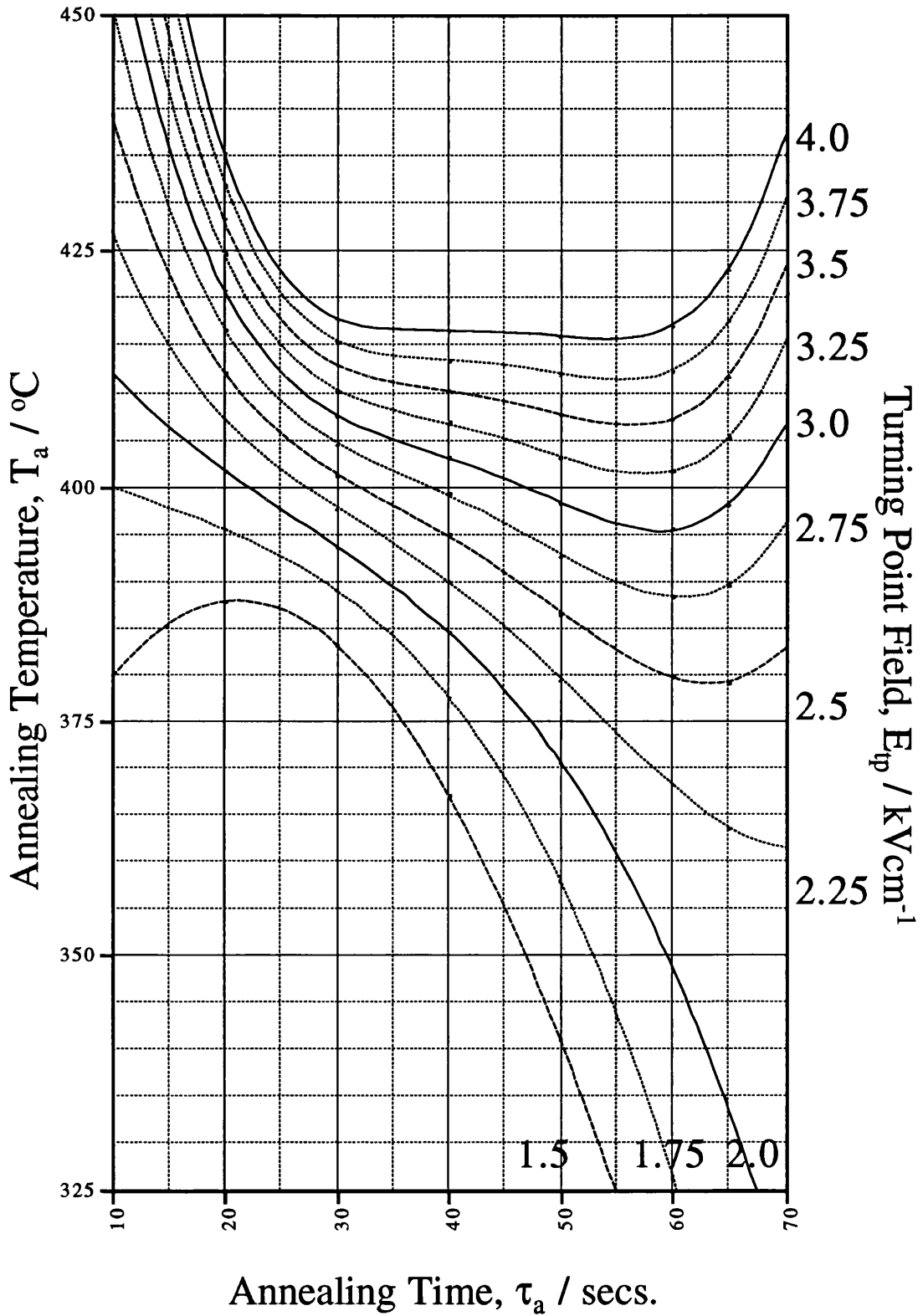


Figure 6.30

Data was obtained from curves displayed on the HP 4145A sweep analyser for a variety of devices with modified contact compositions. Figure 6.31 presented curves obtained from plotting the discontinuity field value against nickel fraction (percentage by weight) for three germanium fraction values. In addition, Figure 6.32 illustrated the lack of correlation between  $g[\Phi]$  and  $E_{dis}$ . For 12 % and 8 % germanium fractions, linear variations of  $\Phi_{dis}$  with nickel fraction were demonstrated, while a slight quadratic dependency was observed at 15 %. The values of discontinuity field were consistently higher at 15 % than 12 % and 8 %, but with the relative magnitudes suggested by the 8 % line demonstrating that no reliable predictive formula was likely to be determined with germanium fraction. Since most samples were implemented with the standardised 15 % germanium fraction, a functional variation was subsequently sought.

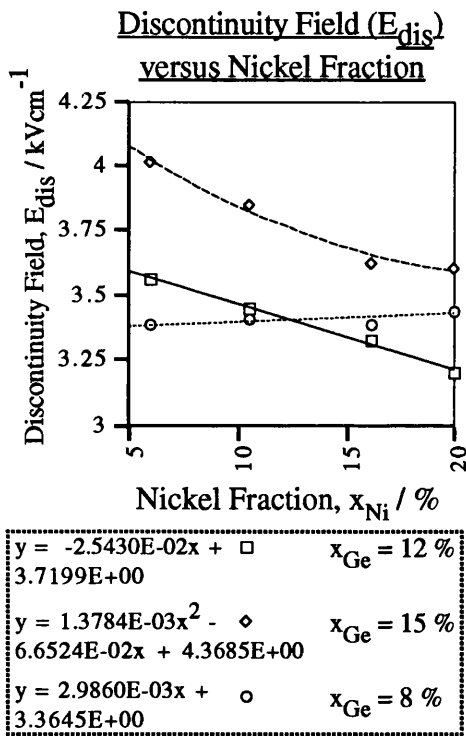


Figure 6.31

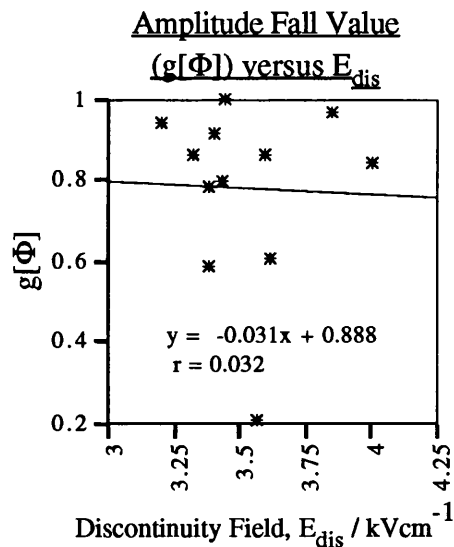


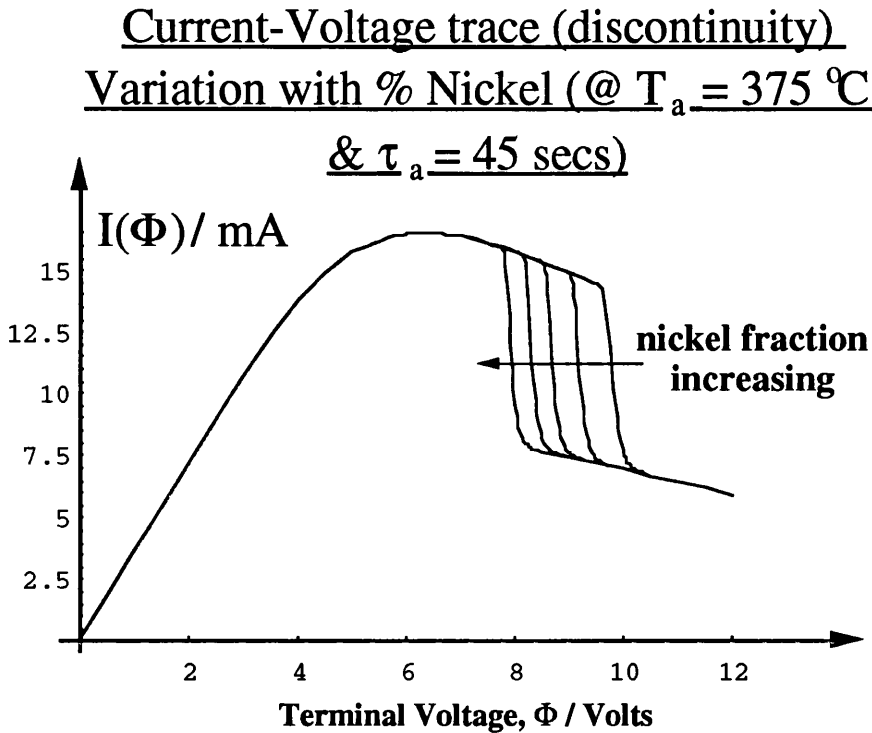
Figure 6.32

The dependency with 15 % nickel fraction, using the quadratic equation from Figure 6.31, was as in the following:-

$$f_{dis}[\Phi] = 1 - g[\Phi] e^{-a[\Phi] L \left[ \frac{1.0083 \times 10^{-4} x_{Ni}^2 - 4.866 x_{Ni} + 0.315}{\Phi} \right]^{100}} \quad \text{---- (6.18)}$$

Sharp discontinuity variations were plotted in Figure 6.33, using the data function given in (6.18).  $g(\Phi)$  was set to 0.5 for convenience. A simple trend was suggested in those devices susceptible

to domain formation (large signal disruption), i.e. as the nickel proportion increased, the voltage for mean current fall was reduced.



**6.4.4 Influence of Annealing parameters upon the Curved-matched I -  $\Phi$  Function**

Curve-matched current-voltage traces could be related directly to annealing time and temperature through the derived dependencies of the  $\eta_0$  and  $\eta_2$ . Curves generated from the  $I(\Phi)$  function at various values of time and temperature were shown in Figures 6.34 and 6.35. These curves matched real traces, in terms of fundamental profile and peak current.

It was demonstrated that increasing the annealing temperature primarily modified the peak current and turning point field, while increasing the annealing time modified additionally the fundamental shape of the curve. Figure 6.35 revealed concave saturation at lower annealing temperatures and times. These trends were observed in the Type A, B and C devices discussed previously. As the annealing time was increased, the influence of the temperature upon the turning point field in particular was diminished. The electric field value corresponding to trace maxima increased with both annealing time and temperature. Similarly, maximum measured current linearly increased with this turning point field.

### Curve-matched Current-Voltage trace

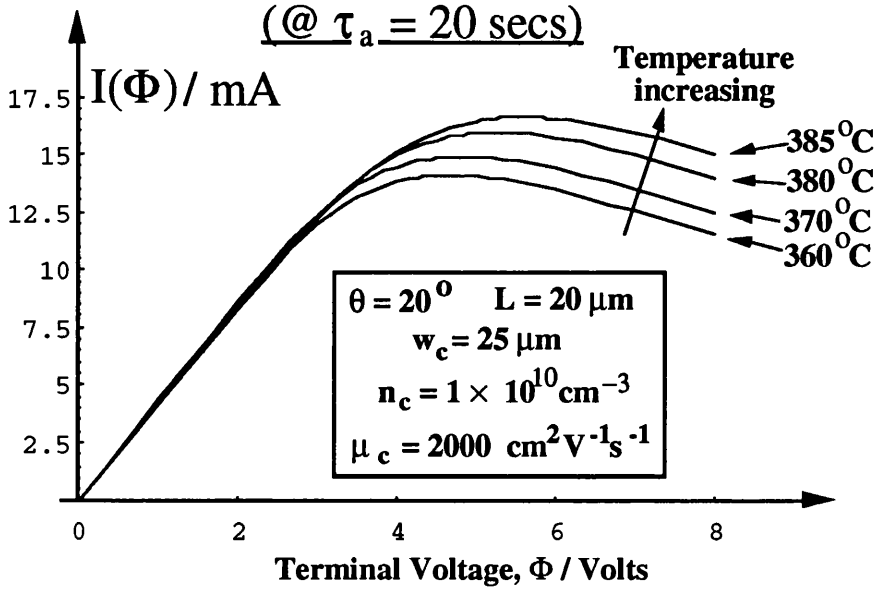


Figure 6.34

### Curve-matched Current-Voltage trace

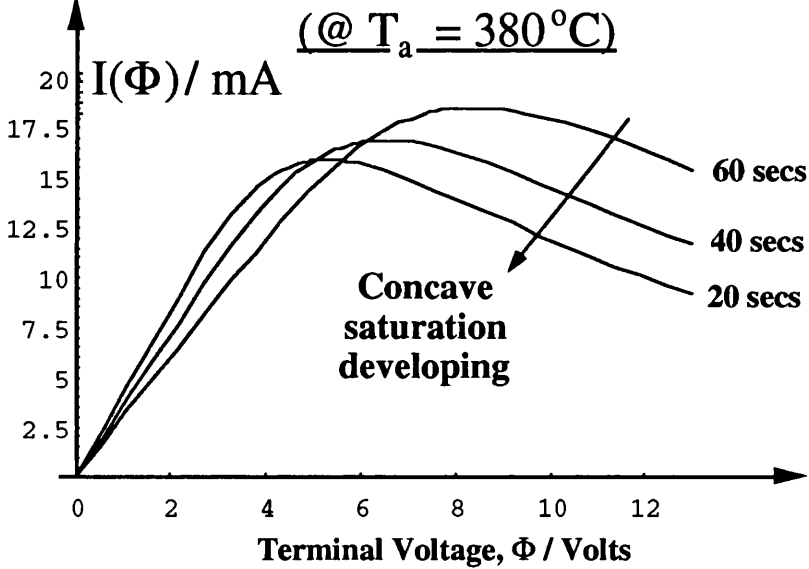
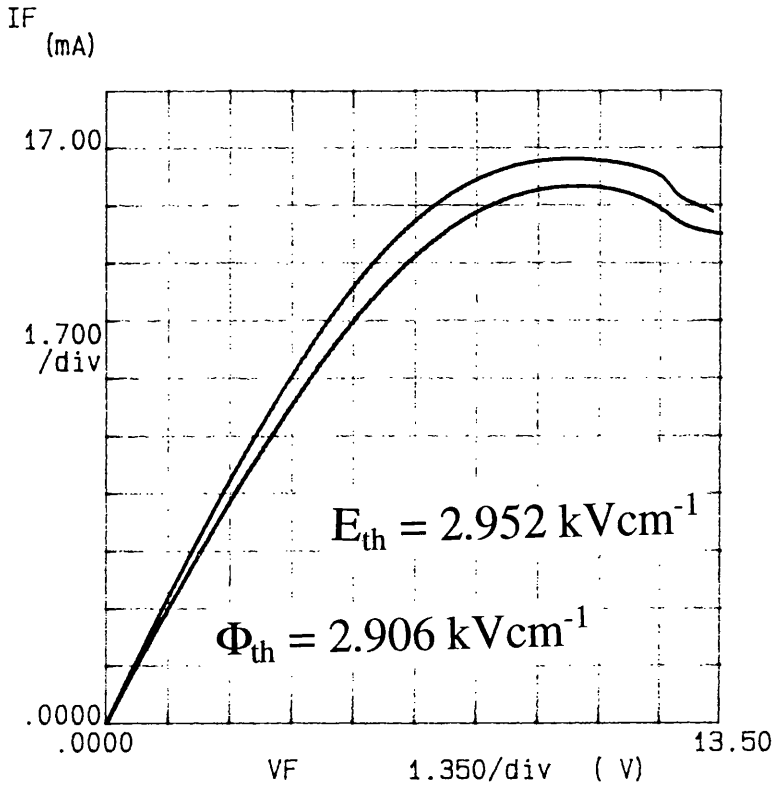


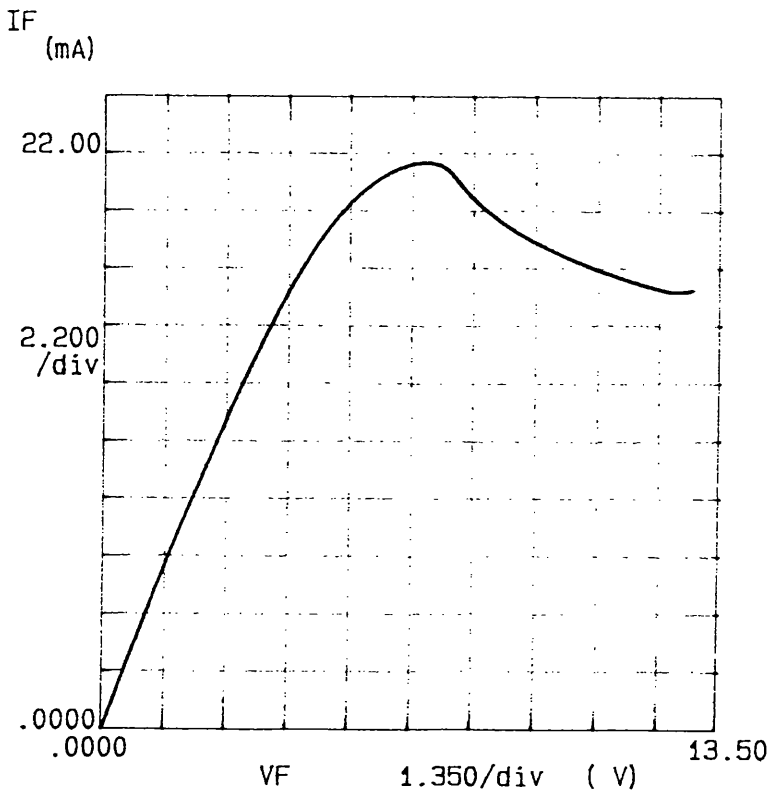
Figure 6.35

The more profound contact annealing at 360 °C - 390 °C and 20 - 70 secs explained the general trends. The constituent elements of the contacts (i.e. Ni, Ge, Au) penetrated further into the wafer surface, generating a more homogeneous transition from surface metal to interior crystal. The implications for the crossover field (Chapter 2) were not immediately obvious, but observations of the decrease of contact resistance with increasing annealing temperature and time was recalled. This suggested a partial explanation for the increase of the sample current for the same device dimensions.

two devices from B157  
(annealed at 395 °C and 60 sec.),  $L = 35 \mu\text{m}$



Curve 7 :- direct comparison curves  
used to assess predictive functions



Curve 8 :- classic "concave" saturation

#### 6.4.5 Comparison between Tapered and Non-tapered Devices

The influence of the taper was examined by comparing curves generated for non-tapered devices where  $\theta = 0^\circ$  and  $w_a = w_c$ , and those with arbitrary  $\theta$ . This comparison was made in Figure 6.36, for the standardised parameter values used for the previous calculations.

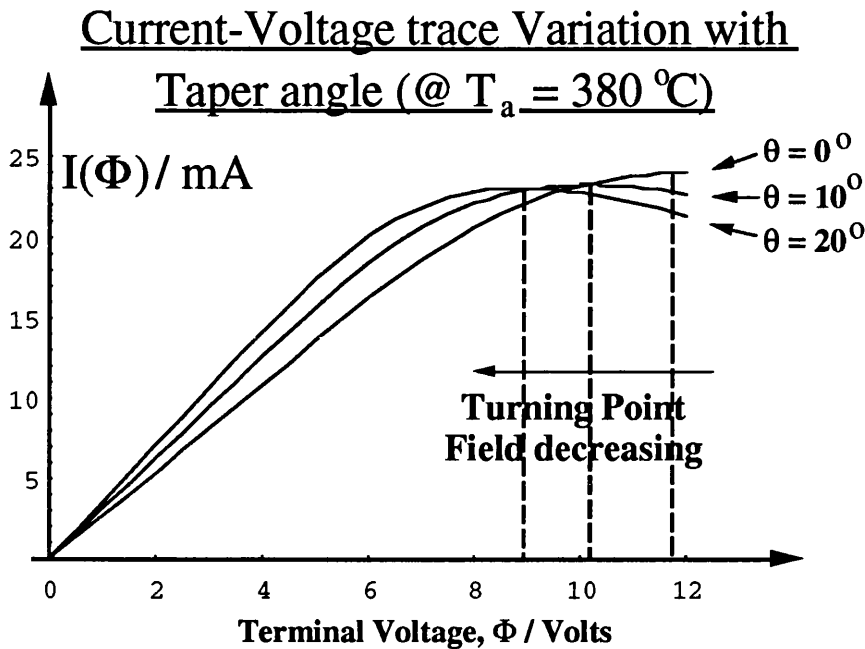


**Figure 6.36**

Increasing the taper angle reduced the turning point field, and slightly modified the peak current. For non-tapered devices, the electric field was higher at all points within the active region. The turning point field was similarly increased.

#### 6.4.6 Comparison between Real Data and Predictive Formulae

Empirical relationships were derived from devices deemed to be "well-behaved", or of standard operation. Figure 6.37 compared the theory function with two traces measured from similar devices (Curve 7). Figure 6.38 indicated the percentage departure of the real traces from the theory at unit voltage points. The greatest discrepancy was at lower voltage values, i.e. in the linear "ohmic" portion of the profile. The real data trace had greater curvature at lower voltage values, suggesting the presence of extensive primary layers in the active region. Disparities between theory and practice became more acute for devices with abnormally low current capacity (high contact resistance) and / or turning point field. Curve 8 typified a device which had post-peak concave saturation with greater curvature than its theoretical equivalent (Figure 6.39).

Comparison between  
Theoretical Curve and Real data

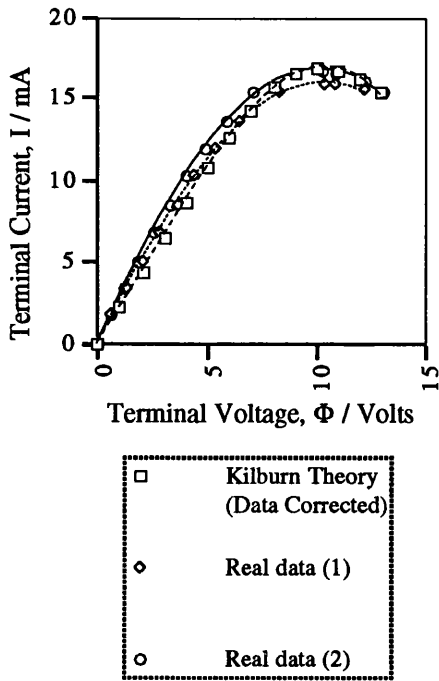


**Figure 6.37**

Absolute value of percentage Error  
between Theory function and Real  
Data 1 and 2 (Curve 22)

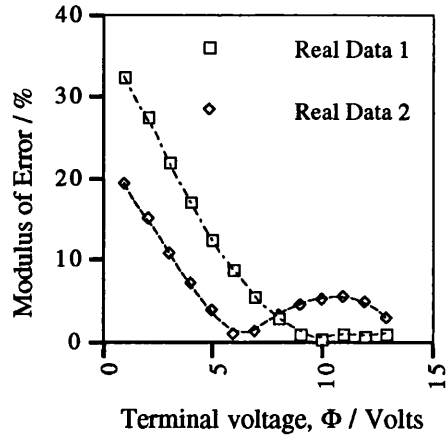


**Figure 6.38**

Comparison between  
Theoretical and Measured Curves

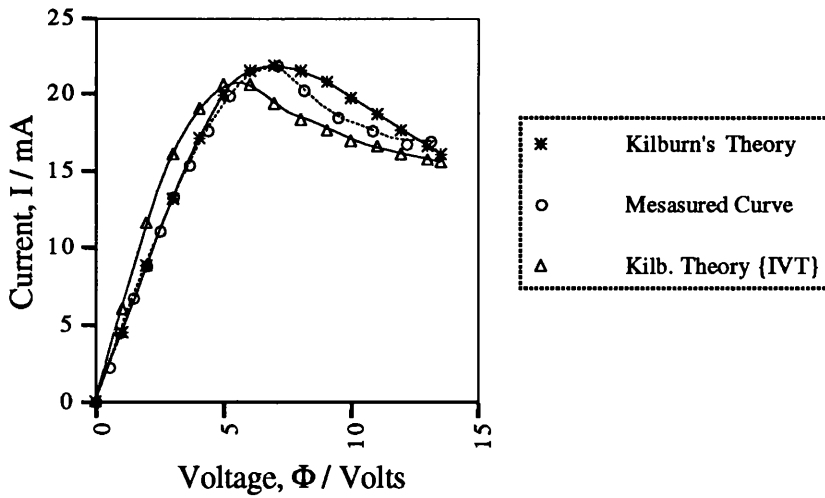


**Figure 6.39**

### 6.5 Conjectured Mechanism For Annealing Dependence

The natural consequence of "well-behaved" cathode boundary conditions is the emergence of orthodox "Gunn" oscillations. As the criteria at the cathode depart from the "perfect", and become "imperfect", unorthodox space charge behaviour emerges. "Gunn" oscillations may develop from these

modes at fields in excess of the inter-valley transfer threshold. Alternatively, Gunn oscillations (i.e. matured dipoles) may be suppressed entirely, and stationary states (monopoles) predominate [19] [20].

All of the above variants were observed in the sizeable array of planar specimens. Current-voltage traces were assessed for their basic shape, and categorised them into three subsets :-

- (1) "Convex" saturation with no discontinuities ;
- (2) "Concave" saturation with no discontinuities ;
- (3) "Concave / convex" saturation with sharp discontinuities.

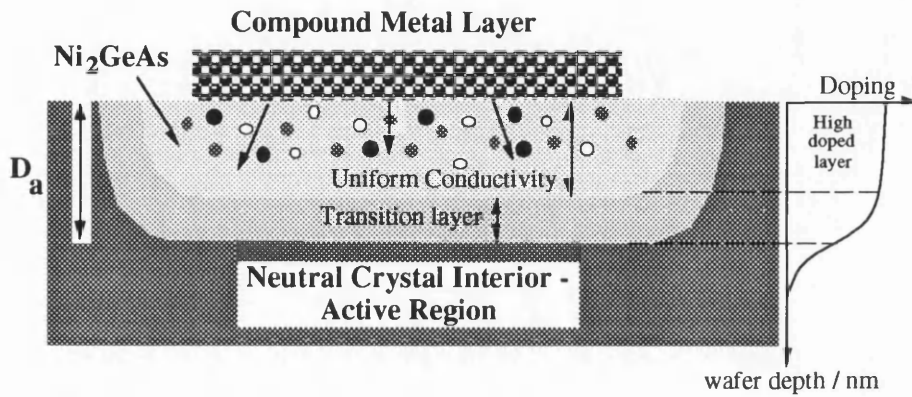


**Figure 6.40 :- Migration of metallic atoms during annealing**

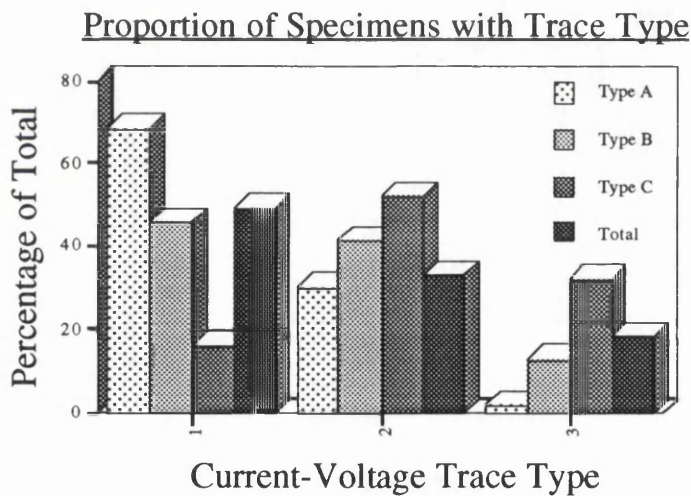


**Figure 6.41**

For Type A, B and C annealing conditions, typical number (%) distributions of these trace types are shown in Figure 6.41. For Type A annealing parameters, type 1 traces predominated, with virtually no type 3 traces evident. Type 1 and 2 trace profiles appeared in similar numbers for Type B samples, while type 3 traces emerged significantly for Type C specimens. A total of 90 devices were used, and a distribution of trace types within the total is given in Figure 6.41. Most devices produced passive type 1 curves, while a smaller proportion were of type 2. Only a small fraction generated

current-voltage profiles with sharp discontinuities associated with dipole disturbance presence. This distribution with annealing parameters could be reconciled with **Kroemer's Control Characteristic Concept**. Two main principles were suggested from Kroemer's analysis :- (i) the further the crossover field is from the inter-valley transfer threshold, the greater the departure of device behaviour from conventional "Gunn" oscillations ; (ii) the nature of spatio-temporal patterns, and the tendency for self-organisation, is determined by the difference in curve gradients at the crossover field ( $F_x$ ).

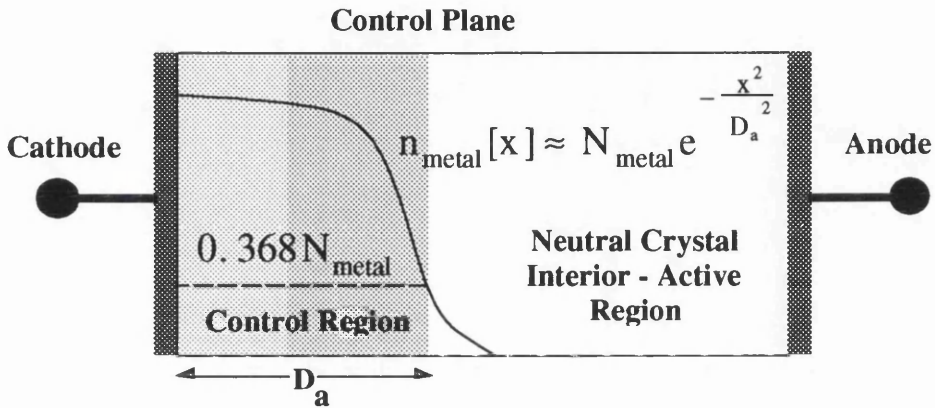


**Figure 6.42 :- Control region definition by metallic infusion**

A conjectured mechanism, accommodating Kroemer's ideology and principles, was then suggested to explain the trends seen in experimental data in this chapter. Initially, it was recognised that the transition from the  $10^{18} \text{ cm}^{-3}$  high-doped layer (100 nm) to the lower-doped active region ( $\approx 10^{16} \text{ cm}^{-3}$ ), was not immediate with wafers grown by MBE. A standard Gaussian was assumed for this transition :-

$$n_{\text{metal}} [x] = N_{\text{metal}} e^{-\frac{x^2}{D_a^2}} \quad \text{--- (6.19)}$$

where  $x$  was the distance from the wafer surface downwards. This distribution was assumed to remain unperturbed in the annealing process. In contrast, the distribution of the infused metallic atoms from the contact was determined by annealing time and temperature. A gaussian spatial variation was also assumed to represent this distribution, with both penetration depth ( $D_a$ ) and surface atom density ( $N_{\text{metal}}$ ) assumed to be arbitrary functions of  $\tau_a$  and  $T_a$ . Hence, consider :-

$$n_{\text{metal}} [x] = N_{\text{metal}} [T_a, \tau_a] e^{-\frac{x^2}{D_a^2 [T_a, \tau_a]}} \quad \text{--- (6.20)}$$

The penetration depth,  $D_a$ , was regarded as signifying the boundary of the **Control Region** in the device (Figure 6.42). The Gaussian distribution suggested that it was comprised of a layer of

pseudo-uniform conductivity, and a transition layer. These transformed the carrier transport properties at the surface to that existing within the **Neutral Crystal Interior** (Figure 6.40).

A further major assumption was that the gold, germanium and nickel atoms acted as efficient carrier-traps at room temperature while no electric field was applied. With localised heating by an applied electric field, the carriers acquire sufficient energy to escape the traps and participate in conduction. Hence, the following field dependence for current-density in the control region could be derived, with  $kT_e < e\Phi_0$ . Net carrier density became :-

$$n_{\text{car}} [x] = n_o[x] - n_{\text{metal}} [x] e^{-\frac{E}{e\Phi_{\text{trap}}}} \quad \text{where} \quad E = \frac{1}{2} m_e \mu_c^2 F_c^2 ; x = D_a ; F \rightarrow F_c \Rightarrow$$

$$J_c[F_c] = n_{\text{car}} [x] e \mu_c F_c = \left\{ N_o e^{-\frac{D_a^2}{D_{\text{dep}}^2}} - 0.368 N_{\text{metal}} e^{-\frac{m_e \mu_c^2 F_c^2}{2e\Phi_{\text{trap}}}} \right\} e \mu_c F_c \dots (6.21)$$

$$\Rightarrow J_c[F_c] = n_o[D_a] \left[ 1 - A_c[D_a] e^{-\frac{F_c^2}{F_{\text{trap}}^2}} \right] e \mu_c F_c ; n_o[D_a(T_a, \tau_a)] = N_o e^{-\frac{D_a^2(T_a, \tau_a)}{D_{\text{dep}}^2}} ;$$

$$A_c[D_a] = \frac{0.368 N_{\text{metal}}}{n_o[D_a(T_a, \tau_a)]} ; F_{\text{trap}} = \sqrt{\frac{2e\Phi_{\text{trap}}}{m_e \mu_c^2(T_a, \tau_a)}} \dots (6.22)$$

### Control Region Characteristic

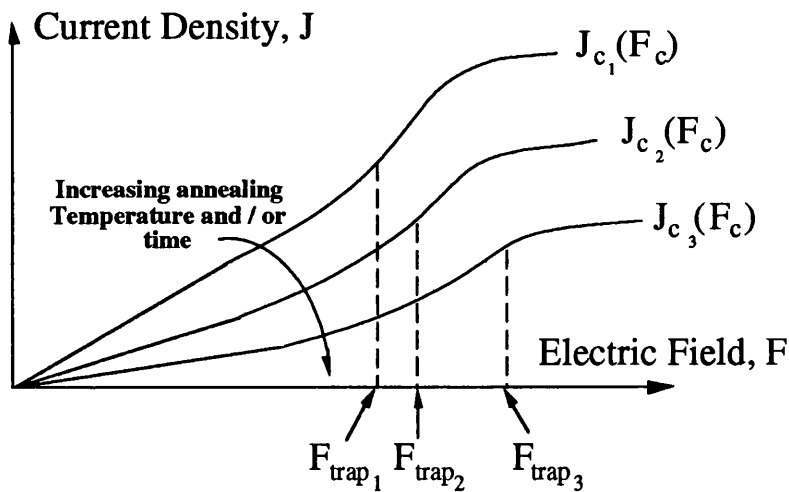


**Figure 6.43 :- Variation of trapping threshold field**

Under the conditions likely to prevail in the sub-surface annealed region, the carrier mobility in the control region,  $\mu_c$ , and hence  $F_{\text{trap}}$ , would be a function of  $\tau_a$  and  $T_a$ . Simple trends, from fundamental principles, were noted for  $\mu_c$ ,  $F_{\text{trap}}$  and  $D_a$  as in the following :-

$$[T_a, \tau_a] \uparrow \Rightarrow D_a[T_a, \tau_a] \uparrow ; \mu_c[T_a, \tau_a] \downarrow ; F_{\text{trap}} [T_a, \tau_a] \uparrow$$

The conjectured variation of  $J_c(F_c)$  was given in Figure 6.43. The current was reduced by increased annealing times and temperatures, as more metallic atoms penetrated deeper into the crystal. Superposing these curves on the neutral crystal interior current density,  $J_n(F_c)$ , different intersection points were possible (Figure 6.44). As  $\tau_a$  and  $T_a$  were increased, the crossover field ( $F_x$ ), and the net difference in curve gradients, were seen to vary.  $F_x$  increased while the gradient difference decreased. These empirical trends coincided with Kroemer's hypothesis. He demonstrated that steep control characteristics (large gradient differential) at the intersection point yielded dipole disturbances. In contrast, nearly "parallel" characteristics were observed to cause stable depletion. These principles coincided with the low proportion of sharp discontinuities seen with devices annealed at higher temperature and / or time. Similarly, an increasing number of sharp discontinuities were observed at lower annealing temperatures and / or times.

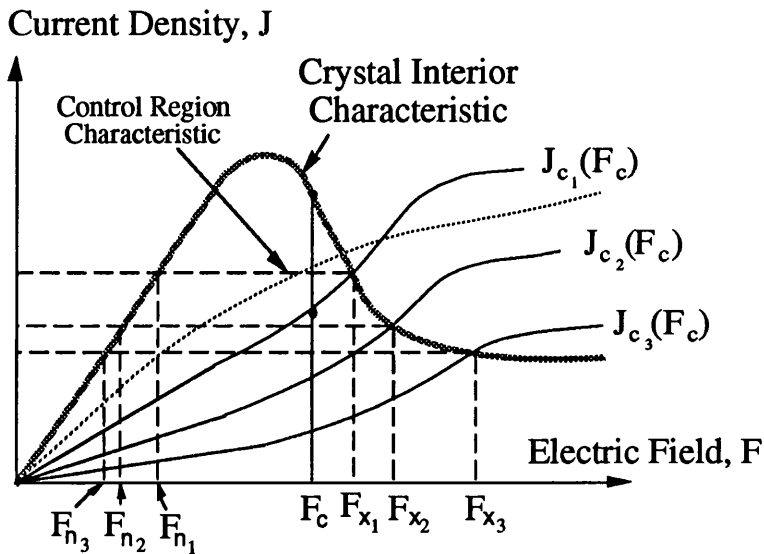


Figure 6.44 :- Intersection between neutral and control characteristics

### 6.6 Injected Cathode Current - the $\eta$ coefficients

An expression for the characteristic decay length was recalled as follows :-

$$\delta[T_a, \tau_a, \Phi] = \frac{\eta_2 [T_a, \tau_a] \beta_{\text{GaAs}} [J_{\text{GaAs}} \{F\}] \Phi^2}{2 \left[ 1 + 2 \frac{L}{w_c} \tan \theta \right]} = \frac{\beta_{\text{ci}} [J_{\text{ci}} \{F_{\text{ci}}\}] \Phi^2}{2 \left[ 1 + 2 \frac{L}{w_c} \tan \theta \right]} \dots (6.23)$$

$\delta[\Phi, \tau_a, T_a]$  was dependent upon the cathode boundary through the annealing parameters. This was quantified in the empirically-derived dimensionless multiplier function,  $\eta_2[\tau_a, T_a]$ . The annealing dependence could be identified as being carried through the **injected cathode current**

density,  $J_{ci}[\tau_a, T_a]$ . This was demonstrated by rearranging the expression for  $\beta$  {Kroemer nomenclature} :-

$$\beta_{ci} [J_{ci} \{ F_{ci} \}] = \eta_2 [T_a, \tau_a] \cdot \beta_{GaAs} [J_{GaAs} \{ F \}] = \frac{\mu_{NDR} \epsilon_{GaAs}}{\left( \frac{J_{GaAs} [F_{ci}]}{\eta_2 [T_a, \tau_a]} \right)^2} \Rightarrow J_{ci} [F_{ci}] = \frac{J_{GaAs} [F_{ci}]}{\eta_2 [T_a, \tau_a]} \quad \dots (6.24)$$

The value of the mobility in the neutral interior,  $\mu_{NDR}$ , the effective active region length,  $L$ , and the dielectric permittivity in GaAs,  $\epsilon_{GaAs}$ , were all invariant with the annealing conditions. The electric field at the metal-semiconductor interface,  $F_{ci}$ , governed the current density of carriers injected directly into the **entrance** of the control region (Figure 6.44). The injected current density,  $J_{ci} [F_{ci}]$ , was entirely distinct from the control plane current density,  $J_c [F_c]$ . Rearranging expressions yielded :-

$$J_{ci} [F_{ci}] = \frac{N_o \mu_{NDR} e F_{ci}}{\eta_2 [T_a, \tau_a]} ; F_{ci} \approx 0.5 - 5.0 \text{ kVcm}^{-1} \quad \dots (6.25)$$

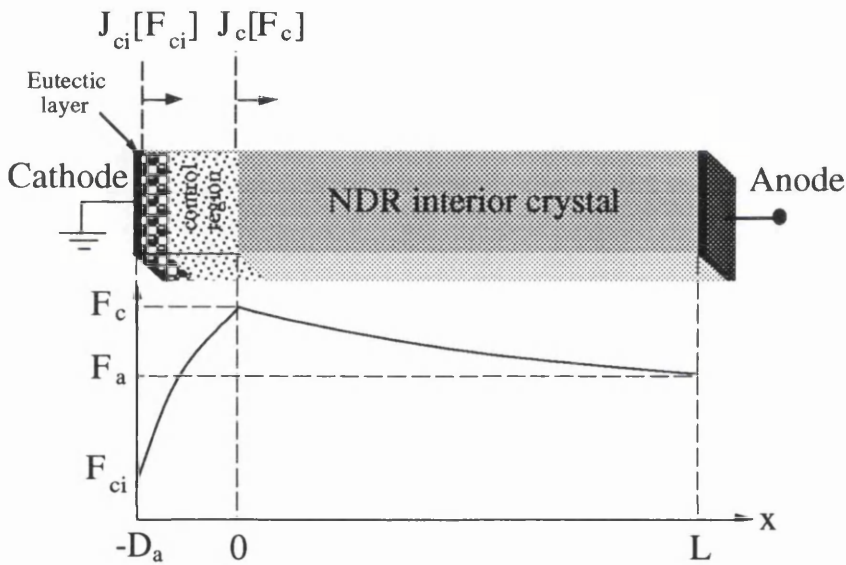
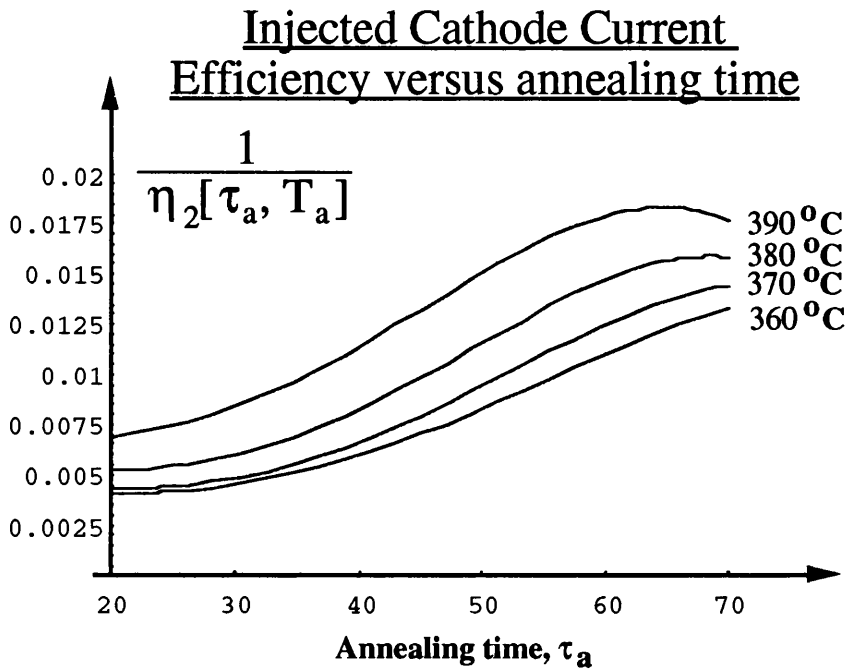


**Figure 6.45 :- Entrance and exit control region current densities**

Data from real current voltage traces in 5000 samples was related to the "shaping" coefficient,  $\eta_2[\tau_a, T_a]$ . In essence,  $\eta_2[\tau_a, T_a]$  mapped out the magnitude variation of the compound dependency of injected cathode current on the annealing parameters. It acted as a functional multiplier of that current density that would have existed in continuous GaAs under the same electric field conditions,  $J_{GaAs}[F_{ci}]$ . The efficiency of current transport from metal to (Ni<sub>2</sub>GeAs sub-layer) semiconductor was therefore shown to be proportional to the inverse of  $\eta_2[\tau_a, T_a]$ , with mobilities of carriers at the immediate interface impeded significantly. The variation of the inverse of  $\eta_2[\tau_a, T_a]$  were shown in

Figures 6.46 and 6.47. Experimentally, it was demonstrated that the characteristic decay length decreased with increasing  $\tau_a$  and  $T_a$ , while current density (and carrier transport efficiency) increased.

The injection limiting effect of contacts annealed at low temperatures and / or times mimicked the role performed by diffusion selectors [40] [88]. However, the presence of space-charge (depletion and/or accumulation) [19] [20] complicates the relation between  $F_{ci}$  and  $F_c$ . It is likely that the natural inclination to space-charge in the crystal leads to an anti-phase relationship between  $J_{ci}$  and  $J_c$ , i.e.  $J_{ci} \uparrow$  as  $J_c \downarrow$ . At the exit of the control region (control plane), and within the region itself, different phenomena influence the current density and carrier population.



The low injection efficiency suggested by these devices demonstrated the existence of a natural potential barrier,  $\Phi_b[\tau_a, T_a]$ , at the metal-semiconductor interface. The level of inhibition was shown to increase as  $\tau_a$  and  $T_a$  were decreased, correlating with a reduction in homogeneity in the eutectic layer beneath the metal. By analogy with current conduction at a p-n junction interface, the injected current density was assumed to be of the form :-

$$J_{ci}[F_{ci}] = \frac{J_{GaAs}[F_{ci}]}{\eta_2[T_a, \tau_a]} \equiv J_{GaAs}[F_{ci}] \left[ e^{\frac{E}{e\Phi_b}} - 1 \right] \Rightarrow \frac{1}{\eta_2[T_a, \tau_a]} \equiv \left[ e^{\frac{m_e \mu_{ci}^2 F_{ci}^2}{2e\Phi_b}} - 1 \right]$$

$$\Rightarrow \frac{F_{ci}}{F_b[T_a, \tau_a]} = \sqrt{\ln \left[ 1 + \frac{1}{\eta_2[T_a, \tau_a]} \right]} \quad \text{where} \quad F_b[T_a, \tau_a] = \sqrt{\frac{2e\Phi_b[T_a, \tau_a]}{m_e \mu_{ci}^2[T_a, \tau_a]}} \quad \text{---(6.26)}$$

Injected Cathode Current Efficiency  
versus annealing temperature

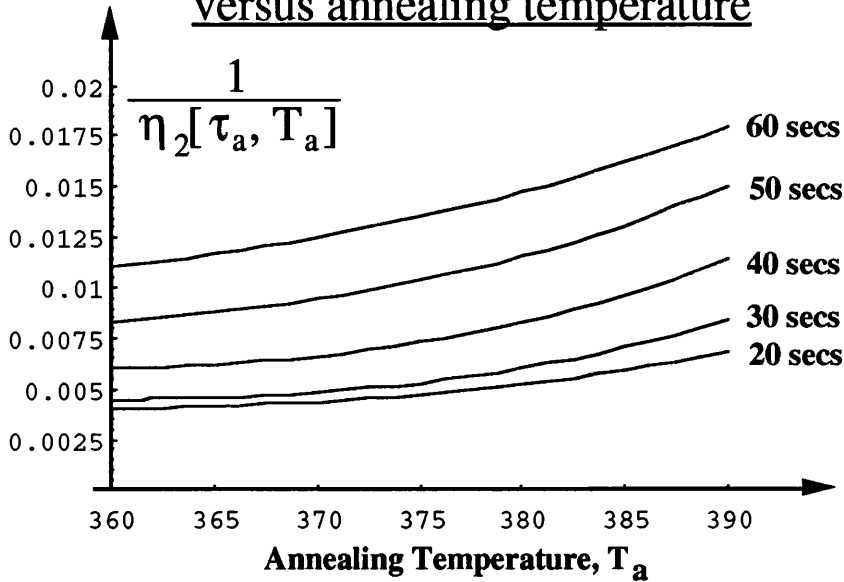


**Figure 6.47**

Only electrons with energy sufficient to surmount the barrier progressed into the control region and neutral interior beyond. Hence, it served the same function as a Schottky contact, doping spike / oxygen damaged zone or notch [40] [71] [77]. The resulting injection field to barrier field ratio was determined with the expression derived in (6.26) as in Figure 6.48.

Cathode Injection Field - Barrier  
Field ratio versus annealing time

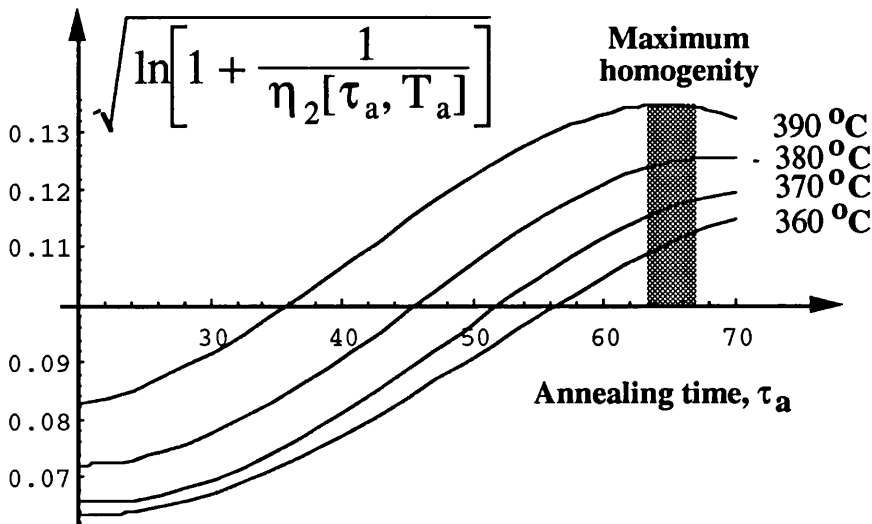


**Figure 6.48**

The barrier field (potential) was demonstrated to vary with the annealing conditions, as expected from fundamental material principles. The field ratio was observed to be an approximate

# "Endfire" Analysis of Wet & Dry Etched Waveguides

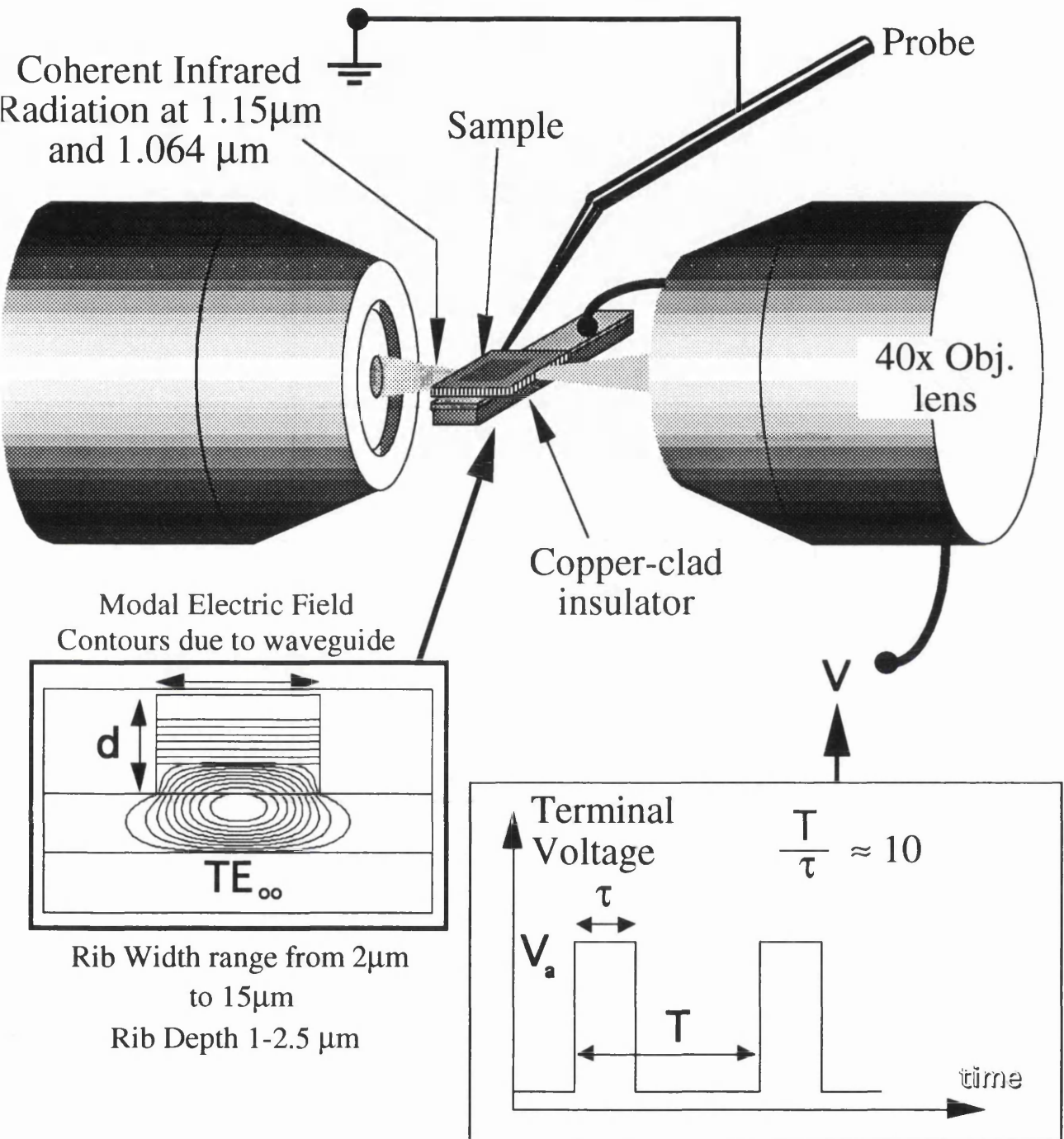


Figure 6.49

scaled version of the turning point field dependency with annealing parameters. An expression for this scaling "constant" with any annealing combination and depletion level was as given in (6.27). For a predetermined value of the injection field {an arbitrary function of depletion voltage}, the barrier field (potential) was estimated through :-

$$F_b [T_a, \tau_a] = \frac{F_{ci} [\Phi_{dep}]}{\sqrt{\ln \left[ 1 + \frac{1}{\eta_2 [T_a, \tau_a]} \right]}} \rightarrow \frac{F_{ci} [\Phi_{dep}]}{\gamma [\Phi_{dep}] \cdot F_{tp} [T_a, \tau_a]} \approx \sqrt{\frac{2e\Phi_b [T_a, \tau_a]}{m_e \mu_{ci}^2 [T_a, \tau_a]}}$$

$$\Rightarrow \gamma [T_a, \tau_a, \Phi_{dep}] \approx \frac{\mu_{ci} [T_a, \tau_a] F_{ci} [\Phi_{dep}]}{F_{tp} [T_a, \tau_a]} \sqrt{\frac{m_e}{2e\Phi_b [T_a, \tau_a]}} \dots (6.27)$$

### **6.7 Optical Experimentation**

To assess the optoelectronic interaction implications of the designed devices, simple experimentation was devised. Radiation at the infrared wavelengths corresponding to 1.15  $\mu\text{m}$  from a He-Ne laser, and 1.064  $\mu\text{m}$  from an extended cavity Nd<sup>3+</sup>: YAG (Yttrium Aluminium Garnet) laser, was used for endfire analysis.

The requirement to apply electrical biasing to the device in-situ, suggested the endfire arrangement shown in Figure 6.49. Two objective lenses (in microscope mounts, 20  $\times$  or 40  $\times$ ) were positioned using "Photon Control" x-y-z manipulators, to align their centre focus (principal axes) with the entrance and exit facets of the rib waveguides. The need to communicate with both the input and output facets of the waveguide (0.5 - 1.0 mm apart) meant that the access window available for electrical biasing was severely restricted. A summary of the problems addressed in this experiment were given in the table of Figure 6.50. Side-wall vertical devices, with substrate "blanket" anode contacts, were mounted on a piece of copper clad PCB, as a complete chip of six devices. Waveguides extended up to 6 mm in length. The cathode contact was accessed through a needle probe and associated manipulator, while the device-bound chip itself was secured by silver-dag or carbon paste. The revised vertical structure, with two top surface contacts, required two individual needle probes for electrical communication. 500-1000  $\mu\text{m}$  waveguide devices were common for the dual anode vertical version. The overall arrangement for experimentation was as shown in Figure 6.51, comprising :- (i) an FPI-25 TecOptics Fabry-Perot interferometer with continuously adjustable free spectral range (FSR) ; (ii) the biasing apparatus and endfire assembly with overhead-mounted zoom microscope (Findlay

optics). Devices were ordinarily too small to probe by eye, and hence a microscope was required (vertically mounted).

Task / Requirement	Potential Problem
(I) Probing of the device with needle probes i.e. electrical communication	<ul style="list-style-type: none"> <li>(a) needle probes prevented alignment through the manoeuvring of the DM1 manipulator</li> <li>(b) Probes progressively destroyed the bonding pads of the device</li> <li>(c) Mechanical relaxation of the probes manipulators applied stress upon the surface of the chip, causing mis-alignment of the waveguide</li> </ul>
(II) Guiding of radiation entering and exiting the rib waveguide	<ul style="list-style-type: none"> <li>(a) For 4 <math>\mu\text{m}</math> by 4 <math>\mu\text{m}</math> facets, objective lenses were required to be very close to the chip for focussing</li> <li>(b) Restriction of the space necessary for electrical access</li> <li>(c) Optical fibre communication was rendered impractical in the absence of dedicated fibre manipulators. Free space interferometry not possible with fibre</li> </ul>
(III) Generation of appropriate bias pulses for the device	<ul style="list-style-type: none"> <li>(a) Philips PG 140 capable of very short pulses (approx. 1 ns), but only up to 5 Volts maximum (too low)</li> <li>(b) Hewlett Packard HP 48 generator provided 20 -30 Volt pulses, with a minimum width of the order of 1 <math>\mu\text{s}</math> (too long)</li> <li>(c) Cable Bandwidth limited for short pulses (distortion of pulse at the device end)</li> </ul>
(IV) Detection and display / analysis of the output signal	<ul style="list-style-type: none"> <li>(a) Semiconductor detectors of limited bandwidth (18 GHz), sensitivity with low absorption coefficient at 1064 nm</li> <li>(b) Oscilloscope display not fast enough for real time analysis. maximum bandwidth of spectrum analyser only 21 GHz</li> <li>(c) Incorrect wavelength (1064 nm) only available. A laser of sufficient power at the correct wavelength of 1.3 <math>\mu\text{m}</math> was not available</li> <li>(d) Finesse of the Fabry-Perot system less than 10 (minimum resolvable bandwidth too large, and stop band signal too large)</li> </ul>

**Figure 6.50 :- Problem assessment table for endfire experimentation**

Efforts to measure oscillation and light modulation in this environment were made using Fabry-Perot interferometry [89] [90] for detection. The conventional approach using semiconductor photodetectors was also pursued, but with limitations imposed by the wavelength of radiation (1064 nm) and the inherent bandwidth of the detector. Commercially available photodetectors (e.g. doped germanium, silicon, InGaAs, avalanche photodetectors (APDs)) offered maximum bandwidths in the analogue domain of 18 GHz. Frequencies in the region of 20 - 21 GHz could be only be measured by inference from the evanescent response characteristics of these detectors. In addition, the sensitivity and noise performance at these frequencies were also significantly depreciated. Optimum absorption was not possible in these detectors for super-micron wavelengths. In contrast, the Fabry-Perot technique

was not subject to practical bandwidth limitations, only minimum resolvable bandwidth limited its efficacy. This was in essence detection in the frequency domain, as opposed to real-time detection in the time domain. The former represented the spectral content of the signal, while the latter indicated a transformed version of the temporal evolution of the signal.

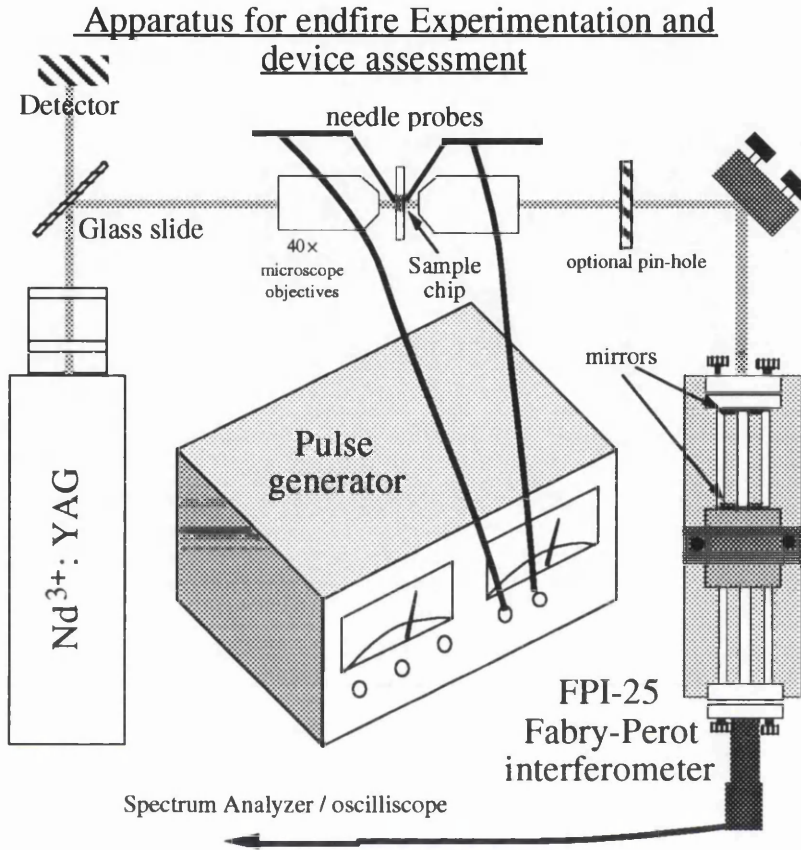
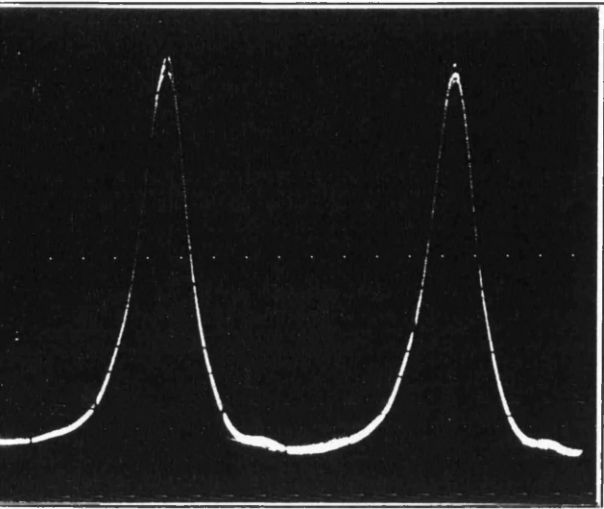


**Figure 6.51 :- Endfire apparatus (over-head microscope omitted)**

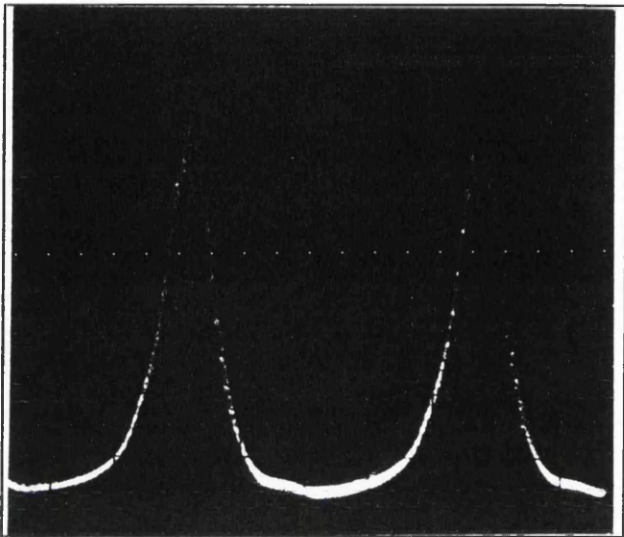
The output display device was either a fast oscilloscope (30 GHz sweep) or a spectrum analyzer (Tektronix 492). Infrared radiation was admitted into the rib waveguide of the vertical and planar devices. Electrical biasing voltage pulses were applied across the device in situ through communicating needle probes. Pulse widths were varied between  $1\ \mu\text{s}$  and  $5\ \mu\text{s}$  within the limitations the Hewlett Packard HP48 and Philips PG 140 pulse generators. After re-adjustments of the objective lens positions to re-optimize the radiation mode and power throughput, the emergent beam was fed into the input of the interferometer. The output (analogue electrical) from the integrated germanium detector in the FPI-25 was displayed on a storage screen oscilloscope.

After conducting the experiment, with an assortment of bias pulse widths and duty cycles, the output as shown in Figure 6.52 was observed. In the absence of separate spikes indicating stable

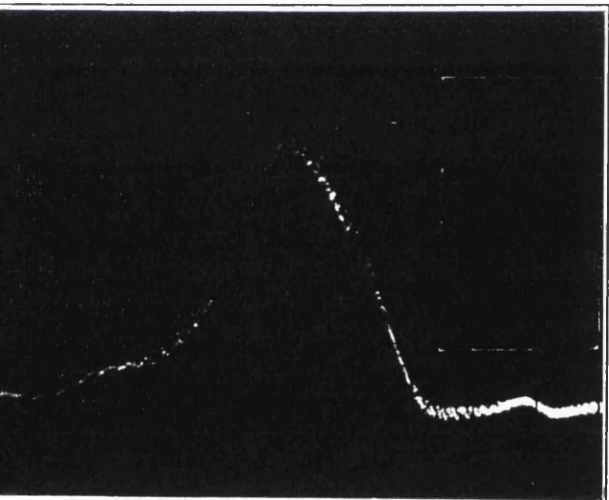
**"Modulation "due to heating -induced absorption by application of pulses**



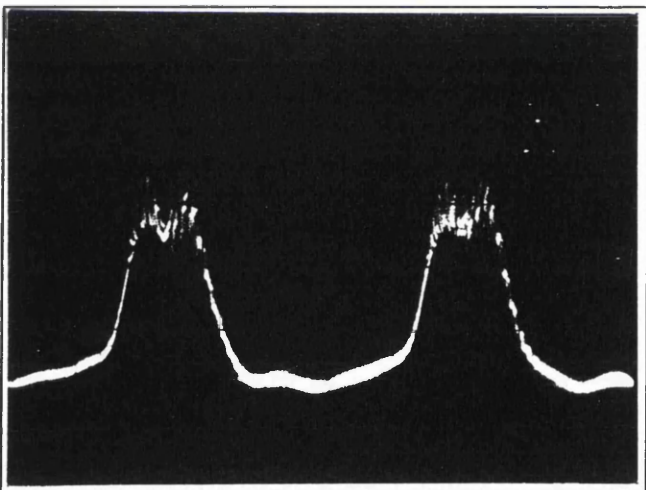
*Low finesse Fabry-Perot trace without pulse application*



*Application of pulses causes AM perturbations on the trace*

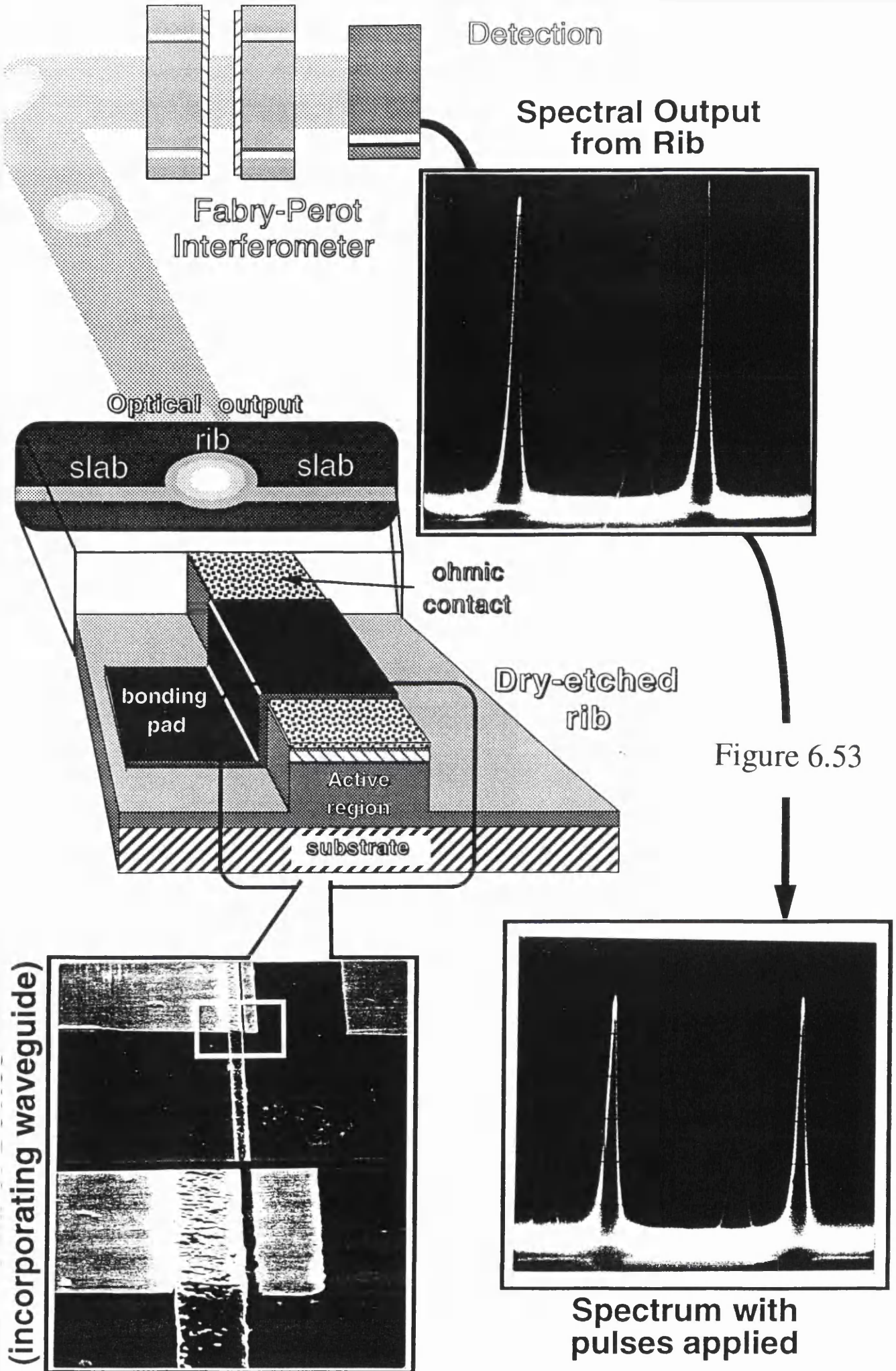


*Expanded trace of that above*



*Degradation of trace due to excessive thermal energy*

**Figure 6.52**



frequency modulation, many smaller amplitude perturbations were superposed upon the whole trace. These corresponded to the effects of thermal power dissipation within the duration of each individual pulse. This voltage pulse, when coupled with current flow, generated "joule" heating of the fabric of the device. Subsequently, the absorption of near band-gap radiation was enhanced by the crystal temperature rise in the duration of each pulse. The perturbation of the signal reaching the detector through the etalon was transferred to the trace shown (two scanned orders shown). This was a form of amplitude modulation (AM), which did not appear as an identifiable secondary peak. Separate transit mode oscillations were not sustained in this or any other device of its format. The presence of clearly detectable thermal effects had significant implications for the vertical device type, with high aspect ratio contacts.

Similar experimentation was performed using the original side-wall structure vertical device, as illustrated in Figure 6.53. No evidence of coherent oscillatory output was observed on either Fabry-Perot interferometer, or conventional silicon or InGaAs p-i-n detectors. The latter were of limited use at the natural 20 GHz potential oscillations, since active regions were generally shorter than the physical intercontact separation.

### **6.8 Simple Resonant Circuit**

Efforts to achieve oscillation were made in a simple resistive environment. A purely resistive cavity could not be achieved due to natural spurious inductance and capacitance incurred through solder, wiring and the nature of real elements at elevated frequencies. The addition of deliberate inductance and capacitance created a resonant circuit or cavity.

The resonant circuit had to exclude D.C. from the output stage, while high frequency R.F. was to be prevented from entering the input of the bias source generator. A single high Q-factor circuit design was produced to cover the anticipated variance in natural frequency of operation in vertical or planar devices. A low-pass input filter section, band-pass filter output section, and global ground plane were included in this circuit to normalise device potential. Planar microstrip circuits had been exploited previously [4] [9] in a variety of applications. It was considered appropriate in these circumstances also. The material combination chosen for its implementation was gold metallisation on gallium arsenide semi-insulating substrate. Gallium arsenide had a large dielectric constant of 12.9, and contained the electromagnetic field distribution in the plane of the circuit. Natural field leakage into the

air around the top surface of the asymmetrical geometry was expected with simple microstrip circuits. The gold was required in a very thick layer ( $> 500$  nm) to minimise series transmission losses, and to carry the large currents necessary to bias the device with inherently large current capacities. The substrate thickness was standardised at  $450\ \mu\text{m}$ , with a high quality wafer sample (2.5 " diameter), intended for use in epitaxial growth by the M.B.E. facility, being used for this purpose. Computer aided design software packages were used to design the physical layout, and optimise the spectral performance of the design. With anticipated natural frequencies in the range 20-40 GHz, only distributed elements were considered feasible. In addition to the design of the circuit pattern itself, a connector-bearing housing was required to hold the wafer and the circuit substrate. Signal coupling in such an arrangement was achieved through commercial "Sealectro K-connectors" (single-moded from D.C. to 18 GHz). The housing itself was milled from a soft metal i.e. Aluminium, to permit fabrication of smaller features.

A coplanar-form upper surface ground plane was incorporated into the circuit, allowing the most convenient contact of the device to be communicated with by appropriate bond-wires. The cathode of the revised vertical or planar implementations were bonded to the ground plane using direct bond, with epoxy resin fixation being used to secure the chip. This is shown in Figure 6.54. The side-wall structure vertical device was adjoined to the ground plane with the anode contact communicating with the plane.

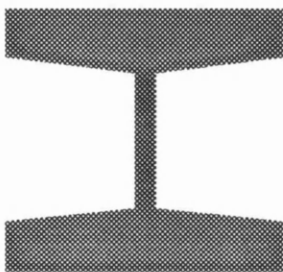


**Figure 6.54 :- Ground plane**

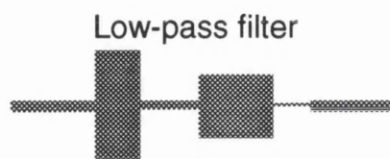


**Figure 6.55[a] :- Low-pass filter**

To filter out any any return high frequency RF from the input of the bias source generator, a low pass filter was implemented in distributed passive elements. The filter was constituted of series connected microstrip of varying length, width and hence characteristic impedance (Figures 6.55[a] and 6.55[b]). The alternating high (narrow) and low (wide) impedance lines generated the intended alternating inductances and capacitances respectively. Impedance-matched termination line sections of

fifty ohm characteristic impedance were used. To establish high levels of transmission (> 90 %) in a 20-40 GHz bandwidth window, at least five sections of a coupled line filter were required for the output section (Figure 6.56).

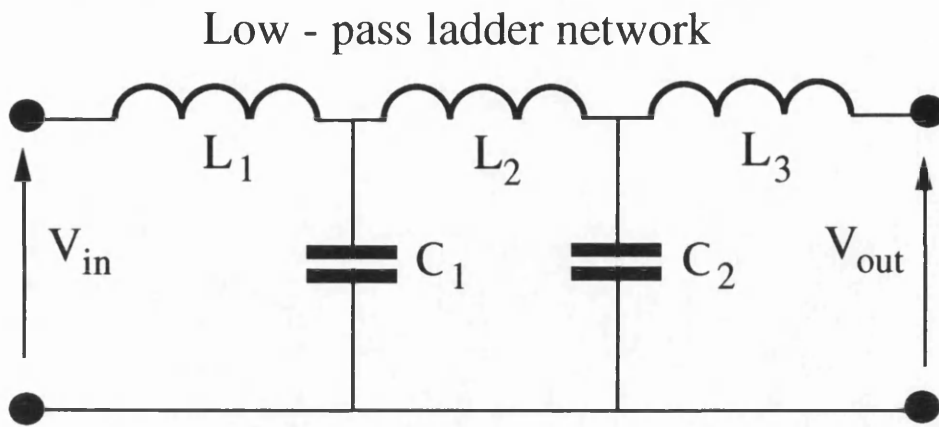


Figure 6.55[b] :- Low-pass ladder network

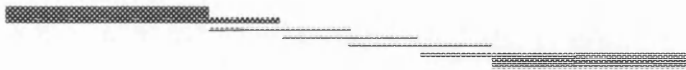


Figure 6.56 :- Output section band-pass filter

"K" connectors were bonded to the gold of the circuit through ceramic beads (0 - 46.5 GHz) at the edge of the housing box. The output was analysed with a Tektronix 492 spectrum analyser. An example of the bonding of a planar device into the circuit is given in Figure 6.57 and the Photograph of Figure 6.58. The splaying of the ends of the 25  $\mu\text{m}$  diameter wire severely restricted the area onto which bonding could be achieved. The two wires were displaced laterally relative to each other, so as to alleviate this difficulty and to prevent inadvertent shorting of the device, with the general arrangement shown in Figure 6.57. The Fourier harmonic implications of the sharp pulses (small rise and fall times) were observed on the spectrum analyser, as shown in Figure 6.59.

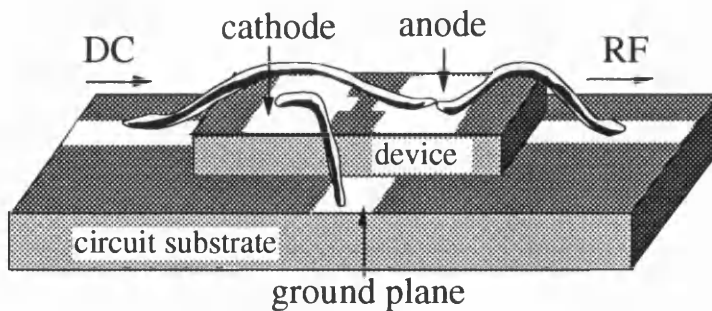
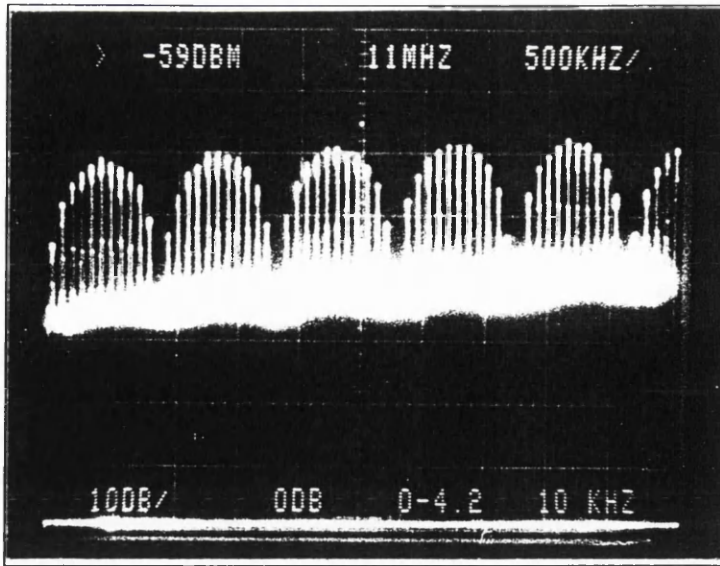
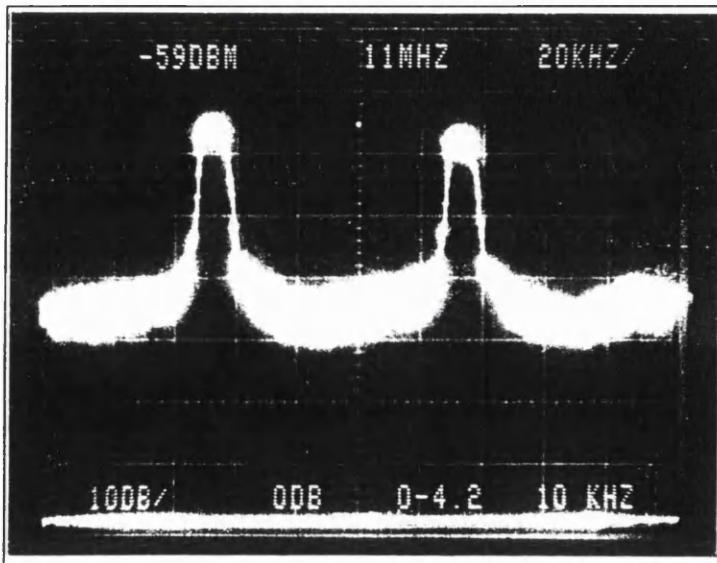


Figure 6.57 :- General bond-wire arrangement for in-situ biasing

Output Traces from Spectrum Analyser



Low frequency Fourier harmonics from sharp bias pulses



Expanded trace of that above

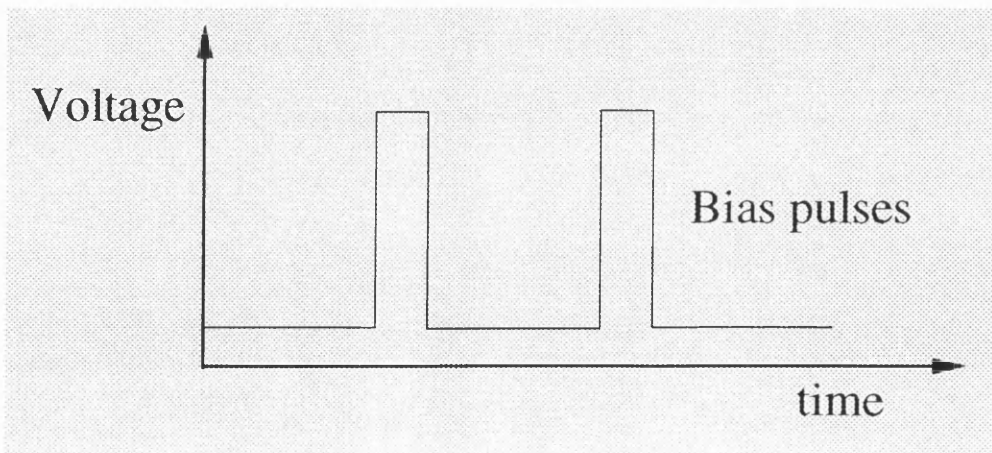
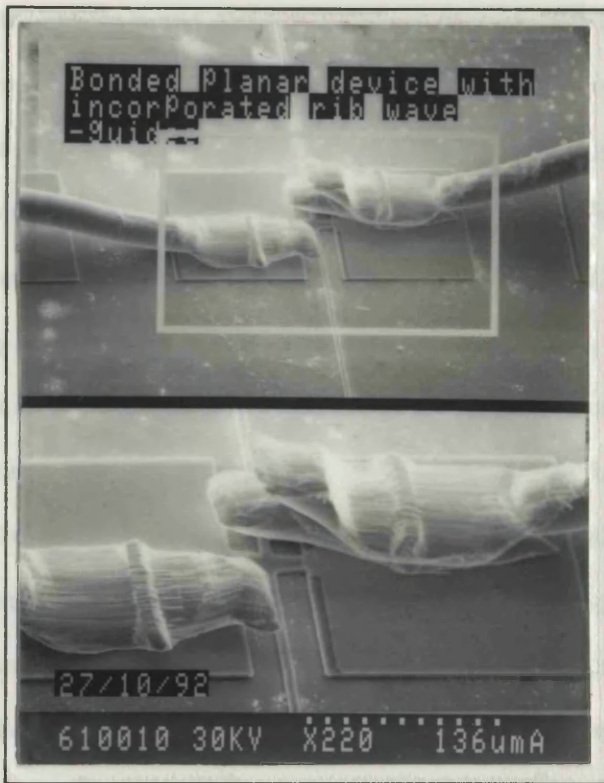


Figure 6.59



**Scanning Electron Microscope Photograph of two-wire (25  $\mu\text{m}$  diameter) bonding arrangement with a planar device in-situ**

**Figure 6.58**

## **6.9 Conclusions**

Experimentation was devised, and an appropriate rig constructed, to attempt to observe modulation events due to optoelectronic interaction. Application of large bias pulses to either the side-wall structure or the revised rib-waveguide vertical devices failed to initiate oscillations prior to thermal annihilation. In the absence of oscillatory activity, no high frequency modulation was observed.

Many unsuitable features of the device structures and the methods of analysis were identified from this experimentation. The inability to acquire a necessary level of heat-sinking, electrical access (non-destructive) in-situ or pulses of sufficient narrowness were all cited as primary inadequacies. These factors culminated in continuous premature thermal disruption of the fabric of the device. The very high aspect ratio of the contacts, was observed to restrict the appearance of dipole disturbances. No evidence of the formation of any spatio-temporal patterns were observed on DC current-voltage traces or spectrum analysers (frequency domain). It was concluded (from empirical observation) that the natural threshold field for oscillations (crossover field) was either in excess of, or in the vicinity of, that threshold signifying destructive thermal waves. In all devices eutectic filaments (AuGe) were perceived to emerge between contacts at elevated bias fields at the instant of annihilation. The MBE grown wafer material was shown to be consistently susceptible to these shorting filaments, hence

rendering the devices invalid. This may have been due to the high level of crystal uniformity and purity with wafer material grown by MBE at the in-house facility (University of Glasgow). In other growth methods, e.g. MOVPE, the level of the impurities are higher, and their nature suitable for reducing mobilities of infusant metallic atoms, (e.g. methyl groups  $\text{CH}_3$ ). This was concluded as being a probable explanation for the high-field fragility of the MBE n-GaAs. It critically reduced the probability of modulation.

In Chapter 4, details were given of the fabrication process of both vertical and planar devices, in which the practical requirements of contact application and their annealing was discussed. It was stated that extra inserted layers (AlGaAs HEI and doping spikes) effectively (superficially) shielded the active region from incursion of the annealed ternary phase alloy  $\text{Ni}_2\text{GeAs}$ , in the case of the vertical devices. A region of low resistivity degenerate metal-semiconductor material was present beneath the metallisation [91] [92] [93]. The same shielding effect, in the absence of these device layers, was not afforded by the planar equivalent. Hence these devices were susceptible and sensitive to the exact composition of metallisation and annealing times and temperatures used to formulate contacts. The cathode contact could be viewed as the injecting interface, while the anode could be regarded as the collecting interface for conduction carriers in the element.

Throughout the discussion of contact types and technology, the generic term "ohmic" was used. Ohmicity was required for effective device operation. Most theoretical evaluations of the transferred electron effect, or any other semiconductor device (e.g. lasers), assume phenomenological ohmicity of the contacts. This implies that there were no injection, accumulation or carrier retardation processes associated with the contact. Ohmicity, by definition, occurs where there is a continuity of all the parameters governing particle transport between the contact region and the interior crystal of the semiconductor. Certain parameters, such as carrier mobility and dielectric constant, governing drift and displacement currents respectively, cannot be continuous between e.g. the ternary phase alloy  $\text{Ni}_2\text{GeAs}$  and gallium arsenide. Consequently, phenomenological ohmicity cannot be supported in real contact technologies. The Au/Ge/Ni/Au regime on n-GaAs approaches ohmicity through continuous global current-voltage characteristics through the origin. A straight line through the origin, by virtue of the global integral nature of mean current at the terminals, was not a guarantee of absolute ohmicity. Ternary phase alloy layers, immediately adjacent with the potential NDR region were responsible for

creating imperfect boundary conditions at the cathode. Increasing annealing temperatures was expected to increase the depth of penetration of nickel, gold and germanium atoms into the active region. The populations of these atoms could be modified by using different ratios of their elements in the metal recipe. The interstitial nature of nickel and gold meant that marked variations in the relative distributions of these elements were expected with temperature of annealing, and separately with annealing time. Deliberate variations in the cathode boundary were then attempted through modifications of the annealing conditions. Extended annealing times were likely to allow the eutectic layer and nickel to penetrate further into the active region. The density and nature of impurity atoms varied between material. The invariance of the band structure meant that inter-valley transfer itself was not directly affected. However, the predominance and spectral distribution of phonons within the material was dependent upon the presence of impurities [76]. Successful inter-valley transfer required transformation of the electron wave-vector (to  $\langle 100 \rangle$ ) through the collision with a sufficiently energetic polar optical phonon. It was assumed that the electron environment was of significance in the success of disturbance formation. This transport environment was determined at a local (inter-atomic) level i.e. microscopically, and sensitive to the "quality" of the GaAs crystal. The exact control characteristic, and that of the neutral crystal interior, would have been determined by such factors. Its relative profile, and not the absolute value of the contact resistance, dictates the activity occurring within the devices [19] [20] [21].

Recalling the analysis of Bonilla and Higuera [21] [22], it was seen from a non-linear dynamic system treatment that a low resistivity contact was expected to nucleate a monopole. Wherever the contact resistivity was in excess of some threshold value, dipoles were nucleated, matured and propagated. The critical resistivity suggested by Bonilla and Higuera may have resided between that created by Type C annealing conditions, and that by increased germanium content. Dipoles appeared in the higher resistivity samples, and monopoles in the lower. For even lower resistivity contacts, no activity was evident.

The following was concluded regarding the application of the curve-matching functions :-

(1) The semi-analytical current-voltage expression ( $I[\Phi]$ ) was developed assuming a steady-state exponentially-decaying electric field distribution. It was regarded as being unperturbed by the presence of matured dipole disturbances. This function was applicable to short devices where disturbance

magnitude was inhibited by insufficient propagation length / time [79] [80] [81]. In devices where fully-matured dipoles were suspected, sharp discontinuities were observed in traces, which were modelled by the multiplier function. These discontinuities were preceded by a section of unperturbed trace with minimal departure from the theory function.

(2) The  $I(\Phi)$  function was regarded as semi-analytical, due to approximations and the incorporation of strategic coefficients ( $\eta_0$ ,  $\eta_1$ ,  $\eta_2$ ). It's ability to predict the underlying nature of the current-voltage trace, and its transformation with annealing temperature and time demonstrated its predictive worth. The general function was developed from fundamental semiconductor principles.

(3) Significant disparities between theoretical and measured traces were attributed to the following :-  
(i) the anomalous nature of a particular device, due to contact non-uniformity (uneven annealing), microplasmas, spurious impact avalanche events, major crystal imperfections etc. ; (ii) the non-incorporation of the waveguide in the original theory ; (iii) susceptibility to current-filamentation and thermal degradation. A device was deemed "unorthodox" or "anomalous" by comparing its D.C. current voltage traces with that theoretically predicted. The theory function was formed from highly-correlated data from a large number of orthodox samples. Unusually high or low peak current, turning point field or low-field "ohmic" gradient were all regarded as anomalies.

(4) Throughout the curve-fitting procedure, the  $\eta_1$  coefficient had been set and maintained at the default value of  $\eta_1 = 100$  {average value of  $\eta_2$ }. It was omitted from dependency relations (with physical parameters) for reasons of clarity and simplicity. The  $\eta_2$  functions were of significant complexity even with constant  $\eta_1$  - superposing an  $\eta_1$  dependency upon this would generate an overall  $I[\Phi]$  function of too great a complexity.

Several conclusions were drawn from the experimental assessment of the annealing dependence and the conjectured mechanism as follows :-

(1) Increased annealing (temperature and/or time) was seen to reduce the effective barrier potential,  $\Phi_b[\tau_a, T_a]$ , promoting electron transmission from metal  $\rightarrow$  eutectic  $\rightarrow$  semiconductor ;

(2) A maxima with  $T_a$  was encountered for the injection field-barrier field ratio. This was thought to correspond to minimum barrier potential and / or maximum homogeneity between metal and semiconductor ;

(3) The low injection efficiencies suggested by the inverse of  $\eta_2[\tau_a, T_a]$  was due primarily to the assumption of a fixed  $10 \text{ kVcm}^{-1}$  field at the entrance of the control region. More reasonable carrier transmission values e.g. 10-15 % could be inferred from lower fields, e.g.  $F_{ci} = 1 \text{ kVcm}^{-1}$  ;

(4) The trends identified in the experimental analysis correlated with observations and hypotheses of Kroemer [20], Bonilla and Higuera [21] [22] and others [71] [72]. Thim [94] recognised the importance of a uniform electric field distribution in the active region. Atalla et al [71] (1969) and Hariu et al [72] (1970) acknowledged the benefits of an injection-limited cathode in securing large-signal oscillations. It was demonstrated that a more direct method of cathode injection limitation was to control the conditions of annealing in the Au/Ge/Ni/Au contact technology. Through this awareness of contacts, the natural yield of LSA, hybrid, and resonant Gunn mode TEDs could be dramatically increased.

(5) In reality, the environment for carrier transport may differ in detailed terms from that proposed. Despite this, the general phenomena of annealing parameter control of the cathode boundary conditions still applies. In the earlier years of TED fabrication, much higher resistivity contact technologies with much smaller atomic penetration depths, were used (e.g. Tin on GaAs). The combined effect with lower quality crystal specimens was the provision of more naturally appropriate conditions for "Gunn" oscillations. It was concluded that the Au/Ge/Ni/Au recipe, developed specifically to provide low resistivities in lasers and FETs, was inappropriate for high-yield TED fabrication.

The Kroemer hypothesis was presented in terms of an identifiable "crossover" field between the intervalley transfer characteristic of the interior crystal, and that unique characteristic imposed by the arbitrary eutectic layer of the contact. The value of the crossover field, relative to the  $3.2 \text{ kVcm}^{-1}$  intervalley transfer threshold field in n-GaAs, ultimately determined the natural internal processes of the device. The device could offer spatio-temporal pattern formation, or simply remain non-oscillatory upto the elevated fields associated with impact ionisation and hence avalanche breakdown. The absence of "concave" saturation or sharp discontinuities in the profile indicated that the device was likely to remain "oscillatory passive", i.e. the conditions for a constructive crossover field value were not met at the cathode boundary. The shape of this cathode current density characteristic determined the crossover field (if such an intersection exists at all), irrespective of the monopole / dipole distinction controlled by contact resistivity. However, there was likely to be a natural relationship

between these two properties of the eutectic layer. To isolate transit mode operation, a very specific combination of criteria had to be satisfied. The window of satisfaction of these criteria in the case of modern ohmic contact technology was narrow, since the gold-germanium based system was optimised for FETs and semiconductor lasers. Natural low resistivities were likely to reduce crossover fields, and initiate sub-optimum monopole disturbances. In the context of the fabricated devices, these situations were to be avoided.

# Chapter 7

## Thermal Feasibility of Vertical Devices

### 7.1 Simple Thermal Resistance Calculations

In previous analyses [95] [96] [97], the concept of the **thermal resistance** of a conducting element has been employed. Inspiration was drawn from its **electrical analogy**. Power division with multipath thermal energy flow is dictated by the relative values of  $R_{\theta}$ , the thermal resistance attributed to a power-guiding element. It characterises the ability of a physical element in resisting the flow of **thermal flux**, when subjected to a temperature differential or gradient. The Ohm's law and  $R_{\theta}$  equivalence was as defined in (7.1) [95] :-

$$R_{\theta} = \frac{h}{\kappa A} \Leftrightarrow R_{elec} = \frac{L}{\sigma A} \quad \Delta T = P_d R_{\theta} \Leftrightarrow V = IR_{elec} \quad \kappa = \rho C_p \alpha \Leftrightarrow ne \mu \quad \text{---- (7.1)}$$

where  $\kappa$  is the **thermal conductivity** of the conducting element, and was defined by analogy in terms of the **thermal diffusivity** ( $\alpha$ ) of energy in the element. For the purposes of future calculations it was assumed that [95] :-

$$P_d \rightarrow 1 \text{ W} \Rightarrow \int_{T_1}^{T_2} dT = T_2 - T_1 = \Delta T \equiv R_{\theta} ; \quad T_{surface} = T_{ambient} + P_d R_{\theta_{Total}} \quad \text{---- (7.2)}$$

Integration of the spatial temperature distribution, when normalised to 1W of thermal power flow and evaluated between extrema, yields the averaged  $R_{\theta}$  for the bulk element [96] [97]. An equivalent circuit representation of the thermal outflow was derived, which incorporated all the paths available for dispersion of thermal energy from the source plane.

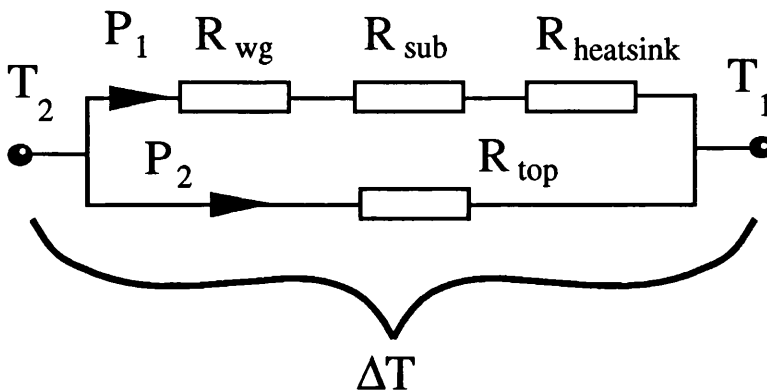


**Figure 7.1 :- Equivalent thermal resistance circuit**

The source of the thermal energy was resistive Joule heating with electrical current flow. Two paths for sinking were shown, the first through the top plane (minimal due to thermal isolation) and

the second through the waveguide, substrate and semi-infinite heatsink in series. The total thermal resistance was evaluated by a simple summation :-

$$R_{\text{Total}} = R_{\text{wg}} + R_{\text{sub}} + R_{\text{hs}} \dots (7.3)$$

and power division occurred in each arm of the circuit.

### 7.2 Thermal Resistance of defined Structures

A functional variation of the power flow direction with the spatial variable must be determined. Previous methods [98] [99] [100] [101] [102] [103] have used a linear dependency with the orthogonal variable (i.e. element thickness, h) e.g. to evaluate the spreading resistance of a circular mesa via a "spreading cone". Little previous work had been performed for waveguide sections, hence this was attempted. In more complex topologies, the functional form is not intuitively obvious, but a reliable first order estimate can be obtained by assuming a linear variation. In the following, this linear variation was imposed upon the rib waveguide / substrate structure. The volume of material below the rib (and hence the source plane) was decomposed into infinitesimally small sections, of thickness  $\delta h$ , and with a temperature differential of  $\delta T$  (Figure 7.2).  $dT/dh$  was then derived.

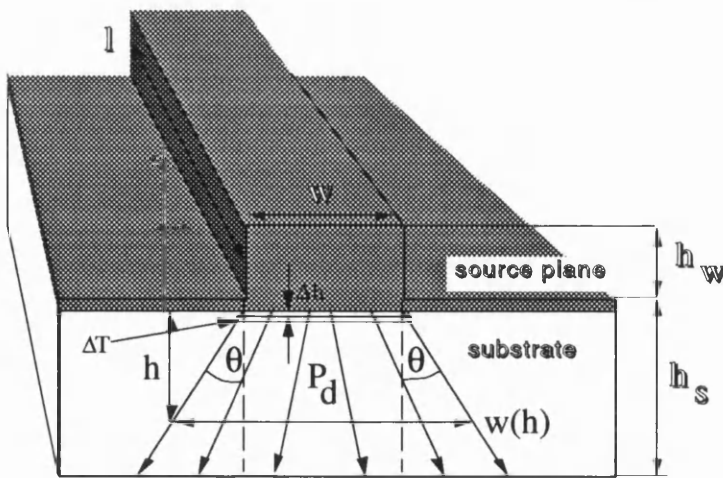


Figure 7.2 :- Thermal outflow through the substrate

The situation shown in Figure 7.2 was considered initially, where  $w$  denotes rib-width,  $l$  denotes rib-length,  $m = \tan \theta$  described the gradient and  $h_s$  was the substrate thickness. A function  $A(h)$  which controlled the variation of the area over which thermal flux flows was inserted into expression (7.1) :-

$$A[h] = 2Lw[h] = 2L\left(\frac{w}{2} + mh\right) \Rightarrow \Delta T \equiv R_{\theta} = \frac{\Delta h}{2\kappa L\left(\frac{w}{2} + mh\right)} \Rightarrow \frac{d(\Delta T)}{d(\Delta h)} = \frac{\frac{w}{2}}{2\kappa L\left[mh + \frac{w}{2}\right]^2} \dots (7.4)$$

The definite integration of (7.4) for the normalised value of  $P_a = 1W$ , evaluated between the limits 0 to  $h_s$  offered the thermal resistance of the element :-

$$T_2 - T_1 = \Delta T = \int_{T_1}^{T_2} dT = \frac{1}{2\kappa L} \int_0^{h_s} \left\{ \frac{\frac{w}{2}}{\left[ mh + \frac{w}{2} \right]^2} \right\} dh = \frac{w}{4m\kappa L} \left[ \frac{1}{\left[ mh + \frac{w}{2} \right]} \right]_0^{h_s} \Rightarrow R_\theta = \frac{h_s}{2\kappa L \left[ mh_s + \frac{w}{2} \right]} \quad \text{---- (7.5)}$$

(NB :- this was equivalent to substituting  $h_s/2$  into equation (7.4), i.e. it served as simple averaging of the cross-sectional area.)

### 7.3 Thermal Calculations with Uniform Current Density

Estimates were made of the **minimum** active region temperature that resulted from current flow in rib-waveguide devices of varying dimensions. Possible variants included rib width, rib length, substrate thickness and etch depth.  $\Delta T$  evaluations were performed assuming minimum electric fields in the active region were  $>3 \text{ kVcm}^{-1}$ . This was defined as the threshold field for critical intervalley transfer in GaAs. The field for the onset of Transit Mode oscillations could be an order of magnitude greater than this value. The thermal resistances of the rib and substrate in series were stated from expressions (7.1) and (7.5) respectively, where the etch depth of the rib was  $h_r$ , and its length  $L$  :-

$$R_{\text{rib}} = \frac{h_r}{\kappa w L} \quad ; \quad R_{\text{substrate}} = \frac{h_s}{2\kappa L \left( mh_s + \frac{w}{2} \right)} \quad \text{where} \quad m \rightarrow 1 \quad \text{---- (7.6)}$$

Heatsinks were assumed to be semi-infinite relative to the other components. The use of a highly thermally conductive material, like copper/gold combinations, substantially reduced the thermal resistance to power flow away from the device ( $\kappa_{\text{GaAs}} = 0.121 \text{ WcmK}^{-1}$  ;  $\kappa_{\text{Cu}} = 1.09 \text{ WcmK}^{-1}$ ). The effective spreading radius of the heat flow in the copper heatsink was obtained at the substrate / heatsink interface. The expression for the thermal resistance of a semi-infinite heatsink due to Holway & Adlerstein (1971) [97] was :-

$$R_{\text{heat sink}} = \frac{1}{\kappa_{\text{Cu}} \pi r_{\text{spread}}} \quad \text{where} \quad w[h_s] \cdot L \equiv \pi r_{\text{spread}}^2 \Rightarrow r_{\text{spread}} = \sqrt{\frac{2L}{\pi} \left( mh_s + \frac{w}{2} \right)} \quad \text{--- (7.7)}$$

and an effective spreading radius of the annular flow approximated. Temperature elevation was evaluated through  $\Delta T = \text{Power supplied} \times R_{\text{Total}}$ , where DC to RF conversion efficiencies were assumed less than 5%, leading to :-

$$P_{\text{elec}} \equiv P_{\text{thermal}} = IV = n_o A v_e V = \frac{n_o A \mu e V^2}{h_r} \quad \text{where} \quad E \geq E_{\text{th}} \Rightarrow V \geq h_r \mu m \times 0.32 \text{ V} \mu m^{-1} \quad \text{---- (7.8)}$$

$$T_{\text{rib}} \geq 25 \text{ } ^\circ\text{C} + \frac{n_o A \mu e V^2}{h_r} \times \left[ \frac{h_r}{\kappa_{\text{GaAs}} w L} + \frac{h_s}{2\kappa_{\text{GaAs}} L \left( m h_s + \frac{w}{2} \right)} + \frac{1}{\kappa_{\text{Cu}} \sqrt{2L\pi \left( m h_s + \frac{w}{2} \right)}} \right] \quad \text{----- (7.9)}$$

where the thermal resistance of the solder had been omitted.

### 7.3.1 Numerical Calculations for Typical Devices

Minimum optoelectronic interaction lengths in vertical waveguide devices were no less than 1500  $\mu\text{m}$  (1.5 mm). At the wavelength of operation (1064 nm), a waveguide of width  $\geq 4 \mu\text{m}$  was imposed to avoid radiation loss through cut-off. The standard inequality for transit mode operation in GaAs linked the active region width ( $h_r$ ) and the background doping density ( $n_o$ ):-  $n_o L \geq 10^{-12} \text{ cm}^{-2}$  and  $f_{\text{GHz}} \times L_{\mu\text{m}} \approx 100$ . Standard values of constants and typical values of parameters used in simulations included :-

$$\begin{aligned} e &= 1.06021892 \times 10^{-19} \text{ C} & \mu &= 8000 \text{ cm}^2 \text{ V}^{-1} \text{ s}^{-1} & n_o &= 3 \times 10^{16} \rightarrow 1 \times 10^{17} \text{ cm}^{-3} \\ w &= 4 \rightarrow 15 \mu\text{m} & L &= 1500 \rightarrow 6000 \mu\text{m} & h_s &= 200 \rightarrow 450 \mu\text{m} \\ \kappa_{\text{GaAs}} &= 0.121 \text{ WcmK}^{-1} & \kappa_{\text{Cu}} &= 1.09 \text{ WcmK}^{-1} \end{aligned}$$

Thermal resistances of **rib**, **substrate** and **heatsink** elements considered separately, were calculated with expressions (7.6) and (7.7). The **global** temperature change due to all the elements in summation was then evaluated. Considering the element closest to the source plane initially, the thermal resistance of the rib had the variation in the width-length plane illustrated in Figure 7.3. It's main feature was a maxima (in the range considered) at the lower  $wl$  product values. As the width and/or length increased, the resistance decreased. Sensitivity to both length and width was observed. This was fundamentally predictable, since as the area decreases ( $wl$  product), there was a reduction in spatial spreading of the thermal flux lines in the media through which conduction occurs. The variation in substrate thermal resistance differed significantly from the rib in that it was insensitive to rib width for sizeable substrate thicknesses (i.e  $h_s = 450 \mu\text{m}$ ). It was highly dependent upon the length of the waveguide, with a large rate of change experienced with this variable (Figure 7.4). Values of thermal resistance were smaller for the thinner substrate than the thicker substrate at corresponding points in the width-length plane. The absolute values of substrate thermal resistance were lower than that for the rib, due to the absence of thermal flux spreading in the rib, in contrast to the substrate. The previous two elements were formed from GaAs, while the heatsink was formed from copper. The significantly lower thermal resistances in comparison to GaAs were due to the very high thermal conductivity of copper.

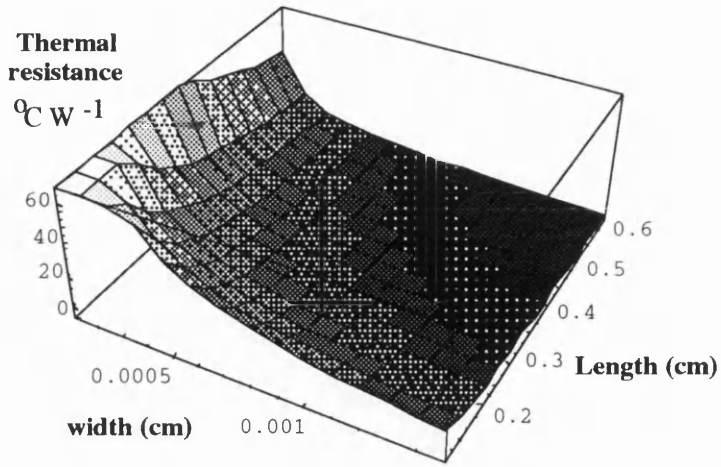


Figure 7.3 :- Thermal resistance due to rib ( $h_r = 3 \mu\text{m}$ )

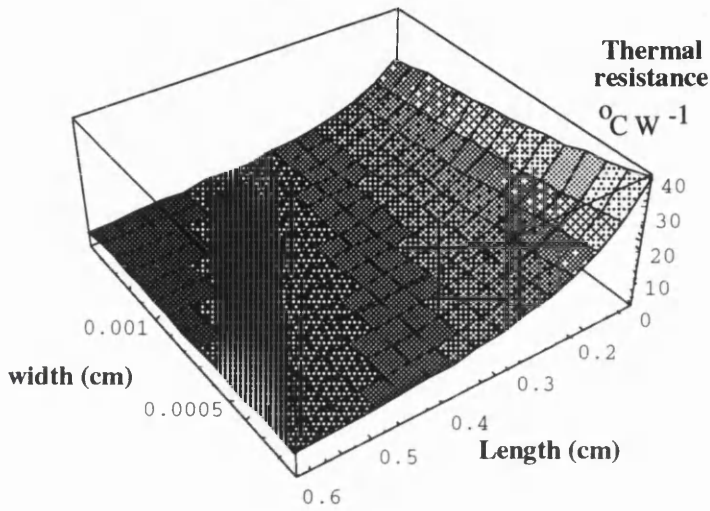


Figure 7.4 :- Substrate Thermal resistance ( $h_s = 50 \mu\text{m}$ )

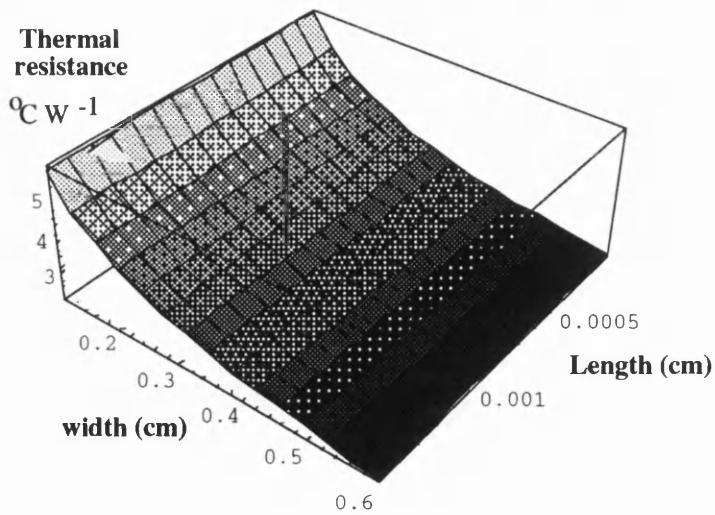
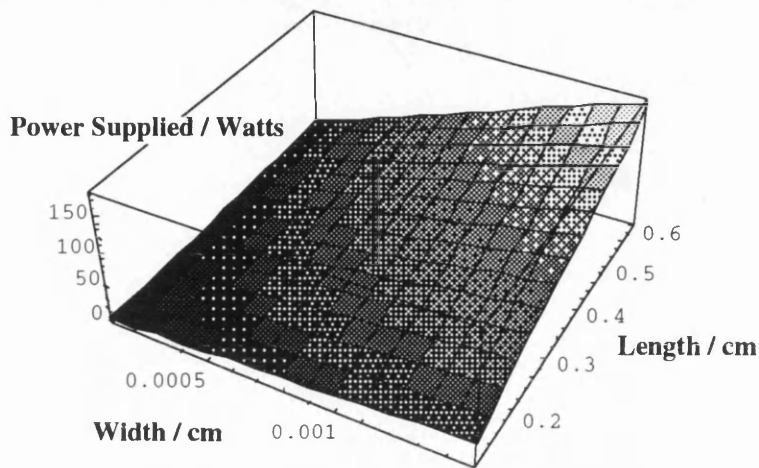


Figure 7.5 :- Resistance due to heatsink

The heatsink resistance was fundamentally insensitive to the waveguide width (Figure 7.5), while the very low values of thermal resistance justified its status as a **heatsink**, since it provided a low resistance path away from the source element.

### 7.3.2 Temperature increase due to electrical biasing

The CW electrical power supplied to element was stated in expression (7.8). The presence of area in the equation implied a variation in the width-length plane. Since the width and length of the guide appeared in simple product form, with all the other components effectively constants, the power multiplier was an acutely-angled flat plane, biased towards L. This was illustrated in Figure 7.6.



**Figure 7.6 :- Thermal power vector**

The global temperature increase,  $\Delta T$ , experienced near to the source plane, was evaluated initially through the summation of the contributions to the total thermal resistance, followed by multiplication by the power vector value. The variation of  $\Delta T$  was shown in Figure 7.7.  $\Delta T$  was observed to be highly dependent upon the width of the waveguide, and relatively insensitive to the length. As the width decreased,  $\Delta T$  increased as predicted from fundamental principles.

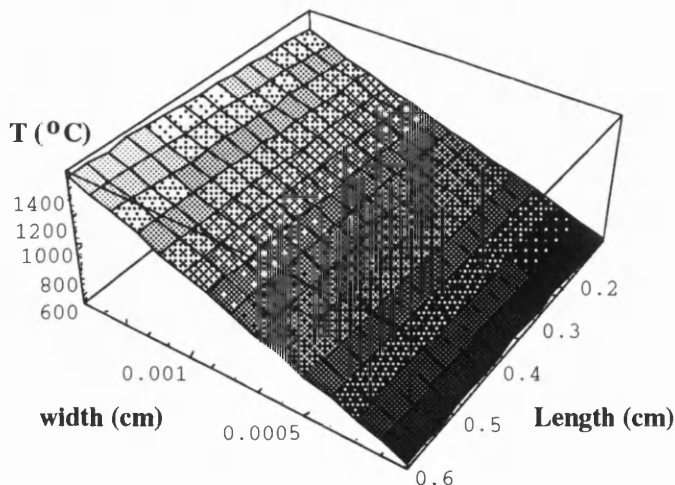


**Figure 7.7 :-  $\Delta T$  for  $h_r = 5 \mu\text{m}$ ,  $h_s = 450 \mu\text{m}$**

### 7.4 Temperature Rise with Pulsed Operation

To avoid thermal annihilation, pulsed biasing was required. To account for the finite thermal rise times (thermal time constants), the concept of **thermal capacitance** was introduced, and was defined as follows [97] :-

$$C_{\text{thermal}} = \frac{4}{\pi^2} h A \rho C_p \dots (7.10)$$

where  $h$  was the element thickness,  $A$  was the cross-sectional area,  $\rho$  was the density of the medium and  $C_p$  was the specific heat capacity. A thermal capacitance was appropriated to each physical component of the device (i.e. rib, substrate, heatsink). They were positioned shorted to ground, in parallel with thermal resistances, in the simple ladder network shown in Figure 7.8. Capacitances limited the rate of temperature rise, and defined characteristic thermal time constants.

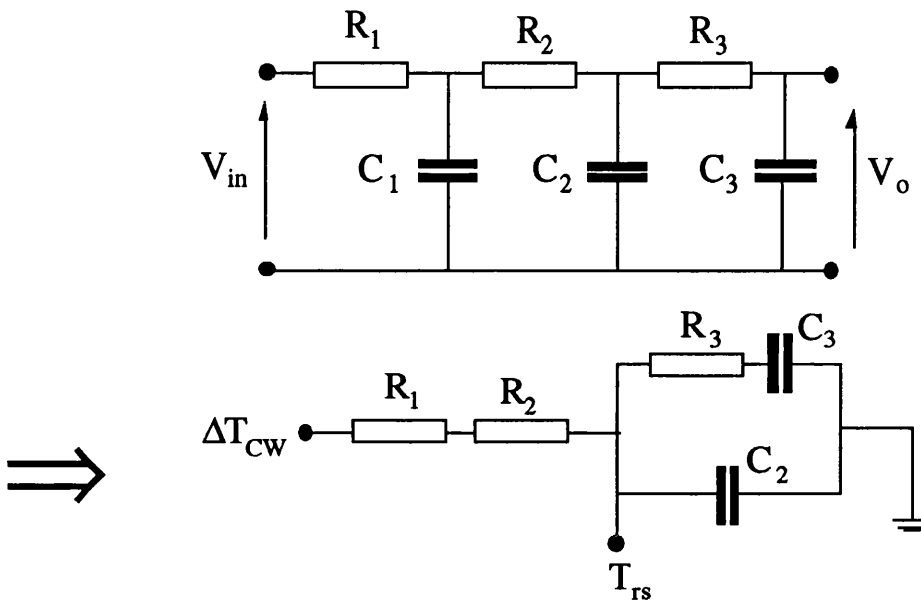


**Figure 7.8 :- Thermal analogue ladder network**

The input to the "circuit" was the Continuous Wave (CW) temperature value, i.e. that temperature reached after transient effects due to thermal capacitance had subsided. Capacitance  $C_1$  was omitted due to its large magnitude, simplifying the circuit and its analysis. Elements given the subscript "1" represented the heatsink, "2" the substrate, and "3" the rib waveguide. Thermal resistances and capacitances were evaluated from the following :-

$$R_{\text{rib}} = \frac{h_r}{\kappa_{\text{GaAs}} w L} ; R_{\text{sub}} = \frac{h_s}{2 \kappa_{\text{GaAs}} L \left( m h_s + \frac{w}{2} \right)} ; R_{\text{hs}} = \frac{1}{\kappa_{\text{Cu}} \sqrt{2 L \pi \left( m h_s + \frac{w}{2} \right)}}$$

$$C_{\text{rib}} = \frac{4}{\pi^2} h_r w L \rho C_p ; C_{\text{sub}} = \frac{8}{\pi^2} h_s L \left( m h_s + \frac{w}{2} \right) \rho C_p ; C_{\text{hs}} = L \kappa_{\text{Cu}} \left( m h_s + \frac{w}{2} \right) \sqrt{\frac{\pi^5 \tau_p}{D \alpha_{\text{Cu}}}}$$

where  $\tau_p$  = pulse width and  $D$  = duty cycle appropriate to pulsed operation. The functional variations of these resistances and capacitances were given in Figures 7.9 - 7.14 for the rib, substrate and heatsink respectively.

**Thermal Resistance of Rib section**

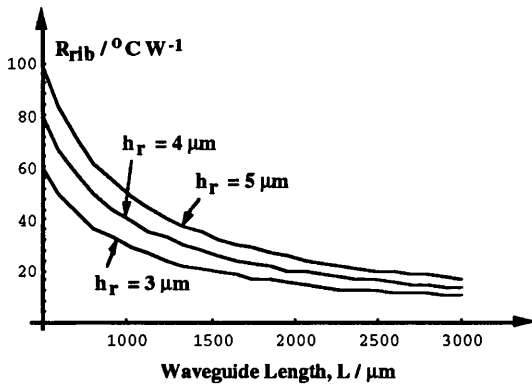


**Figure 7.9**

**Thermal Capacitance of the rib section**

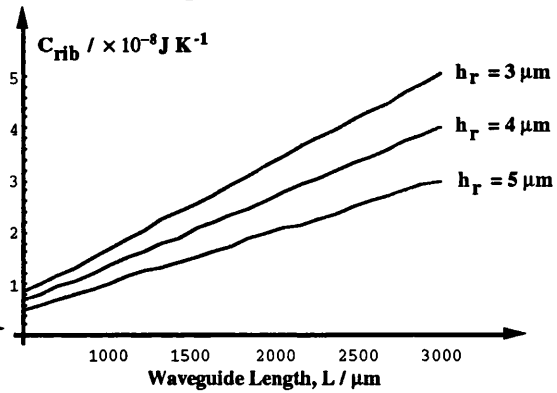


**Figure 7.10**

**Thermal Resistance of Substrate**

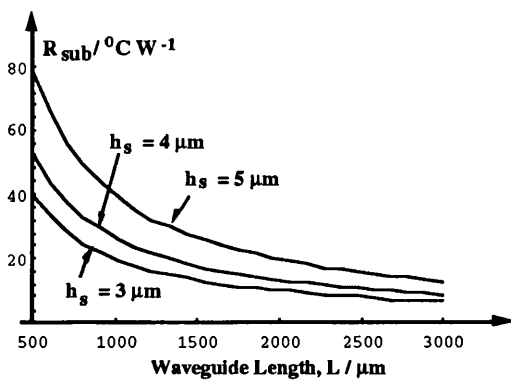


**Figure 7.11**

**Thermal Capacitance of the Substrate**

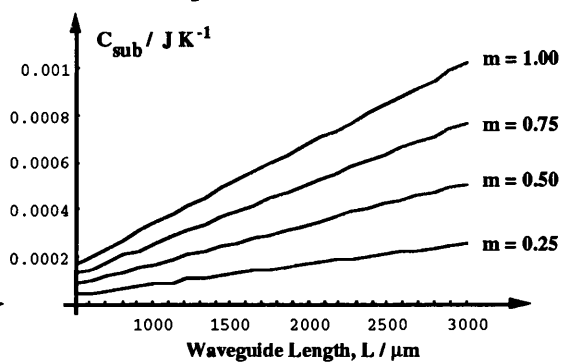


**Figure 7.12**

**Thermal Resistance of Heatsink**

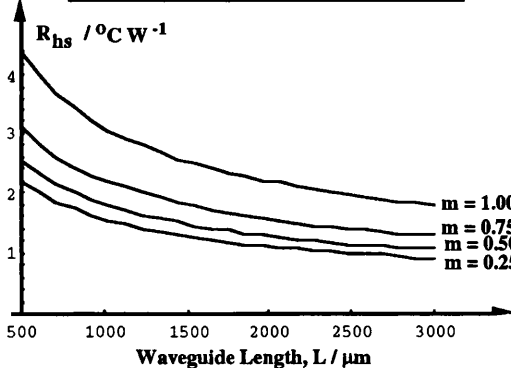


**Figure 7.13**

**Thermal Capacitance of the Heatsink**

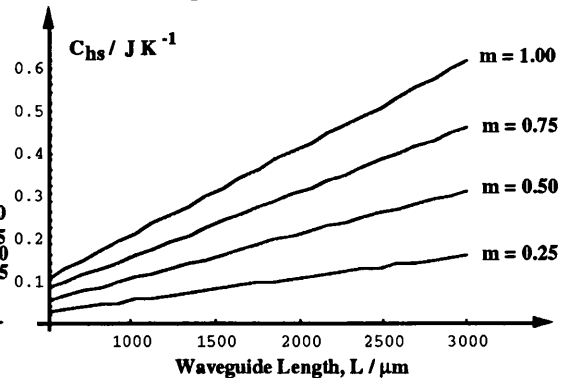


**Figure 7.14**

**7.4.1 Evaluation of the Temperature at the Rib-Substrate Interface**

The effective temperature at the intersection of rib and substrate in the equivalent circuit, was found as in the following. Simple potential division indicated that :-

$$\begin{aligned} \frac{T_{rs}}{\Delta T_{cw}} &= \frac{\frac{1}{j\omega C_2} \left\| \left( R_3 + \frac{1}{j\omega C_3} \right) \right\|}{[R_1 + R_2] + \left\{ \frac{1}{j\omega C_2} \left\| \left( R_3 + \frac{1}{j\omega C_3} \right) \right\| \right\}} = \frac{\frac{1}{s[C_2 + C_3]} \left[ \frac{1 + s\tau_1}{1 + s\tau_2} \right]}{[R_1 + R_2] + \frac{1}{s[C_2 + C_3]} \left[ \frac{1 + s\tau_1}{1 + s\tau_2} \right]} \\ &\Rightarrow \frac{T_{rs}[s]}{\Delta T_{cw}[s]} = \frac{1 + s\tau_1}{\alpha\tau_2 s^2 + [\alpha + \tau_1]s + 1} \rightarrow \frac{1}{\alpha\tau_2} \frac{1 + s\tau_1}{\left[ s + \frac{1}{\tau_3} \right] \left[ s + \frac{1}{\tau_4} \right]} \\ \tau_3 &= \frac{1}{\left[ \frac{\alpha + \tau_1}{\alpha\tau_2} \right] \left\{ 1 + \sqrt{1 - \frac{4\alpha\tau_2}{[\alpha + \tau_1]^2}} \right\}} ; \tau_4 = \frac{1}{\left[ \frac{\alpha + \tau_1}{\alpha\tau_2} \right] \left\{ 1 + \sqrt{1 - \frac{4\alpha\tau_2}{[\alpha + \tau_1]^2}} \right\}} \dots (7.11) \end{aligned}$$

$$s \equiv j\omega ; \tau_1 = R_3 C_3 ; \tau_2 = \frac{C_2 C_3 R_3}{C_2 + C_3} ; \alpha = [R_1 + R_2][C_2 + C_3] \dots (7.12)$$

The "s" notation was necessary for Laplace Transform representation. Separate characteristic time constants ( $\tau_1$  and  $\tau_2$ ) were identified from combinations of  $R_1$ ,  $R_2$ ,  $C_2$ , and  $C_3$ . Rationalisation yielded a quadratic denominator and linear numerator for the s-domain transfer function.

$\tau_4$  was three orders of magnitude (ms) greater than  $\tau_3$ ( $\mu$ s), with fundamentally different variations with the parameters chosen (Figure 7.15). The rate of exponential growth with  $\tau_4$  was significantly lower than for the  $\tau_3$  component.  $\tau_3$  was demonstrated to increase with the spreading gradient and the substrate thickness, while it was invariant with the waveguide length. In contrast,  $\tau_4$  was shown to be only slightly dependent upon the spreading gradient and variant with the waveguide length (Figure 7.16).

## 7.4.2 Application of Laplace Transforms

The variation of the rib-substrate temperature in the time domain was obtained from the frequency domain definition of  $T_{rs}[s]$  with the Laplace transform pair as follows :-

$$\begin{aligned} F[s] &= L[f(t)] = \int_0^{\infty} f(t)e^{-st} dt \Leftrightarrow \frac{1}{2\pi} \int_0^{\infty} F[s]e^{st} ds ; v_i(t) \leftrightarrow V_i[s] ; v_o(t) \leftrightarrow V_o[s] \\ V_o[s] &= H[s]V_i[s] \Rightarrow v_o(t) = \frac{1}{2\pi} \int_0^{\infty} H[s]V_i[s]e^{st} ds \dots (7.13) \end{aligned}$$

It was assumed that the input to the circuit,  $\Delta T_{cw}$ , was an instantaneous rise in temperature under CW operation. The input function in the s-domain ( $\Delta T_{cw}[s]$ ), and the time domain variation ( $T_{rs}(t)$ ) were given by :-

$$\Delta T_{cw}[s] = \frac{\Delta T_{cw}}{s} \Rightarrow T_{rs}(t) = \frac{1}{2\pi} \left[ \frac{\Delta T_{cw}}{\alpha\tau_2} \right] \int_0^{\infty} \left\{ \frac{1 + s\tau_1}{\left[ s + \frac{1}{\tau_3} \right] \left[ s + \frac{1}{\tau_4} \right]} \right\} e^{st} ds \dots (7.14)$$

**Exponential Characteristic Time Constant,  $\tau_2$**

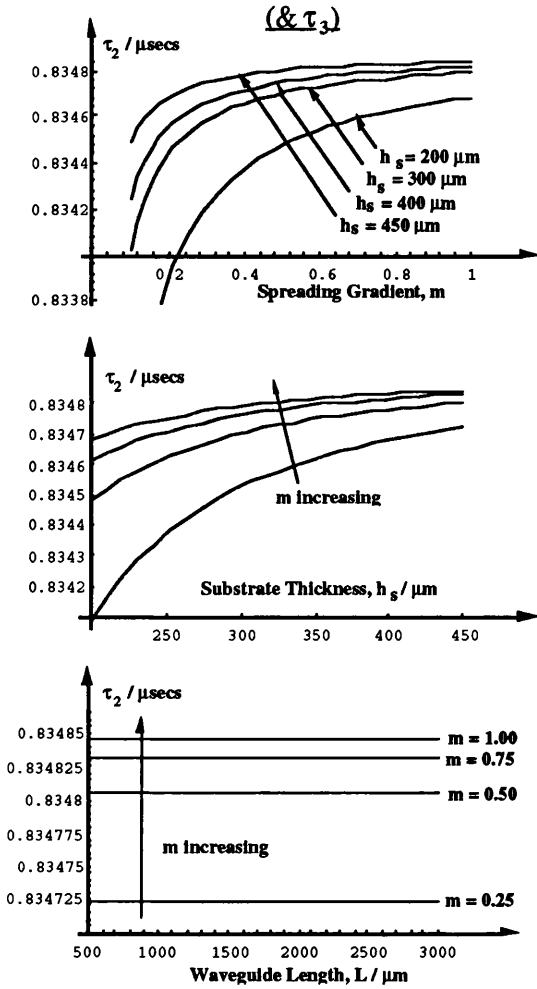


**Figure 7.15**

**Exponential Characteristic Time Constant,  $\tau_4$**

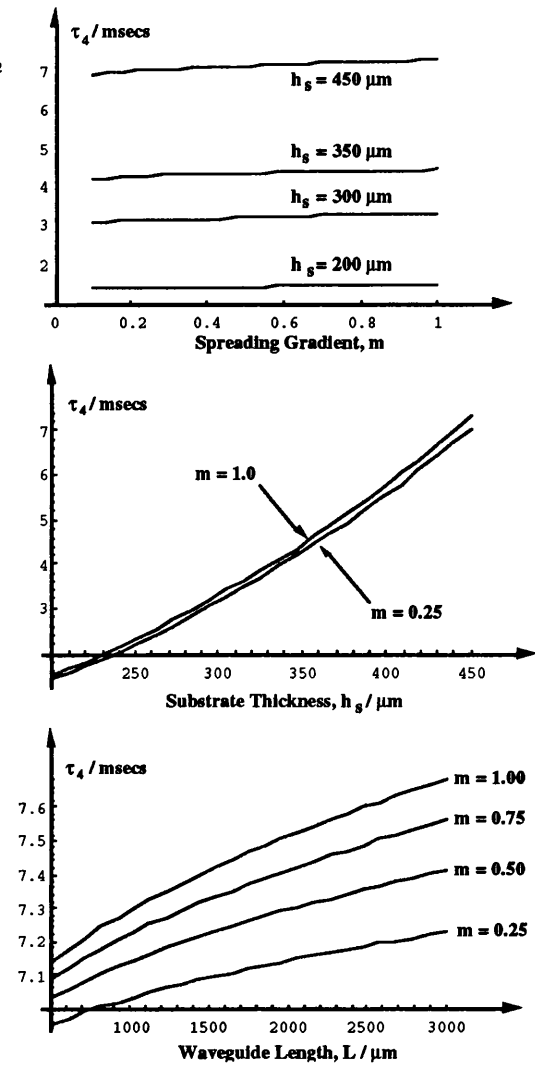


**Figure 7.16**

By separating the function using partial fractions, standard inverse Laplace transforms were

used to induce the time domain function as follows :-

$$\frac{1 + s\tau_1}{s \left[ s + \frac{1}{\tau_3} \right] \left[ s + \frac{1}{\tau_4} \right]} = \frac{\alpha\tau_2}{s} + \frac{\left( \frac{\alpha\tau_2[\tau_2 - \tau_1]}{\sqrt{[\alpha + \tau_1]^2 - 4\alpha\tau_2}} \right)}{\left[ s + \frac{1}{\tau_3} \right]} + \frac{\left( \frac{\alpha\tau_2[\tau_1 - \alpha]}{\sqrt{[\alpha + \tau_1]^2 - 4\alpha\tau_2}} \right)}{\left[ s + \frac{1}{\tau_4} \right]}$$

$$T_{rs}(t) = \Delta T_{CW} \left( 1 + \left[ \frac{[\tau_2 - \tau_1]}{\sqrt{[\alpha + \tau_1]^2 - 4\alpha\tau_2}} \right] e^{-\frac{t}{\tau_3}} - \left[ \frac{[\tau_4 - \tau_1]}{\sqrt{[\alpha + \tau_1]^2 - 4\alpha\tau_2}} \right] e^{-\frac{t}{\tau_4}} \right) \dots (7.15)$$

Strategic inequalities of the time constants lead to the following simplification :-

$$\tau_3\tau_4 = \alpha\tau_2 ; \tau_3 \rightarrow \tau_4 \Rightarrow \tau_4 \rightarrow \alpha$$

$$\alpha (\approx \tau_4) \gg \{\tau_2 \approx \tau_1, \tau_3 \approx \tau_1\} \Rightarrow \frac{[\tau_2 - \tau_1]}{\sqrt{[\alpha + \tau_1]^2 - 4\alpha\tau_2}} \rightarrow 0 ; \frac{[\tau_4 - \tau_1]}{\sqrt{[\alpha + \tau_1]^2 - 4\alpha\tau_2}} \rightarrow 1$$

$$T_{rs}(t) = \Delta T_{CW} \left[ 1 - e^{-\frac{t}{\alpha}} \right] = \left\{ \frac{n_o \epsilon \mu w L V^2}{h_r} \cdot [R_{rib} + R_{sub} + R_{hs}] \right\} \left[ 1 - e^{-\frac{t}{[R_{hs} + R_{sub}] [C_{sub} + C_{rb}]}} \right]$$

--- (7.16)

Hence,  $T_{rs}(t)$  was simply stated as an exponential growth function, in which the original resistance / capacitance subscripts were inserted. A macro-calculation, based on this analysis, was performed with previously defined parameter values, and a correction made to the expression for the heatsink thermal capacitance [97]. The result of these calculations was presented in Figures 7.17 and 7.18.

### Exponential Growth of Normalised Rib-substrate Interface Temperature

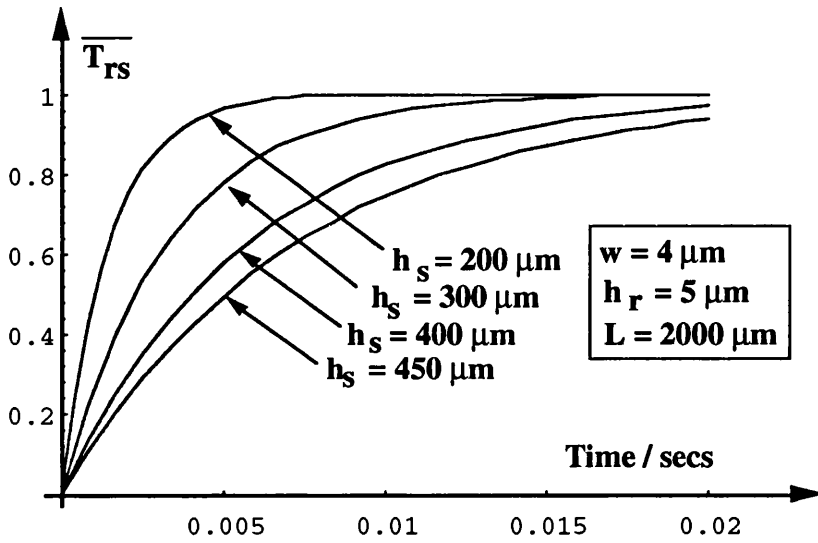


Figure 7.17

### Exponential Growth of Normalised Rib-substrate Interface Temperature

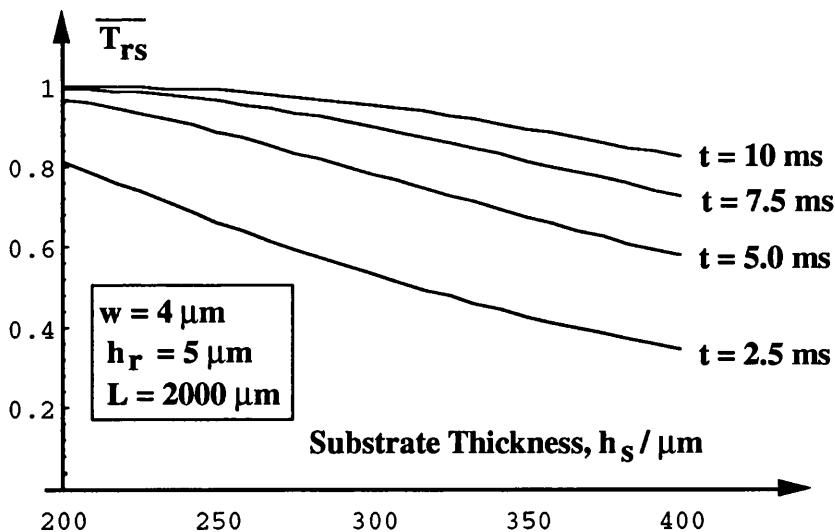


Figure 7.18

## 7.5 Estimation of the Maximum Permissible Bias-pulse Width

An estimate of the maximum permissible bias pulse width was required. Transposition of expression (7.16) allowed the time duration to be calculated for a defined temperature increase :-

$$\Delta T_{\text{crit}} = \Delta T_{\text{CW}} \left[ 1 - e^{-\frac{t_p}{\tau_{\text{therm}}}} \right] \Rightarrow t_p = \tau_{\text{therm}} \cdot \ln \left[ \frac{\Delta T_{\text{CW}}}{\Delta T_{\text{CW}} - \Delta T_{\text{crit}}} \right] \dots (7.17)$$

To evaluate the maximum permissible pulse width, the lattice temperature at which the Transferred Electron Effect critically ceased to exist was estimated ( $\Delta T_{\text{crit}}$ ). The collapse of NDM occurred where thermal energy competed with electric field in the promotion of conduction band electrons. The maximum permissible crystal temperature has been demonstrated to be approximately 243 °C in GaAs at room temperature [40].

$\tau_{\text{therm}}$  and  $\Delta T_{\text{CW}}$  were dependent upon the dimensions of the device, implying similar dependencies for the maximum pulse width  $t_{\text{max}}$  (Figure 7.20). The trends seen were those expected from fundamental principles governing thermal dissipation. A greater value of  $t_{\text{max}}$  implied a slower rate of increase of temperature, while smaller values of  $t_{\text{max}}$  implied a higher rate of increase. A minimal increase in  $t_{\text{max}}$  was observed with increasing waveguide length, while it decreased as the waveguide width was increased. This implied that thermal dissipation requirements became more stringent for wider waveguides (Figure 7.20). Similar variations were observed with both substrate thickness and applied electric field. The latter contributed directly to the magnitude of the power to be dissipated, and hence larger field values lead to faster rates of increase of temperature, and smaller  $t_{\text{max}}$ . The value of  $t_{\text{max}}$  remained in the range 0.1 - 3 ms, and hence within the normal capabilities of voltage pulse generators.

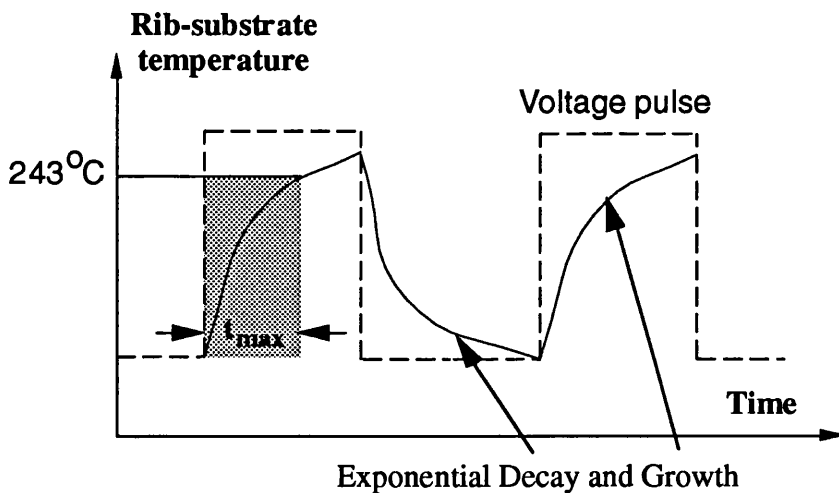


**Figure 7.19 :- Temperature rise limit**

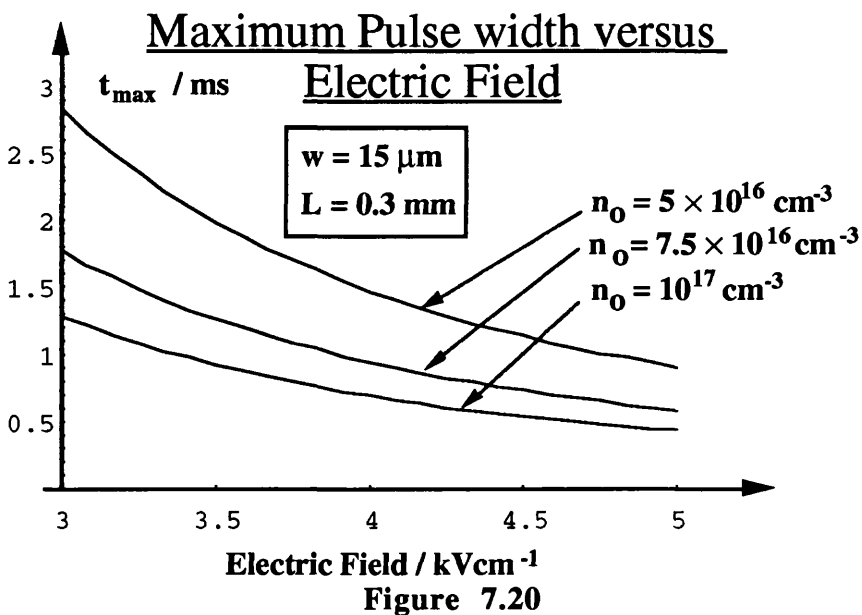
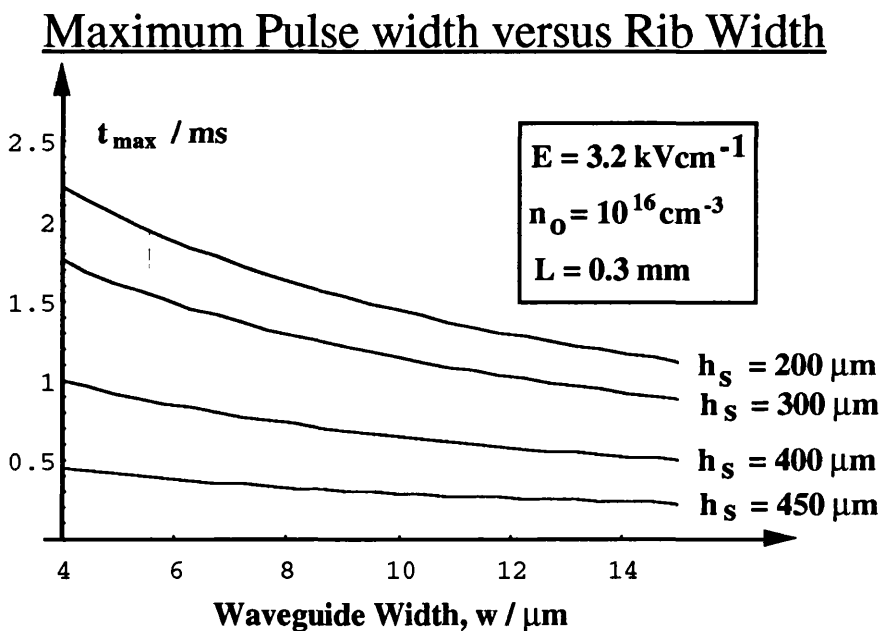
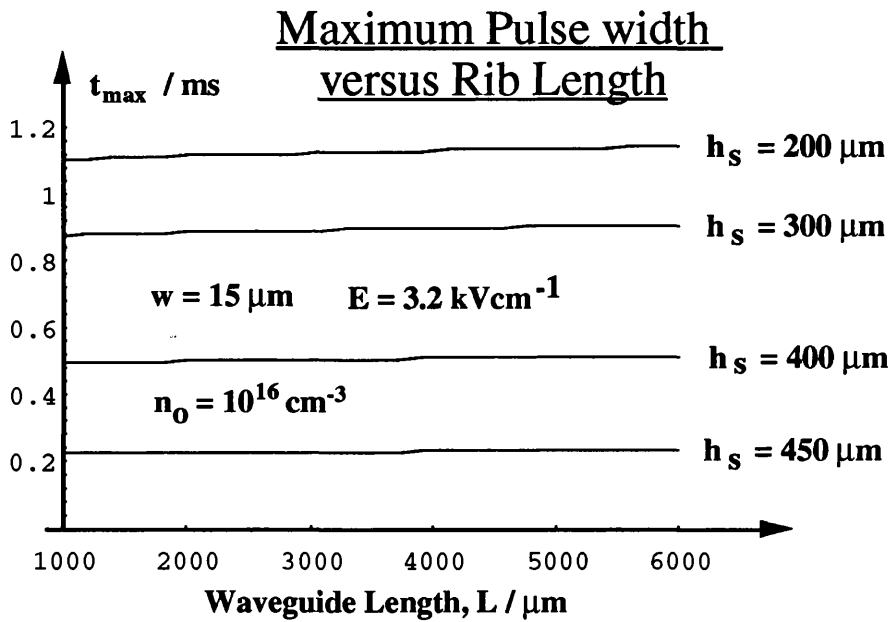


Figure 7.20

Stage 1 -  $\text{SiCl}_4$  dry-etch with NiCr mask

Stage 2 - Ohmic contact definition

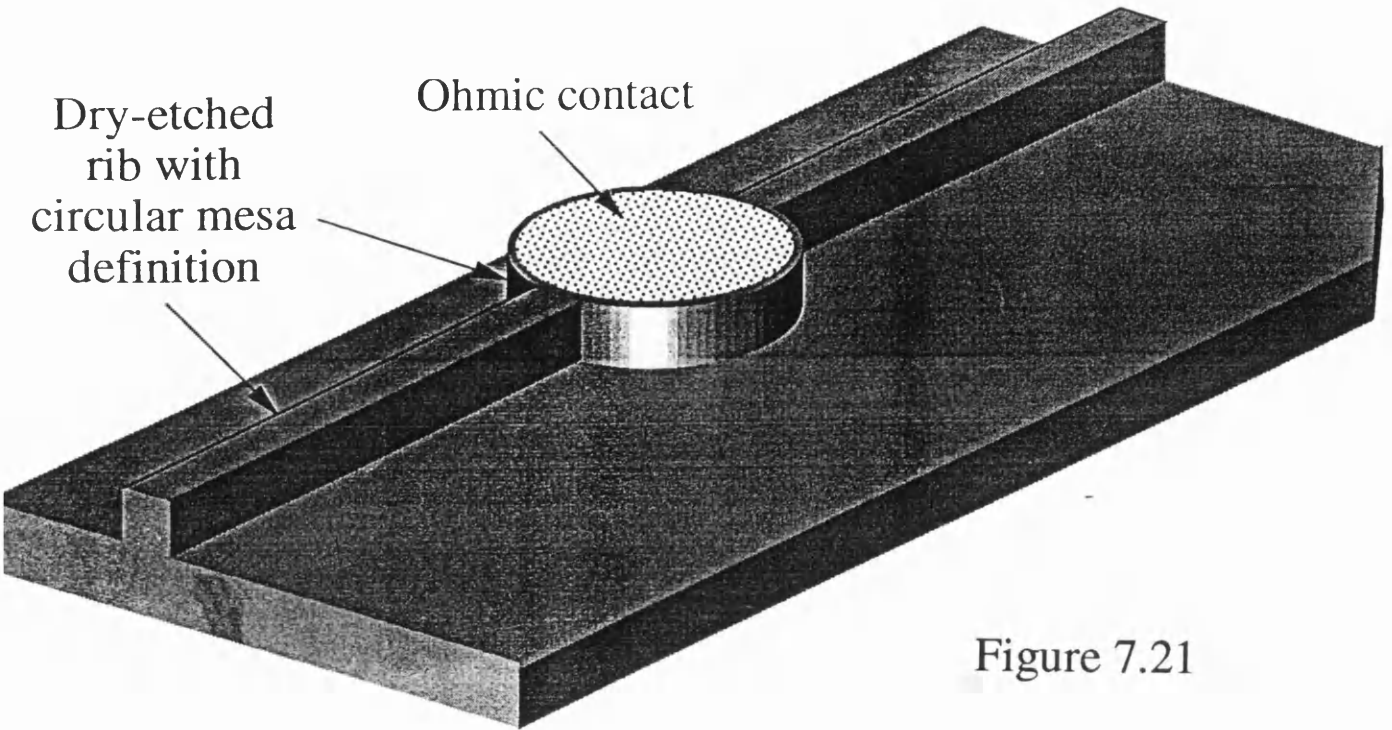
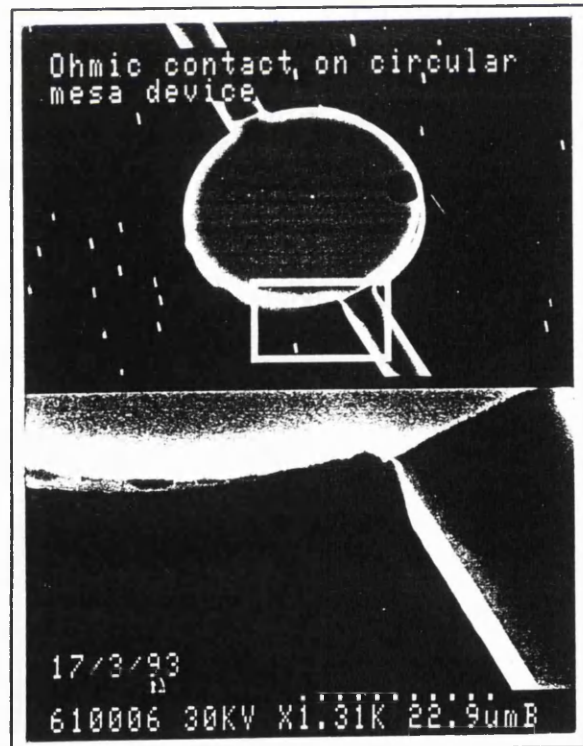


Figure 7.21



Photograph 1 - clean etch walls symptomatic of NiCr mask quality

Photograph 2 - photolithography for the definition of a coincident ohmic contact

Stage 3 - Silica deposition (1  $\mu\text{m}$ )

Stage 4 -  $\text{C}_2\text{F}_6$  etching to define window

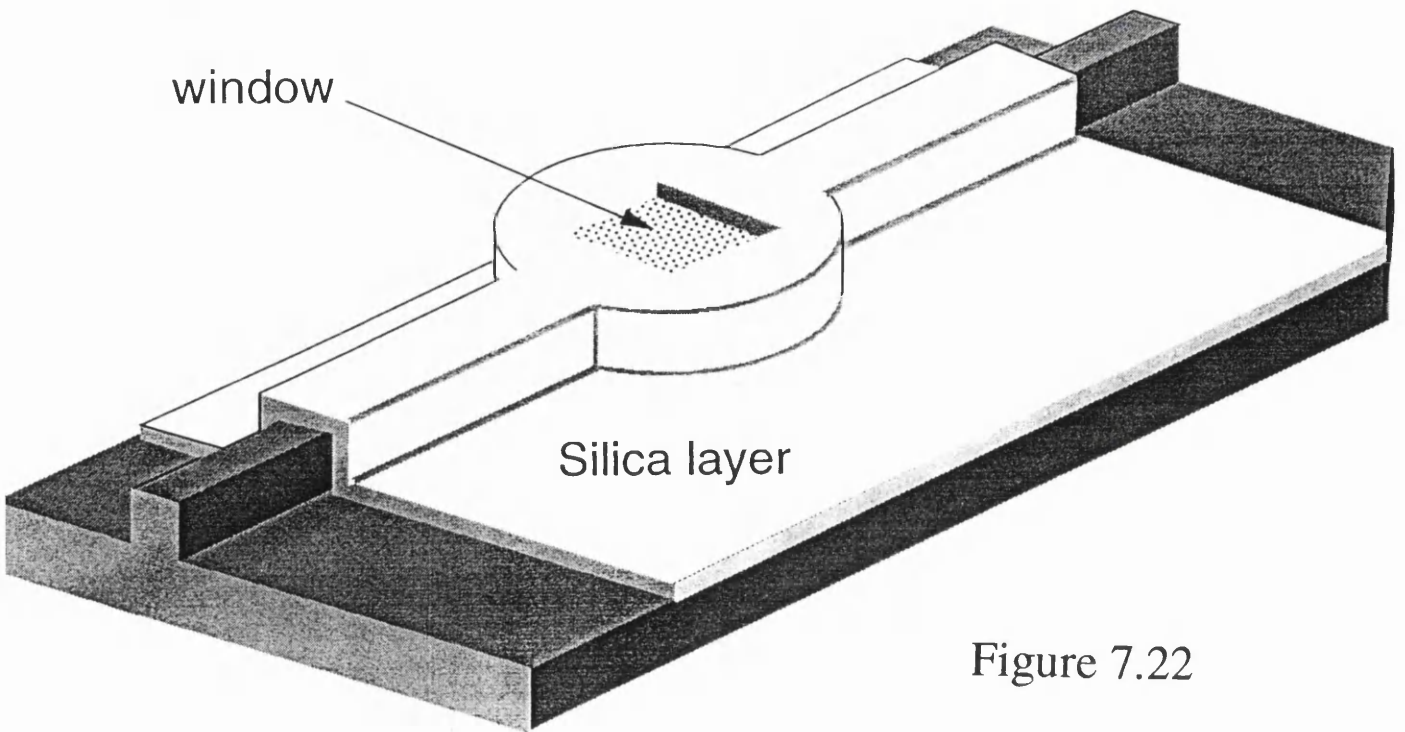
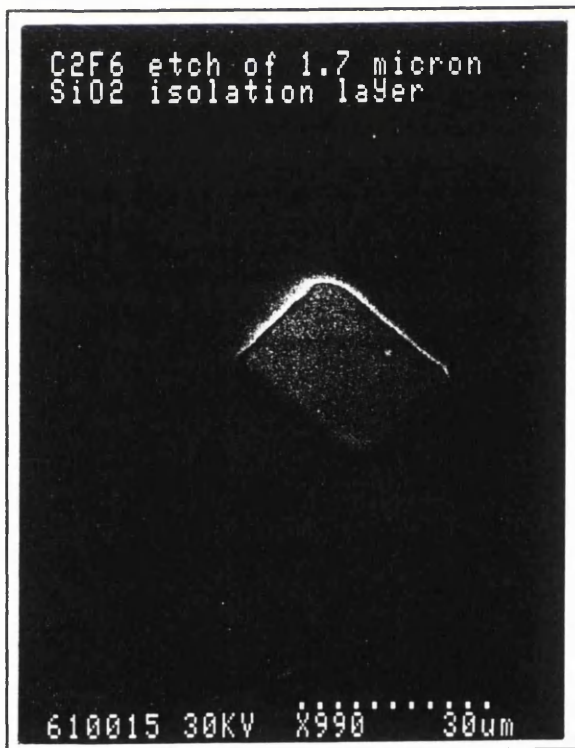
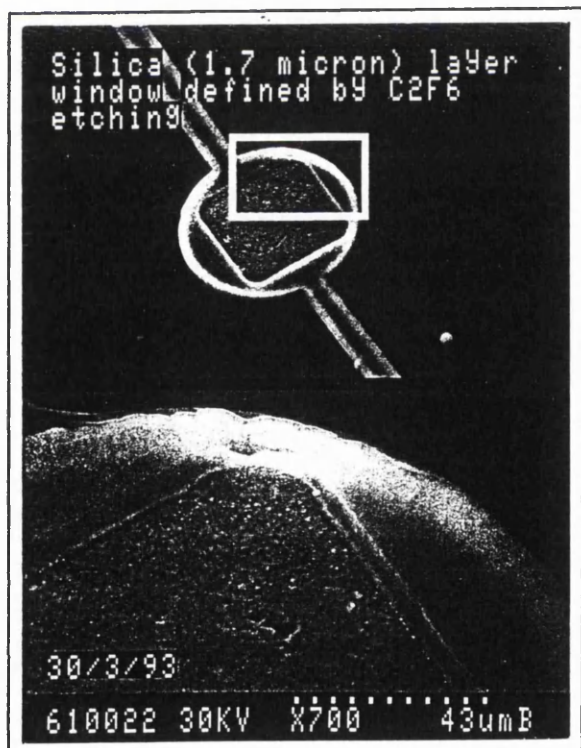


Figure 7.22

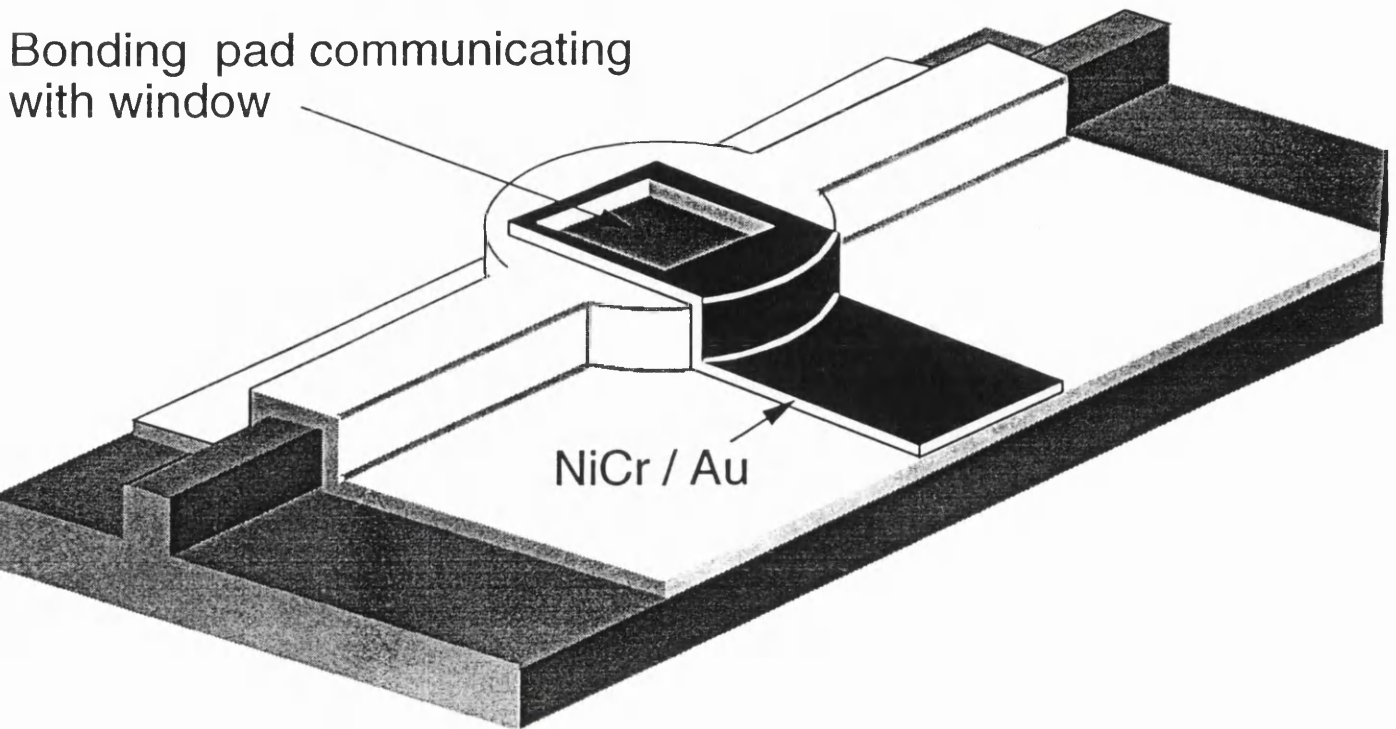


Photograph 3 - window defined with AZ4620A resist remaining



Photograph 4 - coincident window in the silica layer to provide access

## Stage 5 - Bonding pad definition for electrical access



Proposed Benefits of the Revised Structure included :-

- {i} Natural symmetry of the circular mesa more appropriate for encouraging space-charge wave activity ;
- {ii} Smaller waveguide disc -continuity  $\Rightarrow$  lower series optical losses ;
- {iii} Greatly reduced / minimised Cross-sectional areas  $\Rightarrow$  lower thermal power dissipation

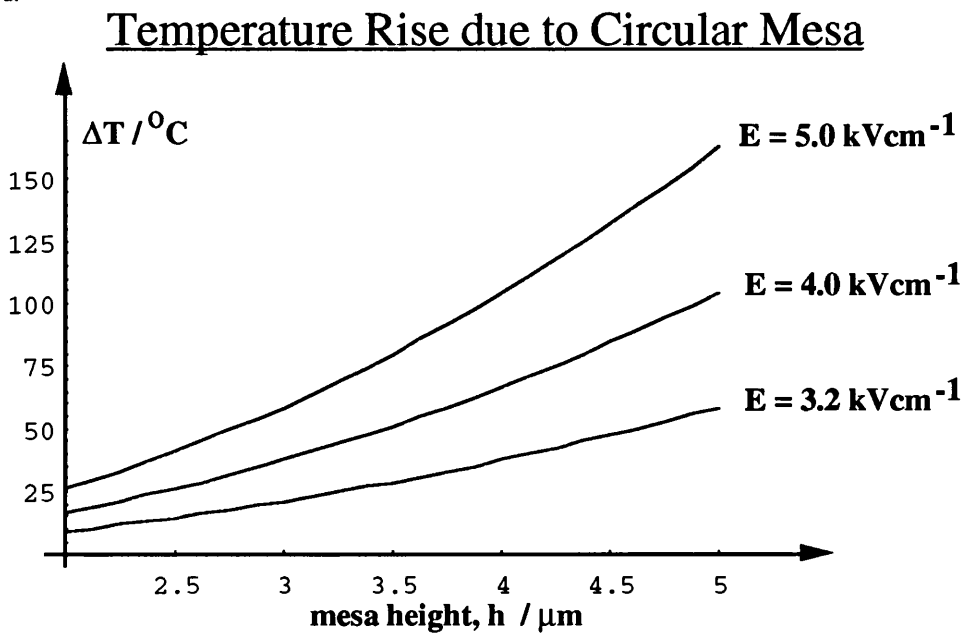
Photograph 5 - communicating bonding pad showing completed device

Figure 7.23

## 7.6 Further Reappraisal of Vertical device

An alternative vertical device was designed, and its fabrication viability verified. This additional reappraisal suggested the structure shown in Figures 7.21 - 7.23. Several notable features of the device were as follows :-

(1) a waveguiding rib was retained in similar dimensions to that considered previously ; (2) the anode contact was returned to the substrate-side of the device, forming an unselective "blanket" contact ; (3) the natural symmetry of a circular mesa was utilised to (i) dramatically reduce the current capacity (cross-sectional area) of the device and remove the coincidence between active region and waveguide and (ii) harness the favourable symmetrical pre-threshold electric field distribution seen in conventional semiconductor microwave devices ; (4) the revised structure required the deposition and selective etching of a comparatively thick layer of  $\text{SiO}_2$  ( $> 1\mu\text{m}$  ). This was achieved by using a photoresist etchmask (i.e AZ4620A,  $> 15\mu\text{m}$  ) ; (5) the separation of cathode and rib waveguide gave extra design freedom. The width of the rib waveguide, and the diameter of the active region mesa, were varied independently of each other. An enhanced variety of devices were generated in this manner, allowing for a more effective optimisation of optical and electrical characteristics ; (6) the device was fabricated with methods used previously for planar and vertical devices i.e. no further fabrication innovations were required.



**Figure 7.24**

Temperature rises incurred in the revised circular geometry device were an order of magnitude below that experienced in the rib-substrate design (expression 7.18). This permitted the device to

remain comfortably within the thermal limits imposed previously, and hence potentially operate CW over wide ranges of electric field and doping levels, despite the quadratic increase with the height of the mesa structure (Figure 7.24).

$$\Delta T = P_d R_{\text{mesa}} = \left[ n_o e \mu h \pi r^2 E^2 \right] \left( \frac{h}{\kappa_{\text{GaAs}} \pi r^2} \right) = \frac{n_o e \mu E^2 h^2}{\kappa_{\text{GaAs}}} \quad \text{--- (7.18)}$$

Finally, it was noted that the potential depth of optoelectronic interaction available in this device was significantly reduced upon that expected in the rib-substrate arrangement. In other terms, its efficiency as a modulator had been forfeited in order to ensure its thermal viability - a significant engineering compromise.

### 7.7 Overall Conclusions

A simple formula for the thermal resistance of a compound rib-substrate device structure was derived. Natural trends, such as the benefits of substrate thinning, were confirmed by this model. **Magnitudes** of thermal resistances were illustrated to be in the range 5 - 100 °C W<sup>-1</sup>. These values were not unusually large for semiconductors in a confined thermal environment. Despite this, sizeable **phenomenological** rises in the global temperature were observed in the calculations.  $\Delta T$  reached a maximum value of **1400 °C**, with a minimum value of **550 °C** at the smallest dimensions considered in the calculation. These temperature elevations could not be sustained in GaAs elements, without significant disordering effects and annihilation of the device. It was not reasonably possible to achieve the electric fields necessary to encourage oscillations while running CW. The calculations confirmed that **high duty cycle pulsed biasing** was critical if temperature elevations were to be significantly curtailed. Elevated fields required elevated voltages, increased the voltage-current product, and generated excessive power. It was concluded that the structures used by Moreland et al, with contact widths and lengths of 15  $\mu\text{m}$  and 6 mm respectively, could not have existed for any substantial duration of time, and were considered to not have any realistic possibility of oscillating, at least when operating CW.

The introduction of thermal capacitances allowed evaluations of the natural time constants governing the rate of rise / fall of crystal temperature. With the assistance of thermal "frequency" domain analysis (Laplace Transforms), the maximum permissible pulse width under varying external conditions were additionally assessed. This indicated that pulse widths and duty cycles necessary to

inhibit temperature rises were unsuitable for practically viable "modulators". Several critical assumptions were made during the analysis :-

(1) Power flow density remained uniform ; (2) The thermal energy source plane was exterior to the substrate ; (3) In accordance with (1), current density and temperature distributions were uniform across the rib. Estimates were made assuming no current-crowding distortions. **Current crowding** results from the non-uniformity of current density distributions induced by physical constrictions of conducting channels. Thermal energy generation (and hence temperature) is functionally dependent on the instantaneous value of the current density (i.e.  $\Delta T[r,t] \rightarrow j[r,t]$ ). Subsequently, current crowding is responsible for initiating "hot-spots" or localised thermal waves. These local areas of elevated temperature have been observed to cause premature destruction of devices through instantaneous current filamentation. In physical terms, current filaments lead directly to eutectic "wires" drawn from anode to cathode, and are constituted of an "alloy" of gold, germanium, nickel and GaAs. They are commonly observed as very high conductance "shorts". Devices operating at elevated fields ( $>3 \text{ kVcm}^{-1}$ ) are therefore susceptible to such thermally-initiated blow-out events.

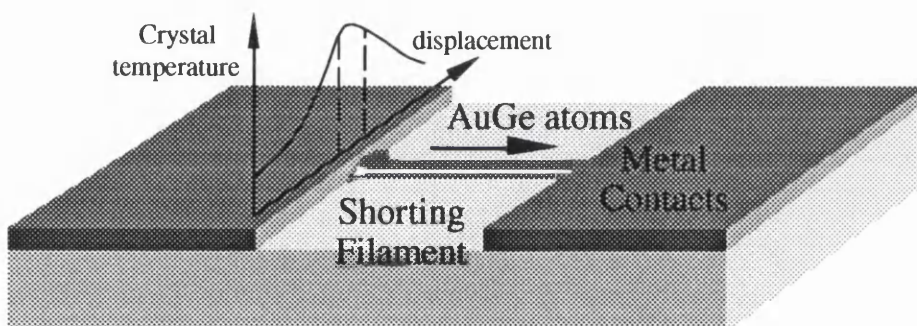


**Figure 7.25 :- Eutectic "wire" shorting filament**

Further problems were envisaged (and observed practically) with rib-substrate devices. Electrical contact variations have been cited [85] as a primary source of thermal waves within semiconductor devices, which are seen to be ultimately destructive in high field environments [86] [87] [104]. Once a thermal wave has been nucleated, its exponential growth rapidly dissociates contacts, disrupts the fabric of the device, and occurs on a time scale too low for "blow-out" events to be suppressed. This has been deemed to reduce maximum permissible temperatures (and hence  $t_{\max}$ ) by one or two orders of magnitude, and increase duty cycles to impractical levels. Analytical calculations have demonstrated that continuous wave (CW) operation of the rib-substrate vertical device was not feasible. Further, it also confirmed that oscillatory operation was only possible when applying narrow

bias pulses at high duty cycles. Neither of these conditions coincided with the original notion of a coherent CW modulator. Considering the naturally high current capacity of the device, it was concluded that heat-sinking alone was not sufficient to ensure feasibility of this structure.

## Chapter 8

### Conclusions

The original research schedule included the pursuit of an optical modulator using an integrated Transferred Electron Device (TED). Outline targets were stated as :- (i) 50 GHz modulation bandwidth and (ii) 60 % modulation (AM) depth (iii) at wavelengths in the range 900 nm to 1.3  $\mu\text{m}$ . Its justification was provided by the work of Lau et al [14] [15]. The incorporation of photo-elastic induced waveguides (in place of ribs) was also proposed. Stress-strain distributions within the sub-surface crystal generate weak guiding and anti-guiding regions. The feasibility of these waveguides in stripe-geometry semiconductor lasers [105] and planar TEDs [13] has been investigated. They were observed to be difficult to control when generated by annealed metallisation.

It became apparent, when the basic principles of engineering were applied to the problems in hand, that critical elements of the original proposals were unfeasible. A major reappraisal of device designs was undertaken and presented in Chapters 4 and 7.

Engineering requirement	"Side-wall" vertical device
A spatial volume where optoelectronic interaction takes place. The volume of this region could be maximised, which in turn optimises the depth of modulation	Volume of interaction site linked to both optical waveguide and electrical conduction. Maximisation leads to devices with too large a current capacity for survivability.
The device must be constructed from a material with large electro / magneto-optic coefficients, such that the optical characteristics could be modified efficiently	To support the transferred electron effect simultaneously, devices constructed from GaAs. The $r_{41}$ electro-optic coefficient is only $10^{-12} \text{ mV}^{-1}$ , implying large electric fields required to induce index changes
The device must provide (i) a rib waveguide for admitting radiation into interaction site, and to couple modulated radiation out of the device and ; (ii) large area bonding pads to allow electrical probing	Extreme aspect ratio of the cathode contact (length / width) was in excess of 600 in devices fabricated with existing masks. This was not conducive to a stable pre- or post-threshold electric field distribution in the active region
The device must provide electrical isolation to prevent shorting and premature dielectric breakdown	The side-wall device suffered from lateral distortion of the electric field distribution, and an increased susceptibility to current leakage and added capacitance
The thermal energy dissipated within the device must be below critical thresholds so that it does not (i) undermine the fabric of the device and (ii) inhibit the optoelectronic phenomena to which the device owes its operation	The potential final crystal temperature with CW biasing could reach $1000^{\circ}\text{C}$ . As observed experimentally, the contacts disintegrated at $450^{\circ}\text{C}$ , while the GaAs itself was undermined at $600^{\circ}\text{C}$ .
The modulation generated must (i) be of the correct form [e.g. AM, FM or PM] ; (ii) comply with minimum recognition thresholds (contrast) defined by the intended communication system.	Maximum modulation depths in practical devices have not surpassed 25 % in any component. Device dimensions became practically unreasonable due to thermal dissipation requirements.
The device must be electrically and optically accessible simultaneously. This must be preserved even while the device is in-situ in a resonant circuit or cavity.	Free space optical access severely restricted by the biasing arrangement, and completely prevented by resonant cavities. Fibre communication impractical for Fabry-Perot analysis

**Figure 8.1 :- Engineering compromises of the "side-wall" device**

The side-wall vertical device was reported to offer 24 GHz modulation [13] [14] [15], to limited modulation depths, in specimens with considerable physical dimensions (relative to semiconductor devices) i.e.  $15\ \mu\text{m} \times 6000\ \mu\text{m}$  (6 mm) rib cathode contact. The requirements for a device to be a modulator, through optoelectronic interaction, automatically imposed several criteria upon that device. Initially, attempts were made to replicate these devices and their modulation capability. It was observed that this structure consistently contravened the necessary engineering requirements, in the manner given in the table of Figure 8.1, and the schematic of Figure 8.2.

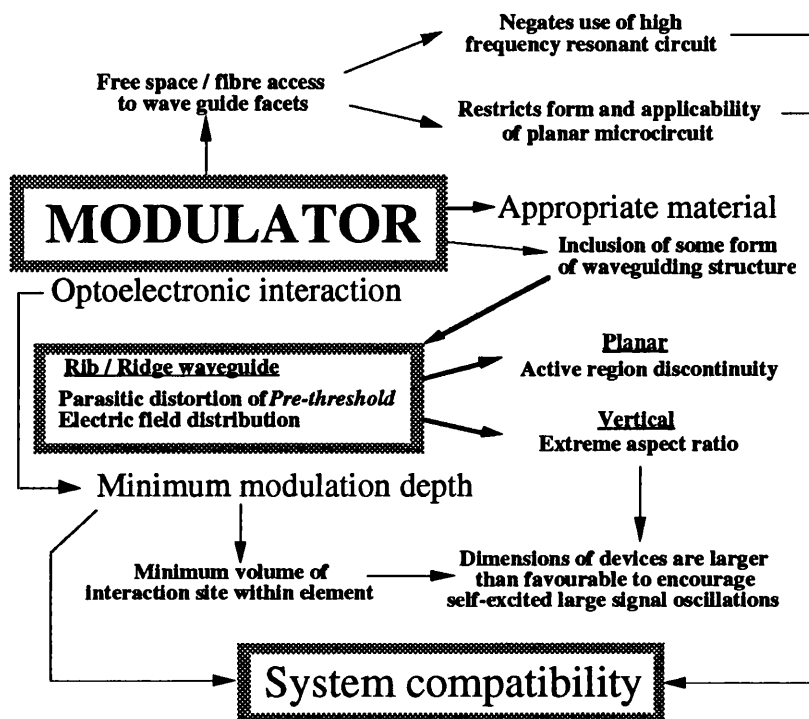


**Figure 8.2 :- System requirements of a viable modulator**

The large number of engineering compromises lead to an inability to secure oscillation or active optoelectronic interaction in these devices. It was concluded that the side-wall structure was not viable for a modulator using the Transferred Electron effect. It was appropriately discontinued.

An alternative vertical design was proposed, where modifications were made to (i) the magnitude of conducting channel ; (ii) the position of the electrical contacts ; (iii) the addition of dielectric isolation layers ; (iv) incorporation of heterostructures (i.e. graded AlGaAs Hot Electron Injector [HEI]). A comprehensive comparison was provided in Chapter 4. This reappraisal was justified by practical observations of these vertical devices.

Despite engineering appraisal, the vertical structure did not offer consistent oscillation or longevity. The inability to prevent thermal runaway and destructive filamentation, impeded attempts to measure stable oscillations on a spectrum analyser. This fundamental problem could not be resolved without removing the essential design of the device i.e. its vertical nature. Similar symptom prevailed in the planar equivalent, however "oscillation" was demonstrated by sharp discontinuities in current-voltage traces. High electric fields could not be applied to the device for extended periods without "burnout".

The influence of the cathode boundary was experimentally investigated using planar devices. The theoretical current-voltage function provided the fulcrum for this analysis, with the following overall conclusions :- (i) The current-voltage trace could be "manipulated" or controlled, as suggested by Bonilla and Higuera [21] [22] and Kroemer [19] [20] ; (ii) Relations between current voltage trace and cathode contact resistance, annealing temperature and time were observed. Predictive functions were derived from a wide variety of real specimens, fabricated from a narrower range of wafer materials ; (iii) It was anticipated that the predictive worth of these functions extended to the immediate wafers and contact types used, and not beyond. Despite this, the general trends and means of modification of cathode conditions were expected to be more universally valid.

It was concluded that the assumptions and approximations used in theoretical analyses were shown to be justified by the proximity of theory curves to that of real devices. Many of the principles discussed in conjunction with this work challenged the long-established notion of "ohmicity" in practical contact technology. A re-examination of the absolute definition of ohmicity was required, such that Kroemers control characteristic concept (Chapter 2) could be accommodated. Three factors were identified which were responsible for non-oscillation or stationary states in vertical and planar devices :- (a) **material considerations** :- impurities, dopants and crystal imperfections in critical population densities, displacements or distributions ; (b) **cathode boundary conditions** :- the relative positions of "crossover" field, control characteristic and that of the neutral interior crystal ; (c) **thermal energy dissipation** :- temperature of the crystal elevated above thresholds signifying cessation of the Transferred Electron Effect, and the destruction of the contacts.

The original design for a Transferred Electron "Modulator", in which Moreland et al reported modulation, was seen to be inappropriate for this task. This side-wall structure contravened many of

the criteria necessary to constitute a viable modulator. Despite attempts to obtain oscillation in TWO revised vertical device designs, thermal dissipation lead to premature "burnout". The requirements of waveguiding and optoelectronic interaction were incompatible with that necessary for microwave oscillation. Only three separate publications have ever reported modulation in TEDs [11] [12] [13]. The first and second were separated by nine years, and the second and third by fifteen years. In these previous publications no more than 24 % modulation depth was ever claimed. The low productivity in this discipline, despite the popularity of TEDs in research publications, paid testimony to the unfeasibility of the concept.

The proposed device was intended to operate in a system with modulation requirements of 60% or greater. Theoretical calculations presented in chapter 3 indicated that it was possible for devices with waveguides greater than 3 mm to achieve these modulation depths, only at wavelengths approaching the natural GaAs bandgap (890 nm). This assumed idealised conditions, i.e. the entire interaction site was at the peak domain field. The fact that no net refractive index change is incurred in one periodic disturbance transit was also ignored - this had severe implications for the Linear Electro-optic effect and the modulation event duration. Additionally, the system wavelength was as long as 1.3  $\mu\text{m}$ ,. which was significantly distant from the natural band-edge of GaAs (892 nm). Hence the opportunity for e.g. Franz-Keldysh electroabsorption was severely reduced at this operating wavelength. Accommodating all the imposed engineering compromises, it was concluded that a modulator with **engineering viability** could not be constructed from a TED. With so many alternative electro or magneto-optic modulators available, the pursuit of new modulators with only token modulation depths is not justified. They will appear as nothing more than physics novelties, despite their elevated operating frequencies. Since the most modern communication systems utilise fibres with longer wavelengths (1.55  $\mu\text{m}$  or 1.3  $\mu\text{m}$ ), modulators implemented from GaAs are likely to be unviable for system use.

In view of the inadequacies of the standard Au / Ge / Ni / Au "ohmic" contact technology, research should be performed to establish detailed mechanisms governing its role in cathode boundary determination. In particular, attention must be paid to the activity of the nickel atoms in this contact technology. The poor yield of TEDs in commercial production could be improved by establishing more appropriate metal contact combinations. Attention must also be paid to the aptitude of epitaxially-

grown GaAs for the nucleation and sustenance of matured dipole disturbances. It is suggested that deliberate and controlled impregnation of neutral impurities into the GaAs bulk crystal could improve the probability of secondary space-charge layer formation in MBE wafers. The persistent susceptibility of this MBE material to instantaneous thermal waves suggested that further investigation into this problem was necessary, otherwise a total transition to MOVPE equivalents cannot be avoided.

Currently, research is being conducted into the construction of a modulator from a Resonant Tunneling Diode (RTD) - a similar principle to that for a TED. An RTD has distinct advantages over TEDs for this purpose, by virtue of its miniscule operating currents (1 - 3 mA max.) and voltages (1.5-3.0 V). Power dissipated per device is as low as 300 mW, compared to 50-70 W in an equivalent rib-waveguide TED. RTD oscillations are determined by electron tunnelling resonance in its double heterostructure barrier, and not by the bulk. Consequently, its operation is not directly sensitive to contact composition or annealing conditions. However, its implementation from GaAs / AlGaAs presents a similar band-edge limitation of operating wavelength. In addition, the natural operating frequency of an RTD is difficult to pre-determine, while oscillation efficiency is adversely affected by tuning circuits. For it to be viable, modulation depths must be maintained at 50 % or greater at wavelengths in the range 1.3  $\mu\text{m}$  to 1.55  $\mu\text{m}$ . Otherwise, it will merely remain as yet another physics novelty in the realm of engineering. In future, research into the "modulation" attributes of microwave devices should be conducted with due trepidation, if conducted at all. The correct approach to achieving faster modulation is to take existing proven modulators and improve their speed, rather than taking fast devices and making them modulate.

## Bibliography & References

- [1] BLAKEMORE, J. S. : "Semiconducting and Other Major properties of Gallium Arsenide", J. Appl. Phys., 1981, 53, 10, pp. R123-R181
- [2] ADACHI, S. : "GaAs, AlAs and  $\text{Al}_x\text{Ga}_{1-x}\text{As}$  : Material Parameters for use in Research and Device Applications", J. Appl. Phys., 1985, 58, 3, pp.R1-R29
- [3] AFROMOWITZ, M. A. : "Refractive Index of  $\text{Ga}_{1-x}\text{Al}_x\text{As}$ ", Solid State Commun., 1974, 15, pp. 59-63
- [4] HOWES, M. J., MORGAN, D. V. : "Gallium Arsenide Materials, Devices and Circuits", Wiley, New York, 1985
- [5] LADBROOKE, P.H. : "GaAs MESFETs and High Electron Mobility Transistors (HEMTs)", Gallium Arsenide for Devices and Integrated Circuits, 1986, Proc. GaAs School, UWIST, Cardiff.
- [6] DUMKE, W. P. : " Intraband Transitions and Maser Action", Phys. Rev., 1962, 127, 5, pp. 1559-1563
- [7] ALFEROV, ZhI., ANDREEV, V. H., KOROL'KOV, V. I., PORTNOI, E. L. and YAKOVENKO, A. A. : " Spontaneous Radiation Sources Based on Structures with AlAs-GaAs Heterojunctions", Sov. Phys. Semicond., 1970, 3, pp. 1107-1110
- [8] YARIV, A. : " The Beginning of Integrated Optoelectronic Circuits", IEEE Trans. Elec. Dev., 1984, 31, 11, pp. 1656-1661
- [9] PRATT, T., BOSTAIN, C. W. : "Satellite Communications", Wiley, New York, 1986.
- [10] GUPTA, K. C., GARG, R., BAHL, I.J. : "Microstrip Lines and Slot-lines", Artech House 1979.
- [11] COHEN, M. C., KNIGHT, S., ELWARD, J. P. : "Optical Modulation in Bulk GaAs using the Gunn Effect", 1966, Appl. Phys. Letts., 8, 11, pp. 269-271
- [12] OHTA, K., KAWASHIMA, M., KATOAKA, S. : "Electro-optic Modulation of a Laser beam by a Travelling High-field domain in a GaAs diode", J. Appl. Phys., 1975, 46, 3, pp. 1318-1321
- [13] MORELAND, D., ROBERTS, J. S., BEAUMONT, S.P. : "Optical Modulation within a Rib Waveguide by Propagating Gunn domains", Elect. Letts., July 1989, pp. 142-143
- [14] LAU, D.K., IRONSIDE, C. N., MORELAND, D., BEAUMONT, S.P. : "Optically-Triggered and Detected Gunn domains", Semiconductor and integrated Opto-electronics (SIOE ' 89), Cardiff, March 1989, pp. 256-257

- [15] LAU, D.K., BEAUMONT, S.P., IRONSDIE, C. N., MORELAND, D., STANLEY, C. R. : "High speed Optoelectronic Properties of Gunn Domains", September 1989, Ninth National Quantum Electronics Conference, Oxford, p. 189
- [16] COUCH, N.R., BETON, P.H., KELLY, M.J., KERR, T.M., KNIGHT, D.J., ONDRIA, J. : "The use of linearly graded AlGaAs injectors for intervalley transfer in GaAs : theory and experiment", 1988, Solid State electronics, 31, pp. 613-6
- [17] COUCH, N.R., SPOONER, H., KELLY, M.J., KERR, T.M., "Hot electron injection in millimetre wave Gunn diodes", 1989, Proc. confer. Phoenix, Arizona 1989, pp. 1056-1058
- [18] KROEMER, H. : "Theory of the Gunn Effect", 1964, Proc. IEEE, 52, p. 1736
- [19] KROEMER, H. : "Non-linear Space charge domain Dynamics in a Semiconductor with Negative Differential Mobility", 1966, IEEE Trans. Elec. Dev., Vol ED-13, pp. 27-40
- [20] KROEMER, H. : "The Gunn Effect Under Imperfect Cathode Boundary Conditions", 1968, IEEE Trans. Elec. Dev., Vol ED-15, 11, pp. 819-837
- [21] BONILLA, L. L., HIGUERA, F. J. : "Gunn Instability in Finite samples of GaAs : I Stationary states, stability and boundary conditions", 1991, Physica D, 52, pp. 458-476
- [22] BONILLA, L. L., HIGUERA, F. J. : "Gunn Instability in Finite samples of GaAs : II Oscillatory states in long samples", 1992, Physica D, 57, pp. 161-184
- [23] DAVIS, R. G., LEESON, M. J., LENNON, H. D. G., LAZARUS, M. J. : "Phase-Locked Millimeter-wave Two-port Second Harmonic Gunn Oscillators", IEEE Trans. Micro. Theory. Tech., 1991, Vol 39, No. 10, pp. 1746-1753
- [24] DAVIS, R. G. : Ph.D Thesis, 1989, University of Lancaster Library, Lancaster, LA1 4YW, England.
- [25] HAYDL, W. H. : "Fundamental and Harmonic Operation of Millimetre-wave Gunn Diodes", 1983, IEEE Trans. Micro. Theory Tech., Vol MTT-31, pp. 879-889.
- [26] RIDLEY, B. K., WATKINS, T. B. : "The Possibility of Negative Resistance Effects in Semiconductors", Proc. Phys. Soc. Lond., 1961, 78, pp. 293-304
- [27] HILSUM, C. : "Transferred Electron Amplifiers and Oscillators", Proc. IRE, 1962, 50, pp. 185-189

- [28] GUNN, J. B. : "Microwave Oscillation of Current in III-V Semiconductors", *Solid State Commun.*, 1963, 1, pp. 88-91
- [29] GUNN, J. B. : "Instabilities of Current in III-V semiconductors", 1964, *IBM J. Res. Dev.*, 8, pp. 141-159
- [30] GUNN, J. B. : "Instabilities of Current and of Potential Distribution in GaAs and InP", *Proc. Sym. Plasma Effects in Solids*, 1964, pp. 199-207
- [31] HUTSON, A. R., JAYARAMAN, A., CHYNOWETH, A. G. : "Mechanism of the Gunn Effect from a Pressure Experiment", *Phys. Rev. Lett.*, 1965, 14, pp. 639-641
- [32] ALLEN, J. W., SHYAM, M., CHEN, Y. S., PEARSON, G. L. : "Microwave oscillation in GaAs<sub>1-x</sub>P<sub>x</sub> Alloys", *Appl. Phys. Lett.*, 1965, 7, 4, pp. 78-80
- [33] McCUMBER, D. E., CHYNOWETH, A. G. : "Theory of Negative-Conductance Amplification and of Gunn Instabilities in Two-valley Semiconductors", 1966, *IEEE Trans. Elec. Dev.*, Vol ED-13, pp. 4-21
- [34] BUTCHER, P. N. : "Theory of Stable Domain Propagation in the Gunn Effect", *Phys. Lett.*, 1965, 19, 7, pp. 841-850
- [35] BUTCHER, P. N., FAWCETT, W. : "Calculation of the Velocity-Field Characteristic for Gallium Arsenide", *Phys. Lett.*, 1966, 21, 5, pp. 489-490
- [36] RUCH, J. R., KINO, G. S. : "Measurement of the Velocity-field Characteristic of Gallium Arsenide", 1967, *Appl. Phys. Lett.*, Vol. 10, pp. 40-42
- [37] BUTCHER, P. N., FAWCETT, W. : "Stable Domain Propagation in the Gunn Effect", *Brit. J. Appl.*, 1966, 17, pp. 1425-1432
- [38] BUTCHER, P. N., FAWCETT, W., OGG, N. R. : "Effect of Field-Dependent Diffusion on Stable Domain Propagation in the Gunn Effect", 1967, 18, pp. 755-759
- [39] BUTCHER, P. N. : "The Gunn Effect", *Rep. Prog. Phys.*, 1967, 60, 1, pp. 97-148
- [40] CARROLL, J. E. : "Hot Electron Microwave Generators", 1970, Edward Arnold, London
- [41] HOBSON, G. S. : "The Gunn Effect", 1974, Clarendon Press, Oxford
- [42] BOSCH, B. G., ENGELMANN, R. H. W. : "Gunn-Effect Electronics", 1975, Pitman Publishing, London

- [43] SHAW, M. P., GRUBIN, H. L., SOLOMON, P. R. : "The Gunn-Hilsum Effect", 1979, Academic press, London
- [44] GORDON, E. I. : "Gunn effect Light Modulator", 1965, US Patent No. 3,475,038
- [45] CHEN, F. F. : "Introduction to Plasma Physics", 1974, Plenum Press, London
- [46] NYE, J. F. : "Physical properties of Crystals", 1957, Clarendon Press, London
- [47] FWAVE III application program running on 68030 co-processor Apple Macintosh
- [48] LWAVE application program running on 68030 co-processor Apple Macintosh
- [49] McDANIEL, E. W. : "Collision Phenomena In Ionised Gases", 1964, Wiley, London
- [50] MASSEY, H. S. W. : "Electronic and Ionic Impact Phenomena", Vol II, 1969, Oxford University Press, London
- [51] MASSEY, H. S. W., BURHOP, E. H. S. : "Electronic and Ionic Impact Phenomena", Vol I, 1969, Oxford University Press, London
- [52] SHAW, D. W. : "Localised GaAs Etching with Acidic Hydrogen Peroxide Solutions", J. ElectroChem Soc. : Solid-State Sci. and Tech., 1981, 128, pp. 874-880
- [53] AUSTIN, M. W. : "GaAs/AlGaAs curved Rib waveguides", 1982, IEEE J. Quantum Elec., Vol QE-18, pp. 795-800
- [54] SETO, M., DERI, R. J., YI-YAN, A., COLAS, E., TOMLINSON, W. J., BHAT, R., SHAHAR, A. : "Fabrication of Sub-millimeter-Radius Optical waveguide Bends with Anisotropic and Isotropic Wet Chemical Etchants", 1990, J. Light. Tech., Vol 8, 2, pp. 264-270
- [55] DERI, R. J., SETO, M., YI-YAN, A., COLAS, E., BHAT, R. : "Diffusion-Limited Etching for Compact, Low-loss Semiconductor Integrated Optics", 1989, Photonics Tech. Lett., Vol 1, pp. 46-48
- [56] ZAPESOCHNYI, I. P., FELTSAN, P. V. : "Optics and Spectroscopy", 1966, 20, pp. 291-308
- [57] Saad Murad, Private communication
- [58] ANDERSON, G. S., MAYER, W. N., WEHNER, G. K. : 1962, J. Appl. Phys., 33 pp. 2991-2997
- [59] HOLLAND, L., STECKELMACHER, W., YARWOOD, J. : Vacuum Manual, Spon, 1974, London
- [60] DAVIS, W. A. : "Microwave Semiconductor Design", 1984, Van Nostrand Reinhold, New York
- [61] DILL, F. H. : "Optical Lithography", IEEE Trans. Elec. Dev., 1975, 22, 7, pp. 440-444

- [62] PACANSKY, J., LYERLA, J. R. : "Photochemical Decomposition Mechanisms for AZ-Type Photoresists", IBM J. Res. Dev., 1979, 23, 1, pp. 42-55
- [63] WOODWARD, J. : "Wet and Dry Processing of GaAs", Gallium Arsenide for Devices and integrated Circuits, 1986, Proc. GaAs School, UWIST, Cardiff, pp. 881-885
- [64] CANAVELLO, B. J., HATZAKIS, M., SHAW, J. M. : "Process for Obtaining Undercutting of a Photoresist to Facilitate Lift-off", IBM Tech. Dis. Bull., 1977, 19, 10, p. 4048
- [65] DUSHMAN, S. : "Scientific Foundation of Vacuum Techniques", 2nd Edition, 1962, Wiley, New York / London
- [66] YARIV, A. ; "Introduction to Optoelectronics", 2nd Edition, 1976, Holt, Rinehart and Winston, London
- [67] ILEGEMS, M., PEARSON, G. L. : "Infrared Reflection Spectra of  $Ga_{1-x}Al_xAs$  Mixed Crystals", Phys. Rev. B1, 1970, 1, 4, pp. 1576-1582
- [68] SHOJI, M., "Functional Bulk Semiconductor Oscillators", IEEE Trans. Electron Devices, Vol ED-14, 9, pp 535-546
- [69] ALTUKHOV, I. V., KAGAN, M. S., KALASHNIKOV, S. G., KUKUSHKIN, V. V., LANDSBERG, E. G. : "Electrical Instability of a Semiconductor with a negative differential Conductivity due to Simultaneous heating of electrons by static and alternating electric fields", 1978, Sov. Phys. Semi., 12, 2, pp. 172-177
- [70] KUROKAWA, K. : "The Dynamics of High-field Propagating Domains in Bulk Semiconductors", 1967, Bell Sys. Tech. J., Vol 16, 10, pp. 2235-2259
- [71] ATALLA, M. M., MOLL, J. L. : "Emitter Controlled Negative Resistance in GaAs", 1969, Solid State Elec., Vol 12, pp. 119-129
- [72] HARIU, T., ONO, S., SHIBATA, Y : "Wideband Performance of the Injection Limited Gunn Diode", 1970, Elec. Lett., Vol 6, pp. 666-667
- [73] HAKKI, B. W., KNIGHT, S. : "Microwave Phenomena in Bulk GaAs", 1966, IEEE Trans. Elec. Dev., Vol ED-13, 1, pp. 94-104
- [74] FOYT, A. G., McWHORTER, A. L. : "The Gunn Effect In Polar Semiconductors", 1966, IEEE Trans. Elec. Dev., Vol ED-13, 1, pp 79-87

- [75] KOWALSKY, W., SCHLACHETSKI, A. : "Transferred Electron effect in  $\text{In}_{0.53}\text{Ga}_{0.47}\text{As}$ ", 1983, Elec. Lett., Vol 19, 6, pp. 189-190
- [76] BAKANAS, R. : "Interaction of a Gunn Domain with a Localised impurity Distribution", 1991, Phys. Stat. Soli., 128, pp. 473-481
- [77] KOSTYLEV, S. A., SHABALINA, R.G., BROVKIN, Yu N. : "Formation of Domain Instabilities in Gunn Diodes in a Transverse Magnetic field", 1978, Sov. Phys. Semi., Vol 12, 6, pp. 700-703
- [78] USANOV, D. A., GORBATOV, S. S., SEMENOV, A. A. : "Variation of the Shape of the Volt-ampere characteristic of a Gunn diode as a function of its microwave operating regime", 1991, Izvestiya VUZ, Radioelektronika, Vol 34, 5, pp. 107-108
- [79] COPELAND, J. A. : "A new Mode of Operation for Bulk Negative Resistance Oscillators", 1966, Proc. IEEE, 54, pp. 1479-1480
- [80] COPELAND, J. A. : "LSA Oscillator Diode Theory", 1967, J. Appl. Phys., 38, pp. 3096-3101
- [81] COPELAND, J. A. : "Doping Uniformity and Geometry of LSA Oscillator Diodes", 1967, IEEE Trans. Elec. Dev., Vol ED-14, p 497
- [82] HASHIZUME, N., KATAOKA, S. : 1970, Electron. Lett., Vol 6, 34 pp. 1478 - 1485
- [83] TAKEDA, Y., SHIKAGAWA, N., SASAKI, A. : "Transferred Electron oscillation in  $n\text{-In}_{0.47}\text{Ga}_{0.53}\text{As}$ ", Solid-State Elec., 1980, 23, pp. 1003-1005
- [84] ZHAO, Y. Y., WEI, C. J., BENEKING, H. : "Transferred Electron oscillations in  $\text{In}_{0.47}\text{Ga}_{0.53}\text{As}$ ", Elec. Lett., 1982, 18, pp. 835-836
- [85] HOLWAY, L. H. : "Filamentary Thermal instabilities in IMPATT diodes", 1977, IEEE Tran. Elec. Dev., Vol ED-24, 2, pp. 80-86
- [86] CHIGOGIDZE, Z. N., KHUCHUA, N. P., GUTNIK, L. M., KHARATI, R. G., VARLAMOV, I. V., BEKIREV, U. A., TYUTYUN, A. A. : "Mechanism of Failure of Gunn Diodes", Sov. Phys. Semi., 1973, 6, 9, pp. 1443-1447
- [87] OLSON, H. M. : "Thermal Runaway in IMPATT diodes", 1975, IEEE Tran. Elec. Dev., Vol ED-22, pp. 165-168
- [88] THIM, H. W. : "Computer Study of Bulk GaAs Devices with Random One-dimensional doping Fluctuations", J. Appl. Phys., 1968, 39, pp. 3897
- [89] HERNANDEZ "Fabry-Perot Interferometers", McGraw Hill, London

- [90] VAUGHN "The Fabry-Perot Interferometer", Pergamon Press, New York
- [91] PATRICK, W., MACKIE, W.S., BEAUMONT, S.P., WILKINSON, C.D.W. : "Low temperature annealed contacts to very thin GaAs epilayers", Appl. Phys. Letters, 1986, 48, 15, pp. 986-988
- [92] BRASLAU, N. : 1983, Thin Film Solids, 104, pp. 391
- [93] KUAN, T. S., BATSON, P. E., JACKSON, T. N., RUPPRECHT, H., WILKIE, E. L. : J. Appl. Phys., 1983, 54, pp. 6952
- [94] THIM, H.W., BARBER, M.R., HAKKI, B.W., KNIGHT, S., UENOHARA, M. : "Microwave amplification in a DC-biased bulk semiconductor", Appl. Phys. Letters, 1965, vol 7, pp 167-168
- [95] ROBERTS, J. K., MILLER, A. R. : "Heat and Thermodynamics", 1960, Blackie, Glasgow
- [96] CHAPMEN, A. J. : "Fundamentals of Heat Transfer", 1987, New York, MacMillan
- [97] BUTTON, K. J. : "Infrared and Millimetre waves", Vol 1, Academic Press, New York, 1979
- [98] WEBB, P. W. : "Measurement of Thermal Transients in Semiconductor power devices and circuits", 1983, Proc. IEEE Pt I, 130, pp. 153-159
- [99] GOELL, J. E., STANDLEY, R. D. : "Loss Mechanisms in Dielectric Waveguides", 1969, Bell Sys. Tech. J., pp. 3445-3448
- [100] JOYCE, W. B., DIXON, R. W. : "Thermal resistance of Stripe lasers", 1975, J. Appl. Phys., 46, pp. 855-862
- [101] DUKA, E. : "Thermal Resistance and temperature distribution in DH lasers : calculation and experimental results", 1979, IEEE J. Q. E., 15, pp. 812-817
- [102] NAKWASKI, W. : "Simple Formulae giving temperature profiles in active layer of stripe-geometry laser diodes with oxide barriers", 1983, Elec. Lett., 19, pp. 368-370
- [103] NAKWASKI, W. : "Dynamical thermal Properties of stripe-geometry laser diodes", 1984, Proc. IEEE, 131, pp. 49-102
- [104] OLSON, H. M. : "A mechanism for Catastrophic failure of avalanche diodes", 1975, IEEE Tran. Elec. Dev., Vol ED-22, pp. 842-849
- [105] WESTBROOK, L. D., ROBSON, P. N., MAJERFELD, A. : "Strain-induced Optical Waveguiding in GaAs Epitaxial Layers at 1.15  $\mu\text{m}$ ", 1979, Elec. Lett., Vol 15, 3, pp. 99-100

